Controlled crystallisation of calcium phosphate and calcium carbonate via bio-inspired approaches: additives and confinement

Bram Cantaert

Submitted in accordance with the requirements for the degree of
Doctor of Philosophy

The University of Leeds
Faculty of Mathematics and Physical Sciences
School of Chemistry

May, 2013

The candidate confirms that the work submitted is his/her own, except where work which has formed part of jointly-authored publications has been included. The contribution of the candidate and the other authors to this work has been explicitly indicated below. The candidate confirms that appropriate credit has been given within the thesis where reference has been made to the work of others.

"Chapter 4: Concerning Positively Charged Additives and their Effect on Crystallization" is based on the paper "*Think Positive: Phase Separation Enables a Positively Charged Additive to Induce Dramatic Changes in Calcium Carbonate Morphology. Bram Cantaert , Yi-Yeoun Kim , Henning Ludwig , Fabio Nudelman ,Nico A. J. M. Sommerdijk , and Fiona C. Meldrum Adv. Func. Mater 22(5), 907-9015*". All the experimental work done is attributable to me, under the supervision of Prof. Fiona Meldrum, except the cryo-TEM work which was done at Eindhoven University by Dr. Fabio Nudelman in cooperation with me.

Acknowledgements

Abstract

This thesis describes the investigation of the two bio-inspired approaches, confinement and additives, to manipulate the crystallization of calcium carbonate and calcium phosphate. The first experimental chapter deals with the investigation of calcium phosphate rods grown in confined environments in the absence and presence of polyaspartic acid. Although similar results were obtained in the absence and presence of the additive, growing calcium phosphate in confinement allowed formation of polycrystalline rods with an orientation comparable to bone. This demonstrated that confinement may play a more significant role in bone formation than previously anticipated. The second chapter deals with the effect of positively charged additives on the crystallisation of $CaCO_3$. Although neglected before in literature, this chapter demonstrates that positively charged additives have a profound effect on the crystallisation of $CaCO_3$ changing the morphology to films and fibers. This morphology change was linked to a phase separation process, forming hydrated amorphous droplets of calcium carbonate by a carbonate-polymer interaction, which had the tendency to coalesce and form films. Fiber formation was attributed to oriented attachment of anisotropic particles due to unequal distribution of charge. In the third chapter, based on bone, the mineralisation of collagen by $CaCO_3$ was investigated. By formation of a highly hydrated liquid-like amorphous phase of $CaCO_3$, it was possible to infiltrate the nanoscale gaps of collagen. After crystallisation, nanocrystals of calcite and vaterite were formed, 5 nm thick, but randomly oriented, demonstrating collagen templates the shape but not the orientation of the crystals. In a final chapter hollow rods of $CaCO_3$ were formed by templating them inside membrane pores. The influence of time, pore size, additives and surface chemistry was investigated. Most hollow rods were formed at early timescales which filled up at later times. By changing the surface chemistry, the amount of hollow rods increased significantly in the 200 nm pores.

Table of Contents

Chapter 1: General Introduction

Chapter 2: General Experimental Methods and Techniques

Chapter 3: Mimicking Bone Formation by Confinement and Addition of Polyaspartic acid

Chapter 4: Concerning Positively Charged Additives and their Effect on Crystallization

Chapter 5: Templating Calcium Carbonate into Nanoscale Plate-shaped Crystals by the Use of Collagen

Chapter 6: Formation of Hollow Calcium Carbonate Rods

Chapter 7: Conclusions and Future Work

References

Appendix: List of Abbreviations

List of Figures

Chapter 1: General introduction

Chapter 4: Concerning Positively Charged Additives and their Effect on Crystallization

Chapter 5: Templating Calcium Carbonate into Nanoscale Plate-shaped Crystals by the Use of Collagen

Chapter 6: Formation of Hollow Calcium Carbonate Rods

Chapter 7: Conclusions and Future Work

List of Tables

Chapter 1: General Introduction

Chapter 1: General Introduction

1.1 Biomineralisation

This thesis is about the investigation and understanding of the formation of biominerals, and the application of this knowledge to the manufacture of new hybrid materials and the development of new fabrication techniques. Biominerals are, as indicated by the name, minerals, or inorganic materials, formed in or by a biological environment (or system). Some examples of biominerals are the exciting structures of the skeletons of invertebrates such as sea shells, nacre, sea urchins, coral and diatoms of algae but also the bones and teeth of vertebrates. Although studied for quite some time, (hard to tell how long but diatoms have been studied in the 1700[1]) much enigma still exists about biominerals. Until now over 60 different kinds biological minerals can be distinguished of which the main ones are: calcium carbonate (as good as most inorganic material for the invertebrates), calcium phosphate (almost all inorganic material in the vertebrates), SiO_2 (as silicic acid in diatoms) and iron oxides (in snail teeth and magnetotactic bacteria)[2].

Biominerals have many functions and are used, for example, for protection of the organism or providing structure (shells and bone). They can also act as tools for grinding and cutting (teeth) or for the facilitation of orientation, e.g. iron oxide crystals in magnetotactic bacteria are used by the organisms to align themselves with respect to the Earth's magnetic field. One fascinating hallmark of biominerals is that they often show little structural resemblance to their synthetic counterpart. For example, sea urchin spines are single crystals of calcite ($CaCO_3$), yet when made synthetically in the lab, rhombohedra (beautiful and single crystal nevertheless) are typically formed. The same accounts for calcium phosphate in bone, which comprises calcium phosphate crystals with a thickness of around 1.5-4.5 nm[3], much thinner than the HAP crystals formed in the laboratory. As well as these elaborate morphologies, biominerals can often be characterised by extraordinary strengths and hardnesses, mainly due to their hierarchical ordering and composite structure being constructed out of an inorganic and organic part. Bone, for example, is a composite material consisting of about 30% organic matrix, collagen, and 70% inorganic material, calcium phosphate, contributing to the remarkable strength of the material which our human body needs. The organic macromolecules are a vital part of the construction of the mineral, being involved in nucleation and growth control, but also in the definition of the material's mechanical properties[4]. The most remarkable feature of biominerals, though, is that they are formed

with these superior properties and characteristics under atmospheric pressure and temperature, which is almost unachievable for man-made synthetic materials.

To illustrate the features discussed above, the structure of nacre is shown below (Figure 1). Nacre (or mother of Pearl) can be found in the inner shell of molluscs and is an inorganic-organic composite material[4-6]. It consists of 99% of hexagonal, plate like crystals of aragonite (mineral of calcium carbonate), together with ~ 1% of thin, less than 10 nm, organic material which acts as a "mortar" between the calcium carbonate "bricks". The platelets themselves are about 0.5 nm thick and 5–15 μm in diameter, and are therefore distinct from aragonite formed in the lab. They are arranged in a parallel fashion and the organic layers are sandwiched in between. Remarkably, each tablet forms at a specific location on the matrix surface but independently from each other and then rapidly grows in a direction perpendicular to the matrix surface. The crystals first grow vertically, until they reach the next organic layer. In the next step they grow only laterally until they meet adjacent tablets[6]. Since the different layers of platelets on the organic matrix are not aligned, the organisation of the nacre looks like a "brick-mortar" structure (see Figure 1). Although the organic content of nacre is less than 1%, this brick-mortar structure gives nacre its remarkable strength, 3000 times higher than aragonite prepared in the lab[7], as crack propagation is inhibited by deflection at grain boundaries and cracks need to find a new way over and over again to propagate, causing the platelets to spring apart and the organic sheets to extend[8]. Since the size of the nacre platelets is in the same order of magnitude as the wavelength of visible light, light gets reflected by the platelets. At the same time, the platelets themselves are very thin, and light can pass through one layer before being reflected by the next. This makes rays of light with different wavelengths interfere constructively and destructively with each other at different angles, giving rise to its beautiful colours.
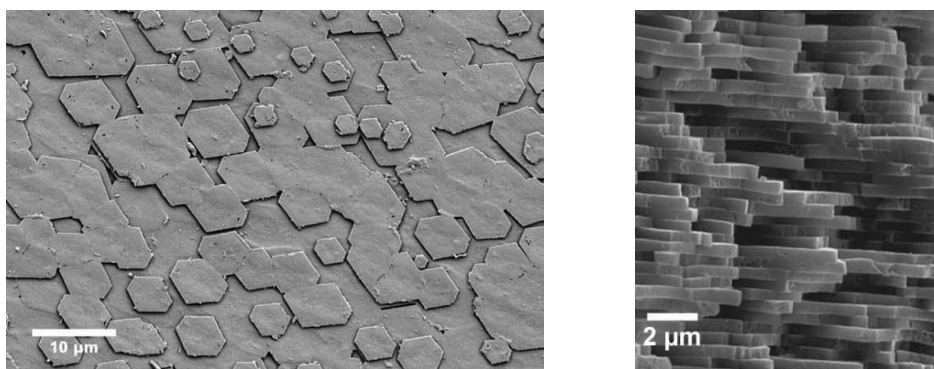
Figure 1: (a) Scanning electron micrograph of the growing layers of nacre. (b) Scanning electron micrograph of the cross-section of a fractured nacre surface demonstrating the layered structure of the nacre. Both images are taken from nacre of the bivalve mollusc *A. rigida.* Image adapted from ref. 6.

Biomineralisation processes can be divided into 2 different classes, based on the degree of biological control[4]. If the precipitation of the mineral happens as a result of interactions between the organism and its surroundings, while little or no control is exerted over the mineralisation process, it is termed "biologically induced mineralisation". If the organism, on the other, hand does exert control over the mineralisation process, relying on a number of key stages such as confining of a space forming an organic matrix, construction of the nucleation site and control of the ion input, the process is called "organic matrix mediated mineralisation" or "biologically controlled mineralisation. The first crucial step in this control of mineralisation is the initial isolation of space which is usually achieved by the use of cellular membranes, vesicles or pre-deposited macromolecular matrix frameworks. Organic macromolecules can then be applied to gain sophisticated control by further functionalization of the mineralisation environment[4].

Inspired by Nature and biominerals, a quest was started to unravel the mechanisms of biomineral formation, not only to understand but also to mimic, use, and even improve[9] the material characteristics. Being able to mimic biomineral formation would allow us to produce extraordinary materials under atmospheric conditions, without the need for energy-consuming techniques based on high pressure or temperature. This is particularly useful considering the strong requirement to produce advanced materials such as semiconductors, solar cells and optical and electronic thin films under environment friendly conditions with a high amount of control over the phase, size,

orientation and morphology of the component crystals[10]. Furthermore, understanding how minerals such as bone and teeth are formed also helps us in the development of new medicines and biomedical devices. Many of the biominerals formed by invertebrates are made from calcium carbonate and have been particularly well-studied because of their accessibility and high degree of crystallographic control[4, 11]. Calcium phosphates which can be found in bones and teeth have also been extensively investigated because of their remarkable mechanical properties and structures and their importance to health related issues[12].

1.2 Crystallisation

A crystal or crystalline material is defined as "a material in which the atoms are situated in a repeating or periodic array over large atomic distances. That is, long range order exists, such that upon solidification, the atoms will position themselves in a repetitive three-dimensional pattern, in which each atom is bonded to its nearest-neighbour atoms"[13]. In general, two different kinds of crystalline material can be distinguished, single crystal and polycrystalline material. A single crystal can be defined as "a solid body with a large coherence length, which shows diffraction behaviour characteristic of a perfect three-dimensional alignment of its building units"[14]. It has a rigid lattice of atoms or molecules at a characteristic location, with the unit cell being its smallest repeating unit. In theory, a perfect single crystal has no grain boundaries and contains a perfectly coherent lattice in all directions. Practically though, this ideal situation hardly ever exists since the crystal lattice is often tilted, twisted and/or shifted by varying degrees due to the presence of impurities and the mobility of crystallographic defects forming grain boundaries. A polycrystalline particle, on the other hand, is an agglomeration of many small crystals or so-called grains, with grain boundaries forming the interface between two ideal crystals in a polycrystalline material. In other words, the lattice planes in a polycrystalline material show no coherence from one grain to the next and as a consequence random crystallographic orientations can be observed[13].

In contrast to a crystalline material, amorphous materials are defined as substances lacking a long range order. "Amorphous" is quite a vague term though, and depending on the analytical technique applied for characterisation, different definitions can be given. TEM and XRD define amorphous materials as having a diffuse diffraction pattern or by the absence of characteristic peaks, indicating lack of structural periodicity

or long-range order. In contrast, under the optical microscope, amorphous character is linked to the characteristic of having a lack of birefringence and staying dark while rotated under crossed polarisers demonstrating they are isotropic[15]. Examples for amorphous material include some metals (dense packings of spheres), glass and silica (continuous random networks), polymers (random coils) and ice[16-19]. Some inorganic materials such as iron oxide[20], many carbonate minerals[21, 22], calcium phosphate[23] and recently calcium sulphate[24] have been reported to form amorphous phases, which can play a major role in biomineralisation as precursors to crystalline phases[20, 22, 23, 25]. As a result of this, there has been a paradigm shift in the past 10 years in the field of biomimetics and bioinspired research, related to the role of amorphous precursors in the fabrication of biomaterials[4, 12, 14, 26, 27] and new kinds of materials. Since these amorphous precursors can be moulded and formed into any shape, they provide the perfect tool for the synthesis of new materials and by subsequent crystallisation of the amorphous phase, crystals with extraordinary morphologies can be obtained[10, 28-31]. It has to be pointed out though, that amorphous precursors are not a necessity for obtaining unusual crystalline morphologies by templating[32, 33].

1.2.1 Polymorphism

An important characteristic of crystal formation is the occurrence of different polymorphs for one compound. Calcium carbonate for example, has three different crystalline polymorphs, being calcite, aragonite, vaterite[4]. Polymorphism is the result of the fact that the atoms or molecules constituting the crystals can be packed together in alternative ways or put together in different conformational arrangements. This means that each polymorph has a different crystal structure and therefore unit cell[34]. Polymorphism is an important aspect of crystallisation since different crystal structures are related to different mechanical, thermal and physical properties which might be wanted or undesirable. Depending on the temperature, pressure, solvent and even stirring speed, different polymorphs can precipitate out of the solution[35]. In some cases, the type of packing that will be selected will be driven by intermolecular interactions, while in other cases, entropic effects will be dominating. Transformation between two polymorphs is also possible and can occur in two different ways: either by reconstructive or by displacive transformation[36]. Reconstructive transformations occur when the two structures are so different from each other that the transition from one into

the other is only possible by a disintegration of the first polymorph followed by a reconstruction of the new one. This can occur readily in solution and the transformation of calcium carbonate aragonite into calcite is an example of this mechanism[36]. Displacive transformation occurs when the two structures are quite alike, and more subtle shifts occur in the molecular arrangements. In this case the nearest neighbours' interactions are preserved and only second neighbours change, which is possible during a solid state transformation with low activation energies and high transformation rates[36].

1.2.2 Crystal system

Briefly, crystals can be organised into 7 crystal systems according to their symmetry elements. The seven systems are shown in the table below along with their typical relative axial lengths and angles, lattice system and an example of a mineral[37].

Table 1: The seven crystal systems with typical axial lengths and angles, lattice system and a mineral example.

Crystal family	Crystal system	Axial lengths and angles	Lattice system	Example
Triclinic		$a{\neq}b{\neq}c$ $\alpha{\neq}\beta{\neq}\gamma{\neq}90°$	Triclinic	Turquoise $(CuAl_6(PO_4)_4(OH)_8)$
Monoclinic		$a{\neq}b{\neq}c$ $\alpha{=}\gamma{=}90{\neq}\beta{>}90°$	Monoclinic	Brushite (CaP)
Orthorhombic		$a{\neq}b{\neq}c$ $\alpha{=}\beta{=}\gamma{=}90$	Orthorhombic	Aragonite $(CaCO_3)$
Tetragonal		$a{=}b{\neq}c$ $\alpha{=}\beta{=}\gamma{=}90$	Tetragonal	Rutile (TiO_2)
Hexagonal	Trigonal	$a{=}b{=}c$ $\alpha{=}\beta{=}\gamma{\neq}90$	Rhombohedral	Calcite $(CaCO_3)$
	Hexagonal	$a{=}b{\neq}c$ $\alpha{=}\beta{=}90, \gamma{=}120$	Hexagonal	Hydroxyapatite (CaP)
Cubic		$a{=}b{=}c$ $\alpha{=}\beta{=}\gamma{=}90$	Cubic	Halite (NaCl)

<u>1.2.3 Classical crystallisation</u>

1.2.3.1 Nucleation

Crystallization can occur when a solution is supersaturated with molecules, or in the case of salts, with different ions. Supersaturation, S, can generally be seen as the thermodynamic driving force for nucleation and can be defined as a measure of the degree by which the concentration of the ions in the solution exceeds their solubility. Several ways exist to induce supersaturation in solution such as increase or decrease of the temperature, change of pressure or evaporation. The expression for supersaturation can be written as

$$S = C / K_{sp}$$
<div align="right">Equation 1</div>

where C represents the concentration of the species and K_{sp} the equilibrium solubility product. Very often multiple species are involved in the expression of the supersaturation and C is in this case the product of the concentrations (or more precisely, the activities) of the individual components present in solution (C = [C_a] [C_b]…). The equilibrium solubility product K_{sp}, is unique for every material, and for the example $CaCO_3$ can be written as

$$K_{sp} = \frac{[Ca^{2+}][CO_3^{2-}]}{[CaCO_3]}$$
<div align="right">Equation 2</div>

where the expression demonstrates the supersaturation is directly related to the solubility of each species. Therefore, another effective way of increasing the supersaturation is the addition of another component to the reaction solution, thereby reducing its solubility by pushing the solubility product to the left (Equation 3).

$$CaCO_{3(s)} \rightleftharpoons Ca^{2+}{}_{(aq)} + CO_3^{2-}{}_{(aq)}$$
<div align="right">Equation 3</div>
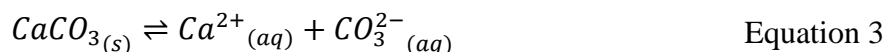
Also since each polymorph of a crystal has a different solubility product, control over polymorph can be achieved by control over concentration and the supersaturation (also see section 1.2.3.4).

Chapter 1: General Introduction

Supersaturation can also be related to the chemical potential and free enthalpy of the system and can be written as

$$\Delta\mu = -k_B T \ln S \qquad\qquad \text{Equation 4}$$

With $\Delta\mu$ the change in chemical potential or change in free energy per mass, k_b the Boltzmann constant, T the temperature and S the supersaturation of the solution.

Once the supersaturation is reached, the ions in solution will come together and form complexes due to local fluctuations of the supersaturation in the solution. These clusters are very unstable though due their large surface and small volume. The Gibbs free energy of ions coming together forming a cluster can be expressed as the sum of a surface and a volume term:

$$\Delta G_i = \Delta\mu_i + \gamma A(i) \qquad\qquad \text{Equation 5}$$

With ΔG_i the chemical potential, $\Delta\mu_i$ the chemical potential of the cluster (usually negative, related to the strength of the new bonds being formed), A(i) the surface area of the cluster and γ the surface free energy, (which is usually positive).

This expression shows the free energy is a pay off between the beneficial formation of bonds in the bulk of the cluster, which is negative, and the cost of energy for the creation of a new surface, which is positive. For a spherical cluster with radius r equation 5 can be written as.

$$\Delta G = \left(\frac{4\pi r^3}{3\Omega}\right) k_b T \ln S + 4\pi r^2 \gamma \qquad\qquad \text{Equation 6}$$

With r the radius of the sphere, Ω is the volume of a molecule inside the crystal, k_b the driving force per molecule of crystal formation and γ the interfacial free energy between the forming nucleus and the solution. The surface term is now proportional to $4\pi r^2$ while the volume term is proportional to $4\pi r^3$.

When the cluster grows, its surface will increase with r^2, while its volume will increase with r^3 (see Figure 2). At the beginning, for small r, the surface contribution will be bigger than the volume factor which means that the free energy will be positive. Yet since the volume increases with r^3, the volume contribution will grow faster than the surface factor and at some point, when the nuclei reaches the size of what is called the critical nucleus at size R^*, the volume factor will compensate for the surface factor and the nucleus will become more stable the larger r gets. The free energy is at a maximum at this point which needs to be reached by the system for nucleation to occur and crystal growth to start. After this point, on continued growth, the gain in lattice bulk energy will further overcompensate for the loss in surface energy and the crystal will continue to grow until no more ions are available (below supersaturation). For highly supersaturated solutions, a high number density of nuclei will be produced. For these kinds of solutions, agglomeration will be the most dominant growth mechanism in the solution, leading to polycrystalline particles[38].
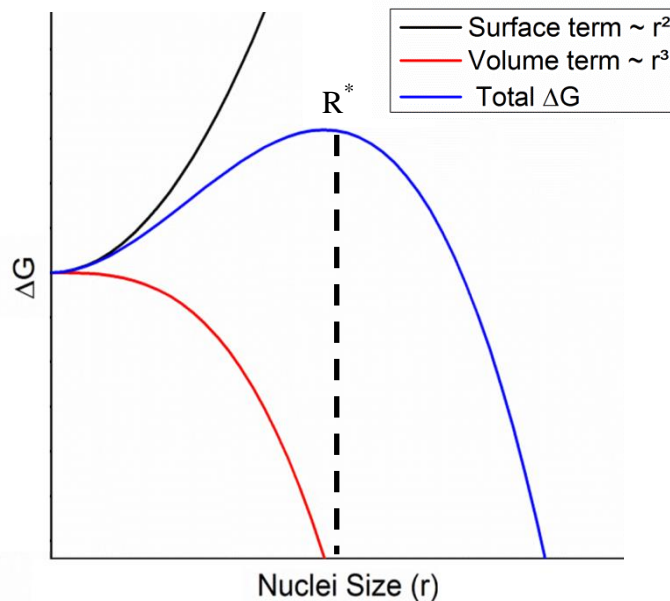
Figure 2: The change in free energy ΔG with size of the sphere (r). R^* represents the critical size for the nucleus.

Finally it needs to be noticed that although a crystal will continue to grow for as long as the solution is above its supersaturation, a nucleation step always has to occur first before the crystal can start to form. If for any reason nucleation cannot occur (for

example due to the presence of additives), supersaturation can be a stable state without any change in solution.

Depending on the presence or absence of a surface, two kinds of nucleation can occur: homogeneous and heterogeneous nucleation. Homogeneous nucleation is the type of nucleation as described in previous paragraphs and takes place in the solution. Heterogeneous nucleation, in contrast, takes place on surfaces or dispersed components already present in the solution, such as dust particles or crystal seeds, which act as nuclei and provide the starting surface for crystallisation. Since a surface is already available during heterogeneous nucleation, the surface energy term will be much decreased and with it also the general entire energy demand for nucleation since the interfacial energy between the cluster and interface is almost always lower than that between the cluster and bulk solution. This makes heterogeneous nucleation less energy-demanding than homogeneous nucleation and is therefore the biggest driving force for crystallisation happening in normal systems. Heterogeneous nucleation will always prevail at low supersaturation, but at high supersaturation, homogeneous nucleation can also occur since the nucleation sites for heterogeneous nucleation will be much more limited in comparison to those for homogenous nucleation.

1.2.3.2 Crystal growth

In the classical picture of crystallisation, growth occurs via a layer-by-layer adsorption of solute molecules and atoms to an existing crystal face. During the crystallisation process "growth units" diffuse to the crystal surface where they can become attached to the surface. These units form the so-called adsorption layer, with a typical thickness of about 1 nm[39] and can then remain at their initial point of attachment, diffuse across the crystal surface and get integrated in the structure of the crystal, or return to solution[38]. Growth of a crystal surface happens when the flux of atoms, ions or molecules attaching to the surface is greater than that of the ones re-entering the solution. The rate at which this happens depends on the ability of the specific surface to catch ions or growth units, which in turn depends upon the strength and the number of interactions that can be made[36].

On the molecular level, before being attached to a surface, an incoming ion can encounter three different environments (see Figure 3) as defined by the Hartman-

Perdock system[40]: a kinked surface, which offers three bonds for attachment (Figure 3a denoted by K), a stepped surface which provides two bonds (denoted by S), and a flat or smooth surface which can make a maximum of one bond with the incoming atom (denoted by F). To reach the binding site on the surface, the growth unit will have to overcome a number of energy barriers such as (partial) desolvation, diffusion across the surface to a step site, and further desolvation to enter a kink site. It has to be stated though that crystal growth is rarely perfect, and a number of imperfections often exist in the form of vacancies or dislocations, with screw dislocations as the most prominent example[14]. As shown in Figure 3b, faces that grow quickly vanish during crystal growth, while slow growing faces will stay, and dominate the final shape of the crystal.
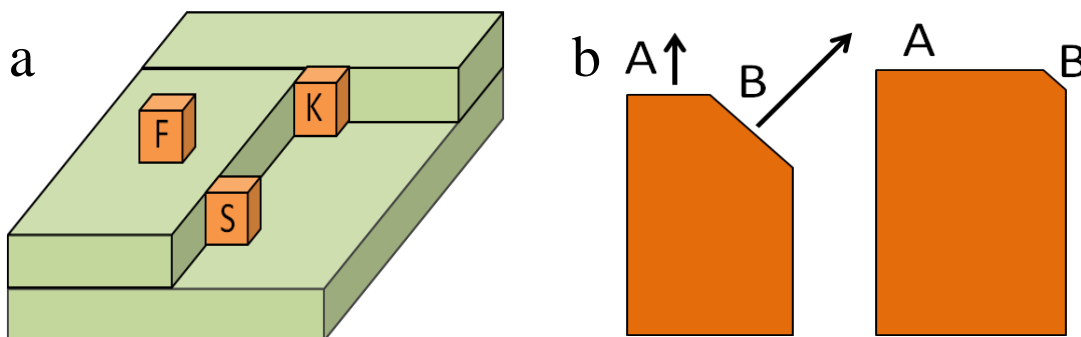
Figure 3: (a) Schematic representation of the growth of a crystal with the face, kink and step sites. The schematic in (b) shows the growth of a crystal where surface B grows much faster than surface A and is finally almost lost in the crystal morphology.

Molecules or ions that are located at the surface of a crystal will not be homogeneously surrounded by other ions or molecules and will therefore be coordinatively unsaturated and unstable and will easily dissolve again[36]. It is known that the solubility of crystals increases with decreasing size which gives rise to what is called Ostwald ripening, producing bigger crystals at the cost of smaller ones. This is caused by the fact that when the solution is in equilibrium with large crystals, it will be undersaturated with respect to the smaller ones. This will give rise the dissolution of the small crystals producing ions for the bigger crystals which those will use to continue to grow. In the end, only big crystals remain.

It is easily understood that binding of an ion to a flat surface will be the most energy-demanding, since in this kind of binding the ion has the least number of neighbours

(only one) in comparison with an atom attaching to a stepped surface (2 neighbours) or a kinked surface (3 neighbours). The attachment of the growth unit will be preferentially at the kinked surface, so the kink moves along the step until it is completed and a new step is started. Because of this, kinked or stepped surfaces are quickly eradicated, explaining why most crystals have flat faces, sharp corners and straight edges. Since attachment and growth mainly occurs at kink and stepped surfaces, it is important for a flat surface to be able to roughen and provide new kink and step sites so that growth can continue to occur. This depends on the energy required to remove one block from a complete face, and using it to start a new layer on a flat surface (Figure 4)[36].
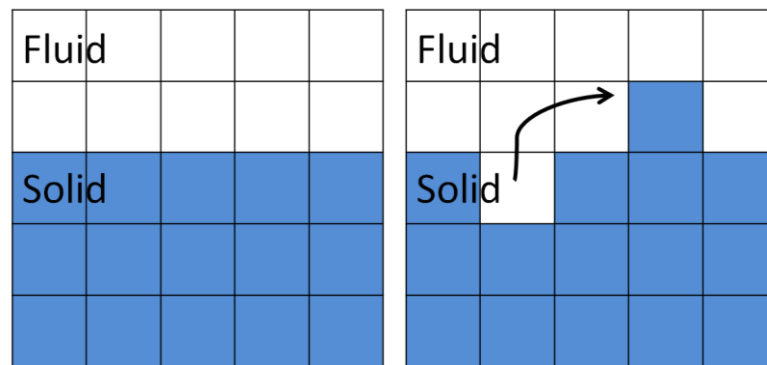
Figure 4: Schematic drawing of the roughening of a solid-fluid interface. The ease by which this one block is moved and the surface is roughened controls the crystal growth mechanism. Adapted from ref. 36.

This energy can be expressed as the sum of three different interaction energies (solid-solid (φ_{ss}), liquid-liquid (φ_{ll}) and solid-liquid (φ_{sl}) interaction energy) and can be written as followed (based on Temkin model)[41]:

$$\Delta E = 2\varphi_{ss} + 2\varphi_{ll} - 4\varphi_{sl} \hspace{3cm} \text{Equation 7}$$

If this energy is low and less than 3 k_BT, the energy required to form a new step will be low enough, and it will be therefore possible to form new kink and step sites on the surface. This guarantees that there will be plenty of growth sites for any incoming ions and growth will be continuous in this case. When the energy is between 3 and 5 k_BT, the inherent roughness of the interface decreases and incoming growth units will find it more difficult to find a growth site. They will therefore return to the fluid phase or will

join other adsorbed growth units to form surface nuclei or islands which will provide steps and kinks for further growth and surface nucleation will become the predominant growth mechanism. When the energy rises above 5 k_BT, step formation is as good as non-existent and growth can only occur by built in lattice defects, such as screw dislocations. In this case, the growth rate will vary widely for the individual crystals[36].

1.2.3.3 Thermodynamically controlled crystallisation growth

From a thermodynamic point of view, the different crystal morphologies that are formed for a certain type of mineral are due to the different surface energies of the crystal faces and also depend on the environmental conditions in which they have grown (pH, temperature, absence or presence of additives). Generally, the interfacial energy of a crystal face depends on the number of "dangling" surface bonds, minus the interaction energy of the crystal surface with the surrounding medium such as solvation or hydration in the case of a liquid medium[14]. It is therefore understandable that very polarisable substances like ionic crystals will have a high surface tension, while organic crystals which are principally based on van der Waals interactions, will have a lower surface energy. Faces that have high surface energies will grow quickly and vanish during crystal growth, while the opposite is true for faces with low surface energies. These will grow slowly and dominate the final shape of the crystal (see Figure 3). By manipulating the surface energies of the surfaces, it is therefore possible to manipulate the shape of the crystals, an observation which is known as Wulff's rule[42]. The use of additives is a common technique to achieve thermodynamic control over crystallisation, influencing the surface energies of the surfaces. This will be further demonstrated in chapter 4. It is important in this case that the concentration of the additives is low enough, since high additive concentrations will lead to a surface coverage of the growing nucleus with additives and therefore a quenching of its growth[14].

1.2.3.4 Kinetically controlled crystallisation and Ostwald's step rule

Thermodynamic control is usually achieved at low supersaturations, allowing the classical crystallization pathway to occur alongside an ion-by-ion growth model. Under high supersaturation conditions though, crystallisation is under kinetic control and can result in the formation of unexpected polymorphs or phases and their associated different morphologies. In general, kinetic polymorph control is mainly based on the modification of the different activation-energy barriers of nucleation, growth and of

phase transformation, and in this case the classical crystallisation pathway will occur according to the so-called Ostwald's step rule, where crystallisation is described as a sequential process involving structural and compositional modifications rather than a single-step pathway[14, 43]. Figure 5 shows the manifestation of Ostwald's "step rule" for calcium phosphate with the energy barriers and transition states that might occur when crystalline hydroxyapatite (HAP) forms from a solution via the traditional ion-by-ion route or an amorphous intermediate (in this case amorphous calcium phosphate (ACP)).
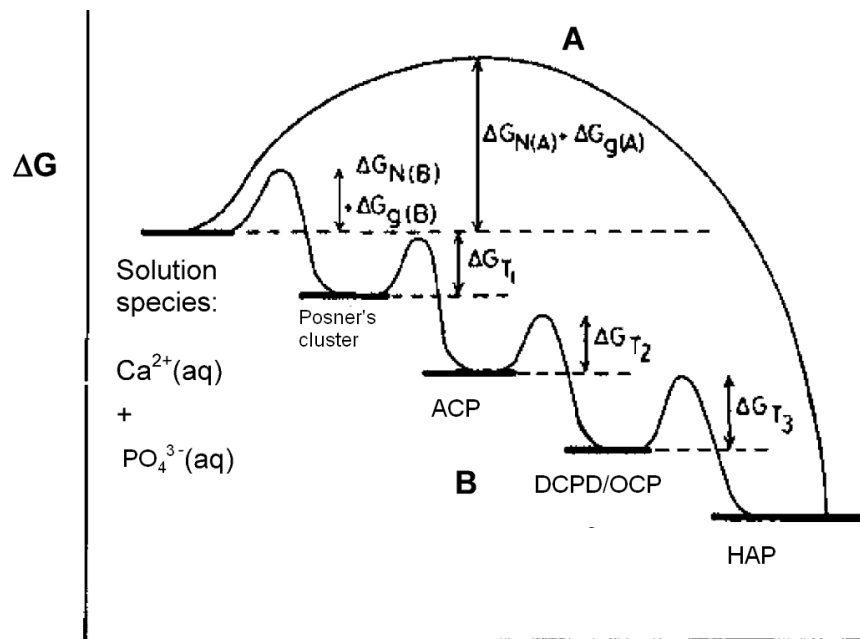
Figure 5: Schematic presentation of Ostwald's "step rule" for calcium phosphate. Route A is the traditional crystallisation pathway under thermodynamic control where HAP is formed by the ion-by-ion route from solution without any intermediate phases. Route B is a lower energy pathway under kinetic control, occurring via the amorphous precursor phase and other metastable phases. (Diagram not to scale). Adapted from ref. 2, 12.

According to Ostwald's "step rule" the less organised and less dense phase is formed first, which is often an amorphous phase such as ACP. In a next step, the amorphous phase dissolves or evolves into more stable, less soluble mineral form such as dicalcium phosphate dihydrate (DCPD) or octacalcium phosphate (OCP), to develop eventually to the most stable phase, hydroxyapatite (HAP). The kinetic transformation is in the order of increasing thermodynamic stability but it has to be noted that all polymorphs or phases do not necessarily appear along such a pathway[14]. The stabilities of the

intermediate phases and their rate of transformation depend basically on the solubility of the minerals or phases, but also on their free energies of activation and nucleation within different environments, something which is controllable by, for example the addition of additives. Previously it has also been stated that for calcium phosphate the amorphous phase is preceded by a Posner's cluster[44-46] which recently could be identified as calcium triphosphate ion-association complexes[47].

Working at high supersaturations might also lead to high nucleation rates and diffusion controlled crystallisation, with dendritic and spherulitic growth processes a as consequence[38, 48].

1.2.4 Non-classical crystallisation pathways

1.2.4.1 Mesocrystal formation and oriented attachment.

In addition to the formation of unstable kinetic crystal forms, kinetic control and high supersaturations also results in the formation of many crystalline nuclei. In a non-controlled way this leads to the formation of polycrystalline particles based on a non-oriented aggregation of nanoparticles. By the use of additives however, it is possible to stabilise the nanoparticles and control their aggregation process. In this case, a different pathway of non-classical crystallization can come into play which involves the oriented attachment and fusion of particles followed by the formation of a product with single crystal characteristics. Often this leads to the formation of a so-called mesocrystal or "mesoscopically structured crystal", which can be defined as "a crystal comprising a 3D array of iso-oriented single crystal particles of size 1–1000 nm (mesoscale dimensions). The highly oriented subunits therefore distinguish a mesocrystal from a randomly oriented polycrystal, and the identifiable nano-sized building units distinguish it from a single crystal containing impurities" [49]. It is emphasised that the term mesocrystal specifically defines the structure of a material rather than its mechanism of formation.[49]

Figure 6 shows a schematic representation of the difference between classical and non-classical crystallisation. As discussed before, in the classical crystallisation model (pathway a), crystallisation starts from primary building blocks such as ions and molecules, forming unstable clusters which form and dissolve again, until the critical nucleus is formed, which leads to a continued growth of the crystal by ion-by-ion into a macroscopic single crystal. The non-classical crystallisation pathway (pathway b and c)

is particle-mediated and involves a mesoscopic transformation process[50-52]. The two main pathways are summarised in Figure 6.[52]
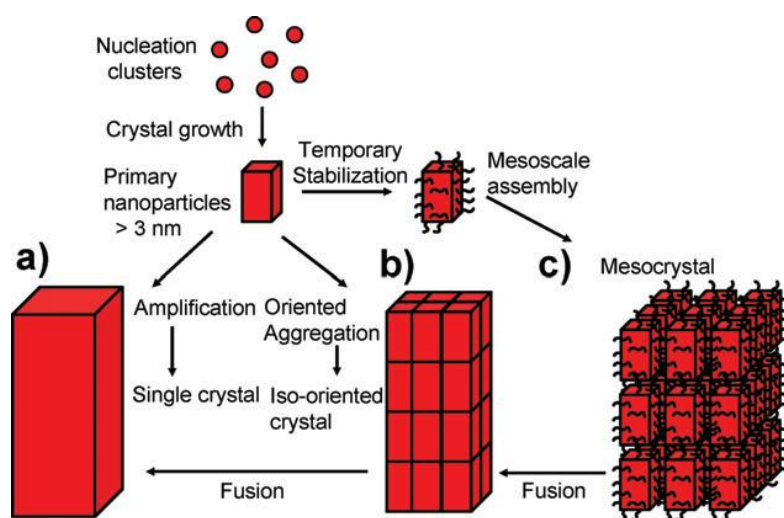
Figure 6: Schematic representation of classical and non-classical crystallization. (a) Shows the classical crystallisation pathway to a single crystal. (b) Shows an oriented attachment pathway of primary nanoparticles, forming an iso-oriented crystal. (c) Shows the pathway for mesocrystals formation via a mesoscale self assembly of nanoparticles, temporarily stabilised by organics. Image reproduced from ref. 52.

Pathway b describes the oriented attachment process which involves the arrangement of primary particles into an iso-oriented crystal (b) as well as the formation of a single crystal after fusion of the nanoparticles (a). Oriented attachment is a well-known phenomenon where primary nanoparticles spontaneously self-organise into a superstructure with a common crystallographic orientation[53, 54]. This is followed by the joining of these particles at a planar interface forming one connected entity. The driving force for this process is a reduction in the surface energy. Two nanoparticles close enough to each other are mutually attracted by van der Waals forces, yet because of their thermal energy they are still able to rearrange themselves to find the low-energy configuration represented by a coherent particle-particle interface[52]. Oriented attachment has been a well known phenomenon in crystallisation and the first experimental observations were made on nanocrystalline titania prepared under hydrothermal conditions[14, 55]. The oriented attachment mechanism is kinetically of second order in the number of primary particles and is particularly relevant in the nanocrystalline regime since in this case, particles with high specific surface areas

preferably fuse together due to the gain of a substantial amount of energy by elimination of two high-energy surfaces[56] and increase in entropy due to displacement of molecules attached on the fusing interfaces.

In principle there are two main ways for achieving mutual orientation of the two nanoparticles. One is the effective collision of particles which have a mutual orientation. The second is a coalescence mechanism made possible by particle rotation in weakly coagulated samples where nanoparticles still have small degrees of rotational freedom[14, 53]. By the help of liquid cell in situ TEM it was recently possible to describe this last mechanism during the formation of iron oxyhydroxide particles by oriented attachment[57]. It was observed that the particles underwent continuous rotation and highly direction-specific interactions, until they found a perfect lattice match. They then jumped into contact over distances of less than 1 nanometer, and merged together following atom-by-atom addition, forming one crystal[57].

Pathway c describes the formation of an iso-oriented crystal through oriented aggregation of stabilized units and the subsequent fusion of those units to form a single crystal. Mesocrystals can be formed via such mesoscale assembly when nanoparticles are coated by organic components. Different mesocrystals have been formed of $CaCO_3$ and other minerals by addition of additives such as polystyrene sulfonate (PSS)[58], block copolymers[59-61] and other kinds of additives[62, 63].

Currently, three different mechanisms have been proposed for the mutual 3D alignment of the nanocrystals into the crystallographic register (see Figure 7). The first mechanism requires the presence of directional physical fields such as magnetic, electric, or dipole fields, or possible other polarization forces. Primary particles with anisotropic properties are essential in this process. A second mechanism is based on the formation of so-called mineral bridges providing the connection between the nanoparticles, generating a coherent single crystal[49, 64]. The concept of mineral bridges has been used before to explain mutual *c*-axis orientation of the aragonite platelets in nacre, where experimental support was given for crystal growth through mineral bridges between successive aragonite tablets[65]. Also during formation of a mesocrystalline structure of the sea urchin spine mineral bridges are believed to play a role[49]. Finally a third mechanism involves precipitation in a constrained environment, where the mechanism is explained by simple geometric arguments and the nanocrystals align by

spatial constraints. Upon growth of the anisotropic nanoparticles in a constrained environment, the particles will align due to space restrictions leading to the formation of a mesocrystal. Depending on the surface energies and interaction potentials of the nanocrystals, it is assumed the pathway will be along pathway (a) (high energies and potentials), (b) (intermediate) or (c) (weak).
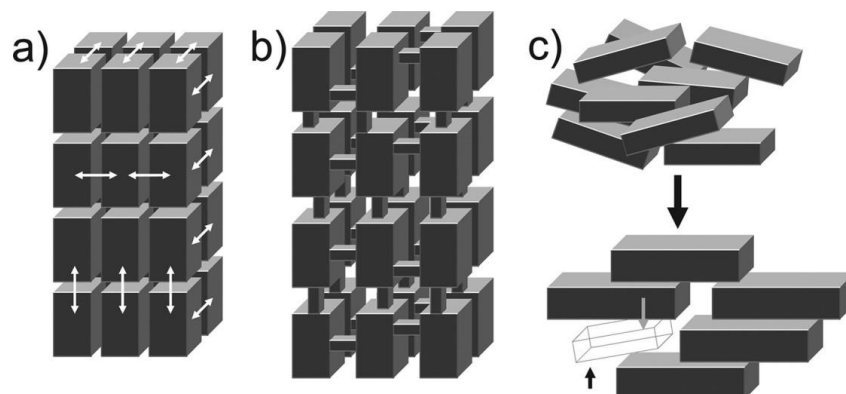
Figure 7: The three principle mechanisms for particle alignment into a mesocrystal. (a) Shows the mechanism where particles align due to directional physical fields such as electric, magnetic or dipole fields. Arrows indicate the mutual alignment. (b) Shows the formation of mineral bridges between two nanoparticles and (c) shows nanoparticle alignment due to spatial constraints. Adapted from ref. 14, 54.

Since classical single crystals and mesocrystals both diffract like a single crystal, it is very difficult to distinguish them from each other. Features such as the appearance of a rough surface, high surface areas, XRD broadening and TEM observation of subunits have been used as proof of mesocrystal formation[64, 66] although this isn't always conclusive.

1.2.4.2 Prenucleation clusters

Recently, it has been shown that $CaCO_3$ nucleation might occur through another non-classical process, where stable, so-called prenucleation clusters (PNC) are formed[67, 68]. By titration of calcium chloride into a solution of carbonate buffer[68], it was found that more calcium was bound before and after nucleation than expected. This was ascribed to the formation of stable clusters before nucleation, so-called prenucleation clusters. The formation of these clusters was found to be present in saturated and under-saturated conditions before and after nucleation and they are believed to exist in a reversible equilibrium with their dissolved components, lying in a minimum of Gibbs free energy

(Figure 8). These PNCs are different from the monomer and dimer clusters described by the classical nucleation theory, since in that case the clusters are formed by a random driving force and are therefore a rare species in solution and very unstable[67]. The composition of the prenucleation clusters is still not very clear, but is believed to be amorphous and hydrated, with estimates for the size between 1.1 - 2 nm hydrodynamic diameter[67] corresponding to roughly 70 calcium and carbonate ions. Through cluster aggregation it is believed these clusters grow into crystalline $CaCO_3$ with or without precipitation of ACC as a precursor[67, 69]. Recent theoretical simulations proved that the calcium carbonate PNCs are actually highly dynamic and form a strongly hydrated polymeric species of alternating Ca^{2+} and CO_3^{2-} ions or a so-called dynamically ordered liquid-like oxyanion polymer (DOLLOP)[70]. It is believed that these structures are constantly changing their structure and remain in equilibrium with the solution, avoiding a phase boundary, which allows them to be stable structures in solution.
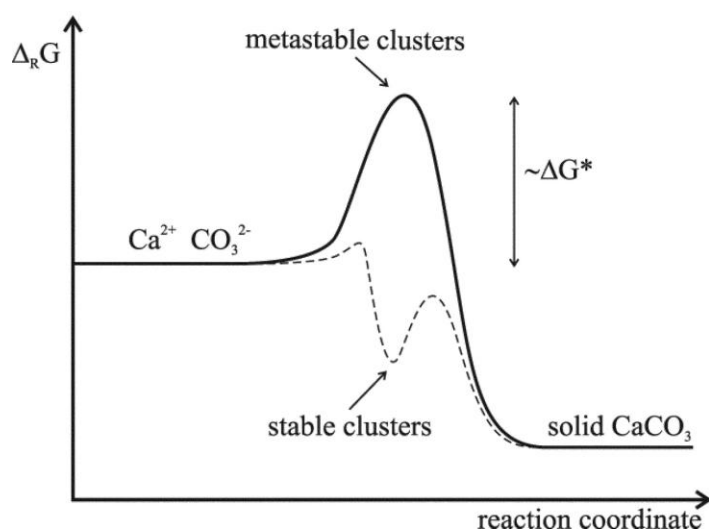
Figure 8: Schematic representation of the free-energy diagram versus the reaction coordinate. Image reproduced from ref. 68. The bold line shows the classical view where metastable clusters form and nucleation occurs once the critical nucleation enthalpy ΔG^{*} is overcome. The dashed line shows an alternative pathway where stable clusters are formed with an activation barrier which is negligible as compared with the thermal energy.

It was further discovered that these clusters were more thermodynamically stable at lower pH than at higher pH values, which appeared to correspond to different cluster structures[68]. It was found that more stable ACC (ACC I) was nucleated from the more

stable clusters at lower pH, with evidence of short-range structures analogue to calcite. The ACC found at higher pH values was less stable (ACC II) and exhibited short-range structures analogue to vaterite[68]. Figure 9 shows a comparison between the classical pathway and non-classical view through formation of prenucleation clusters.
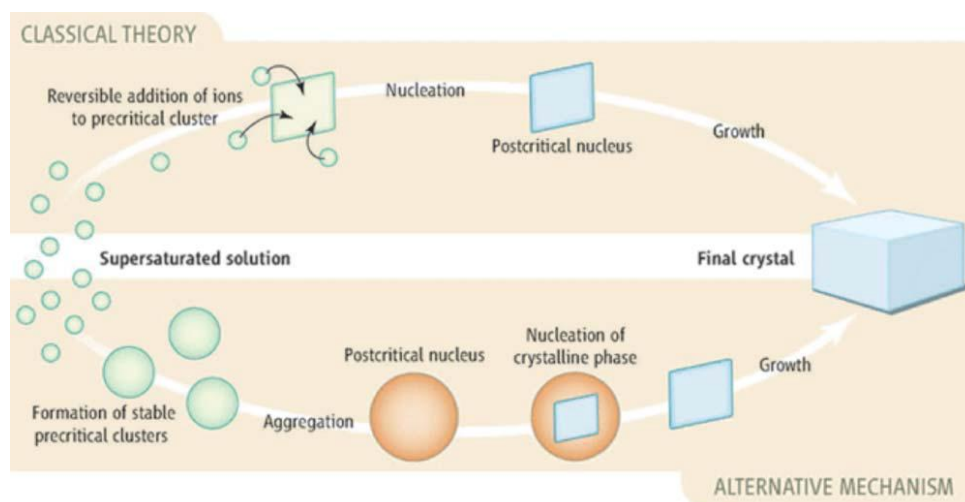
Figure 9: Schematic representation of classical and non-classical crystallisation pathways including the formation of prenucleation clusters. Image reproduced from ref. 67, 71.

Nucleation models involving pre-nucleation clusters have been proposed for organic systems[72, 73] and other inorganic systems[74] such as calcium phosphate[46]. More recent research though showed that the observed PNC clusters of calcium phosphate are in fact soluble ion association complexes $[Ca(HPO_4)_3]_4$ that form aggregates in solution[47]. These aggregates do not actually represent a fixed structural unit as was postulated for the original model of PNCs, but its chemistry changes stepwise towards the composition of the final product hydroxyapaptite, the most stable mineral of calcium phosphate. These complexes are identified with an excess of free energy which lowers the energy barrier to nucleation. Since this identifies the PNCs as merely ion-association complexes it is possible to agree their existence with the classical nucleation theories[47].

Recent findings based on molecular dynamic simulations reported the formation of an ion-rich fluid phase, that forms readily by a liquid-liquid phase separation within the range of concentrations for which pre-nucleation clusters of calcium carbonate are observed[75]. The liquid initially occupies a relatively small volume and therefore forms

a population of clusters which increase their mean radius as time to the one-third power. This spinodal decomposition mechanism might also give an alternative explanation for the observed features of PNCs, while preserving the long-standing physical concepts of the classical nucleation theory.

1.2.4.3 Polymer-induced liquid precursor (PILP)

The polymer-induced liquid precursor (PILP) phase was first observed during the investigation of the effect of polyaspartic acid (PAsp) on the crystallization of $CaCO_3$[76]. PAsp was chosen to mimic the function of highly acidic proteins found in biominerals. It was observed PAsp had the effect of inducing the formation of films, tablets and fibers of $CaCO_3$ on a substrate, by the formation of a liquid-like amorphous precursor phase[76, 77]. Later, it was discovered that a similar result could be obtained with the commercially cheaper negatively charged polymer polyacrylic acid (PAA)[12, 78].

Figure 10 shows a schematic illustration of the proposed PILP process. Polyaspartic acid (PAsp) or polyacrylic acid (PAA) are added to the calcium solution with concentrations ranging from 1 to 100 µg/ml, depending on a variety of factors such as molecular weight, the use of other additives (such as Mg^{2+}) and the organic matrix[12]. By gradually increasing the supersaturation through the build-up of carbonate in the solution during the ammonium carbonate vapour diffusion technique[79] (see section 2.1.4.), a critical concentration is reached, at which point the solution undergoes a so-called liquid-liquid phase separation (Figure 10a). It is believed that a highly hydrated amorphous precursor phase is formed, which behaves like a liquid, and is much more hydrated and mouldable then ACC formed in the absence of additives[12, 80]. Due to their liquid-like behaviour, the amorphous particles are able to settle and adsorb to the substrate and coalesce into a film or coating (Figure 10b). In this way, an amorphous film is formed which crystallises over time into a birefringent film of crystalline $CaCO_3$, excluding the polymeric impurity (Figure 10c, d). By the use of atomic force microscopy (AFM) the topology of the deposited films was investigated, showing that they consisted of nanoscale colloidal particles remaining from the original droplet precursor[81].
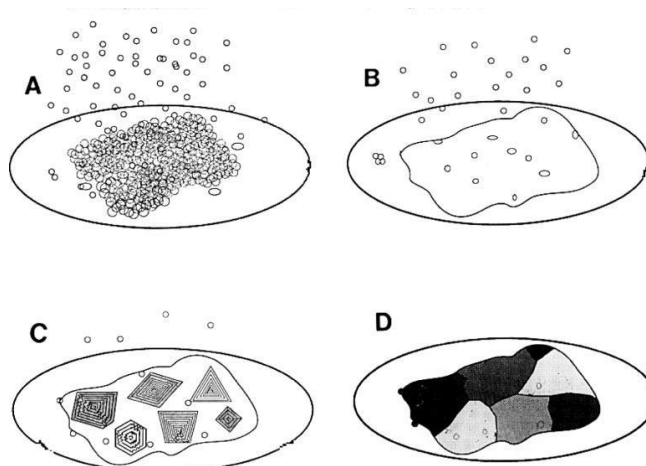
Figure 10: Representation of the polymer-induced liquid precursor (PILP) process. By addition of the polymer, isotropic droplets of 2-5 μm in size phase separate out of the solution when a critical concentration of Ca^{2+} and CO_3^{2-} is reached (a). The droplets have a liquid-like character and coalesce on the surface of the glass slide forming a continuous isotropic film (b). The film starts to crystallise (c) and patches within the isotropic film become birefringent. Due to diffusion-limited exclusion of polymeric impurities, the transformation process happens in an incremental fashion and transition bars may form. By time a complete crystalline film is formed (d) with a thickness of about half a micron, and composed of single-crystalline patches of calcite, or spherulitic patches of vaterite, which can range to hundreds of microns in diameter. Image reproduced from ref. 12, 77.

Although they have similar appearances, the PILP process differs from the oriented attachment process since the end product is formed by non-oriented ACC aggregation instead of an oriented aggregation of nanoparticles. In addition to the formation of films, the PILP process also induced the formation of calcite and vaterite fibers with diameters ranging from 100 to 800 nm[76, 82]. The exact formation mechanism of these fibers hasn't been clarified, although it is believed an oriented attachment mechanism might actually play a role in this case[83] (See chapter 4).

An important property of the PILP process, particularly with regards to this thesis, is the preservation of the shape of the precursor phase as round particles, and its ability to create thin films and tablets, fibers[77] or templated and moulded crystals[12, 81]. Taking advantage of this process, it was later demonstrated that it was possible to template complex shapes[84] and to fill the nanosized pores of track-etched membranes by capillary

action, allowing for the formation of single crystal rods of calcite[29]. Based on indications such as coalescence of the droplets which grow from tens of nanometers to a couple of microns, and light scattering studies suggesting an aggregation of the precursor particles rather than an atom-by-atom growth, it was put forward a phase with liquid-like behaviour was formed[81]. Further experiments done with track-etched membranes which become infiltrated with amorphous CaCO$_3$ by capillary action supported this suggestion[29]. Recent investigation with analytical centrifugation and nanoparticle tracking analysis further proved its emulsion and liquid-like properties[85].

Although the existence of a precursor liquid phase has mostly been demonstrated for CaCO$_3$ in the presence of PAsp and PAA, other studies have shown many polyelectrolytes are able to generate thin films of calcium carbonate via a PILP phase such as DNA[86], ovalbulmin[87], a calcification-associated peptide[88], short synthetic polypeptides[89] and the positively charged polyelectrolyte poly(allylamine hydrochloride) (PAH)[28] (see chapter 4).

In addition, it has been shown to be possible to form a highly hydrated amorphous phase of CaCO$_3$ with a similar appearance, by a liquid-liquid phase separation in the absence of additives at certain pH ranges[21, 85, 90]. It was therefore believed that this is a characteristic feature of the homogeneous formation of calcium carbonate itself[91]. Rieger et al. studied the precipitation of calcium carbonate at high supersaturations and observed the formation of emulsion-like structures preceding the precursor phase by means of Cryo-TEM. The authors speculated about a spinodal phase separation between a denser and less dense phase[92].

PILP phases have also been observed for other carbonate systems such as strontium carbonate and barium carbonate[83] and for amino acids[93], where for example microspheres of DL-glutamic acid with a hierarchical structure were formed through a PILP process by addition of the oppositely charged polyelectrolyte poly(ethyleneimine)[94]. Later studies indicated however, that the existence region and the amount of PILP phase produced, were rather very small as compared with the thermodynamically stable crystalline phases[95]. The existence of PILP phases of calcium phosphate[96] and calcium oxalate[12], have also been suggested, even though conclusive evidence is still missing.

The early structure of PILP, and its connection to PNCs has been unravelled in a recent paper[85], where it was shown a liquid crystalline phase (LCP) was stabilised by addition of PAsp. This LCP was preceded by PNC formation and was observed to exist also in

absence of polymer at neutral pH ranges. It was proposed that the LCP phase is formed by a bicarbonate-biased Ca^{2+} interaction distinct from the Ca^{2+} interaction with carbonates-bicarbonate in bulk solution. The role of PAsp was attributed to stabilisation of the LCP, inhibiting nucleation of $CaCO_3$.

1.3 Control of crystal morphology

As mentioned in the introduction, most biominerals are structurally composite materials, constructed out of inorganic crystals, surrounded by organic components. These organic components are key mediators during the mineralisation process and were shown to consist of soluble, hydrophilic polymers, such as proteins, glycoproteins and polysaccharides, together with a preformed and insoluble macromolecular matrix such as collagen or chitin[2, 4, 97]. The organic components have multiple functions in controlling the mineralisation process, including the formation of a confined mineralisation environment, acting as a structural framework for mechanical support, or influencing actively nucleation by interaction[2, 4], guiding the developing mineral phase. The organic macromolecules are often present up to a few weight percent[2, 4, 98, 99], and it is thought that certain key protein sequences and biomacromolecules are responsible for controlling the crystal polymorph[100, 101], morphology and texture[102], by binding to certain crystal faces changing the interfacial surface energy[98, 103, 104], or by providing a confined templated environment for crystallisation[2, 4, 10].

1.3.1 Effect of additives on crystallisation

1.3.1.1 Calcium carbonate

Although Nature has many ways to control the formation of biominerals, it is the research on the use of soluble macromolecules that has received the most attention in the past years since this process is much easier to mimic[4, 14, 30, 56, 98, 105]. Additives can control the crystal habit in many ways, mostly by binding to specific faces, influencing the growth rate of the faces, changing the morphology of the crystal according to Wulff's rule (see 1.2.3.3). Furthermore, inclusion of the additives into the mineral particles are also thought to enhance their solubility, influencing their size and aggregation mechanism[106].

Inspired by Nature, a sustained effort has been made to extract and characterise biomacromolecules associated with biominerals[107-112] and it was early on discovered that the biomacromolecules occluded mainly within calcium carbonate biominerals were highly acidic, being rich in aspartic and glutamic acid[113-117]. This led to subsequent investigations over the past 40 years using molecular analogues in the form of negatively charged small soluble additives[118] such as polymers[58, 119, 120], dendrimers[11] and block copolymers[104, 121], to obtain similar control over the mineralization process.

In the specific case of calcium carbonate, this led to the observations of crystallites with morphologies including spheres, dumbbells, whiskers, rods and flowers, produced by addition of polymeric acids[4, 11, 78] and variable block copolymers[4, 11, 14, 30, 103, 122-125]. As mentioned before, another intriguing effect of the addition of polymeric acids, such as polyaspartic acid (PAsp) and polyacrylic acid (PAA), is the stabilisation of amorphous calcium carbonate (ACC) as a so-called PILP (polymer-induced liquid precursor) phase, enabling the formation of crystalline films and fibers[77, 126]. Furthermore, biopolymers extracted from sea urchins[127], molluscs[128], corals[129] and brachiopods[130] have been used to manipulate the growth of biominerals in an *in vitro* system. Under synthetic conditions, biopolymers such as soluble collagen, have been shown to support the formation of spherulitic aggregates of calcite, and the stabilisation of vaterite (7 days) and ACC (14 days)[131]. Simple ions such as Mg^{2+}, and molecules such as citric acid or malic acid, also have a profound effect on the morphology of calcium carbonate[129, 132]. Computer simulations suggested that Mg^{2+} ions preferentially absorb to certain faces[133], forcing these facets to be expressed in the final morphology by altering their respective growth rates. Mg^{2+} ions were further shown to induce the formation of polycrystalline crystals with dumbbell and spherical morphologies[129]. The addition of citric and malic acid allowed the formation of $CaCO_3$ crystals elongated along the *c*-axis capped with well-defined {104} faces through adsorption to the {011} facets. Interactions of other simple additives, such as dicarboxylic acids, malinate, succinate and ethylenediaminetetraacetic acid (EDTA) has furthermore been rationalised in terms of interactions with specific symmetry related crystal planes, directing calcite growth[134-136]. In contrast to the specific adsorption mechanism described above for small molecular additives, block-copolymers allow the formation of exotic structures, via an aggregation based process, where the polymer initially stabilises small precursor crystal units, and then directs their aggregation in a highly oriented way, leading to well-

defined morphologies[11, 59]. Chapter 4 will discuss further the effect of positively charged additives.

By the use of these soluble additives it was therefore possible to control the morphology in a one-pot method. In comparison with the use of templates though, the outcome of the final morphology by the addition of additives is not always predictable from the choice of the components.

1.3.1.2 Calcium phosphate

For calcium phosphate, similar influences could be observed. Small ions such as Mg^{2+} and Zn^{2+} are known to inhibit the formation of hydroxyapatite (HAP) and other forms of calcium phosphate[137, 138]. A similar inhibition effect on HAP formation was observed for citrates and phosphocitrates[139]. Notably, the addition of fluorine atoms produces fluorapatite, exhibiting a characteristic dumbbell structure in certain pH ranges of 5-7[140]. Larger molecules such as proteins, carbohydrates, polyelectrolytes and other macromolecules showed a similar inhibition effect on the formation of HAP and other forms of calcium phosphate[137, 138, 141-143]. Furthermore it was discovered these could also influence the morphology by absorption to specific faces inhibiting growth[137, 138, 141, 143, 144] changing the size and shape of the crystals. Spherical structures with aggregates of fibers of octacalcium phosphate were prepared in the presence of poly-L-aspartic acid[145, 146] whereas precipitation in a double-jet experiment in the presence of polyaspartic acid gave rise to crystallisation of a "hollow snowball" structure composed of single crystal HAP platelets[147]. The effects of polyaspartic acid will be further discussed in chapter 3. Furthermore by addition of additives such as cetyltrimethylammonium bromide (CTAB), nanobelts of octacalcium phosphate were constructed[148], while PSS gave rise to different HAP morphologies from ribbons to microspheres constructed from nanofibers to nanorods or nanoplates[149]. Finally block copolymers allowed formation of morphologies such as flower-like nanostructured hydroxyapatite hollow spheres[150] and porous dicalcium phosphate dihydrate crystals with channel-like features constructed from 100-nm-sized rod-like primary particles[151]. More examples can be found in[143].

1.3.2 Effect of confinement on crystallisation

A general feature of biomineralisation is that mineralisation often occurs within localized small volumes, allowing organisms to exert great control over the mineralization process[10, 152]. By mineralising within these environments, organisms can actively select the mineral phase, morphology, orientation and localization of the biomineral product formed. This is achieved through a tight control of the precursor ions and phases, and via a close interaction with soluble organic macromolecules and insoluble matrices located within[2, 4]. As demonstrated in chapter 3, interesting examples are the formation of teeth and bone, where small calcium phosphate crystals are formed inside the nanoscale gaps of collagen[3, 153]. Other examples can be found in magnetotactic bacteria which form magnetite crystals in specially evolved phospholipid vesicles[154]. Furthermore vesicles in general, as present in coccoliths and diatoms of respectively $CaCO_3$ and silica, can further act as mineral deposition containers, compartmentalizing mineralization[155].

To study the effect of compartment on crystallisation, much work has been done on freezing phenomena, where a depression of the melting point as well as the freezing point was observed with a reduction in the sizes of cylindrical nanopores[156]. In higher levels of confinement with pore diameters of less than about 5-10 molecular diameters of the confined substance, the formation of any crystalline phases was often even prevented. Furthermore, precipitation within confined volumes can also lead to stabilisation of metastable crystal polymorphs and amorphous phases due to critical size or kinetic stabilization effects. This was demonstrated for organic[157-159] but also for inorganic crystals[152, 160]. In studies for example of $CaCO_3$, a stabilisation of amorphous calcium carbonate (ACC) was demonstrated when precipitated in confined systems such as vesicles[155], droplet arrays[161] and an annular wedge[152]. Recently it has also been shown the same accounts for calcium sulphate where amorphous calcium sulfate (ACS) and calcium sulfate hemihydrate (bassanite,) were stabilised and observed even at micron-scale separations[160]. The stabilisation of the two different minerals was attributed to two different mechanisms, one due to kinetic effects and restricted contact with the solution (ACC), and the other due to hindered diffusion and aggregation (ACS), demonstrating that confinement effects can operate on many levels[160].

As demonstrated in chapter 5 and 6, confinement can also provide an effective route in controlling crystal size and shape by templating, where the product crystal adopts

complex morphologies imposed by the confining volume[29, 31, 32, 162, 163]. Based on the example of Nature, many synthetic templates have been developed, including colloidal crystals[33, 164], ice[165], macroporous polymers[166], bicontinuous microemulsion systems[167] and biological templates such as pollen grains[168] and sea urchin skeletal elements[169], producing porous 3D structures of calcium carbonate and other biominerals. A very interesting example was done in our group, where by the use of sea-urchin skeletal replicas, calcite crystals with a macroporous, sponge-like structures and curved surfaces were formed[166, 170, 171]. This was done in the absence of amorphous calcium carbonate (ACC) and was shown to be possible for a range of crystalline materials including $PbCO_3$, $SrSO_4$, $NaCl$ and $CuSO_4.5H_2O$[32]. As further discussed in Chapter 6, previous research showed it is possible to produce rod-shaped single crystals of calcite by stabilisation of an amorphous precursor phase and the use of track-etched membrane pores as templates[29, 31, 172]. Another interesting technique is the use of gels which allows a slow, diffusion-controlled growth of large crystals[4, 173, 174]. Calcite crystals have been grown in all kinds of gels such as silica and agarose gels, giving rise to some fascinating morphologies[4, 175]. Work done by Estroff et al. demonstrated further that growth of crystals inside a gel can result in the occlusion of impurities into growing crystals producing composite materials and porous crystalline structures[176, 177].

Templates have many advantages such as easy fabrication procedures, various compositions of materials, and ability to obtain uniform sizes[178]. Drawbacks are the difficulty to scale up the synthesis process, limitation of the dimensions of the product by the dimensions of the templates, removal of the template and the necessity of finding suitable templates, neither of which are straightforward[30, 178]. The effect of confinement on calcium phosphate crystallisation is further discussed in chapter 3.

Chapter 2: General Experimental Methods and Techniques
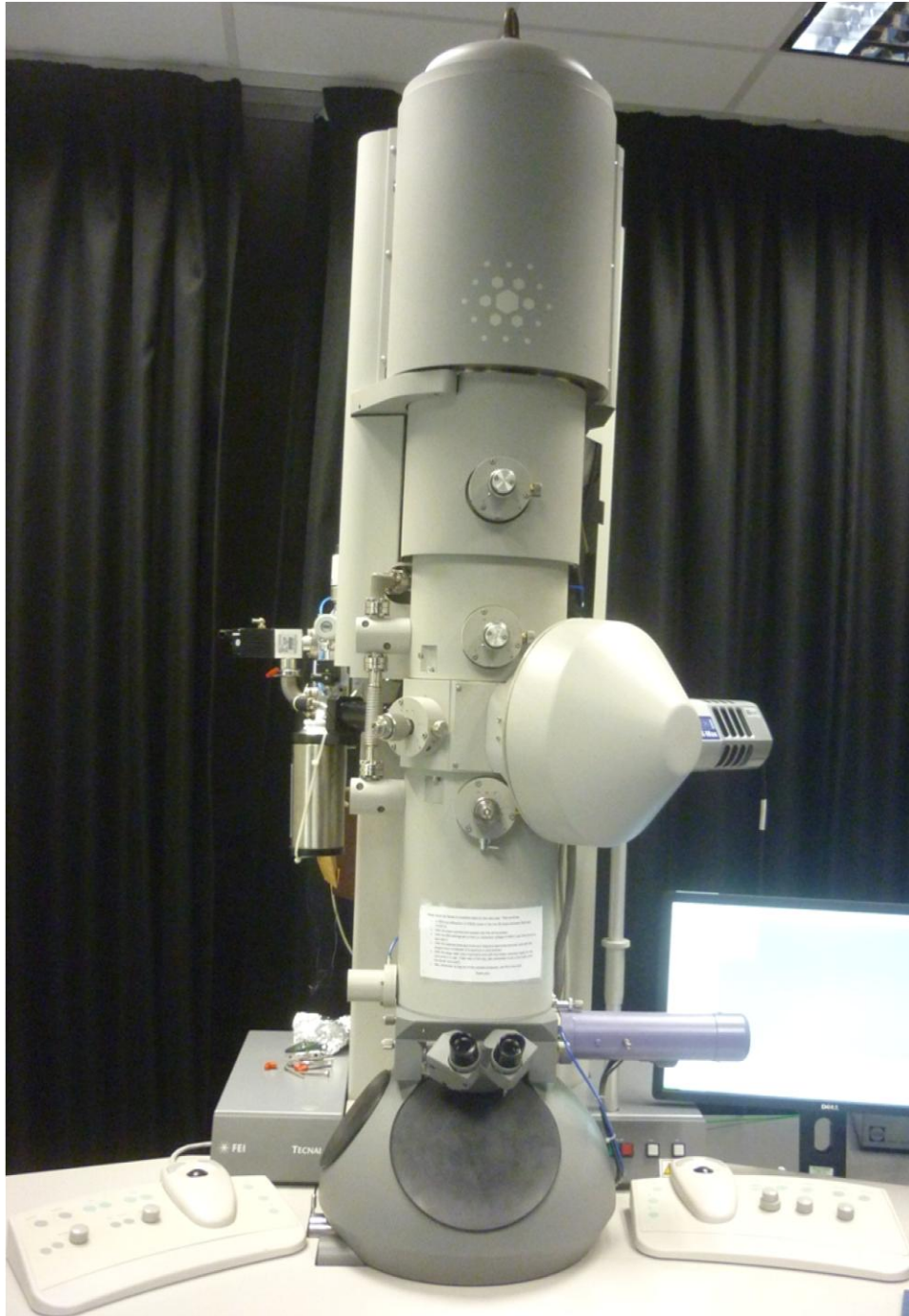
Chapter 2: General Experimental Methods and Techniques

2.1 General preparation methods:

2.1.1 Piranha solution

Many of the crystallization experiments described in this thesis were executed on glass slides and additionally almost all microscopy carried out with FEGSEM was performed after putting the sample on a clean glass slide. Therefore, the preparation of clean small glass slides was crucial for the experiments. At first, glass slides were cut into pieces measuring 1.5 cm by 1.5 cm with a glass cutter and were then put in a glass beaker containing Piranha solution. Piranha solution was prepared by mixing H_2SO_4 (67 vol-%) and H_2O_2 (33 vol-%). Due to the mixing being an exothermic reaction great care had to be taken when combining the two reactants. Piranha solution is highly effective in cleaning the substrates due to its ability to act as an oxidising agent and thus to remove organics from glassware. This is the result of two processes acting simultaneously in the solution. Firstly, Piranha solution is extremely effective in removing O and H from organic residues in water due to its strong dehydrating characteristics. Furthermore, the combination of H_2SO_4 and H_2O_2 increases the oxidizing capability of H_2O_2 by the formation of elemental oxygen. This allows removal of elemental carbon left after the initial and faster dehydration step.

$$H_2SO_4 + H_2O_2 \longrightarrow H_3O^+ + HSO_4^- + O$$
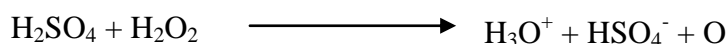
Additionally, due to its strong oxidising abilities, Piranha solution will also increase the hydrophilicity of the glass slides by hydroxylation of the surface. In addition to the oxidising characteristics, the solution also has a high acidity which will contribute to the cleaning ability by dissolving mineral deposits such as carbonates and oxides, making it a perfect cleaning agent for our experiments.

For our experiments, glass slides were left in solution for 3 h whereafter the Piranha solution was disposed of and the glass slides were washed 10 times with deionised water. The glass slides were dried with dry N_2 air and stored in a closed beaker.

2.1.2 Precipitation methods of CaCO$_3$

Generally three approaches can be used to precipitate $CaCO_3$ in the lab. In a first, quite general technique, Ca^{2+} and CO_3^{2-} are mixed in concentrations exceeding the saturation

limit, until crystals precipitate out of the solution. In a second method, called the Kitano method[179, 180], calcium carbonate is dissolved in water by saturating the solution with carbon dioxide, whereafter it is reprecipitated on release of the carbon dioxide from the solution. A third method is the ammonia diffusion method (see Figure 1) where a calcium ion solution is exposed to ammonium carbonate vapour. This technique has been used in most experiments concerning $CaCO_3$ throughout this thesis. The procedure works as follows[181]: A solution of $CaCl_2.H_2O$ with or without additives is placed inside a desiccator containing a petri dish filled with $(NH_4)_2CO_3$ powder (usually 5 gram) which was covered with parafilm pierced 4 times with a needle. The presence of holes affects the rate of gas diffusion into the $CaCl_2.H_2O$ solution and therefore the rate of increase of the CO_3^{2-} concentration and $CaCO_3$ nucleation and growth[182].

$$(NH_4)HCO_{3(s)} \longrightarrow NH_{3(g)} + CO_{2(g)} + H_2O_{(l)} \quad\quad (1)$$

$$NH_{3(aq)} + H_2O_{(l)} \longrightarrow NH_4^+{}_{(aq)} + OH^-{}_{(aq)} \quad\quad (2)$$

$$2CO_{2(aq)} + 2H_2O_{(l)} \longrightarrow HCO_3^-{}_{(aq)} + CO_3^{2-}{}_{(aq)} + 3H^+ \quad (3)$$

$$CaCl_{2(aq)} + H_2O_{(l)} \longrightarrow Ca^{2+}{}_{(aq)} + 2Cl^-{}_{(aq)} + H_2O_{(l)} \quad\quad (5)$$

$$Ca^{2+}{}_{(aq)} + CO_3^{2-}{}_{(aq)} \longrightarrow CaCO_{3(s)} \quad\quad (6)$$
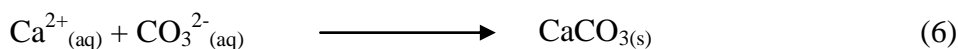
The first step of the reaction is given by the decomposition of ammonium carbonate powder into ammonia and carbon dioxide (step 1). Both gasses diffuse into a petri dish or vial containing the calcium chloride solution. The CO_2 (from step 1) acts as the actual source of the CO_3^{2-} ions (step 3) in the solution and reacts with the Ca^{2+} ions to form $CaCO_3$ (step 6). The ammonia works as a buffer system and keeps the pH at a value of 9.5, decreasing the solubility of $CaCO_3$ and thus promoting its growth. Diffusion of CO_2 alone would lead to a decrease in the pH, thereby increasing the $CaCO_3$ solubility and supersaturation would never be reached. The ammonia diffusion method can be considered as a close mimic to biomineralisation processes where $CaCO_3$ crystallization is initiated by an increase in enzymatically released CO_2[102, 181]. Glass slides were usually added to the solution as substrates for crystallization to occur on.
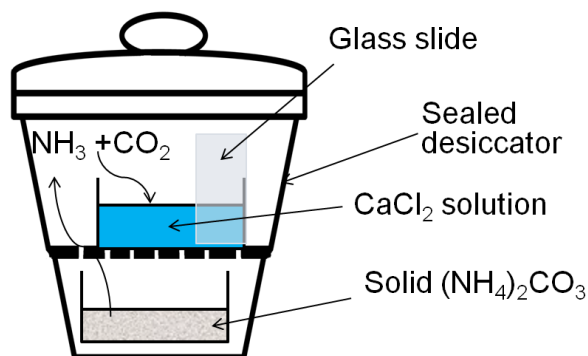
Figure 1: Representation of the ammonia diffusion method.

<u>2.1.3 Precipitation within track-etched membranes</u>

Calcium carbonate and calcium phosphate crystals were precipitated in two types of membranes: track-etched (TE) membranes made of polycarbonate (see chapter 3, 4, and 6), and porous alumina membranes (POM) (see chapter 3).

2.1.3.1 Plasma cleaning of track-etched membranes

Before the membranes were placed in solution they were plasma treated with a plasma cleaner (Harrick Plasma PDC-32G) in order to remove organic impurities and to increase the hydrophilicity of the membranes. The procedure can be described as follows. The membrane is put into the plasma cleaner which is then closed and put under vacuum. Due to the low mass of membrane, it needs to be held down by a small weight to prevent it from getting sucked into the vacuum system. Subsequently, the vacuum pump is switched on and the chamber is closed allowing the pressure to drop to ~ 0.1 mbar. In a next step the electric field is switched on, leading to the ionisation of the oxygen molecules in the air, thus creating a plasma which can contain a number of species such as ions, electrons, radicals and photons. The energetic gaseous species are very reactive and bombard the surface to remove material or in the case of active gases (e.g. oxygen) get involved in chemical reactions. The unwanted residues are in this way volatilized and removed by the vacuum system. Moreover, the hydrophilicity of the surface is increased. The plasma is usually applied for ~ 1 min whereafter the electric field and the vacuum pump are switched off. Opening of the valves allows the pressure to drop to 1 bar and the membranes are taken out to usually be put in solution for the degassing step.

2.1.3.2 Degassing step

When the membranes were immersed in the crystallisation solution, they were first degassed to ensure that the crystallisation solution is fully infiltrated into the membrane pores. Therefore, after plasma cleaning, the membranes were placed in glass vials containing water or the crystallizing solution ($CaCl_2.2H_2O$ with or without additive), which were placed in a plastic desiccator connected to a vacuum pump, and the pressure was reduced to 20-40 mbar. The glass vials were also covered with Parafilm to avoid solution "popping" out of the vial and a hole was made to allow air to leave the solution. They were held under this pressure until no more gas bubbles were seen forming on the membrane surface. The pressure was brought back to atmospheric pressure and the membranes were left in solution overnight to allow infiltration of the pores with the crystallising solution.

2.1.3.3 Dissolution of the membranes

After variable amounts of time, the membranes were removed from solution and washed with ethanol. The surfaces of the membranes were then wiped clean with the edge of a thin clean glass cover slip, to remove the possible crystals that were located on the surfaces of the membranes, and washed again with ethanol. Next, the membranes were sonicated in a vial of ethanol for 10 minutes, rinsed in ethanol and air dried.

To remove the TE membranes, they were dissolved in a centrifuge tube (1.5 cm) filled with dichloromethane (DCM) and sonicated for 2 minutes followed by centrifugation for 4 minutes at 13.2 rpm. The DCM was decanted, taking care not to remove any sample from the eppendorf, and fresh DCM was added to the eppendorf again. The sonification, centrifuging and DCM change was repeated for another four times to be sure all of the remaining membrane was removed. Eventually, all of the DCM was removed from the centrifuged sample and the eppendorf was this time refilled with methanol whereafter the samples were sonicated again for 2 minutes and centrifuged for 4 minutes. Eventually the methanol was changed for ethanol and the process was repeated 3 more times. In the end the ethanol was almost completely removed.

To isolate the crystals from the PAM, the membranes were dissolved in a centrifuge tube (1.5 cm) containing 0.5 M NaOH and left for 1 day. Then the samples where centrifuged for 4 minutes at 13.2 rpm and the NaOH solution was removed followed by washing of the membranes with ethanol. Next they were sonicated for two minutes and

centrifuged at 13.2 rpm to separate the inorganic precipitate. Finally the membranes were washed 3 more times with ethanol as described for the TE membranes.

For preparation of samples for TEM, 50 μl of fresh ethanol was pipetted into the eppendorf containing the sample. The sample was sonicated for a minute to suspend the sample in the ethanol, and a drop was placed on the TEM grid and allowed to dry. For FEGSEM, 50 μl of fresh ethanol was pipetted into the eppendorf which was sonicated for 1 minute and then a drop of each sample was placed onto clean glass slides placed on an SEM stub.

2.2 Analytical Techniques

2.2.1 Atomic Absorption

Atomic absorption (AA) allows the quantitative determination of chemical elements in a sample by measuring the absorption of light by free atoms in the gaseous state. After dissolving the sample in a 10% HNO_3 solution, the atoms are ionized by passing through a flame and their absorption of light at a specific wavelength provided by a dedicated lamp, enables the determination of their concentration according to Beer's law:

$$A = \varepsilon b c \qquad\qquad \text{Equation 1}$$

With A the absorbance, ε the molar absorptivity in L mol^{-1} cm^{-1}, b the path length in cm and c the concentration in mol/L

For the experiments, AA was performed using a Perkin Elmer Atomic Absorption spectrometer.

2.2.2 Dynamic light scattering (DLS)

Dynamic light scattering is a technique used to determine the size distribution of particles or polymers in a solution based on intensity fluctuations due to Brownian motion[183]. When a light source such as a laser hits the particles, the light will be scattered in all possible directions and a time-dependent fluctuation in the measured

scattering intensity is observed due to Brownian motion and related to constructive and destructive interference. By the analysis of these intensity fluctuations it is possible to obtain information about the velocity of the Brownian motion and therefore the particle sizes.

DLS measurements for this thesis were conducted using a NanoZetasizer (Malvern instruments).

2.2.3 Infrared (IR) spectroscopy and Raman microscopy

Infrared and Raman spectroscopy are analytical techniques based on the absorption (IR) and inelastic scattering (Raman) of light with a certain frequency which is characteristic for the structure of the molecule. IR is based on the fact that light from a certain source will be absorbed by a vibrating molecule at certain frequencies. The characteristic frequencies are related to the structure of the molecule. Raman is based on the inelastic scattering of light by a vibrating molecule. The photons interact with the molecule to induce transitions between vibrational energy states, resulting in a shift in the energy of the photons. This shift in energy gives information about the vibrational modes and the structure of the system. Raman of crystalline structures is usually fairly simple since the atoms in the crystalline structure have to move or vibrate in phase to be observable. Most IR machines these days are called FTIR (Fourier Transform Infrared) which allow measurement of the whole wavelength range at once.

IR and Raman were respectively performed using a Perkin Elmer Spectrum 100 ATR and a Renishaw inVia-Raman microscope using a 785 nm diode laser as excitation source. The Raman was equipped with a 50x (NA ¼ 0.75) objective to focus the laser beam on specific parts of the sample, enabling the polymorph of the individual particles to be determined.

2.2.4 Optical microscopy

Optical microscopy was performed using a Nikon Eclipse LV 100 with objectives of 10x, 20x, 50x and 100x. The microscope is equipped with a polarisation filter to investigate the crystallinity of the formed products.

This latter is possible since almost all anistropic crystals are birefringent. This optical property is particularly present in calcite, and is due to a different refractive index depending on the propagation and polarisation of the light entering the crystal. Hexagonal crystals such as calcite are anisotropic and have crystallographically distinct axes. Therefore, the mechanism of interaction with incoming light depends on the angle of the incoming light with respect to the orientation of the crystal lattice. The light will therefore encounter different refractive indices depending on the angle of entry.

The effect of birefringe is especially useful to investigate crystals when placed under crossed polarisers. If the crystal is isotropic, such as amorphous materials, the incoming light will not be affected or polarised by the material and will be blocked by the second polar. In this case the material appears black. If the material is anisotropic and is able to polarise light, the light will be split into two orthogonal components. This can be used to identify the crystal lattice orientation since whether light is transmitted or not depends now on the orientation of the crystal. If the incident light is parallel to the refracted components, the crystal will be in extinction. If the crystal is turned 45 degrees the incident light will be perpendicular and will be transmitted making the crystal appear bright in a dark background. If the crystal is turned another 45 degrees (so 90 degrees to the first position), the crystal will be in extinction again. Every anisotropic crystal will have two orthogonal extinction positions when the polars are crossed. When the light enters the crystal along its optical axis (the axis of rotational symmetry) however, it will interact with the crystal in a similar way as an isotropic crystal and extinction will be observed in all orientations. In the case of calcite this is the (001) direction and it is the only axis which isn't birefringent.

2.2.5 Scanning electron microscopy (SEM)

SEM allows to image the surface of a sample with a resolution down to 1 nm. The principle of SEM can be explained as follows: firstly, electrons are generated and accelerated using a field emission gun (FEG) or thermionic sources, and subsequently focused on the sample by the use of condenser lenses. To avoid interaction of the electrons with the surrounding air, the imaging has to be carried out under vacuum. Subsequently, by the use of a lens system, the electron beam is focussed to a size of 0.4 nm to 5 nm, and the surface of the sample is scanned section by section forming a

raster. When the electrons hit the surface they lose their energy within a teardrop-shaped interaction volume, which extends from less than 100 nm to around 5 μm in the surface, depending on the characteristics of the sample. Different interactions between the electron beam and the investigated material can occur, of which the formation of inelastically scattered secondary electrons (<50 eV) is the most important. The secondary electrons emitted by the sample are detected and amplified by the detector to be finally represented on a screen as a grey dot where the intensity corresponds to the measured intensity. Depending on the topography of the sample more or less electrons will reach the detector and the spot will appear more or less bright giving a three-dimensional appearance. By synchronised scanning of the electron bundle across the sample with the image on the screen, an image is constructed and a linear magnification is realised according to the equation

$$Magnification = \frac{Length\ of\ monitor}{size\ of\ the\ raster}$$
<div align="right">Equation 2</div>

By changing the size of the raster on the sample the magnification can be altered and a value of up to 500 000 x can be reached. In addition to secondary electrons, high energy backscattered electrons and X-rays can also be detected, yielding information about the specimen's chemical composition and orientation. Finally, it has to be mentioned that samples for SEM analysis have to be stable under vacuum and conductive to avoid charging of the surface.

Experimentally high resolution FEGSEM for this thesis was performed on a LEO 1530 Gemini FEGSEM microscope operating at 3.00 kV, equipped with an inlens detector (Leeds) and XL ESEM FEG (FEI) operationg at 15 kV (Eindhoven). Low resolution SEM images were obtained using a JEOL Neoscope benchtop SEM at a 5-30 kV operating potential. Before the samples could be analysed with SEM, they were mounted on SEM stubs with adhesive carbon pads, followed by sputter-coating them with 10 nm Pt/Pd (80/20) using an Agar High Resolution Sputter Coater (Leeds) or with carbon using a Cressington 208 carbon coater (Eindhoven).

2.2.6 Synchrotron small and wide angle X-ray scattering techniques (SAXS/WAXS)

2.2.6.1 Synchrotron radiation

Synchrotron radiation is generally produced in a synchrotron facility where particles are accelerated to ultrarelativistic speeds. Synchrotron radiation has many advantages over X-ray radiation provided by a common laboratory source of which the most important one is the high brilliance, which leads to a very low signal to noise ratio, allowing the collection of time-resolved data with acquisition times as low as 1 ms. Additionally, since the X-ray beams produced at a synchrotron facility have a low divergence, it is possible to carry out SAXS measurements under diffracted angles as low as ~0.05°. Figure 2 represents the principle of the generation of synchrotron light.
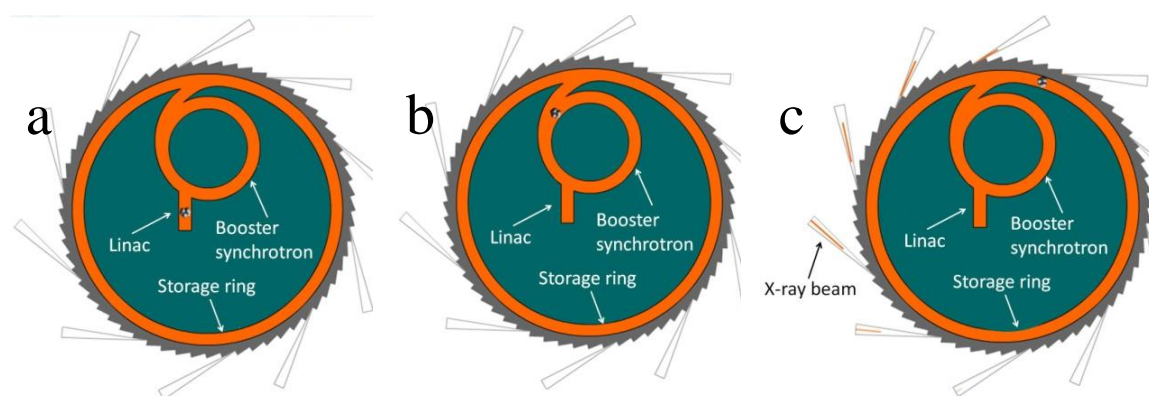
Figure 2: Schematic representation of the synchrotron light scource at the European synchrotron research facility (ESRF). a: Electrons are emitted by an electron gun and accelerated in a linear accelerator (linac). (b) They are transmitted to a circular accelerator (booster synchrotron) where they get accelerated. Finally, these high energy electrons are injected into a large storage ring (c) circulating in a vacuum environment for many hours (Adapted from ref. 184).

After the electrons are generated in the electron gun at an energy of 90 keV, they are accelerated within a linear accelerator (linac) to 100 MeV. Subsequently they are transmitted into the circular accelerator (booster synchrotron), were they are accelerated to a maximum speed close to the speed of light to obtain the desired energy of 6 GeV. These high energy electrons are then injected into a large storage ring (844 circumference) where they circulate in a vacuum environment for many hours at a constant energy. The path of the electrons is maintained by bending magnets and synchrotron light is produced when the electrons pass through these bending magnets.

Additionally, in the straight sections, the electrons are oscillated by undulators and wigglers, which also produce synchrotron light. The synchrotron light is used in many different applications such as EXAFS (extended X-ray absorption fine structure), XAS (X-ray absorption spectroscopy), and high energy diffraction and scattering.

2.2.6.2 Small and wide angle X-ray scattering (SAXS and WAXS)

Just like XRD, SAXS and WAXS are non-destructive elastic X-ray scattering techniques that allow the characterisation of solid phases. WAXS stands for wide angle X-ray scattering and is based on the same theory and principles as XRD. Yet, the angle resolution of the WAXS patterns is often much lower in comparison with conventional powder XRD and results are therefore in principle far less accurate and precise. Nevertheless, WAXS can still be very useful to obtain information on time resolved experiments and in theory, all the analysis on XRD patterns can also be performed on WAXS patterns such as determination of the unit cell parameters, size and strain, and quantification of the polymorph phases [6, 185, 186].

SAXS stands for small angle X-ray scattering (in general angles of 0.1 - 5°) and in comparison with WAXS the distance from the sample to the detector is much longer. Small angle scattering is related to large scale features and gives information about particle size, particle volume and morphological features such as size and shape[187, 188]

SAXS patterns are usually plotted as intensity profiles over the scattering vector, $q(Å^{-1})$:

$$q = \frac{4\pi}{\lambda}\sin\theta = \frac{2\pi}{d} \qquad\qquad \text{Equation 3}$$

Figure 3 gives an example of such a plot.
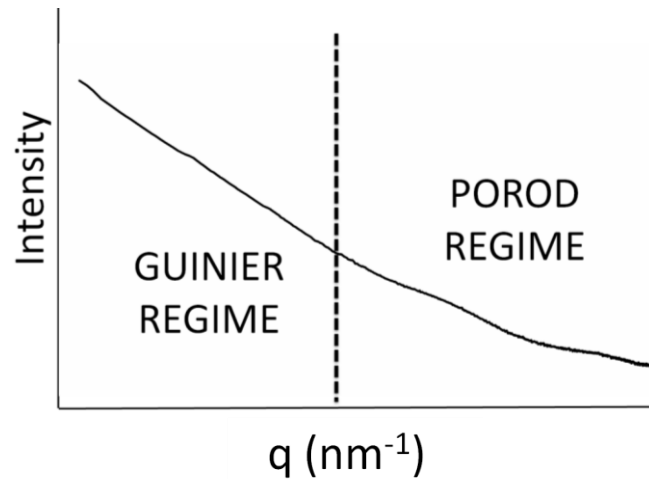
Figure 3: Example of a SAXS plot with Guinier and Porod regime indicated.

Plotting the intensity over q brings about two areas of interest: the Guinier regime which mainly gives information about the radius of the scattering objects, and the Porod regime which provides additional information about the interface morphology in a two phase system. In the Guinier regime, the relationship between the measured intensity and the q value can be described as[187-189]

$$I(q) = I_0 \exp\left(-\frac{q^2 R_g^2}{3}\right)$$

Equation 4

with I_0 representing the extrapolated intensity of the signal at q = 0 and R_g being the radius of gyration. R_g is the weighted average radius of all cross sections through a particle and can be obtained from plotting $\ln(I(q))$ vs. q^2 of the Guinier region and determining the slope of the graph. Depending on the shape of the particles, morphological characteristics such as the object radius can be calculated from R_g[187]. This is particularly useful, especially if the heterogeneities are spherical and the sample is monodisperse.

In addition, a very important parameter is obtained from the Porod regime which is called p or the Porod slope. This gives information about the particle shape and morphology. By analyzing the intensity of the SAXS data in a Log-Log plot, it was discovered that depending on the morphology, the graph had a certain slope, and it was found that for all systems the equation[190, 191]:

$$I(q) \propto q^{-p} \qquad\qquad \text{Equation 5}$$

holds with p the Porod slope. Once determined it is then possible to extract some more information from p about the fractal dimensions and surface morphologies of the scattering particles. If p= 4 the interface is smooth, if 3<p<4 the particle has a fractal surface and if 1<p<3 the particle is a mass fractal[192].

2.2.7 Transmission electron microscopy (TEM)

TEM is a second electron microscopy technique and allows materials to be analysed down to the sub-Å range[193]. Samples a few nm thick (preferably not more than 100 nm) are put on a TEM grid which is loaded into the instrument with the help of a dedicated holder. When the electron beam passes through the sample, it interacts with the sample and an image is formed on a viewing screen.

A TEM usually comprises four main parts[194], the gun, the lens system, the detectors and screens, and finally the sample holder (see Figure 4).
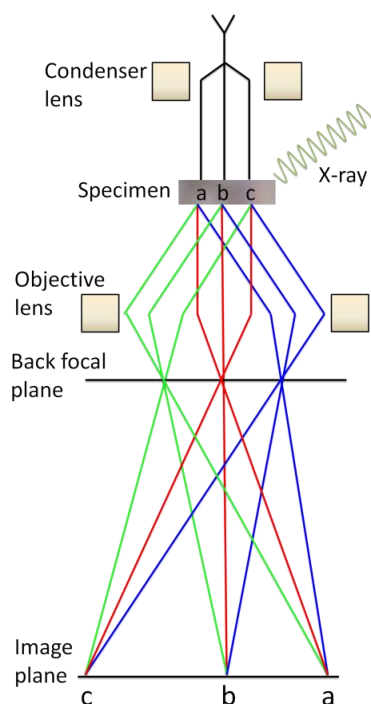
Figure 4: Working principle of a transmission electron microscope. The electrons emitted by the gun are focussed onto the sample by the condenser lenses. The electrons hit the sample and along with inelastically and elastically scattered electrons, characteristic X-rays are created. After transfer through the specimen a diffraction

pattern is created in the back focal plane by the objective lens and the magnified image of the illuminated area is produced on the image plane.

The gun accelerates the electrons and sends them to two or more condenser lenses which focus the electrons from the source and transfer them to the specimen. By adjusting the condenser lenses the user can control the beam diameter and intensity as it hits the specimen. The specimen holder carries the sample and together with the objective lens it makes up the heart of the TEM. At this point, below the objective lens, the objective and selected area electron diffraction (SAED) apertures can also be inserted. After transfer through the sample and the objective lenses, the magnified images and diffraction patterns of the specimen are created, and a series of other projector lenses are responsible for the magnification of the image and for the selection of the image or diffraction plane. Therefore the first projector lens is capable of switching between two modes: image mode and diffraction mode which respectively places the image plane and the back focal plane of the objective onto the viewing screen. Finally the image is projected onto the viewing screen, often a fluorescent screen or computer display via a detector such as a charge-coupled device (CCD) camera, by a series of projector lenses.

Since the resolution of a microscope depends on the wavelength of its source (for simplicity resolution $\approx \lambda/2$)[194], the use of electrons in an electron microscope instead of, for example light, allows us to image materials with a much higher spatial resolution than in a light microscope. This is illustrated by Louis de Broglie's equation, which describes the relationship between the wavelength of electrons and their energy, E, as

$$\lambda = \frac{1.22}{E^{1/2}}$$

Equation 6

with E given in electron volts (eV) and λ in nm. From this equation it can be worked out that for a microscope equipped with a 100 keV gun, the wavelength of the electrons will be about 0.004 nm or 4 pm, hence much smaller than the diameter of an atom. Obviously this is only a theoretical value and lenses within TEM are far from perfect, yet much development has been done and breakthroughs in spherical- and chromatic-aberration corrections allow TEM image resolution below the 0.1 nm (1 Å) barrier[193].

The formation of images in the TEM can happen in two different ways, bright field and dark field imaging; where respectively the electrons that are in the direct beam are used for bright field imaging and the electrons that are diffracted and not in the direct beam are used for dark field imaging. Contrast in the images is obtained in 3 ways: amplitude contrast, phase contrast and diffraction contrast. Amplitude contrast originates from variations in mass and thickness of the sample since the electrons have to interact with different amounts of material. This contrast is related to the incoherent, elastically-scattered electrons and is a strict function of the atomic number Z and thickness of the specimen (with elements exhibiting a higher atomic number leading to stronger scattering and thus darker regions in the image). This kind of contrast is most important when looking at non-crystalline materials such as polymers. Diffraction contrast is controlled by the crystal structure and orientation of the specimen. In this case the contrast arises due the fact that electrons are Bragg diffracted so images will appear darker at positions where more Bragg diffraction happens. Bragg diffraction occurs when the electron beam passes through a crystalline region, and if this crystal is oriented in the right way with respect to the beam then increased diffraction and thus contrast will result.

Phase contrast results from the differences in the phase of the electron waves when they interact with and are scattered by the atomic columns in the specimen, and allows us to image the atomic structure of crystalline materials (and image for example defects). To maximise the use of phase contrast it is important to prepare samples that are thin enough not to induce any changes in the amplitude of the transmitted beam.

Since TEM yields a 2D representation of 3D objects, there is no real depth sensitivity and caution has to be exerted when analysing TEM data. A way to get around this problem is provided by electron tomography where a sequence of images is taken at different tilt angles, which can be combined to create a 3D image[143]. Another issue to be considered with TEM is beam damage, especially in the case of polymers and biomaterials such as the ones discussed in this thesis. All organic species (and under high magnification even inorganic species) suffer from degradation due to the effects of the high-energy electrons, giving rise to ionisation, chemical reactions and rearrangements, and the introduction of circular voids. Recent developments such as Cryo-TEM, low-noise charged-coupled device cameras and low-dose microscopy

techniques where the sample is only irradiated for a short period of time during the acquisition of the image, help in dealing with problems such as beam damage.

2.2.7.1 Interactions within the transmission electron microscope.

The accelerated electrons within the electron microscope are able to interact with the investigated matter in many ways. Besides inelastically and elastically scattered electrons, characteristic X-rays are produced which can be used for Energy Dispersive X-ray spectroscopy (EDX). The emitted X-rays are characteristic of each atom and by measurement of their energy using an energy-dispersive spectrometer it is possible to obtain information about the chemical composition of the sample. The inelastically-scattered electrons, on the other hand, can be used for Electron Energy-Loss Spectrometry (EELS). In this case the amount of energy loss of the inelastically scattered electrons can be measured via an electron spectrometer and information about the composition of the sample can be obtained. Also, when the electrons pass through crystalline matter they can be diffracted by the atoms of the material, giving information about the atomic arrangement of the material and crystalline structure.

2.2.7.2 Electron diffraction (ED):

Just as with X-rays, electron beams can interact with the atoms of a material and undergo diffraction, giving rise to a diffraction pattern according to Bragg's law

$$n\lambda = 2dsin\theta \qquad\qquad \text{Equation 7}$$

with λ representing the wavelength of the electron beam, d the spacing between the lattice planes and 2θ being the angle of the diffracted wave. Figure 5 shows a simple illustration of two parallel incident electron beams that are diffracted by the lattice planes of the crystal. It can be seen that, for the two waves to remain in phase, the distance from point 1 to 2 to 3, which is equal to $2dsin(\theta)$, has to be equal to n times the wave length, with "n" being an integer number.
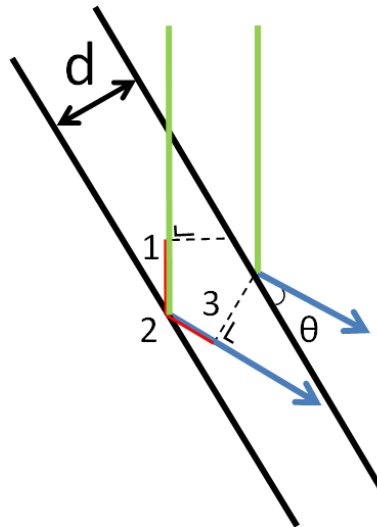
Figure 5: Schematic representation of Bragg diffraction. Two parallel incident beams are diffracted and can only be in phase if nλ equals the path length difference (distance of 1 to 2 to 3 in red) which equals $2dsin(\theta)$.

Although electrons get diffracted in a similar way as X-rays there are some important differences:

1. Electrons have a much shorter wavelength than the X-rays commonly available in the lab (2 pm for 300 KeV microscope instead of an average of 0.1 nm for X-rays).

2. Since the electrons interact with both the nucleus and the electrons of the scattering atoms through Coulomb forces, they are scattered much more strongly. This has the advantage that the diffracted electron beams have a much higher intensity and the exposure times are in the order of a few seconds or less which means that the ED patterns can be viewed directly on the viewing screen.

3. Since electrons are charged particles they can be easily controlled with electromagnetic lenses.

4. It is also possible to obtain ED patterns of small crystallites or of only a small area of a big crystal, depending on the SAED aperture size (usually a few 100 nm).

As mentioned before, by adjusting the electromagnetic lenses, the back focal plane or diffraction plane instead of the image plane can be focussed on the viewing screen. In this way a diffraction pattern of the material can be obtained. Depending on characteristics of the material the diffraction pattern can consist of an array of spots for

a perfect single crystal, rings of spots for a polycrystalline material or diffuse rings for an amorphous material. Measuring the distance between the spots and rings can then give information about the crystal structure and orientation, and even polymorph of the investigated material. This characteristic is one of the most important features of TEM since it can relate the crystallography of the diffraction pattern to the images we see and a very small area can be analysed. Although generally very useful, analysis of electon diffraction (ED) patterns can be very complex due to a number of limiting factors such as specimen thickness and objective lens defocus.

2.2.7.3 Low Dose and Cryo-TEM

Cryo-TEM is a special type of TEM technique where the sample is embedded in a thin film of vitrified amorphous ice[195]. The sample is kept in this state by cooling the sample holder with liquid nitrogen. Advantages of this technique are that beam damage, which is usually associated with classical TEM, is much reduced, and objects of interest can be studied in the native environment or suspended medium, preserving their mutual temporal and spatial arrangements without having to deal with drying-out effects, which is usual the case with normal TEM. Considering the fact that biominerals are usually surrounded by an organic matrix in an aqueous environment, this technique gained much interest over the past few years for the study of biominerals. In this technique a 100 nm thin film of solution containing the particles of interest is formed on a TEM grid, which is subsequently plunge freezed in the appropriate coolant, often liquid ethane at -183° C, embedding the nanostructures in vitrified amorphous ice. Afterwards the sample is transferred from the preparation chamber to the Cryo-TEM sample holder and the microscope. During transfer it is important that ice formation from atmospheric water is avoided. Due to phase contrast, the need for staining is also overcome and the samples can be studied in their near-native hydrated state. Drawbacks of this technique are the complicated sample preparation method and difficulties in changing samples.

TEM measurements for this thesis were performed using four different microscopes. The TEM measurements in Leeds were performed using a FEI Tecnai TF20 operating at 200 kV and Philips CM200 operating at 200 kV. TEM measurements in Eindhoven were performed by Dr. Fabio Nudelman using a FEI Tecnai 20 (Type Sphera) equipped with a LaB_6 filament operating at 200 kV. The Cryo-TEM measurements were done in

Eindhoven using a TU/e CryoTitan (FEI) Cryo-TEM equipped with a field emission gun of 300 kV and with a post-column Gatan energy filter to enhance the quality of the image. The images were recorded using a 2k x 2k Gatan CCD camera.

2.2.8 Thermogravimetric analysis (TGA)

During thermogravimetric analysis the physical and chemical properties of the samples are measured as a function of the temperature and or time. Usually the TGA is operated in such a way that the weight loss of the sample is recorded as a function of the temperature with time, by increasing the temperature with a constant heating rate. Based on this, information about the composition, degradation mechanisms and organic and inorganic content can be extracted. Analysis in our lab was performed using a Modulated DSC-TGA Q200.

2.2.9 X-Ray diffraction (XRD)

X-ray diffraction (XRD) is a non-destructive elastic X-ray scattering technique used to analyse solid structures. It is based on the principle of Bragg diffraction where X-rays are scattered by the atoms in a crystal (also see section 2.2.6.2). Bragg diffraction is the outcome of the interference behaviour between X-ray waves being scattered from different crystal planes, giving rise to constructive and destructive interference. The condition of constructive interference is given by Bragg's law:

$$n\lambda = 2d\sin\theta \qquad \qquad \text{Equation 8}$$

with λ the wavelength of the electron beam, d the spacing between the lattice planes and θ the angle of the diffracted wave. Depending on the crystal structure/characteristics and related d-spacings, constructive interference will occur at different angles giving rise to a characteristic XRD pattern as a fingerprint for the crystalline material.

For this thesis, XRD was performed using a Bruker D8 Advanced diffractometer equipped with an X-ray source emitting Cu Kα1 radiation. Samples were placed on a piece of corundum wafer, and XRD data were collected in an angular range between 5° and 60° in intervals of 0.02°, with a scan rate of 1° min^{-1}.

Chapter 3: Mimicking Bone Formation by Confinement and Addition of Polyaspartic acid
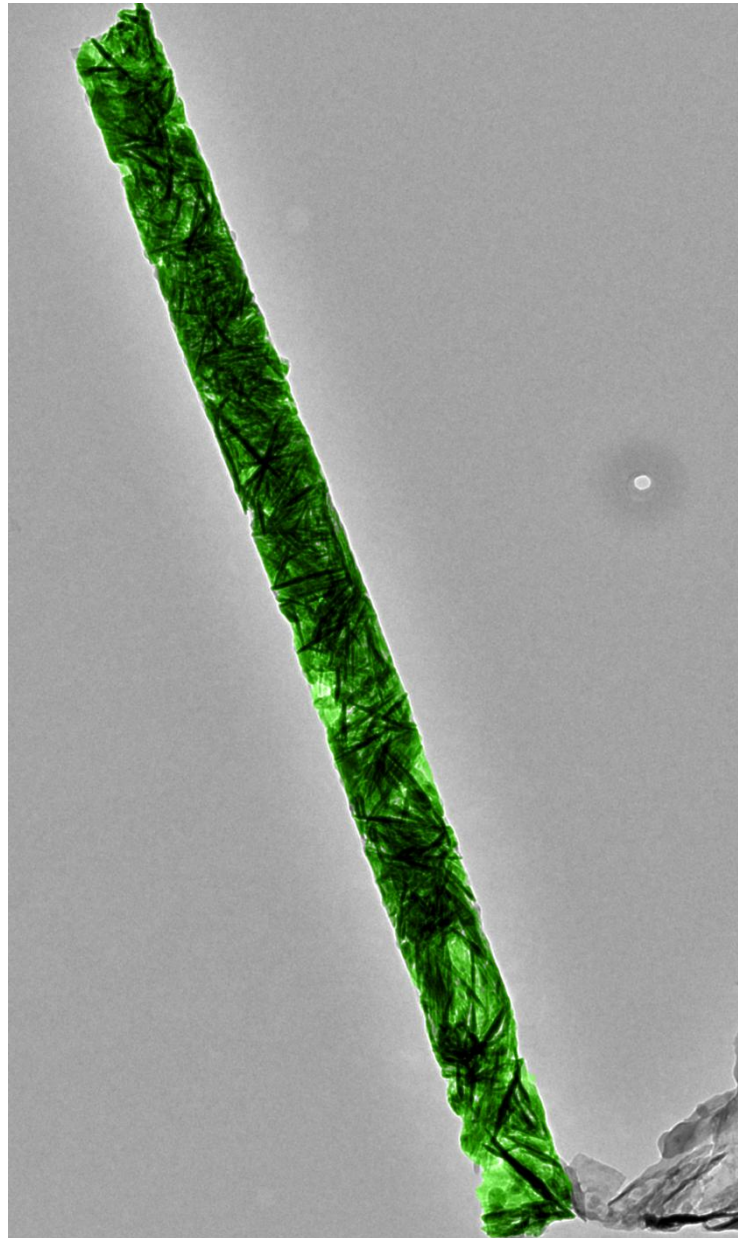
This work investigates the effect of confinement on the nucleation and growth of calcium phosphate (CaP) crystals in the presence and absence of additives, with the aim of better understanding the biological processes which lead to the formation of bones and teeth. It is known mineralisation of calcium phosphate in bone takes place in confinement environments[3] and previous research has shown that polyaspartic acid (PAsp) can influence the mineralisation of CaP in a similar way to the acidic non-collagenous proteins (NCPs) present in bone, leading to the effective infiltration of CaP into the gap regions in collagen[78, 196, 197]. To investigate this further, calcium phosphate was precipitated in the presence and absence of polyaspartic acid (PAsp), within nanosized pores of track-etched membranes, to mimic the effect of confinement. A high yield of particles was obtained and the majority of particles were polycrystalline hydroxyapatite rods with a typical length of 1 to 2 µm and aspect ratios of 5 or 20, according to the pore size used. Some single crystal octacalcium phosphate rods were also formed, particularly in 50 nm pores. Interestingly, the polycrystalline rods showed an orientation of the containing HAP crystals with their *c*-axis oriented along the length of the rod, similar to the structure of mineralised collagen in bone. These results therefore demonstrated, this orientation might be the mere effect of confinement alone, and independent of the collagen structure as previously believed[196, 198, 199]. The addition of PAsp didn't seem to have any major effect on the infiltration mechanism challenging the idea that a polymer-induced liquid-precursor (PILP) phase forms in the CaP/ PAsp system.

3.1 Introduction to calcium phosphate

Calcium phosphates (CaPs) are the most important biominerals in vertebrate systems and the main constituents of bones and teeth. They have a great importance in many areas such as biology, industry, geology, medicine and last but not least dentistry. Accordingly they also have various interesting applications[137] which is reflected in the many industries they are produced, in such forms as ceramics, medicines, dentifrices, nutrient supplements, bone implants, stabilizers for plastics and in agricultural fertilizers[137, 200]. All CaP materials are white solids and most of them are sparingly soluble in water, sometimes even very insoluble, but all dissolve in acids[201] (see Figure 1). They are the main inorganic constituents of biological hard tissues such as teeth and bone and are responsible for the stability, hardness and strength of these organs. They

also can be found in other pathological minerals such as dental calculus, kidney stone formation and atherosclerosis[200]. Although they are both composed of CaP, bones and teeth obviously have different uses, properties and biomineral features. As a consequence, their tissues are created from different lineages: bones and dentin (the inner structure of the tooth) are respectively formed by osteoblast and dentinoblast cells, while dental enamel is formed by ameloblast cells, derived from epithelial tissue[12]. In theory, calcium phosphate covers orthophosphates (PO_4^{3-}), pyrophosphates ($P_2O_7^{4-}$) and poly- ($(PO_3)_n^{n-}$) phosphates, but in general the term calcium phosphate is used to describe calcium orthophosphates since these are the main components of all calcified tissues and are the most abundant type of calcium phosphate[200].

3.1.1 General overview of calcium phosphates

There are eleven known calcium phosphates, where the calcium to phosphate ratio ranges from 0.5 to 2.0: monocalcium phosphate monohydrate (MCPA), dicalcium phosphate dihydrate (DCPD) or brushite, dicalcium phosphate anhydrous (DCPA) or monetite, octacalcium phosphate (OCP), β-tricalcium phosphate (β-TCP) , two forms of α-tricalcium phosphate, amorphous calcium phosphate (ACP) hydroxyapatite (HAP), and finally tetracalcium phosphate (TTCP). Substitution of the hydroxide ion with halide ions gives fluorapatite (FAP) or chlorapatite (ClAP). In the presence of Mg-ions or carbonate respectively, whitlockite and carbonated apatite (CO_3AP) can be formed[137].

Important parameters to distinguish between the calcium phosphate phases are the molar Ca/P ratio and the solubility of the crystals (see Table 1 and Figure 1). The lower the Ca/P ratio, the more acidic and soluble the calcium phosphate phase will be[138]. Out of Figure 1 it can be seen that at a pH of around 7, HAP is the least soluble and therefore the most stable phase, followed by β-TCP and OCP. The pH dependency is due to the fact that orthophosphoric acid is both a weak and polybasic acid, resulting in the fact that the concentrations of HPO_4^-, $H_2PO_4^-$, and PO_4^- change dramatically with the pH of the solution[137].

Table 1. Abbreviations, ratios and solubility products of calcium phosphates[137, 201].

Name and abbreviations	Formula	Crystallographic characteristics	Ca/P	-log K_{sp} at 25 °C
monocalcium phosphate monohydrate (MCPM)	$Ca(H_2PO_4)_2.H_2O$	Triclinic $P\bar{1}$	0.50	highly soluble
dicalcium phosphate dihydrate (DCPD)	$CaHPO_4.2H_2O$	Monoclinic C2/c	1.00	6.59
dicalcium phosphate anhydrous (DCPA)	$CaHPO_4$	Triclinic P1	1.00	6.90
octacalcium phosphate (OCP)	$Ca_8H_2(PO_4)_{6.}5H_2O$	Triclinic P1	1.33	96.6
α-tricalcium phosphate	α- $Ca_3(PO_4)_2$	Monoclinic P21/a	1.50	25.5
β-tricalcium phosphate (β-TCP)	β- $Ca_3(PO_4)_2$	Rhombohedral R3c	1.50	28.9
Whitlockite	$Ca_{18}(MgFe)_2H_2(PO_4)_{14}$	Rhombohedral R3c	1.29	
hydroxyapatite (HAP)	$Ca_5(PO_4)_3OH$	Hexagonal P6$_3$/m	1.67	58.4
fluorapatite (FAP)	$Ca_5(PO_4)_3F$	Hexagonal P6$_3$/m	1.67	60.5
chlorapatite (ClAP)	$Ca_5(PO_4)_3Cl$	Hexagonal P6$_3$/m	1.67	
carbonated apatite (CO$_3$Ap) or dahllite	$Ca_{10}(PO_4)_6CO_3$	Hexagonal P6$_3$/m		
tetracalcium phosphate (TTCP)	$Ca_4(PO_4)_2O$	Monoclinic P21	2.00	38
amorphous calcium phosphate (ACP)		/	1.50	24.8[202, 203]
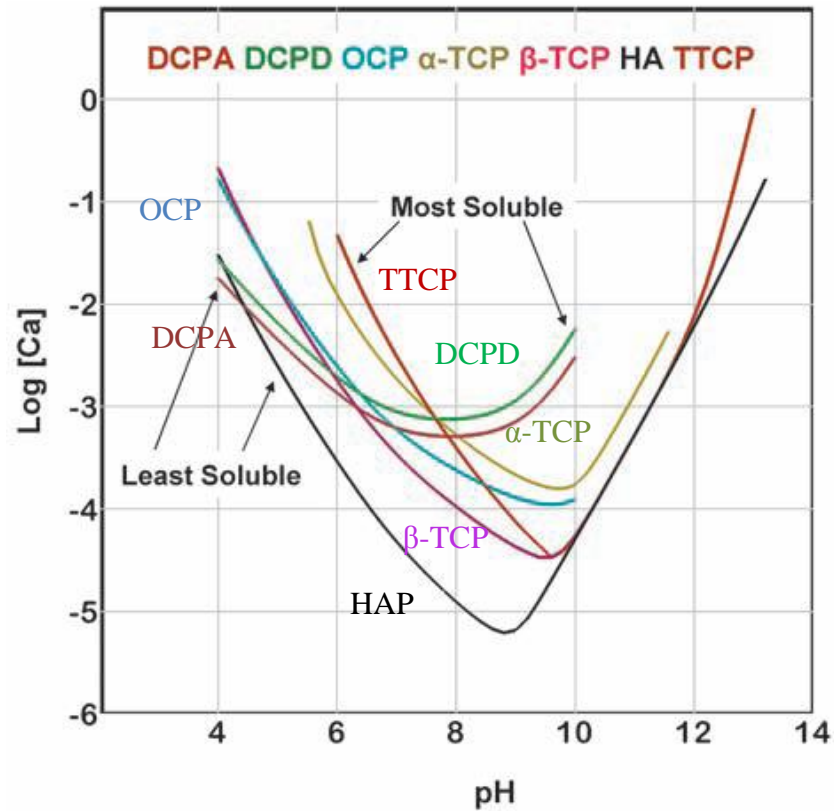
Figure 1: Solubility phase diagram of CaP as function of the pH. Adapted from ref. 204

Naturally occurring hydroxyapatite (HAP) is the main mineral component of vertebrate bones, mammalian teeth, fish scales and the mature teeth of some chiton species[12, 141]. It can be described by a unit cell consisting of a right, rhombic prism, with a length along each edge of the basal plane of the cell of a = 9.432 Å and c = 6.881 Å (space group P63/m) (see Figure 2)[205].
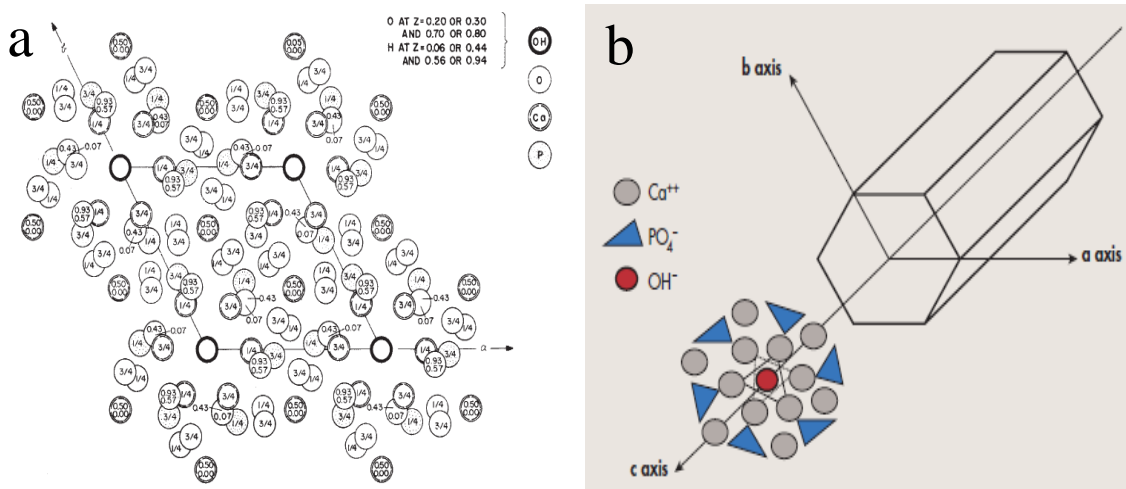
Figure 2 (a) Crystal structure of hydroxyapatite (reproduced from ref. 205) with (b) simplified presentation (reproduced from ref. 206).

HAP is the least soluble calcium phosphate mineral and is preferentially formed under neutral or basic conditions[138]. The atomic formula of HAP can be given by $Ca_5(PO_4)_3OH$ but is often written as $Ca_{10}(PO_4)_6OH_2$ since this formula gives the full hexagonal spatial symmetry of the structure.

The term apatite in general refers to a mineral structure with the chemical formula $A_4B_6(MO_4)X_2$, where for calcium phosphate, A and B are mostly calcium, MO_4 is a phosphate group and X is a hydroxide ion[141, 207, 208]. Biological apatite, which is found in bones and teeth, however often contains significant carbonate substitutions, OH$^-$ deficiencies, and imperfections in the crystal lattice and is therefore often called carbonated apatite $Ca_{10}(PO_4, CO_3)_6$[138, 141] or dahllite. The apatite crystals are often needle or plate-like and are only a few hundreds of nm in size[200].

In addition to HAP, dicalcium phosphate dihydrate (DCPD) or brushite and octacalcium phosphate (OCP) are two other important mineral forms of calcium phosphate formed under ambient conditions. They are often encountered under neutral or acidic conditions[209]. Both minerals have been implicated as possible precursors to the formation of apatite, but no real evidence has been found for *in vitro* formation[138].

The unit cell of OCP is approximately equivalent to two unit cells of HAP and its atomic formula can be given by $Ca_8H_2(PO_4)_6.5H_2O$[137]. The crystals are typically small, platy, almost invariably twinned, and are triclinic with space group $P\bar{1}$. Due to their

similar structures, distinction between HAP and OCP can be difficult but can be achieved with ^{31}P magic-angle spinning NMR, IR, Raman and X-ray diffraction (due to the characteristic (100) reflection of OCP)[141].

OCP was found as a precursor in mouse calvaria bone mineralisation[210] and is believed to be a general precursor in bone formation[138, 208]. However this was never truly proven and much controversy still exists around these results[211]. There is little doubt, however, that OCP occurs as an initial phase in pathological deposits such as kidney stones and calculus[138, 208] and some strong evidence has been presented for its occurrence as a precursor in teeth enamel[208, 212-215]. Intriguingly, many biological and some synthetically produced apatites often contain a central OCP inclusion (also known as a "central dark line") when studied by TEM. This feature is often used as evidence for the hypothesis that OCP acts as a precursor phase to biological apatites[214, 216]. Its occurrence was later explained by an inherent lattice mismatch between OCP and HAP during the transformation of OCP to HAP[214, 216, 217].

DCPD, on the other hand, has been found to occur in small quantities in urinary and dental stones[147, 218, 219], and has been proposed as an intermediate in both bone mineralisation and enamel dissolution[138, 220]. DCPD ($CaHPO_4.2H_2O$) consists of chains of $CaPO_4$ arranged parallel to each other with the lattice water molecules interlayered between the calcium phosphate chains[208, 209]. DCPD is rarely seen *in vivo* although it is suggested this might be due to difficulties in its detection, as a consequence of its weak X-ray diffraction pattern[138, 209].

ACP or amorphous calcium phosphate is the amorphous form of calcium phosphate lacking the long-range, periodic atomic scale order of the crystalline materials. It is often found as a precursor for the fabrication of the other crystalline calcium phosphates[205, 221, 222]. From early on, ACP was put forward as a precursor for HAP in bone formation[45] and has been widely discussed since then[12, 208, 210, 211, 223], but was recently proven to be the case for fin bones of zebrafish[224]. Furthermore, it was also proven that ACP played a crucial role in the precipitation of HAP during enamel formation (for example in chiton teeth[23] and murine tooth enamel[215]). Amorphous calcium phosphate was first discovered in 1953 by Watson et al.[208, 225, 226] but was only fully described by Aaron S. Posner in 1965[221]. It is the first phase to appear on mixing

of solutions at concentrations sufficiently high to produce an immediate precipitation[208] and exists in the form of spherical grains of diameter 300 – 1000 Å. X-ray radial distribution studies concluded that a definite local atomic order is present and microcrystallinities or clusters of about 9.5 Å can be found[227]. It is believed that ACP forms by the aggregation these $Ca_9(PO_4)_6$ clusters, the so-called Posner's clusters (Figure 3)[45, 46] forming a hydrated calcium phosphate phase $(Ca_3(PO_4)_2 \; xH_2O)$ with a Ca/P ratio of around 1.50[45, 138, 221], although the chemical composition strongly depends on the solution pH value and the concentrations of the calcium and phosphate ions[138, 200].
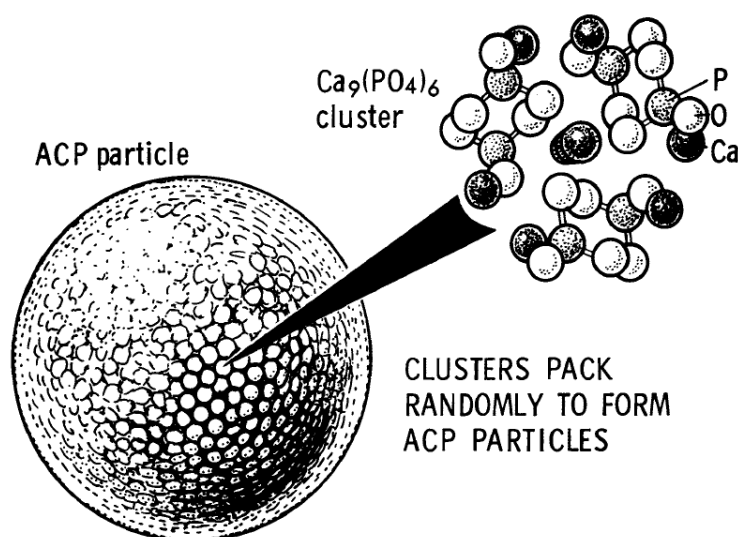
Figure 3: Model of amorphous calcium phosphate with the structure of the Posner cluster highlighted[228, 229]. Image reproduced from ref. 228, 229.

The existence of the Posner clusters was initially answered with much sceptism[230], but recent reports demonstrated the presence of nanometre sized building blocks[46, 47] similar to the Posner clusters, during the precipitation of amorphous calcium phosphate, corresponding with the non-classical precipitation method of prenucleation clusters[46, 67]. Later it was discovered these clusters were in fact calcium triphosphate ion-association complexes, which were able to aggregate into branched three-dimensional (3D) polymeric structures. Through simultaneous binding of calcium, the polymeric solution structures form $\approx$ 1.2 nm post-nucleation clusters of amorphous calcium phosphate which aggregate and precipitate as spherical particles. Finally these clusters transform

into HAP or OCP which both also contain the calcium triphosphate complex as their structural unit[47]. During this transformation, the morphology changes from amorphous polymeric strands to amorphous nodules and aggregated spheres, followed by ribbons and plates of OCP which eventually transform into plate-like HAP.

In general, ACP is a highly unstable phase and transforms into HAP directly or through precursor phases in the presence of water. Its lifetime depends on the presence of additive molecules and ions, pH, ionic strength and temperature[138, 231]. As rule of thumb, ACP converts directly to HAP above pH 9, while at lower pHs, OCP is initially formed[137, 208].

3.1.2 Structure of bone

The structure of bone has been described in a number of reviews[3, 96, 232] and can have quite variable shapes and constituents depending on its function[3]. Early studies showed that the minerals in bone consists out of apatite[233] associated with organic collagen fibrils[234]. In general, the formation of bone happens in 2 main stages[96, 105, 141], the primary and secondary osteogenesis. During the first osteogenesis, the epiphyseal cartilage (stiff yet flexible connective tissue present at each end of the bone) serves as the locus for primary bone formation, and consists of a combination of solid substance made out of carbonated hydroxyapatite (dahllite) and an organic matrix containing loose, small fibrillar bundles of collagen (10-20 nm in diameter[96, 235]). Collagen itself consists of an assembly of approximately 300 nm long and 1.5 nm thick triple-helical collagen molecules, called tropocollagen, and is deposited by the skeletal or osteoblasts cells, after which it assembles into fibrils. Successive molecules are arranged by staggering of parallel molecules with a periodicity of D= 67 nm, generating a characteristic pattern of gap zones of 35-40 nm length and overlap zones of 32-27 nm length within the fibril (Figure 4)[3, 141].
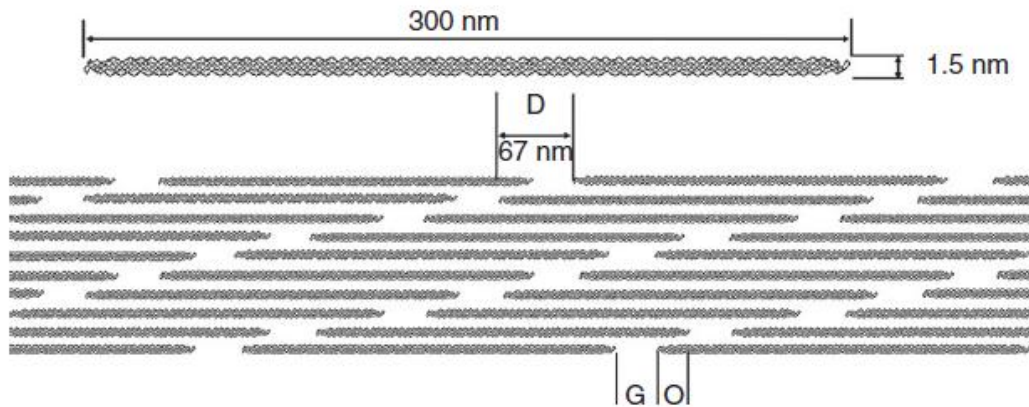
Figure 4: Schematic representation of the structure of collagen. Adapted from ref. 197. 300 nm long and 1.5 nm thick triple-helical collagen molecules are organised into fibrils by staggering of the molecules in a parallel way. Each molecule is shifted 40 nm in the axial direction with respect to its neighbour, giving rise to the 67 nm periodic pattern or D-period (D), consisting of gap (G) zones (35-40 nm length) and overlap (O) zones (32-27 nm length).

The mineralisation is relatively fast and unorganised, and leads to the formation of a primary "woven" bone microstructure which consists of extrafibrillar calcium phosphate crystals together with a random organisation of collagen fibrils[78, 96].

This structure is remodelled during secondary bone formation forming a more highly organised lamellar structure[236]. Therefore, collagen fibrils are secreted again by the osteoblasts cells, but are larger than those in primary bone with a mean diameter of 78 nm[3, 96].

CaP crystals form within the collagen fibrils during secondary bone formation, and the organisation of these crystals is directed by the collagen fibrils[196]. Collagen fibrils are therefore filled and coated by small mainly flat plates of HAP crystals which are mostly arranged parallel to each other but also parallel to the long axis of the collagen fibrils[153] such that the [001] axes of the HAP crystals are coincident with the long axis of the collagen fibrils. This orientation is believed to be achieved by an epitaxial match between the HAP nanocrystals and the amino acid side groups on the collagen fibrils[196, 198, 199]. The HAP crystals have a thickness of around 1.5-4.5 nm and are understood to nucleate mainly within the less dense 40 nm long and 2 nm thick gap zone of the collagen[3, 197, 237, 238]. In this way they occur at regular intervals along the fibril, with an approximate repeat distance of 67 nm, corresponding with the distance by which adjacent collagen molecules are staggered as explained before (Figure 5)[3]
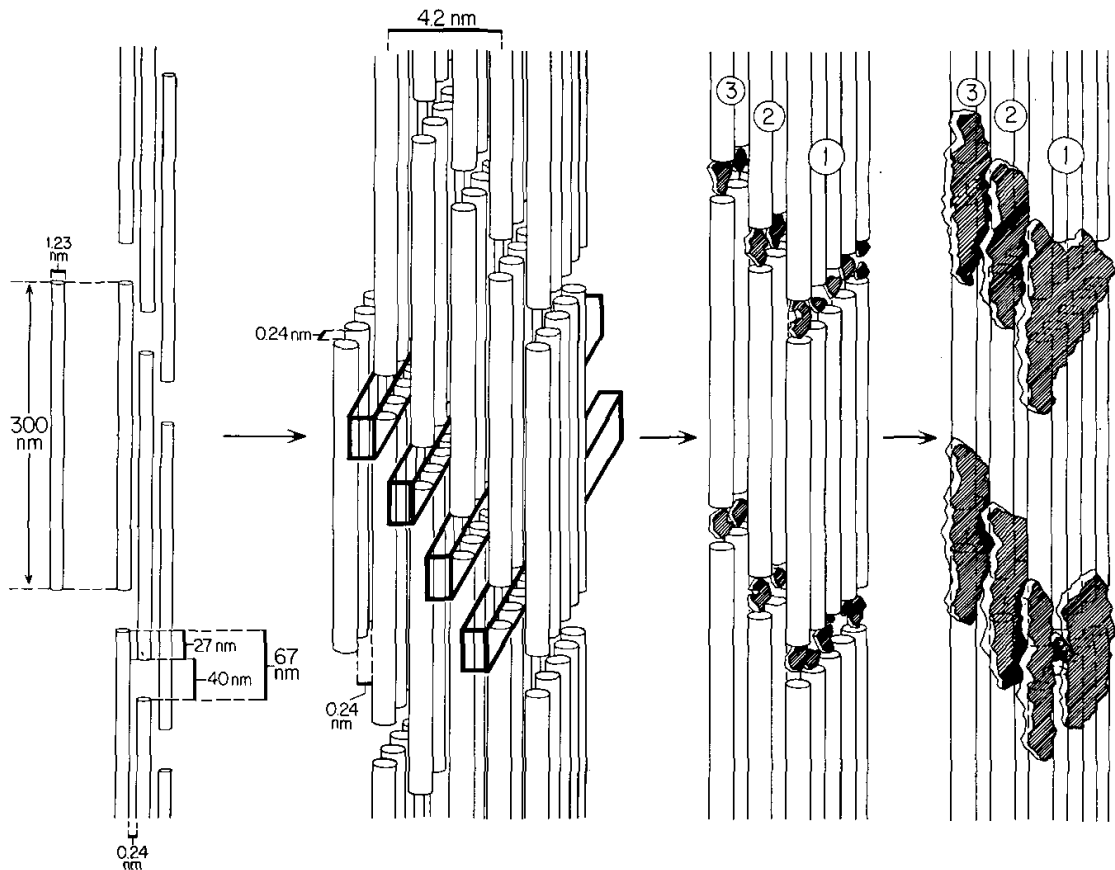
Figure 5: Schematic representation of the mineralisation of collagen by Landis et al.[237], based on *ex situ* observations using high-voltage TEM. On the left side the structure of collagen is illustrated again. The spaces between the assembled collagen units is 0.24 nm[238]. On the right the mineralization of the collagen fibrils is illustrated. The collagen fibrils are filled and coated by small flat plates of HAP which are mostly arranged parallel to each other and parallel to the long axis of the fibrils. Adapted from ref. 96, 153.

This leads to extremely small intrafibrillar crystals within the collagen, which would not be thermodynamically stable if they were not embedded within the organic matrix[96, 200]. As well as intrafibrillar crystals, interfibrillar crystals may also form, between the collagen fibrils and on the surface. In this way a biocomposite is constructed from carbonated hydroxyapatite ($\approx$50-60 wt%) and an organic matrix which principally contains lamellar organised collagen ($\approx$30-40 wt%)[200].

In addition to collagen, non-collagenous proteins (NCPs) can also be found close to the mineralisation front, some of which are highly charged from an abundance of carboxylate groups. Although these proteins are low in concentration and comprise only 10-15% of the organic matrix, it is believed they still have an important role during

the infiltration and the mineralisation process of the collagen fibrils[12, 78, 141]. Besides proteins, there is also a high occurrence of extracellular and intracellular vesicles originating from the osteoblasts cells[239], ensuring that the calcium phosphate ions are brought to the mineralization front in the extracellular matrix[240-242].

A complete overview of the structure of bone is out of the scope of this thesis but a clear description is given by Weiner et al.[232] where they identified seven levels of hierarchy (Figure 6). In the first level, nanoscopic platelets of hydroxyapatite (HAP) (first level) are aligned (second level) and oriented within the self-assembled collagen fibrils (third level) as described before. In the next steps the collagen fibrils are then layered in a parallel arrangement within lamellae (fourth level) that are concentrically arranged around blood vessels to form osteons (fifth level). Finally, the osteons are either packed densely into compact bone, or form into a trabicular network of microporous bone (sixth level) (spongy or cancellous bone) from which the bone is made (seventh level).

The research described in this work primary focuses on the second level.
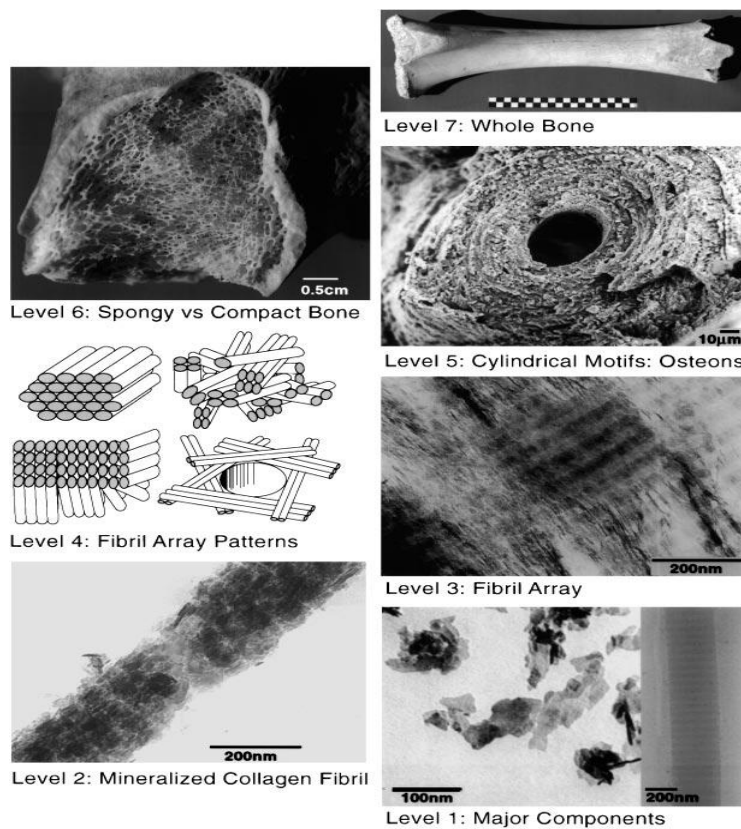
Figure 6: The 7 hierarchical levels of organization of the bone family of materials. Image reproduced from ref. 232.

3.1.3 Structure of teeth.

Teeth are built up from dentin (inside), enamel (outside), pulp and cementum[141, 200] and are the second major calcification present in mammals[105]. Dental enamel is the hardest and most mineralized tissue in the human body and makes up the uppermost 1-2 mm of the tooth crown[215]. On the mesoscale level, enamel consists of three main structural components: the rod, the interrod, and the aprismatic enamel[141, 243]. The main components are the enamel rods which consist of a dense array of needle-shaped carbonated apatite crystals (dahllite), 50 nm across and tens of microns long, with their crystalline *c*-axes aligned along the rods[141, 200, 215, 243]. These minerals form a complicated three-dimensional micro-fabric that provides the bulk of enamel. The second structural component is the interrod which surrounds and packs between the rods. They differ from the rods by the orientation of the HAP crystals which in this case are much less ordered. The third structure is aprismatic enamel and refers to the structures containing HAP crystals that show no mesoscale or macroscale alignment. These have been considered as primitive areas of the tooth, serving as a toughening mechanism due to its flexibility[141].

In contrast to mature enamel which consists of more than 95 wt% of carbonated apatite, the forming early secretor enamel is composed of approximately 30 wt% mineral, 20 wt% organic matrix and 50 wt% water[215, 244]. This matrix, which is thought to regulate the shape and the organisation of mineral particles, contains a number of proteins, with amelogenin the major enamel protein[245]. The assembly of amelogin has been shown to be crucial for the development of enamel, providing a template for mineral formation and is considered to be analogous to collagen in bone[141, 245]. The amelogin is considered to self-assemble into spherical subunits which adsorb to and elongate the hydroxyapatite crystals[12, 141, 245]. During maturation almost all of the proteins are proteolytically degraded and removed. The crystals subsequently thicken and fill 85% of the enamel volume[12, 215, 245]. Recent research has shown that the newly formed enamel mineral is amorphous calcium phosphate (ACP) which eventually transforms into apatite crystals[215].

Dentin lies below enamel, forming the bulk of the tooth. The structure of dentin is a little bit more complex, and for this work it is only important to know that, as with

bone, collagen fibrils direct the mineral growth such that platelets of HAP grow in the [001] direction along the long-axis of the fibril[12, 141].

3.1.4 Infiltration of collagen with HAP in bone

Although bone has been a massively studied material[3, 12, 96], it is still unclear how the final HAP crystallites form within the collagen fibrils[96, 196] during secondary bone formation[3, 55], where much controversy still exists about the role of the collagen matrix and the non-collageneous proteins (NCPs). It is generally believed calcium phosphate first nucleates within intracellular or matrix vesicles, which are formed and released from the outer membranes of osteoblasts and other related cells[141, 239, 246], allowing a high enough supersaturation in a local environment to trigger nucleation and mineralisation. These matrix vesicles have been isolated as the initial site of calcification in cartilage bone, dentin and turkey tendon[246]. The HAP, or possibly other calcium phosphate forms, then breaks through the vesicle as it grows, and is in this way exposed to the extracellular fluid. This would be an active process[200] and according to this theory, the initial mineral formation would be under cellular control (phase 1), whereas mineral propagation would be mediated in some way, by collagen or other proteins in the extracellular matrix (phase 2)[200, 246]. The reoccurring proof of ACP as a precursor for HAP in bone formation[45, 96, 208, 210, 223] brought up the idea that ACP is formed first in the matrix vesicles and is then transported to the collagen matrix.

Another possibility is the idea of a passive process which arises from the observation that blood serum is supersaturated with respect to calcium phosphate. It is suggested mineralisation could therefore occur spontaneously at a suitable nucleus, in this case a collagen fibril[200].

Either way it is still not very clear how exactly the final HAP crystallites form within the nanoscopic spaces of the collagen fibrils in bone. Research has shown that the acidic noncollagenous proteins are essential for effective intrafibrillar mineralisation[247, 248]. This may be because of their binding to the gap region, which could cause nucleation to occur within the fibrils[249]. Another interesting model is the "size-exclusion model" where it is suggested that the large noncollagenous proteins actually inhibit the mineralisation outside the fibrils. Since their size is too big, the noncollagenous proteins cannot penetrate into the gap regions and consequently nucleation will only occur within the gap region[250].

Finally, a promising hypothesis is one from Oslzta et al.[96], who apply capillary forces and a fluidic mineral precursor to explain the infiltration within collagen fibrils (see Figure 7). They used simple anionic polypeptides such as polyaspartic acid (PAsp) to mimic the polyanionic character of the NCPs, proposing that these act as a process-directing agent. The polymer enables the formation of a polymer-induced liquid-precursor (PILP) phase which establishes the generation of an amorphous liquid-phase mineral precursor to HAP. Because of the fluidic character of the amorphous precursor phase, it is drawn into the 40 nm nanoscopic gaps in the collagen fibrils by capillary action, (see Figure 7a) thereby facilitating the intrafibrillar mineralization of type-I collagen (see Figure 7b). Subsequently, the precursor crystallizes according to Ostwald's "step rule" into the more thermodynamically stable phase upon loss of hydration waters, which enables the nanoscopic hydroxyapatite (HAP) crystals to be embedded within the collagen fibrils (see Figure 7c). Electron diffraction patterns showed that the HAP crystallites were preferentially aligned with the [001] along the axis of the fiber, identical to natural bone. Importantly, they stated that epitaxial-type interactions with NCPs were not needed to stimulate and orientate crystal nucleation. Instead, they proposed that the primary template for crystal organisation is collagen, emphasising that this is only possible with crystals formed from an infiltrated amorphous precursor.

The same was discovered by Beniash et al[247] with the important difference that they stated that "the initial mineralization occurs in PAsp/collagen fibril complex and not in the bulk solution as it is proposed by Oslzta et al."[247]. Secondly, Beniash et al. suggested that the organisation and morphology of the particles is fixed in the amorphous phase, while Oslzta et al claimed that the organisation and morphology of the mineral particles was regulated during the mineral phase transition and was determined primarily by the physical constrains of the collagen fibril, where the amorphous phase was homogeneously distributed in and around the fibrils[96, 247].
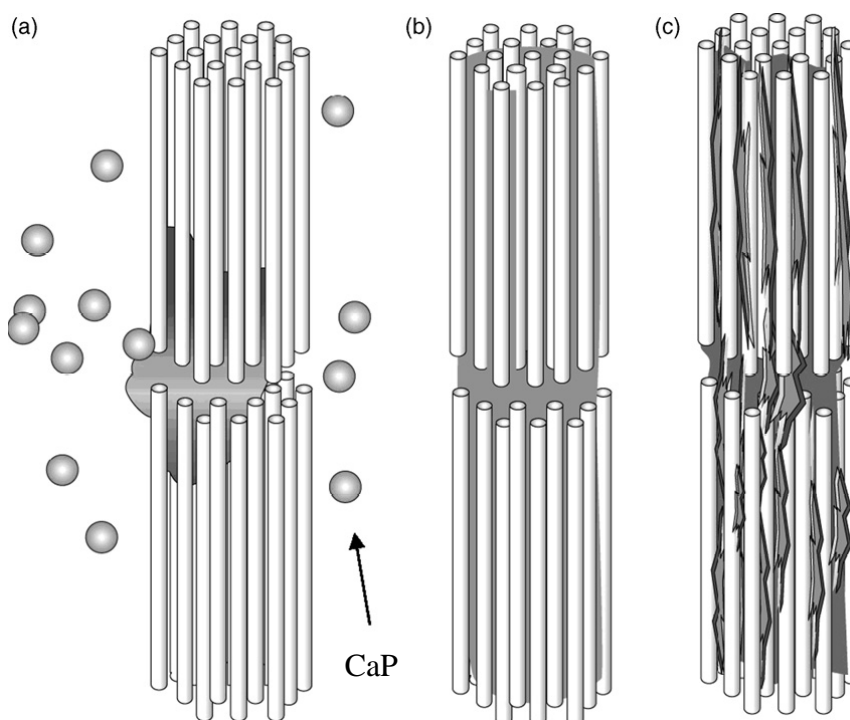
Figure 7: Schematic Figure of a proposed mechanism of intrafibrillar mineralisation of collagen. Adapted from ref. 96.

In recent research it was shown fetuin was also able to mimic the effect of the NCP, allowing the infiltration of collagen with CaP[251, 252]. In addition to the effect of fetuin, it was also demonstrated that an ACP precursor phase was formed in the presence of PAsp which infiltrated the collagen fibrils prior to crystallisation to HAP[196], consistent with previous claims[45, 96, 223]. Interestingly Nudelman et al. showed that the infiltration of the mineral into the fibril doesn't depend on the availability of space but occurs due to a specific interaction between the amorphous mineral phase and the collagen at this location[196]. Since the ACP-PAsp complex forms a negatively charged complex, the most favourable entry sites in the collagen for the ACP-PAsp complex should be the ones with the highest positive charge and therefore the lowest electrostatic potential energy to interact with the complex, which was indeed observed[196]. Further analysis showed that once crystallised, the nanocrystals were distributed evenly between the gap and overlap regions. It was also shown that once the ACP enters the fibril, the collagen controls the nucleation directly, and the charged amino acids appeared to act as nucleation sites for apatite formation[196]. A recent piece of work demonstrated though a clear role for the collagen matrix in directing the morphology and orientation of the HAP crystals without the presence of additives. It was shown that collagen molecules

also got infiltrated with HAP crystals by simply using reaction solutions containing very high concentrations of calcium and phosphate ions[253] in the absence of any type of additive mimicking the working of NCPs. The mechanism of this remained unclear though.

3.1.5 Effect of polyaspartic acid on the crystallisation of CaP:

Considering the content in this chapter, the effect of polyaspartic acid (PAsp) on the crystallisation of calcium phosphate will be discussed. Previous research showed that PAsp had the ability to massively slow down the kinetics of the amorphous to crystalline transformation[147, 196, 251]. By addition of the PAsp, it was observed that a stable colloidal species was formed, where the PAsp chains are cross-linked by the ACP clusters, keeping the calcium phosphate as stable amorphous intermediates[147]. After crystallisation a "hollow snowball" structure was formed, composed of single crystal HAP platelets. Additionally, it was also observed that the amorphous particles grow larger in the presence of PAsp[251]. PAsp has also been suggested to stabilise the formation of OCP by site-specific adsorption onto the hydrated layer of the (100) and (010) faces of OCP[254, 255] whereby the stabilisation takes place by preventing the OCP crystals of splitting along their *c*-axis and transforming into HAP[254]. Interestingly, PAsp was able to sufficiently inhibit the OCP growth by 20% by covering only 1% of the (100) face[255]. This showed indications for a dynamic adsorption/desorption equilibrium mechanism as was found for PAsp adsorption onto the (010) face of DCPD[256]. PAsp has also been shown to influence the morphology of OCP[145, 146], with formation of spheres and reducing its dimensions, and of DCPD[257], where crystals were obtained containing a leaf-like appearance with fragmented stripes. Research on the influence of PAsp on HAP formation showed that HAP was inhibited by PAsp[258] and smaller crystal sizes were formed[247]. The crystals had a more spindle or needle-like shape and often deposited as clusters of tiny crystals with a plate-like morphology[142, 144]. The crystals got smaller with increasing amounts of PAsp used[247].

3.1.6: Previous studies of the effect of confinement on calcium phosphate crystallisation.

As illustrated above, one of the key features of the deposition of calcium phosphate in bones and teeth during biomineralisation, is that the calcium phosphate is generated

within confined volumes. This is particularly true for bone and dentin, where 2 to 10 nm thick CaP platelets form within the nanoscal gap regions of collagen[153, 237].

Previous research has shown before that with reduction in volume, surfaces become increasingly important and can dominate the crystallisation process[259] which can have a significant effect on the nucleation and growth phases of the mineral[29, 152, 160].

Consequently, in the past few years, many interesting systems have been developed to investigate the effect of microenvironment on CaP precipitation. Very interesting systems are reverse micelles and microemulsions which have been widely used to manipulate the precipitation of CaP particles, leading to the control over their size, shape and phase[260-262]. For example, by using reverse micelles of calcium bis(2-ethylhexyl) phosphate, it was possible to form calcium phosphate nanofilaments, 2 nm in width and 300 μm > long, which are characteristic of aggregation-based growth[263]. Double-hydrophilic block copolymer aggregates have been used as dispersed templates for the controlled precipitation of calcium phosphate, where outgrowth of nanofilaments resulted in an arrangement of unusual neuron-like morphologies[264], while bicontinuous microemulsions have been used to template the formation of skeletal CaP frameworks[265]. Using larger reaction volumes, CaP has been precipitated within giant block copolymer vesicles[266] and anionic liposomes[267, 268], where the latter work suggested that the liposome membrane may support nucleation. Calcium phosphate has also been precipitated within uniaxially deformed gelatin films, allowing to investigate the effects of confinement on the crystallisation of calcium phosphate[14]. This resulted in alignment of the *c*-axes of the CaP crystals with respect to the axis of deformation[269] while cross-linked gelatine nanoparticles supported the formation of HAP particles via a transformation of sequential ACP and octacalcium phosphate (OCP) phases[270]. Finally growing CaP in agar gels allowed formation of OCP spherulites consisting out of an assembly of plate-like crystallites or whiskers[271].

3.2 Aims of the project

All these systems provided examples of CaP products formed in small volumes and confined areas which vary from those which would be formed in bulk solution under similar reaction conditions. Yet, due to their compositional complexity and often dynamic character, it is often difficult to clarify the effects of individual experimental variables, and in particular importance for this chapter, to isolate the effects of

confinement. In order to gain further understanding of the influence of confined reaction volumes on CaP precipitation, the experiments were carried out here using a model system where crystallization was performed within the pores of track-etched (TE) and porous alumina membranes (PAM). TE membranes are commercially-available filtration membranes (Millipore, Nucleopore) and are made out of polycarbonate material or polyester with an approximate thickness of around 10 μm. By bombarding this nonporous sheet with nuclear fission fragments, damage tracks are created in the material which are subsequently etched into cylindrical pores. This way a porous material is fabricated, containing randomly distributed nanochannels of uniform diameter, ranging from 0.015 μm to 12 μm with pore densities of 10^9 pores cm^{-2} [272]. Porous alumina membranes are also commercially available, with well-defined pore sizes and thickness of 60 μm, but it is often desirable to tune the pore sizes and oxide thickness. Therefore they can be fabricated in the lab by a simple anodisation process giving pore sizes of as low as 15 nm [273, 274]. Both therefore provide controlled environments, enabling study of the effects of a constrained volume, as defined here by the diameter and shape of the pore, on the mechanism and product of CaP precipitation.

3.3 Alumina membranes.

Porous alumina membranes (PAM), or also called anodic aluminium oxide (AAO) membranes, are often used for templating, and are applied widely in many applications such as the production of metallic nanowires [275], semiconductor nanowires [262], metallic nanotubes [276] and carbon nanotubes [272, 277, 278]. The form of these membranes can be described as a honeycomb structure of fine channels, characterised by a close-packed array of columnar hexagonal cells, each of which contains a circular pore in the centre. As compared with track-etched (TE) membranes, porous alumina membranes contain pores with little or no tilt with respect to the surface normal, resulting in an isolated, non-connecting pore structure [279, 280]. Pores with a uniform diameter can be achieved and porous alumina membranes also exhibit higher pore densities of 10^{11} pores cm^{-2} instead of 10^9 pores cm^{-2} for TE membranes, and pore sizes down to 15 nm. Over the past four decades, intensive research has been done on the lab synthesis of porous alumina membranes using electrochemistry. Membranes with pore diameters, oxide thickness and pore densities ranging respectively from 10 nm to 400 nm, 0.3 μm to 200 μm and 10^9-10^{11} pores cm^{-2} can be easily generated by changing the processing

conditions such as temperature, operating voltage and electrolyte[262, 281, 282]. In addition to these main advantages, other useful properties include the high resistivity of 10^{18} Ω cm^{-1}, the optical transparency, the wide energy band and the chemical stability[279, 281].

3.3.1 Synthesis of alumina membranes

Alumina membranes are fabricated in acid solutions by anodisation of pure aluminium under a constant electric field. Various electrolytes such as sulphuric acid, oxalic acid and phosphoric acid can be used, leading to different pore diameters and inter-pore distances as shown in Table 2. In addition to the type of electrolyte, the applied voltage also has a great influence on the pore diameter and inter-pore distances. In the work described in the following section, oxalic acid was used as an electrolyte and the applied voltage was 40V.

Table 2: Different electrolytes with their corresponding pore diameters, inter-pore distances and applied voltages[262, 273, 274, 278, 279, 283, 284].

Electrolyte	Pore diameter (nm)	Inter-pore distance (nm)	Voltage (V)
Sulphuric acid (H$_2$SO$_4$)	15-35	60	20-27
Oxalic acid (H$_2$C$_2$O$_4$)	20-100	95	30-80
Phosphoric acid (H$_3$PO$_4$)	180-400	500	100-195

The chemical reaction involved in the production of the alumina membranes is given below (see Figure 8).

$$Al \rightarrow Al^{3+} + 3\ e^- \text{ (reaction 1 at metal/oxide interface)}$$

$$\frac{3}{2}H_2O \rightarrow 3H^+ + \frac{3}{2}O^{2-} \text{ (reaction 2 at oxide/electrolyte interface)}$$

$$6H^+ + 6e^- \rightarrow 3H_2 \text{ (reaction 3: cathode reaction)}$$

$$2Al + 3H_2O \rightarrow Al_2O_3 + 3\ H_2 \text{ (reaction 4: general reaction)}$$
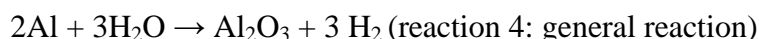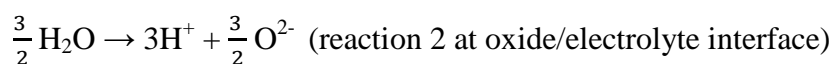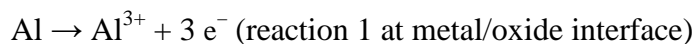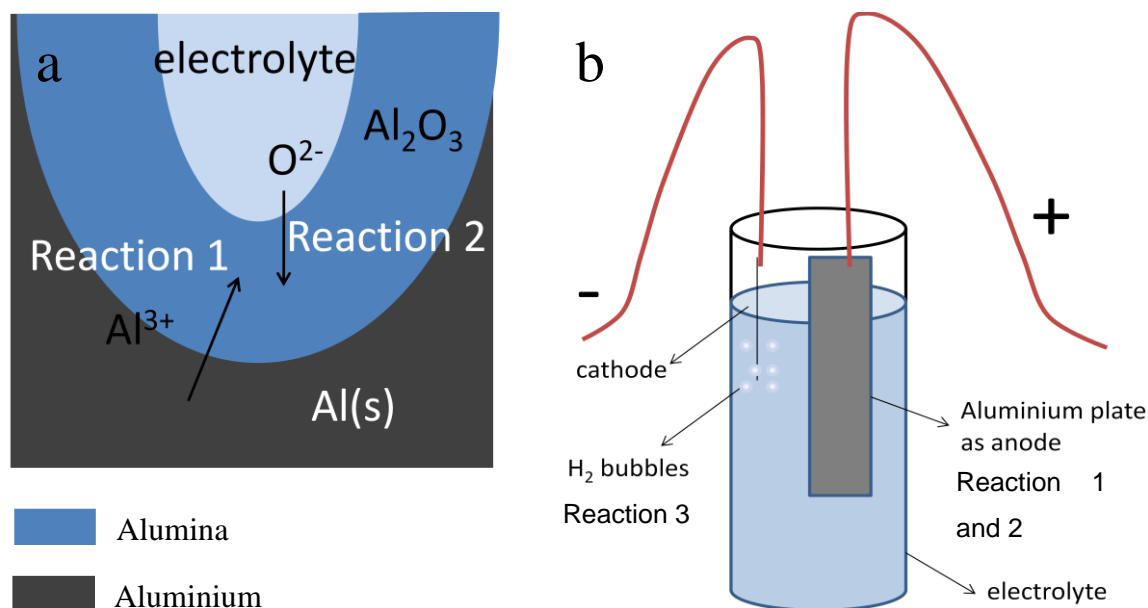
Figure 8: (a) Schematic representation of the reactions taking place at the aluminium surface during anodisation of aluminium. (b) Overview of the electrochemical cell.

The aluminium is connected to the positive terminal of the power supply and electrons are withdrawn from the metal. In this way Al^{3+} ions are formed at the metal/oxide interface (reaction 1) which migrate into the oxide layer. The O^{2-} oxide-ions formed during the water splitting reaction at the oxide/electrolyte interface (reaction 2) migrate from the oxide/solution interface towards the metal/oxide interface to form Al_2O_3[273, 281]. At the cathode, hydrogen gas is formed which escapes from the solution (see Figure 8b).

Alumina membranes are usually produced according to a technique developed by Masuda and Fukada[285, 286] where the first anodisation step is followed by wet chemical etching to remove the first porous oxide film (see Figure 9). This etching step is necessary since the pores produced in the first anodisation step are not parallel to each other. The porous film contains a barrier layer at the bottom, consisting of periodically arranged cavities and shoulders. After removal of the porous film, the periodic concave patterns that remain act as a self-assembled template for a second anodisation process, resulting in an ordered nanopore array. This second anodisation takes place under the same conditions used for the first anodisation. The longer this second anodisation step, the thicker are the formed membranes.
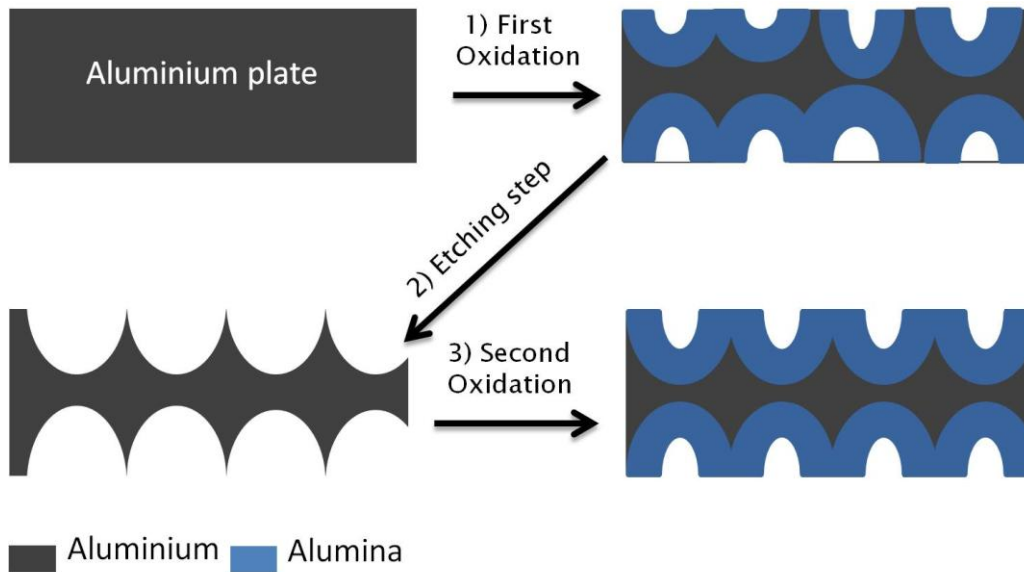
Figure 9: Schematic representation of the anodic anodisation for the fabrication of porous alumina membranes. 1: Formation of the porous alumina layer after first anodic oxidation process. 2: Etching of porous alumina layer. 3: Second anodic oxidation process, producing porous alumina membranes

According to Masuda and Fukada, pore regularity is improved upon using longer anodisation times under appropriate conditions[286]. During anodisation, the surface of the aluminium heats up, so a cooling system has to be used to keep the temperature constant. Local heating also brings about inhomogeneous electric field distributions at the bottom of the pores, leading to electrical breakdown, local thickening of the barrier layer and pore branching of the oxide due to weak acidity[279, 281]. Since temperature also strongly affects the self-ordered pore growth, the temperature for the following experiments is held at 5° C by the use of a cooling system.

3.4 Experimental

Calcium phosphate (CaP) was precipitated within the confines of the pores of track-etched and anodised aluminium oxide membranes in the presence and absence of poly(aspartic acid) (PAsp), and the influence of the pore diameter and the reaction conditions on the resulting particles was investigated.

3.4.1 Preparation of porous alumina membranes

High purity aluminium foil (99.99%, 0.5 mm and 0.01 mm thick) was used as a starting material. Before anodisation, the aluminium foil was annealed at 500 °C overnight. Subsequently, the foil was degreased in acetone for 5 min, etched in 5 wt % NaOH for 2 min and electro-polished in an 5:1 v/v solution of $EtOH/HClO_4$ at 6°C for 1 min. PAM were then prepared according to the two-step anodisation process. In a first step the prepared aluminium foils were anodised in a 3 mM oxalic acid solution for 10 h, under a constant voltage of 40 V. A carbon plate was used as the cathode. Temperature was kept at 5 °C at all times by the use of a cooler system where water circulated around the oxalic acid solution (Figure 10). The anodised aluminium was subsequently immersed in a mixture of 5 w% H_3PO_4 and 1.8 w% H_2CrO_4 at 60°C for 12 h, to remove the sacrificial alumina layer. To avoid evaporation due to the high temperature, the chromic acid solution was placed in a hermetically-sealed bomb calorimeter. The anodisation was then repeated again under the same conditions as the first step, resulting in porous alumina layers.
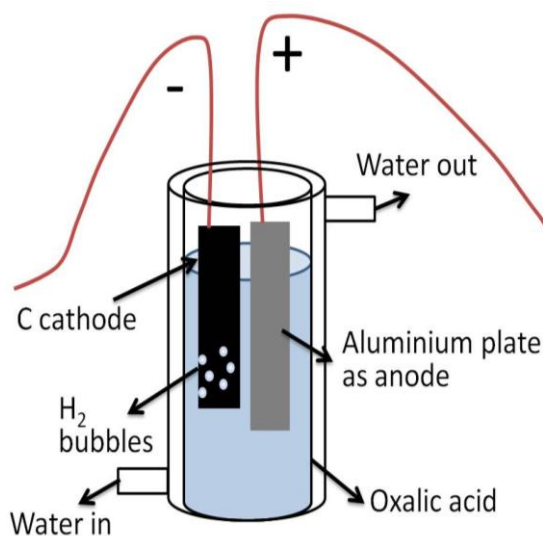
Figure 10: Experimental set-up of the electrochemical cell.

Eventually, the alumina layer was isolated from the support. This was done with two different techniques. In the first technique, the membranes were immersed in 5 wt% H_3PO_4 solution for half an hour, which allowed pore widening and removal of the remaining Al_2O_3 barrier layer. A second technique which proved more efficient was the voltage pulse technique[287, 288] whereby the sample was immersed in a solution of ethanol/perchloric acid (1:1), which was cooled to 5 °C and a voltage of 65 V was

applied for 2-3 s making the alumina layer separate from the support. After removal of the barrier layer the porous alumina membranes were washed with water 5 times and kept in water for storage.

3.4.2 Precipitation of calcium phosphate in membrane pores.

Following the experiments by Olszta et al[96], a Tris-Saline buffer was prepared by dissolving 8.77g of NaCl, 6.61g of Tris-HCl and 0.96g of Tris-base in 1L UltraPure H_2O. The pH of this solution was measured as 7.59 at 25°C. This buffer stock solution was then used to prepare separate solutions of 9 mM $CaCl_2.2H_2O$ and 4.2 mM $K_2HPO_4.3H_2O$, where the pH of both solutions was adjusted to 7.4 at 37°C using NaOH. In addition to the buffer stock solution, stock solutions of 9mM $CaCl_2.2H_2O$ and 4.2mM $K_2HPO_4.3H_2O$ in UltraPure DI water were also prepared (pH respectively 5.62 and 8.42). Isopore GTTP polycarbonate track-etched membranes with 50 nm and 200 nm pore sizes (Millipore) and PAM (commercially available anodic 25 from Whatman with pore sizes of 200-300 nm and home-made with pore size of 30 nm) were used for the study. The membranes were transferred into clean vials containing $CaCl_2.2H_2O$ solution (in Tris-buffer solution or just DI UltraPure water). Polyaspartic acid sodium salt solution (Poly-(alpha,beta)-DL-aspartic acid sodium salt Mw 2000 - 11000 Da) was added to half of the vials with a concentration range of 10 µg/ml to 100 µg/ml. The solutions were then degassed under vacuum and left overnight to allow saturation of the surface and penetration of the calcium ions into the membrane pores.

3.4.3 Mineralisation of calcium phosphate.

To synthesise the CaP crystals inside the membrane pores two different techniques were used. The immersion method and the double diffusion (U-tube) method (see Figure 11). In the immersion method (Figure 11a), a membrane which had been previously soaked in the buffered $CaCl_2.2H_2O$ solution was placed in a vial containing 5 ml of 9 mM $CaCl_2.2H_2O$ solution. To half of the experiments, polyaspartic acid (PAsp) was added to the solution to give final concentrations between 10 and 100 µg/ml of PAsp. In the final step, 5 ml of 4.2 mM K_2HPO_4 was added to the solution to give final concentrations of 4.5 mM $CaCl_2.2H_2O$ and 2.1 mM $K_2HPO_4.3H_2O$. To avoid crystals precipitated in the bulk solution from falling onto the surface of the membranes, the

membranes were placed vertically in the vials. In the double diffusion method (Figure 11b), a membrane was sealed between a pair of U-tube arms. To make sure a watertight seal was formed, the joints were wrapped in several layers of Teflon tape and eventually both parts were pinched together. Covering of the joints with Parafilm before mounting the membrane also proved to be beneficial to avoid leaking. Solutions containing the desired amount of polymer (10 µg/ml to 100 µg/ml) were prepared, and 1.6 ml of the 9 mM $CaCl_2$ solution and 1.6 ml of the 4.2 mM K_2HPO_4 were added to the respective arms using plastic syringes fitted with long needles in order to prevent formation of air bubbles adjacent to the membrane. Tapping of the central part of the U-tube also helped to remove the air bubbles and the arms were refilled so that there were roughly equal volumes of both solutions.

To avoid evaporation of the solution, the open tops of the tubes were sealed with Parafilm.
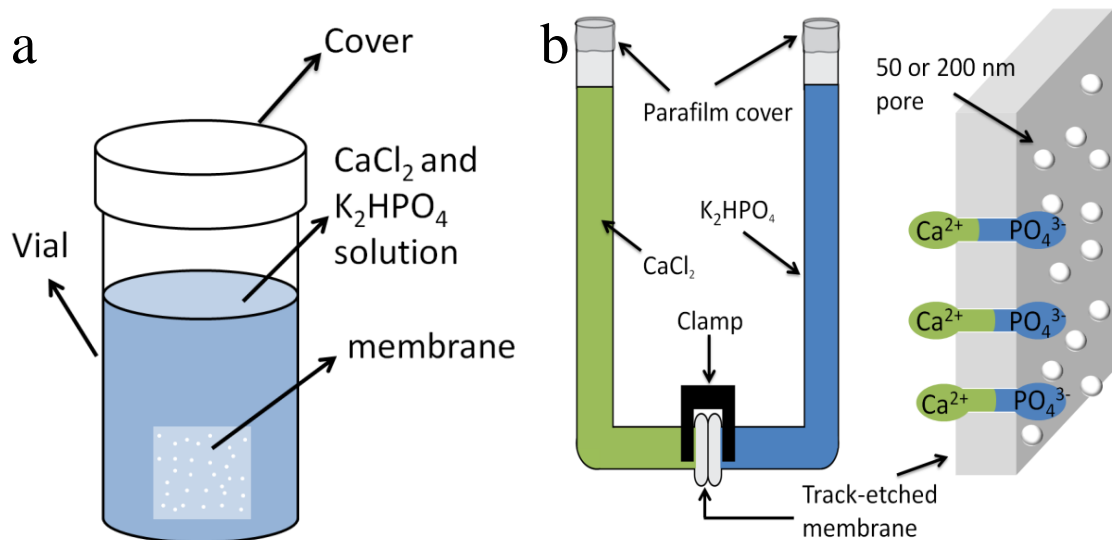
Figure 11: Immersion method (a) and double diffusion setup (b).

The different set-ups containing the membranes were then incubated at 37°C in an oven for 3 h to 6 days yielding eight different solution conditions as shown in Table 3.

Table 3: Different solutions used for the synthesis of CaP rods.

Solution	Presence of buffer	additive	Method
1	Tris-buffer	No additive	Double diffusion
2	Tris-buffer	Polyaspartic acid	Double diffusion
3	No buffer	No additive	Double diffusion
4	No buffer	Polyaspartic acid	Double diffusion
5	Tris-buffer	No additive	Immersion
6	Tris-buffer	Polyaspartic acid	Immersion
7	No buffer	No additive	Immersion
8	No buffer	Polyaspartic acid	Immersion

At the end of the reaction, the membranes were removed from the reaction solution and the TE membranes were dissolved in DCM while the PAM were dissolved in NaOH (see 2.1.3.3).

3.4.4 Control experiments.

Control experiments were also carried out under identical reaction conditions, but in bulk solution. Glass slides were placed at the base of the reaction vials, in order to sample the precipitated crystals, and these were removed from the solution after 1 h to 6 days, before being washed with ethanol and dried with nitrogen. Ni TEM grids were also placed in the solution to observe precipitates inside the solution by TEM, after which they were washed in ethanol and left to dry.

3.4.5 Analysis of the samples.

The isolated CaP crystals were characterized using SEM and TEM to determine their dimensions and morphologies. Samples for SEM were prepared by placing a droplet of an ethanol suspension of CaP particles onto a glass slide, allowing it to dry. Alternatively the ethanol suspension was filtered through a track-etched membrane to get rid of unwanted particles. After drying, the filter membrane was mounted on an SEM stub. TEM was performed by placing an ethanol suspension of the CaP particles on a carbon-covered Cu TEM grid. Identification of the kind of calcium phosphate

present was achieved using electron diffraction, carried out in the TEM using selected area electron diffraction techniques (SAED), micro-Raman spectroscopy and XRD.

3.5 Results

3.5.1 Analysis of the porous alumina membranes:

During the first oxidation process the current decreased from 0.1 to 0.02 A and bubbles appeared at the cathode due to the production of H_2. After 10 h, a white layer had formed on the aluminium sheet. Placing the aluminium sheet in chromic acid for 12 h removed the white layer making it dark grey. After the second anodisation step at the same conditions as the first anodisation step, an alumina membrane is produced as shown in Figure 12.
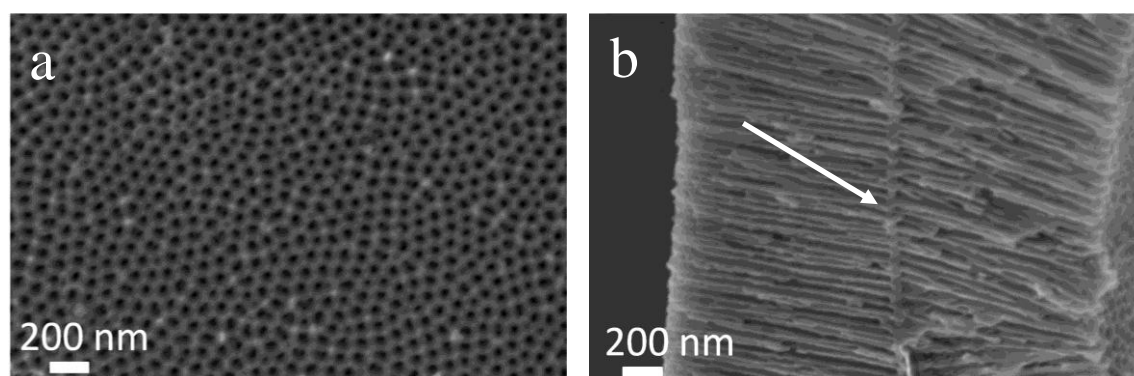
Figure 12: SEM images of top view (a) and cross-section view (b) of porous alumina membranes produced in a double anodisation process. To show the complete thickness of the membrane an anodised aluminium foil of 0.01 mm thick is shown.

Pore sizes and inter pore distances of the membranes ranged respectively from 20 nm to 40 nm and 20 nm to 50 nm with an average of respectively 33 nm and 37 nm. In this way, pore densities of 10^{10} pores cm^{-2} were obtained (see Figure 12a). Figure 12b shows a cross-sectional view of a membrane. The pores are straight through the whole thickness until they meet in the middle (see Figure 12b arrow) and are parallel aligned to each other with almost no intercrossing. The diameter of the pores corresponded with the ones seen on Figure 12a (~30 nm).

To remove the alumina membranes from the remaining aluminium two different techniques were employed. In one technique, they were immersed in 5 w% H_3PO_4

solution for half an hour. This allowed pore widening and removal of the remaining Al_2O_3 barrier layer. SEM analysis showed that the pores went all the way through (Figure 13c and d) but the pore size differed on the two membrane surfaces (Figure 13a and b). The pore size at the top side had increased to 80 nm (Figure 13a) while at the bottom side this was still 40 to 50 nm (Figure 13b).
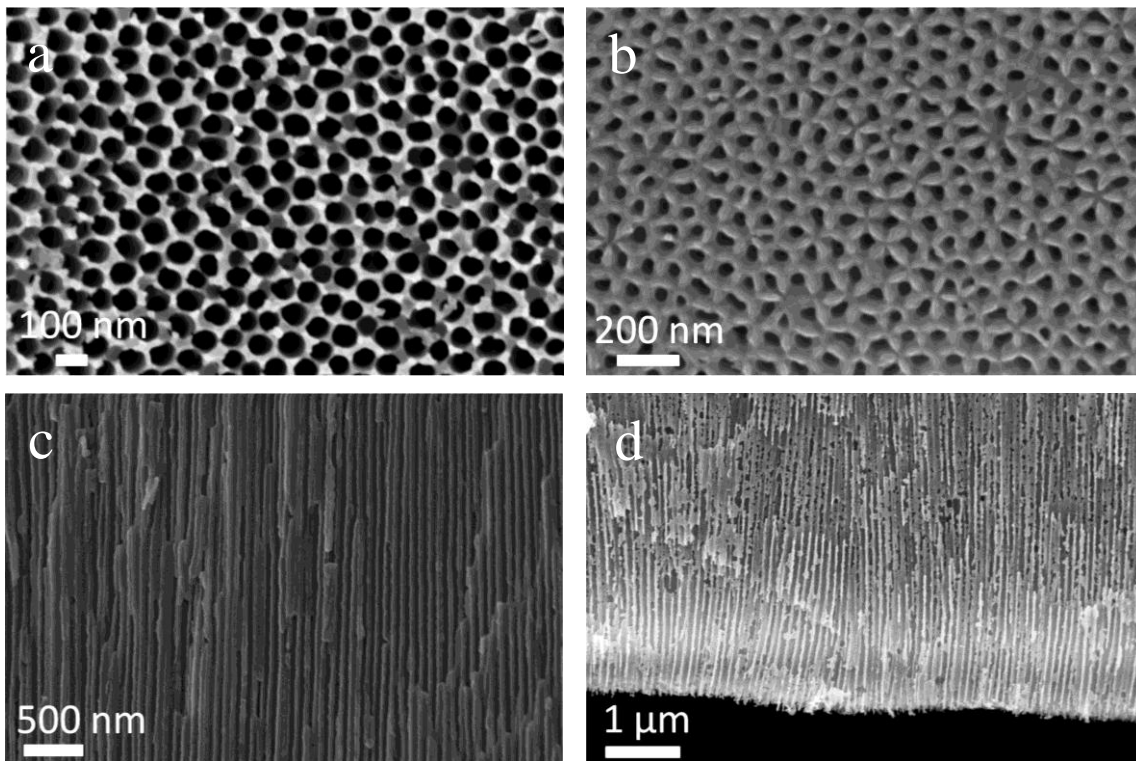
Figure 13: SEM images of porous alumina membranes produced in a double anodisation process whereafter the remaining aluminium is removed by immersing the membrane in 5 w% H_3PO_4 solution for half an hour. (a) Shows the top side while (b) shows the bottom side. (c) And (d) show a side view and show the pores are now the whole way through.

Another technique used is the voltage pulse technique, which allowed the porous alumina membrane just to "fall off" the support. SEM analysis (Figure 14) showed that the pores were again all the way through the membrane, but the pore size had remained constant in this case (20 nm to 40 nm).
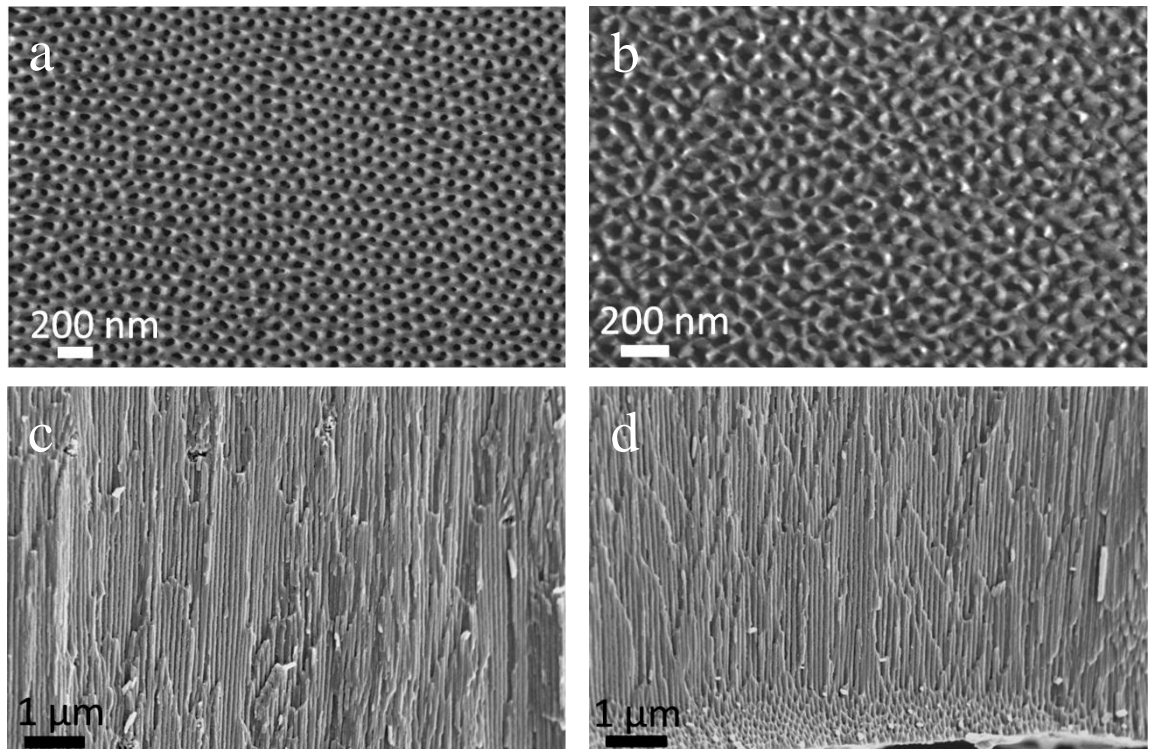
Figure 14: SEM images of a cross-section view of the porous alumina membranes produced in a double anodisation process whereafter the remaining aluminium is removed by a voltage pulse technique. (a) And (b) show top and bottom side, (c, d) show the side view.

Commercially available alumina membranes (anodic 25 from Whatman) were also analysed. Although the pore size stated on the package was 20 nm, analysis with SEM (Figure 15) showed this was actually only true for the top side while on the bottom side the pores were ≈ 200 nm.
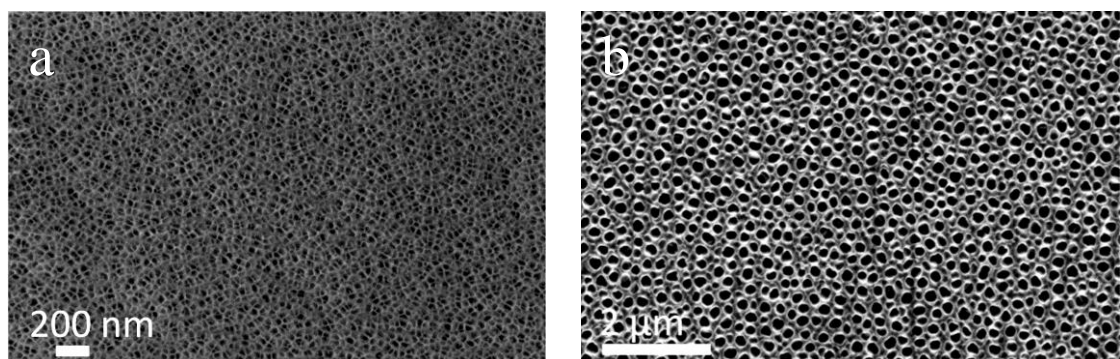
Figure 15: SEM images of commercial available alumina membranes (anodic 25 from Whatman). The top side (a) has pores of ≈ 20 nm while for the bottom side (b) the pores were actually 200 nm.

3.5.2 Analysis of track-etched membranes.

Prior to use, track-etched membranes were also imaged using FEG-SEM (Figure 16).
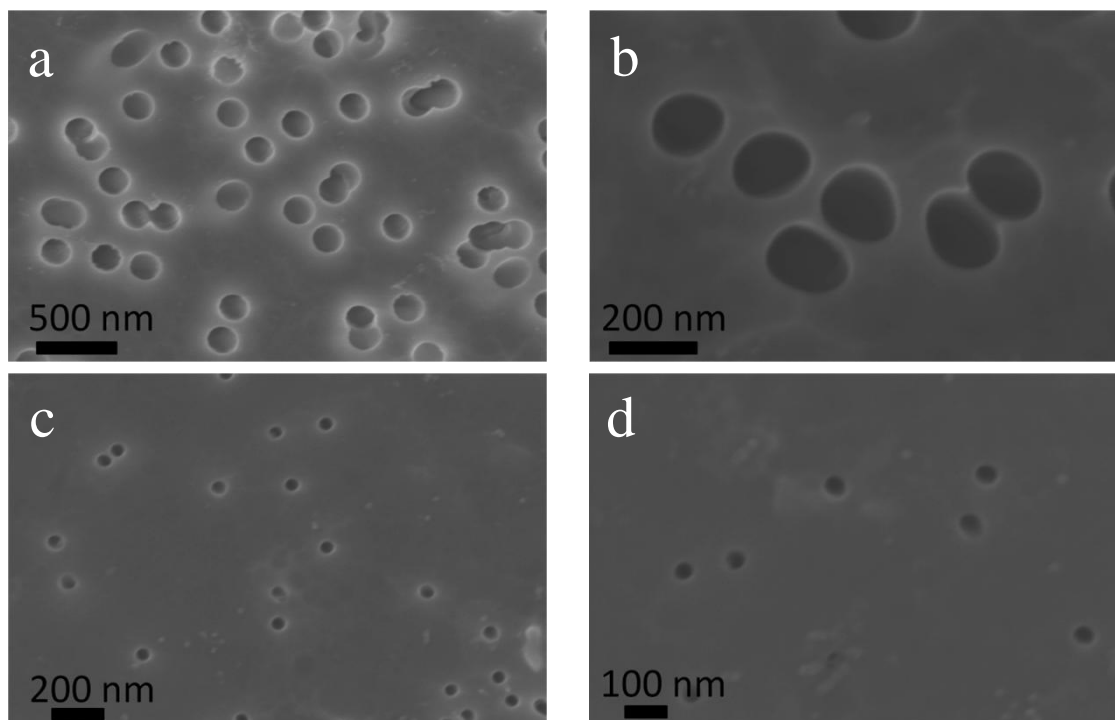
Figure 16: SEM image of Isopore GTTP membrane filters (Millipore) polycarbonate track-etched membranes with pores of 200 nm (a,b) and 50 nm (c,d).

Analysis of the track-etched membranes showed that the pores are not uniformly distributed, that they were of low density (10^8 pores per cm^2) and that the pore sizes ranged from 250 nm to 150 nm for the 200 nm pores and 40 nm to 100 nm for the 50 nm pores. These membranes are sold for filtration applications, and thus the pore diameter quoted is the pore size at the membrane surface, rather than the internal diameter. Some pores also intercrossed and formed double pores (Figure 16a, b). Despite these disadvantages (non uniformly distributed pores, intercrossing of the pores, low pore density), they were still chosen because they are relatively cheap, they could easily be dissolved in DCM, and were not as brittle as the alumina membranes.

3.5.3 Analysis of material obtained in bulk solution.

As a first experiment to evaluate the effects of confinement on calcium phosphate (CaP) precipitation, control experiments were conducted where CaP was precipitated from

bulk solution, as well as in the presence and absence of PAsp. In the absence of PAsp, the material isolated after 1 h consisted out of amorphous CaP particles with average sizes of 10 nm, as shown by TEM and EDX (Figure 17a). After 2 h these amorphous particles had grown to 20 nm in size (Figure 17b) and additional crystalline octacalcium phosphate (OCP) platelets of 20 nm in size (Figure 17c) were also observed.
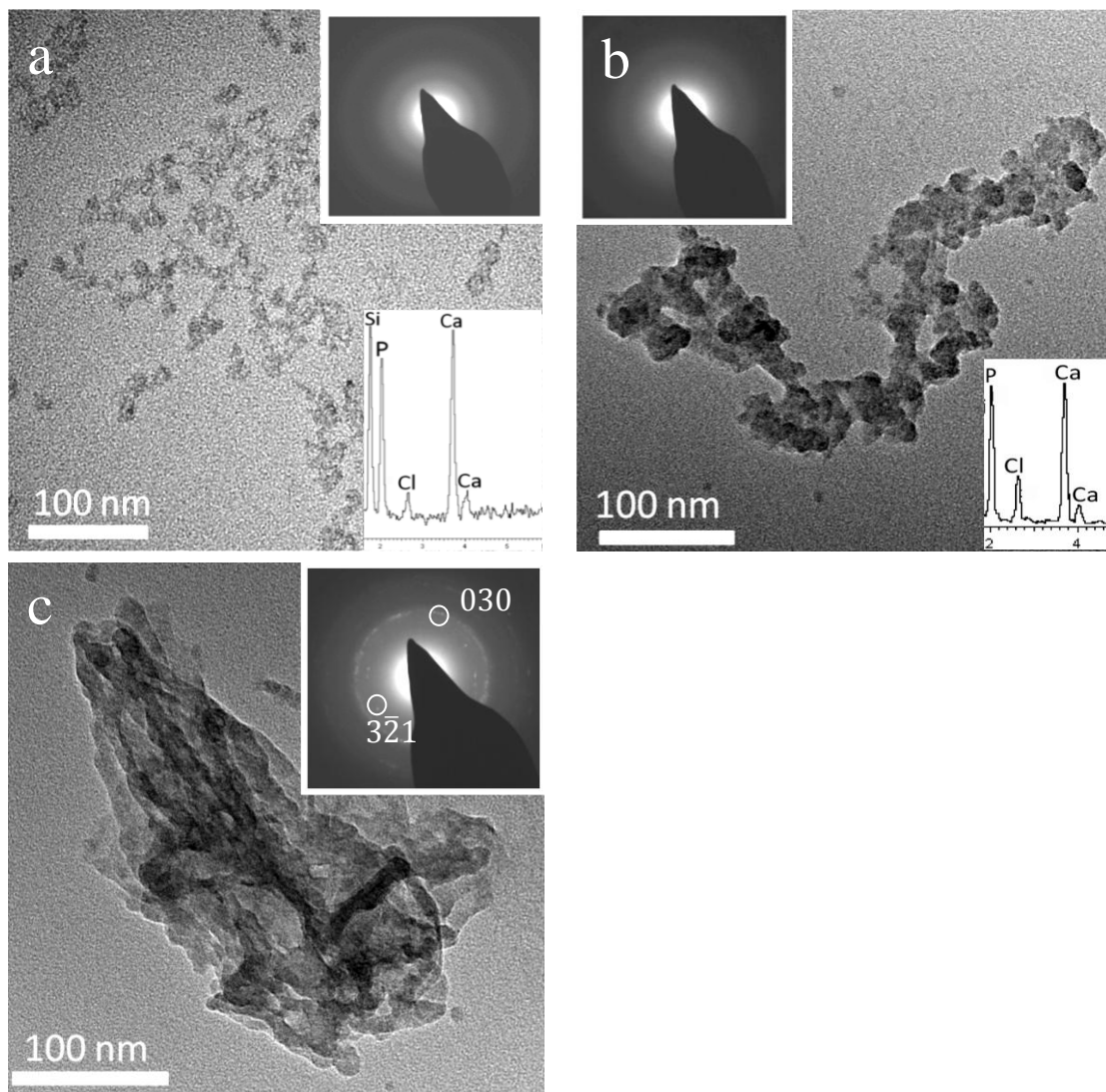
Figure 17: TEM images, electron diffraction patterns and EDX data of CaP particles precipitated from a buffered solution of calcium phosphate in the absence of PAsp. (a) After 1h the particles were amorphous and exhibit a Ca/P ratio of 1.15. The Si peak comes from the grid while the Cl peak comes from the $CaCl_2$. After 2h, both amorphous particles (b) and OCP crystals (c) were observed, where the amorphous particles exhibit a Ca/P ratio of 1.01 and the crystalline OCP particles are identified by the characteristic $(3\bar{2}1)$ and (030) reflections of OCP.

Complete transformation into hydroxyapatite (HAP) occurred after 3 h as was confirmed by Raman microscopy and XRD (Figure 18 and 19).

Figure 18 shows the Raman spectrum of the obtained material with peaks at 961 cm^{-1}, totally symmetric stretching mode (v_1) of the tetrahedral PO_4 group (P−O bond), 590 cm^{-1}, bending mode (v_4) of the PO_4 group (O−P−O bond), peaks at 443 cm^{-1} and 429 cm^{-1}, the doubly degenerate bending mode (v_2) of the PO_4 group (O−P−O bond), and a very weak peak at 1043 cm^{-1}, which is part of the triply degenerate asymmetric stretching mode (v_3) of the PO_4 group (P−O bond) comparable with literature figures[289]. These peaks and in particular the last peak at 1043 cm^{-1} confirm that this material was HAP, as was expected[96]. XRD was also used to confirm the calcium phosphate mineral (Figure 19) with the presence of the peak at 31.78° (121) and the absence of any peak at 4.71° confirming the mineral was indeed HAP and not OCP[289]. Examination of the HAP crystals under TEM showed that they were plate-shaped and approximately 150 nm wide and 200 nm in length (Figure 20a).
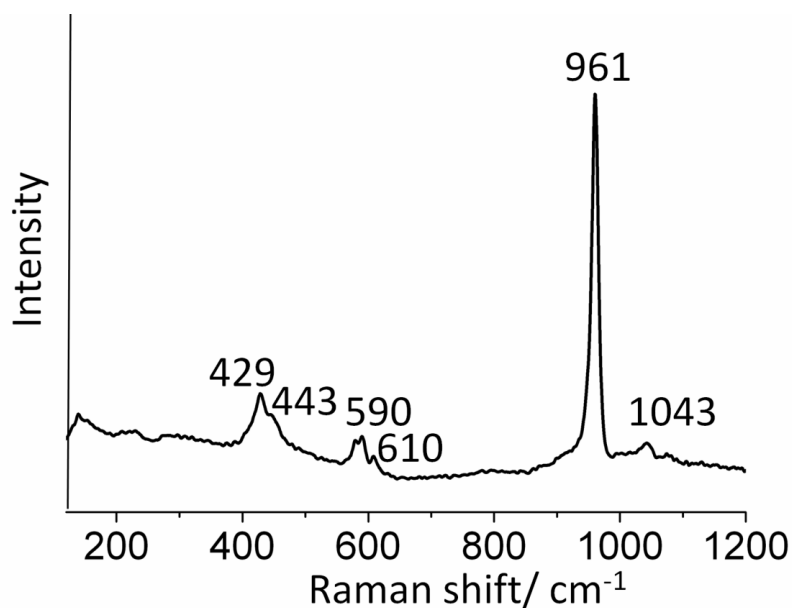
Figure 18: Raman spectrum of CaP produced in bulk solution. Analysis of the spectrum showed the produced material was HAP.
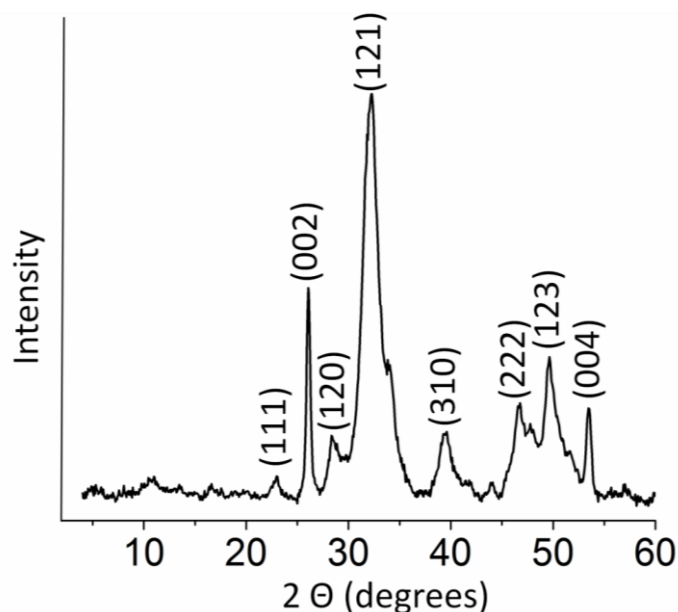
Figure 19: X-ray diffraction pattern of precipitate obtained in the bulk solution after 3 h, corresponding with HAP.
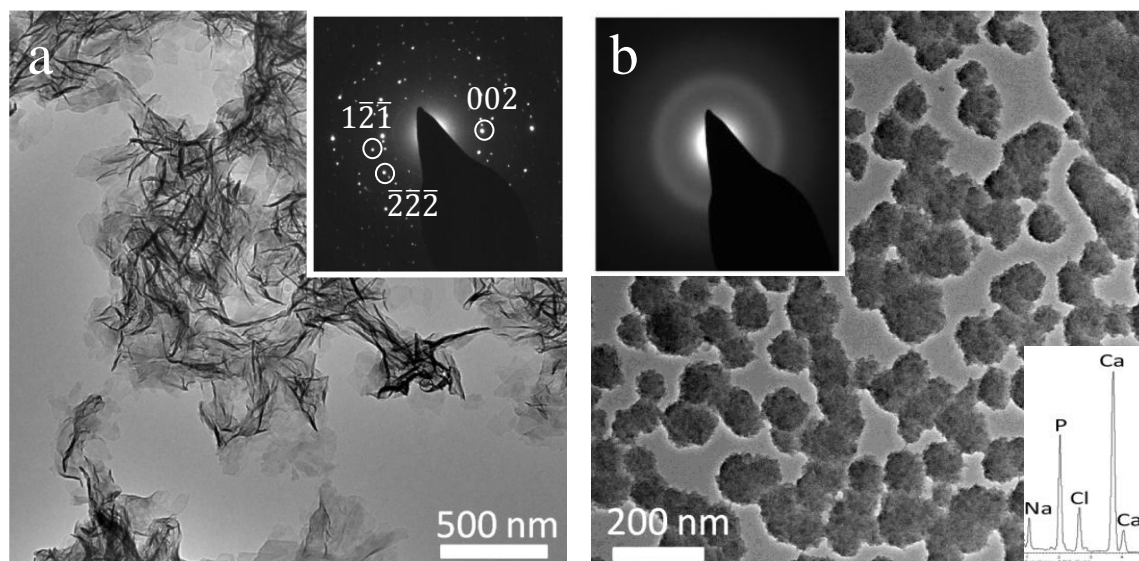
Figure 20: TEM images and corresponding electron diffraction patterns of CaP particles precipitated from buffered solutions of calcium phosphate. (a) HAP crystals precipitated in the absence of PAsp without additives after 3 h. (b) Amorphous CaP particles precipitated in the presence of 50 μg/ml PAsp after 6 days. The corresponding EDX spectrum shows that the particles contain Ca and P in a Ca/P ratio of 1.52. The Na and Cl peaks originate from $CaCl_2$ and NaCl of the buffer solution.

Adding PAsp to the system at concentrations of 10 and 100 μg/ml had a marked effect on the precipitation process where it was observed that the polymer retarded the crystallization process, stabilizing an amorphous calcium phosphate (ACP) phase. Investigation with TEM of the CaP particles isolated from solutions containing 50 μg/ml PAsp after 6 days showed that they were spherical in shape and ≈ 80 nm in diameter, and electron diffraction demonstrated that they were still fully amorphous (Figure 20b).

When left longer in solution (of between 1 week with 10 μg/ml and 3 weeks with 50 μg/ml), the amorphous CaP particles transformed into apatite as confirmed by TEM and SAED. However, they were significantly smaller than the particles precipitated in the absence of additives with average diameters of 40 nm (Figure 21).
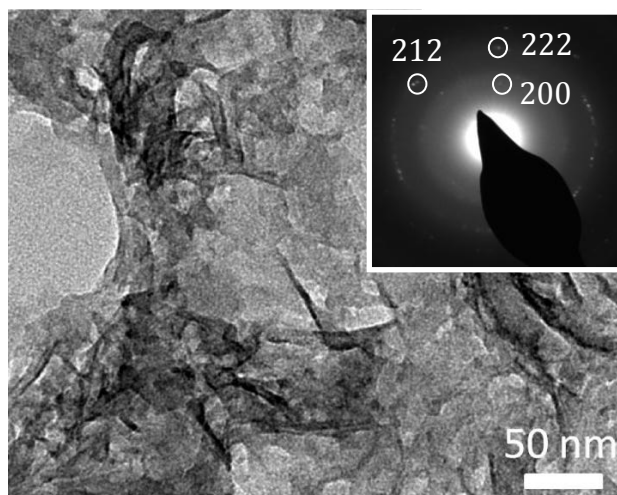
Figure 21: TEM image and corresponding electron diffraction pattern of CaP particles precipitated from a buffered solution of calcium phosphate containing 50 μg/ml PAsp after 3 weeks. The particles are ≈ 40 nm in length, and are confirmed to be HAP by the characteristic spots of the (200), (212), and (222) planes.

The CaP crystals formed without a buffer solution gave similar results (Figure 22). Analysis of the particles with TEM showed that in the absence of additives, amorphous particles of around 10-150 nm diameter (Figure 22a) directly formed after mixing, which quickly transformed after 1 h into crystalline material (Figure 22b) with average dimensions of 100 nm length and 50 nm wide. Diffraction showed the crystalline particles were HAP, and EDX confirmed the amorphous particles contained calcium phosphate.
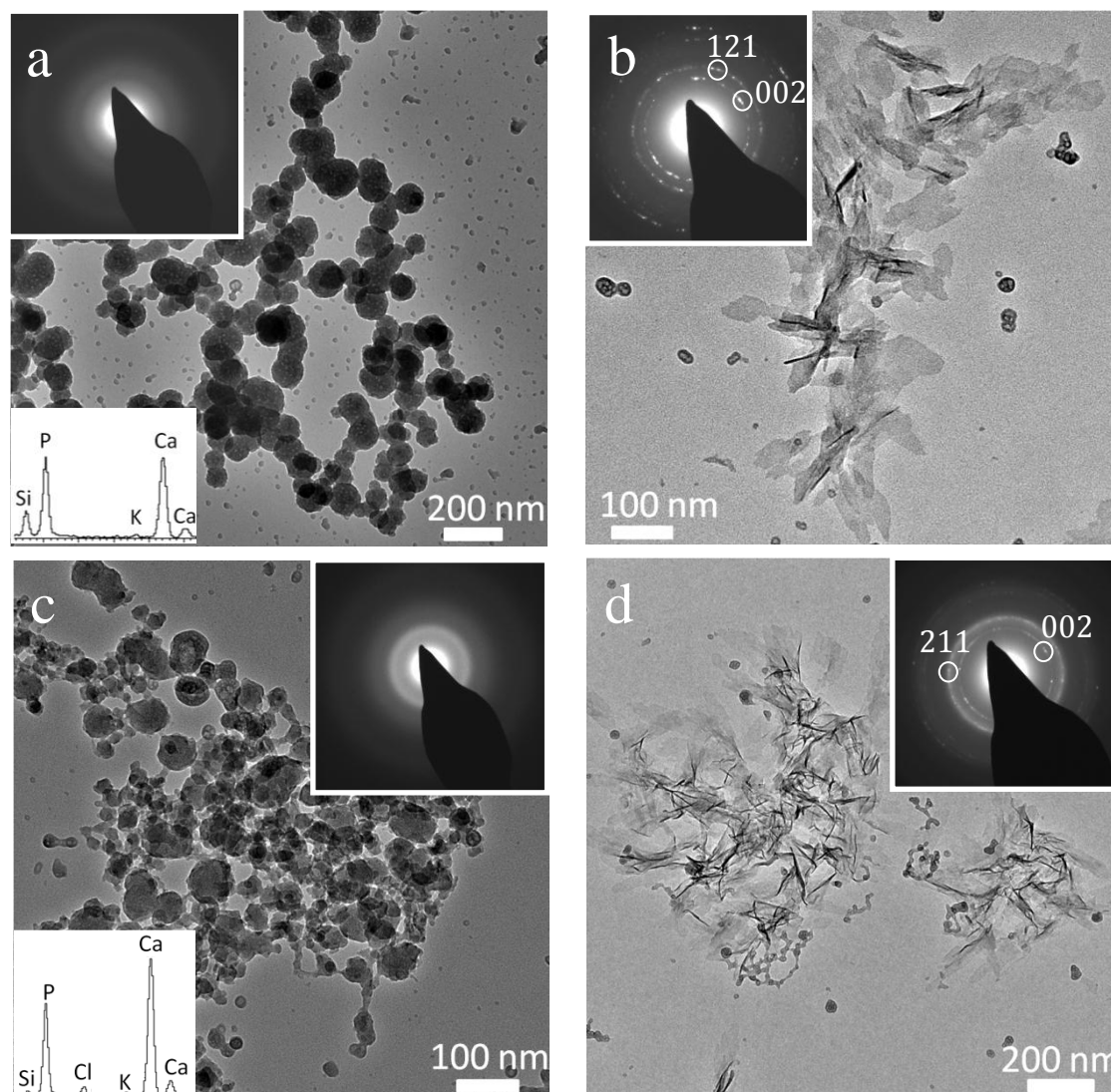
Figure 22: TEM images with corresponding electron diffraction patterns and EDX spectra of CaP particles precipitated from a non-buffered solution of calcium phosphate without the addition of PAsp (a and b) and with addition of 50 μg/ml PAsp (c and d). Without PAsp amorphous particles were formed directly, which quickly transformed into crystalline HAP (b). With PAsp the amorphous phase was stable longer than 1 h (c) and crystalline HAP was found after 12 h (d). The EDX patterns in (a) and (c) shows the amorphous particles contain Ca and P with a Ca/P ratio of 0.96 and 1.46 respectively. The Si peak must be originating from the grid and the Cl and K peaks from $CaCl_2$ and K_2HPO_4.

Addition of PAsp extended the lifetime of the ACP and after 1 h only amorphous particles were formed with variable sizes of 10 nm to 70 nm in diameter (Figure 22c). After 12 h crystalline material (100 nm long and 40 nm wide) also started to form

(Figure 22d) which was identified as HAP. After 3 days all particles were crystalline HAP.

3.5.4 Analysis of material obtained inside the membrane pores

3.5.4.1 Double diffusion method

In a first attempt, crystals were grown using the double diffusion method since this technique was considered most likely to produce crystals inside the membrane pores. Given that they were easier to work with, TE membranes were principally used for the experiments.

In the absence of additives, the double diffusion method allowed the production of a high yield of rods (90% of the pores filled) with uniform lengths of around 1 μm to 2 μm, and thicknesses of 200 – 250 nm (as produced in the "200 nm" pores) and 50 – 100 nm (as produced in the "50 nm" pores) (Figure 23). These correspond to aspect ratios of 5 and 20 respectively as shown in Figure 23. As discussed in paragraph 3.5.2, these membranes are sold for filtration applications, and thus the pore diameter quoted is the pore size at the membrane surface, rather than the internal diameter. Since the membrane thickness is ≈ 10 μm, the CaP only seem to partially infiltrate into the pore. SEM images of the membranes before dissolution show that they were almost all completely filled (Figure 23a and b) and images of the isolated rods show that the majority of rods were solid (Figures 23a, b, c, f), although some hollow rods were also identified, particularly in the 200 nm pores (50% of the total rod population) (Figure 23d and e arrowed). TEM examination of the rods further revealed their internal structure, and demonstrated that most of them were composed of small, needle-like particles of around 100 nm in length for rods precipitated in the 200 nm pores (Figure 23g) and 30 nm in length for rods precipitated in the 50 nm pores (Figure 23i).
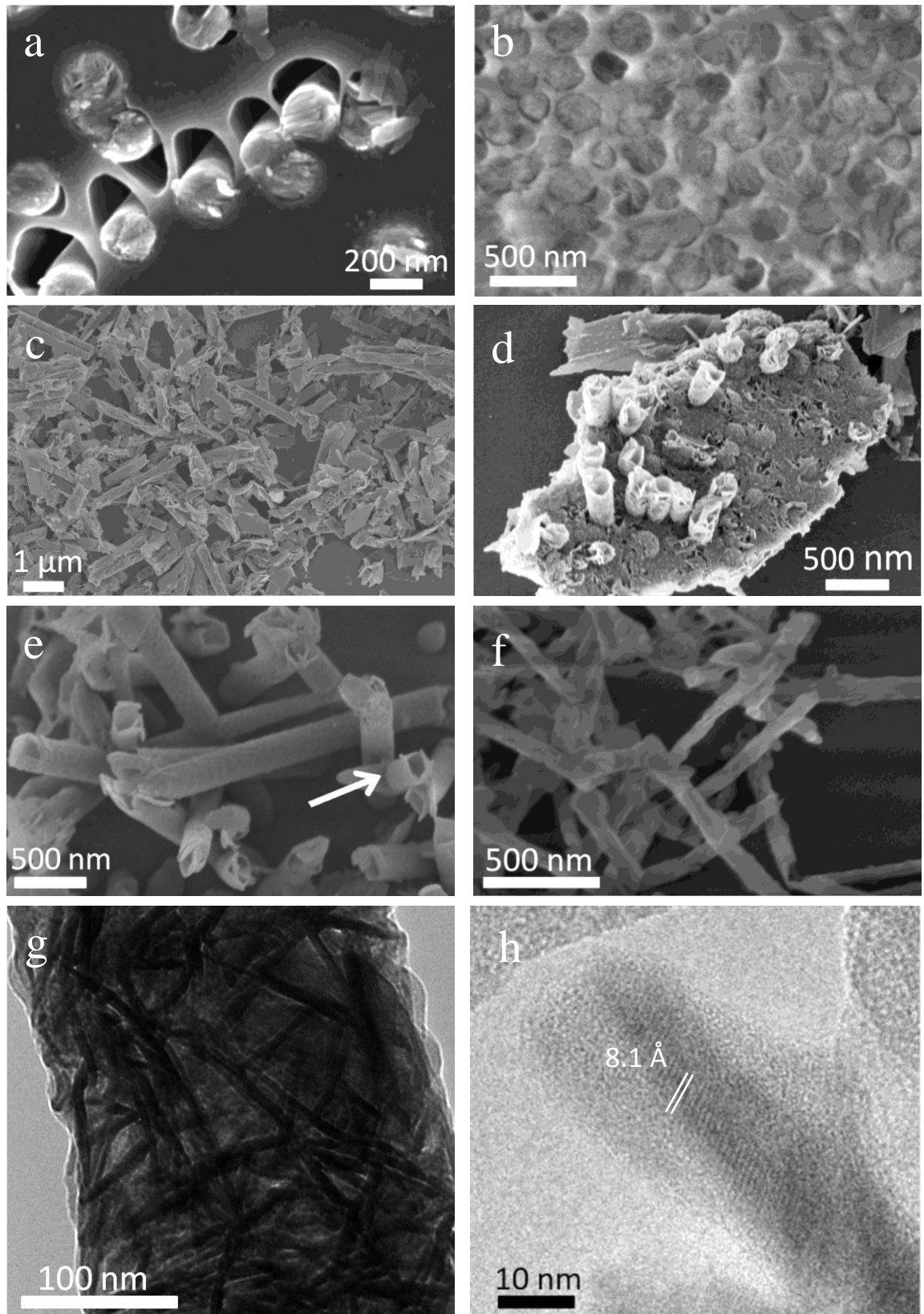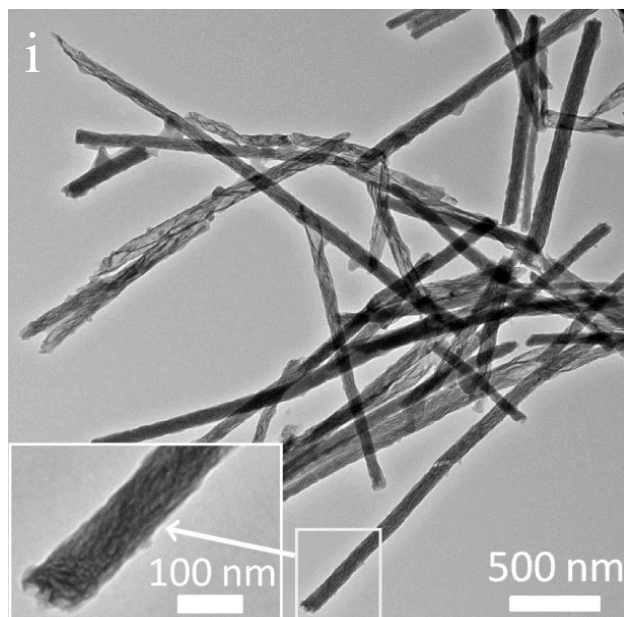
Figure 23: SEM images (a-f) and TEM images (g-i) of rods formed by the double diffusion method, in the absence of additives. (a), (b), (e) and (f-i) Were prepared in a buffered solution while (c) and (d) were in DI water. With the exception of (b), which was formed in alumina membranes with pore sizes of 200 nm, all of the membranes were TE membranes with pore sizes of 200 nm (a,c,d,e,g,h) and 50 nm (f,i). Uniform rods were formed and almost completely filled all of the membrane pores (a and b). Most of the rods where solid although hollow rods were found too, especially in the 200 nm pores ((d) and arrowed in (e)). (h) Shows a TEM image of a 200 nm rod showing the needles are crystalline and measurement of the distance between the lattice fringes confirmed the material was HAP (d = 8.1 Å, (100) plane).

Measurement of the lattice spacings (Figure 23h) and analysis of the diffraction pattern (Figure 24) of the rods showed these were built up from HAP crystals. D-spacings of 3.41 Å (002), 2.77 Å (112) and 3.1 Å (102) were found and the measured angle between (002) and (102) (22°) corresponded to the HAP mineral.
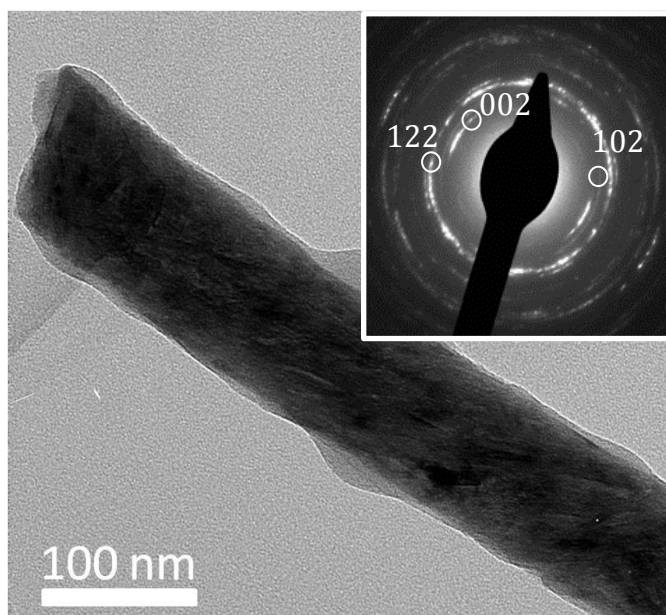
Figure 24: TEM images and corresponding diffraction pattern of crystals obtained by the double diffusion method with a buffer solution, in the absence of polymer, in TE membranes with pore sizes of 50 nm. The diffraction pattern corresponded to HAP and showed that the rods were oriented according to the [001] direction (angular spread $\pm$ 15°) along the long axis of the rod. The additional amorphous material on the surface of the rod is residual polymer from dissolution of the track-etched membrane.

Raman analysis of the rods confirmed they consisted out of hydroxyapatite (Figure 25) with characteristic peaks at 963 cm^{-1} coming from the totally symmetric stretching mode (v_1) of the tetrahedral PO$_4$ group (P−O bond), at 434 cm^{-1} which is part of the double degenerate bending mode (v_2) of the PO$_4$ group (O−P−O bond) and at 353 cm^{-1}, which is a O−P−O bending mode (v_2) of the HPO$_4^{-2}$ group.
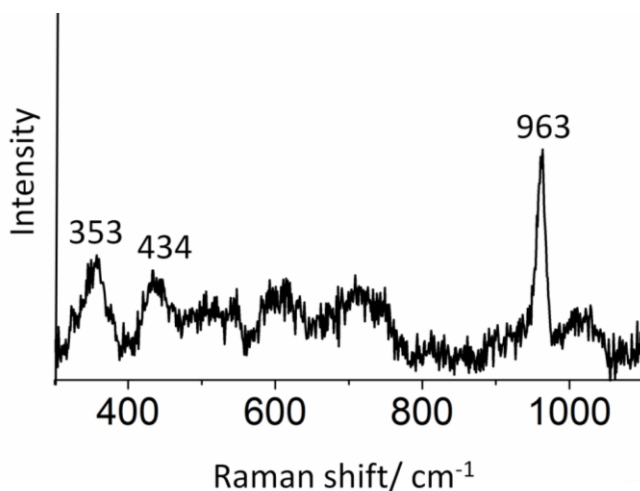
Figure 25: Raman spectrum of particles produced in 200 nm membrane by using the double diffusion method, in the absence of additives. Analysis of the spectrum showed the produced material was HAP.

Interestingly, although the surface chemistry of the membrane itself couldn't direct the orientation of the HAP crystal at nucleation, the selected area electron diffraction (SAED) patterns of the rods revealed that many of these polycrystalline HAP rods exhibited a marked degree of orientation which is shown by the presence of arcs in the SAED pattern (Figure 24 angular spread 32 degrees). This corresponds to a preferential alignment of the [001] axis of HAP with the long axis of the rod (Figure 24 and Figure 26a, b). This alignment was observed for rods formed in both the 50 nm and 200 nm pores, but was more significant for the 50 nm pores where 95% of the HAP rods were oriented as compared with 75% in the 200 nm pores (Figure 26). A diffraction pattern from a non-oriented rod of HAP is shown in Figure 26c.
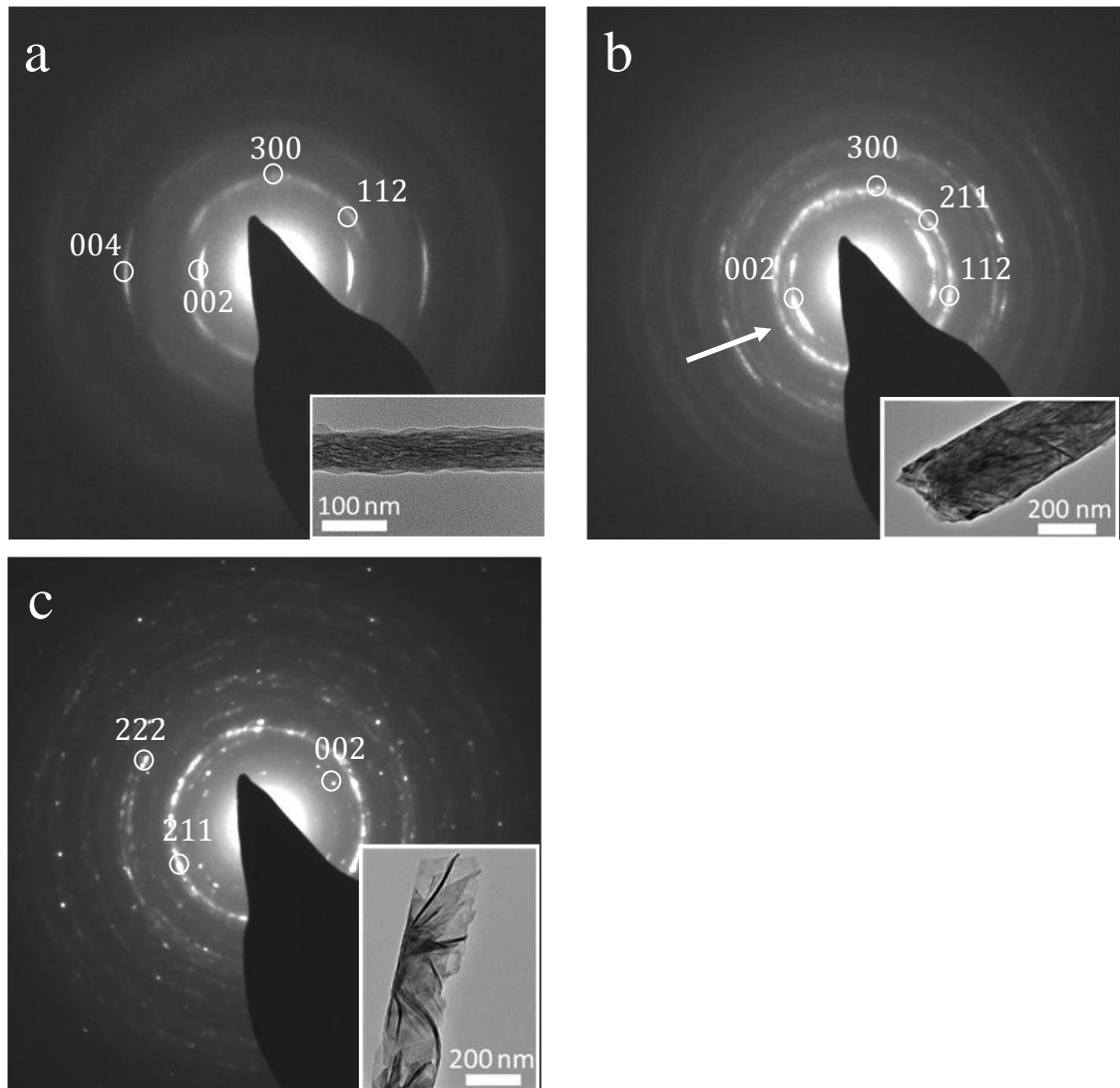
Figure 26: Selected area electron diffraction (SAED) images with corresponding TEM images (inset) of HAP particles produced using the double diffusion method, in the absence of PAsp. (a) And (b) show images from a rod precipitated in a 50 nm pore (a) and a 200 nm pore (b) where the long axis of the rod is coincident with the [001] direction (angular spread $\pm 20°$ (a) and $\pm 25°$ (b)). The arrow in (b) indicates the lack of orientation of a sub-population of HAP crystallites oriented in different directions in the 200 nm pores. (c) Shows a non-oriented rod formed in a 200 nm pore. All diffraction patterns were identified as HAP.

Analysis of multiple samples with TEM and SAED showed that the angular spread of the arcs was $\pm$ 15-25° for both the 50 nm and 200 nm oriented rods, which is comparable to that found in bone[290]. However, the oriented 200 nm rods often showed evidence of a sub-population of HAP crystallites oriented in different directions, as indicated by additional weak reflections in the SAED pattern at wider angle (behind the

(002) reflection, arrowed in Figure 26b). This further shows that this orientation effect was dependent on the size of the pores and was further confirmed by growing rods in bigger and smaller pore sizes.

In commercial alumina membranes pores of 300 nm, the diffraction pattern was completely polycrystalline and almost no preferred orientation was observed with arcs of more than 90° (Figure 27a). The TEM image of the corresponding rod confirmed this result, were random oriented crystals were seen. To allow investigation of the effect of smaller pore sizes, alumina membranes were prepared in the lab by anodisation of aluminium. In smaller pores of 30 nm, small rods with lengths of only a couple of 100 nm and diameters of 30-60 nm were formed (Figure 27b). In this case the diffraction pattern showed the rods were much more oriented with arcs of $\pm$ 10°. This supports our theory that the orientation effect was dependent on the size of the pores.
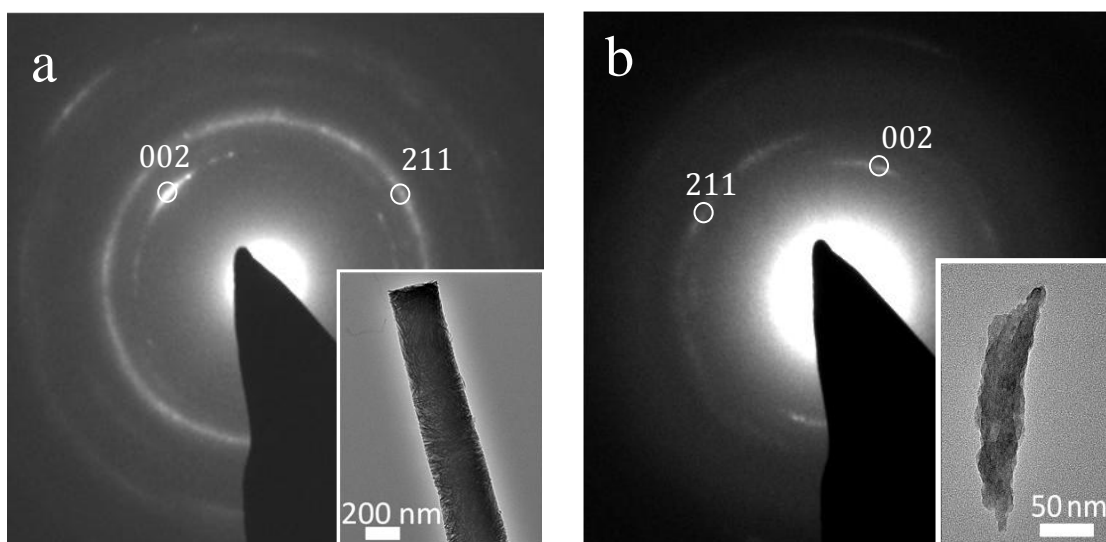
Figure 27: Selected area electron diffraction (SAED) images with corresponding TEM images (inset) of HAP particles produced using the double diffusion method. (a) Shows images from a rod precipitated in a 300 nm pore of a commercial porous alumina membrane in the presence of 50 µg/ml PAsp and (b) from a rod grown in a home-made 30 nm pore porous alumina membrane. The diffraction pattern in (a) shows the orientation is completely random. In (b) the long axis of the particle is coincident with the [001] direction (angular spread of slightly more than $\pm$ 10°) demonstrating a better orientation in smaller pore sizes.

Figure 28 shows a histogram for spread of the crystal orientation of the different pore sizes.
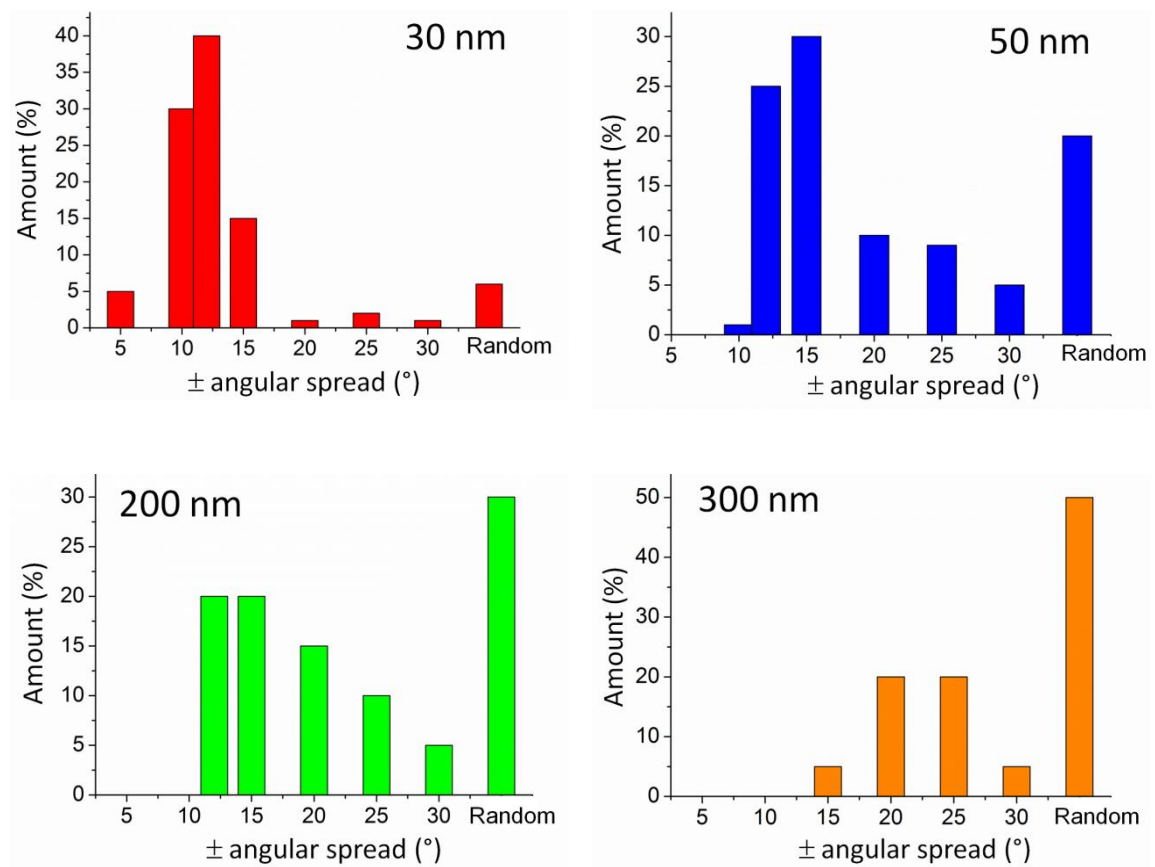
Figure 28: Histogram for the crystal orientation for the different pore sizes used

In addition to polycrystalline hydroxyapatite rods, some single crystal octacalcium phosphate (OCP) rods were also found (Figure 29a) (0.1% of the total rod population), where the low-contrast layer seen coating the rod in this Figure is likely to correspond to residual polymer resulting from dissolution of the membranes. This coating was commonly observed.
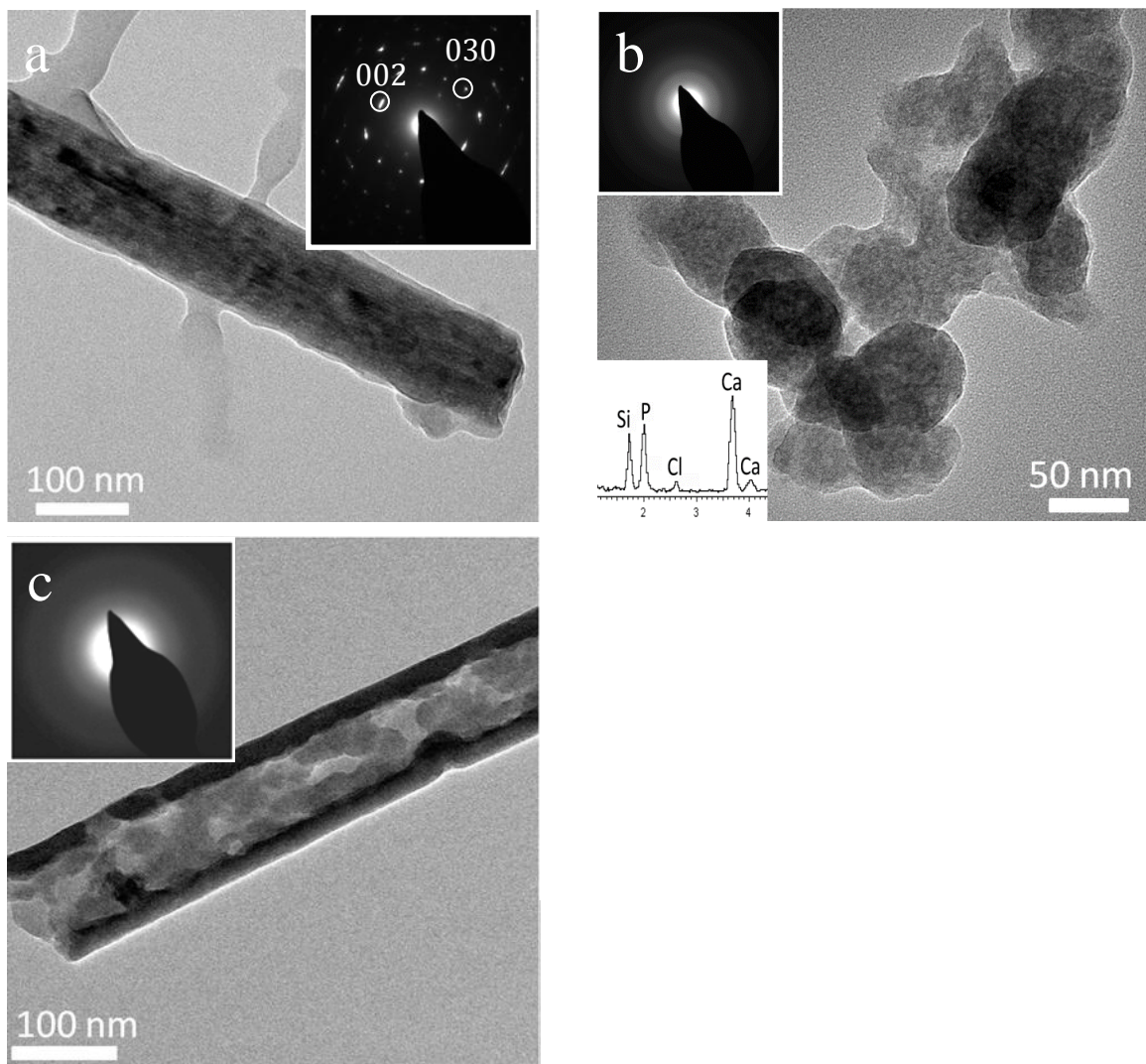
Figure 29: TEM images of particles produced using the double diffusion method, in the absence of PAsp, in 50 nm (a, c) and 200 nm (b) pores. (a) A single OCP crystal rod isolated after 6 days with its long axis corresponding to the [001] direction. (b) Amorphous particles isolated after 3 h which have an average size of 65 nm, and EDX demonstrates a Ca/P ratio of 1.38. (c) A hollow, amorphous CaP particle isolated after 6 h with corresponding electron diffraction and EDX showing a Ca/P ratio of 1.36. The Si and Cu peaks in the EDX patterns must be originating from the grid and the Cl peak from $CaCl_2$.

These OCP rods were of low abundance and were comparable in size to the polycrystalline HAP rods but showed no preferential orientation with respect to the membrane pores.

By isolating the rods at different reaction times the structural evolution of the intra-membrane particles was also investigated. After reaction times of 3 hours, only aggregates of spherical, amorphous particles approximately 65 nm in size were present (Figure 29b), while after 6 hours both crystalline rods and amorphous rods were identified in addition to amorphous particles (Figure 29c). These amorphous rods often had a hollow morphology and the quantity of the amorphous rods and particles continued to decrease with time such that all material isolated after 1 day was crystalline.

As highlighted before, PAsp has been shown to influence CaP precipitation and stabilise the amorphous phase[147, 247]. Recently, addition of PAsp is also suggested to promote CaP infiltration into small pores, through formation of a "Polymer-Induced Liquid Precursor" (PILP) phase, although this assessment has been made based on infiltration into collagen fibers only[96]. To investigate this further, the effect of PAsp on the precipitation of CaP in the membrane pores was investigated here. In the presence of 10 to 100 μg/ml PAsp, it was found amorphous particles had formed after 6 days (Figure 30). These particles were spherical and were similar in appearance and size to the particles produced in the control experiments (around 150 nm in diameter). Sometimes, rod-shaped particles which comprised poorly-packed spherical particles were also observed (Figure 30).
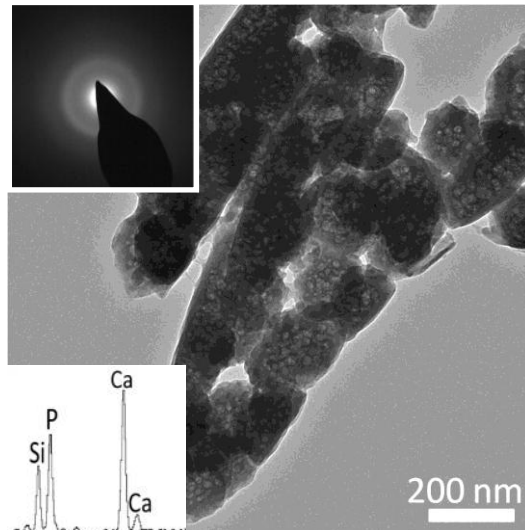
Figure 30: TEM image of amorphous, rod-shaped particles isolated after 6 days obtained by the double diffusion method with the addition of 20 μg/ml, in membranes with pore sizes of 200 nm with corresponding diffraction pattern. The rods have a Ca/P ratio of 1.44 and the voids observed within the component spherical particles are due to beam damage. The Si peak originates from the grid

Surprisingly though, although no crystalline material was formed in the bulk solution under the same concentrations of PAsp and reaction time, polycrystalline HAP rods were obtained in the membrane pores after 6 days (Figure 31a). These rods were identical in size and morphology to those obtained in the absence of PAsp. However the amount of rods formed was much lower than those formed in comparable reactions performed in the absence of PAsp (Only 30% of the pores were filled). This was attributed to the inhibitory effect of PAsp on the precipitation and crystallisation of CaP[247].
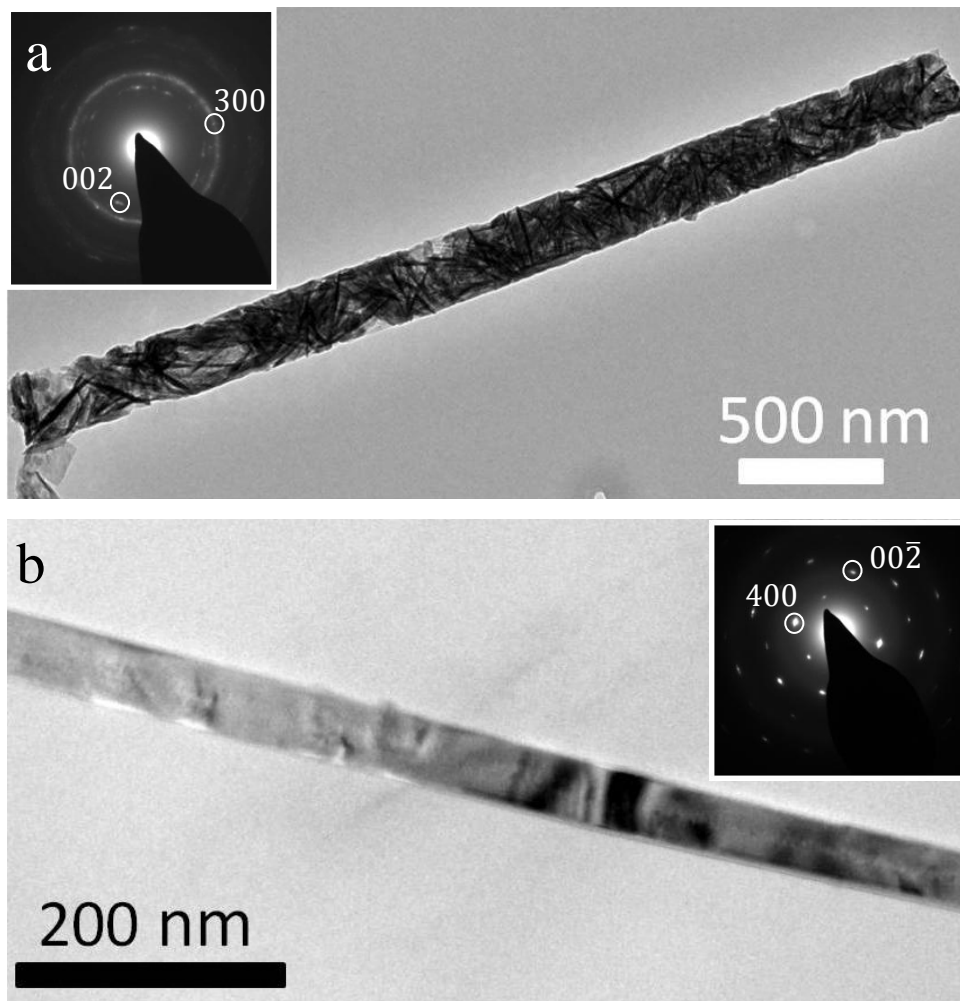
Figure 31: TEM image of crystals isolated after 6 days obtained by the double diffusion method with the addition of 20 µg/ml (a) and 100 µg/ml PAsp (b), in membranes with pore sizes of 200 nm (a) and 50 nm (b) with corresponding diffraction pattern. (a) A polycrystalline HAP rod. (b) A single crystal OCP rod, where the long axis of the rod corresponds to the [100] direction.

Most rods were again polycrystalline HAP (Figure 31a) with similar structure and orientation as observed in the absence of PAsp. In addition, single crystal rods which were identified as OCP (Figure 31b), were also found again (1% of total rod population). These were still mainly randomly oriented, but were present in a higher yield (about 10 times more) than in the absence of PAsp.

Without the buffer solution similar results were obtained where addition of PAsp resulted in the formation of some single crystal rods, together with polycrystalline rods

(Figure 32). Their size, shape and orientation were similar as prepared in the buffer solution.
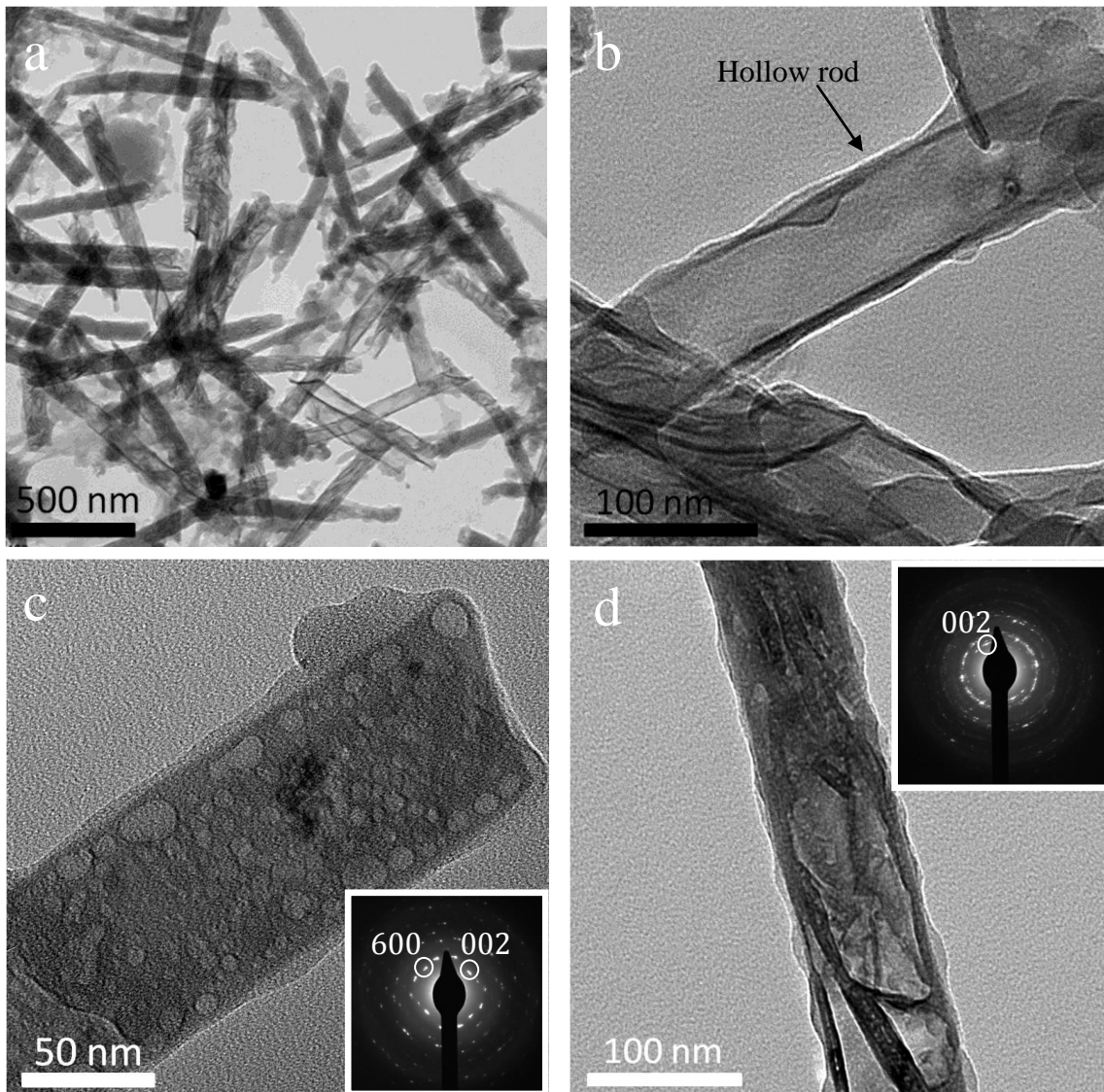
Figure 32: TEM images and SAED of crystals obtained by the double diffusion method after 1 day, with a DI water solution, and addition of 100 μl/ml PAsp, in membranes with pore sizes of 50 nm. Single OCP (c) and polycrystalline HAP (d) rods were obtained, aligned according to the [001] direction along the long axis of the rod. Beam damage can be observed in Figure (c). Some of the rods appear to be hollow as shown in (b).

TEM images showed that some rods are hollow (see Figure 32b) and analysis of the diffraction pattern showed that the single crystal material was again OCP (Figure 32c).

The OCP crystal was in this case oriented with the [001] axis along the long axis of the rod, although this wasn't always the case.

3.5.4.2 Immersion method

Although the double diffusion method proved to be a very valuable method, the setup wasn't ideal to study the improvement of the infiltration of the pores in absence and presence of PAsp, since it seemed to lead to effective particle formation even in the absence of PAsp. This was due to the configuration of the method, where precipitation occurs on combination of the calcium and phosphate ions within the membrane pores. Therefore, an "immersion method" was also explored where the membrane was simply immersed in the reaction solution. In this way, it was hoped to get a better idea of the function of the PAsp additive.

Figure 33 shows SEM images of rods produced in a buffer solution in membranes with pores of 50 nm (a) and 200 nm (b). As can be seen in the SEM images, the rods resembled those produced with the double diffusion method. However, the yield of the rods was considerably lower than with the double diffusion method by a factor of 10 (10-20% of the pores filled). Similar results were obtained with DI water.
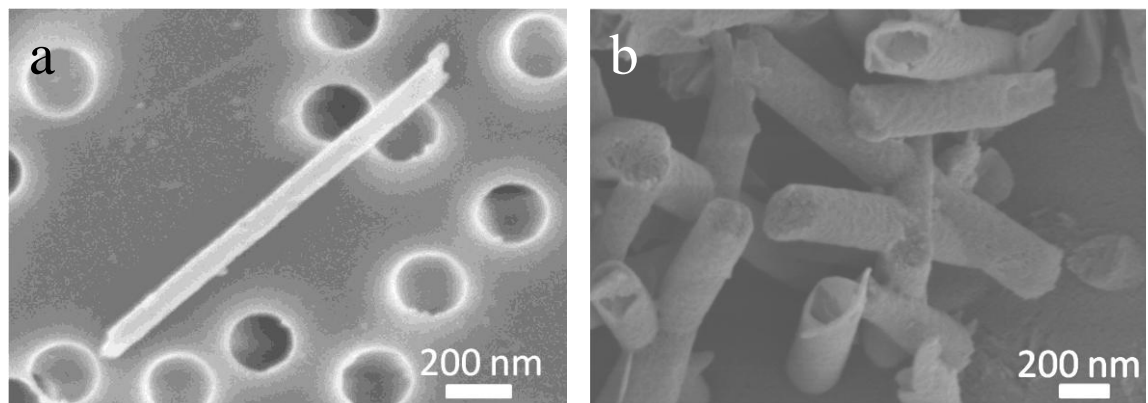
Figure 33: SEM images of rods formed by the immersion method, in a buffer solution, in membranes with pore sizes of 50 nm, with 100 µg/ml PAsp (a) and without additives in 200 nm pores (b) after 6 days. Most rods were solid, although some with a hollow-like appearance were found in the 200 nm pores (b).

TEM analysis showed that with the buffer system without the addition of PAsp, the intra-membrane CaP particles were polycrystalline HAP, oriented with the long axis

corresponding to the [001] direction (Figure 34), and thus were very similar to those produced under the same condition using the double diffusion method. In this case, the particles were uniquely polycrystalline HAP, and no OCP rods were observed. With the DI water solution and without the addition of additives, no rods were found.
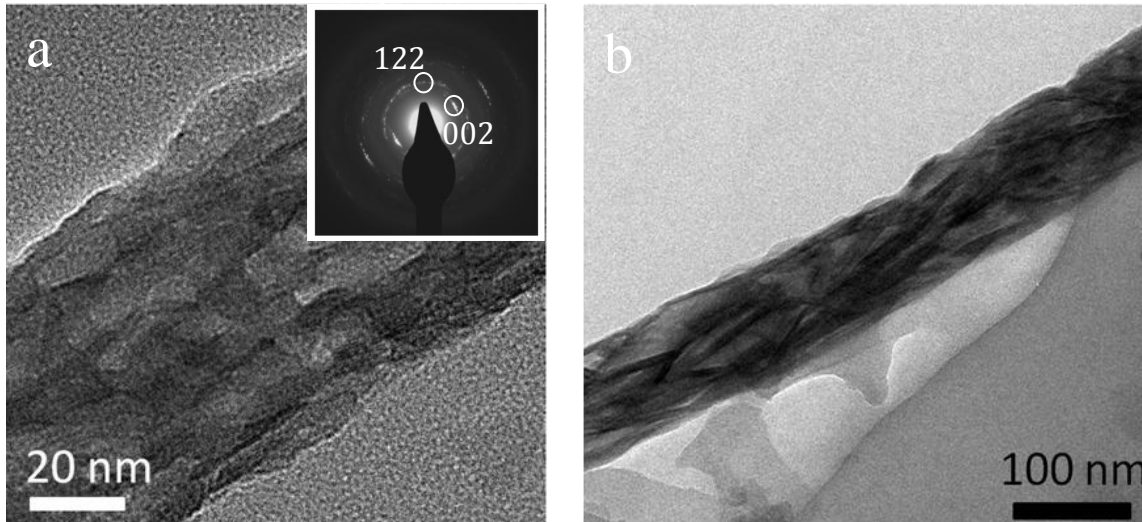
Figure 34: TEM images of crystals formed by the immersion method, with a buffer solution, without the addition of polymer, in membranes with pore sizes of 50 nm.

Addition of PAsp to the system had an identical effect on the crystallization as was obtained for the double diffusion method, resulting in a reduction in the yield of rods but in a marked increase in the proportion of these which were single crystal OCP rods (5% of the total rod population), as well as with the buffer and water solution (Figure 35). Most rods were oriented according to [001] direction although no preferred orientation was found. Again, no considerable increase in the yield of rods was observed in the presence of PAsp (10% of the pores filled).
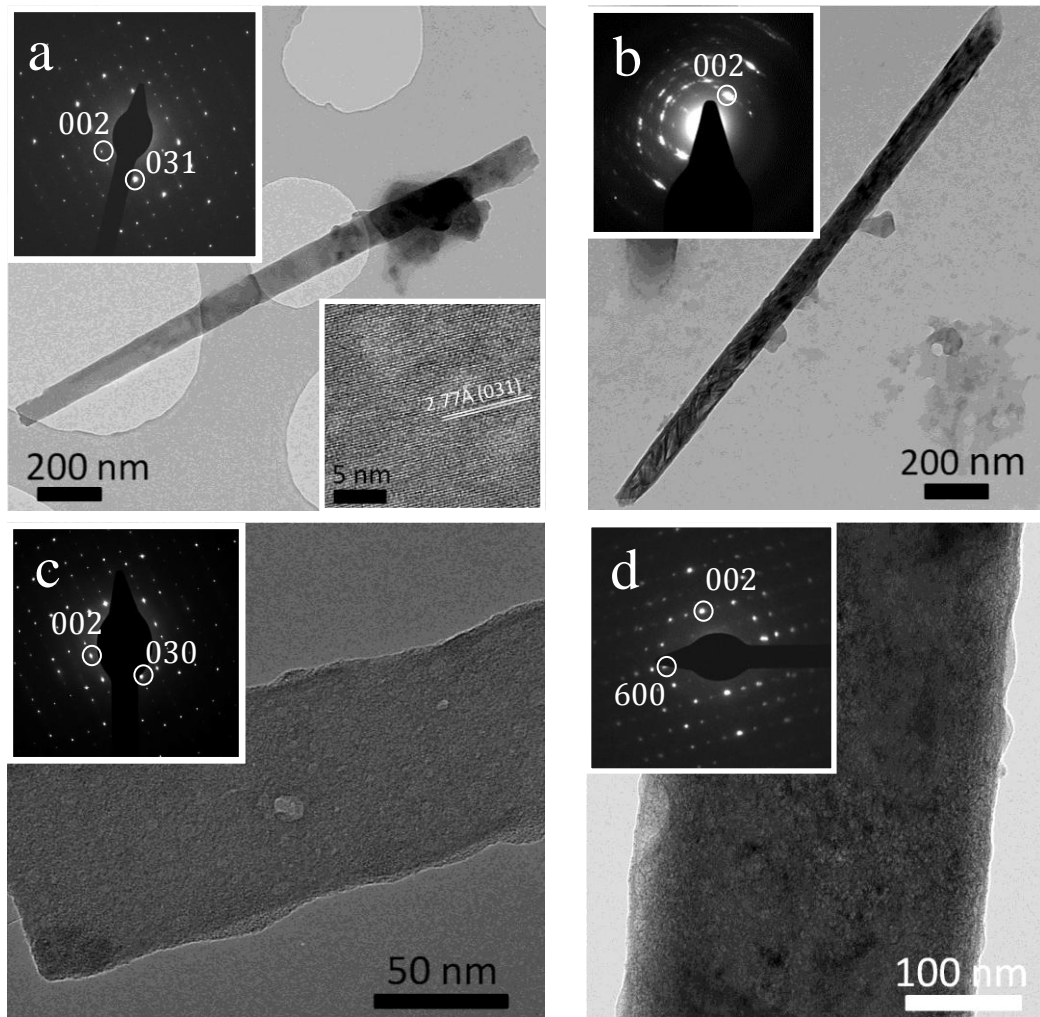
Figure 35: TEM images and electron diffraction patterns of crystals obtained by the immersion method after 6 days. (a,b) Formed in a buffer solution, with 50 µg/ml (a) and 100 µg/ml PAsp (b), in membranes with pore sizes of 50 nm. (a) A single crystal OCP rod which is oriented with its [001] direction coincident with its long axis, where the inset in (a) shows a high resolution TEM image of the same rod with the (031) lattice plane (d spacing of 2.77 Å) highlighted. (b) Polycrystalline HAP rod oriented according to the [001] direction. (c, d) Formed within DI water, with 50 µg/ml PAsp, in membranes with pore sizes of 50 nm (c) and 200 nm (d). (c) Shows a single crystal OCP rod oriented according to the [001] direction. (d) Single crystal OCP rod with his long axis oriented 20° to the [001] direction.

Finally, the influence of longer incubation times on the structures and characteristics of the intra-membrane CaP particles was also investigated (Figure 36). Instead of isolating the membrane after 1 or 6 days, a polycarbonate TE membrane was left in solution for one month, where CaP was precipitated using the immersion method. The vial was

sealed to avoid significant solution evaporation. After dissolution of the membrane, the obtained particles were analysed using TEM, which showed that all rods were now crystalline. Just as with shorter reaction times, a mixture of polycrystalline and single crystal rods were observed, where the majority of the rods were polycrystalline HAP. Analysis of the single crystal rods showed that in contrast to the OCP rods present after a reaction time of 6 days, now these were single crystals of HAP (10% of the total rod population), oriented with their [001] direction coincident with the long axis of the rod (Figure 36).
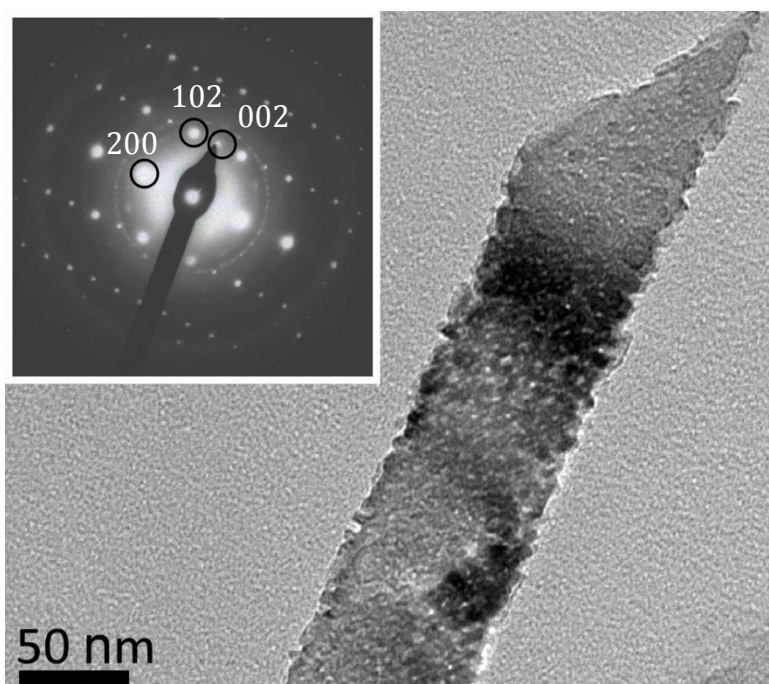
Figure 36: TEM image and electron diffraction pattern of a crystal isolated after 1 month, obtained by the immersion method in a buffer solution, with 100 μg/ml PAsp, in membranes with pore sizes of 50 nm. Analysis of the diffraction pattern showed the single crystal rods were HAP and that they were oriented with the [001] direction along the long axis of the rod.

Table 4 and Figure 37 summarises the above results. It should also be noted that smaller pore sizes, 50 nm instead of 200 nm, tend to form more single crystal material.

Table 4: Summary of results

Solution	Presence of buffer	additive	Method	Results
1	Tris-buffer	No additive	Double diffusion	High yield (90% of pores filled), polycrystalline HAP rods.
2	Tris-buffer	Polyaspartic acid	Double diffusion	Polycrystalline HAP (30% of pores filled) and single crystal OCP rods (1% of total rod population).
3	No buffer	No additive	Double diffusion	High yield (90% of pores filled), polycrystalline HAP rods.
4	No buffer	Polyaspartic acid	Double diffusion	Polycrystalline HAP and single crystal OCP rods.
5	Tris-buffer	No additive	Immersion	Low yield (20% of pores filled), polycrystalline rods.
6	Tris-buffer	Polyaspartic acid	Immersion	Low yield (10% of pores filled), polycrystalline HAP and single crystal OCP rods (5% of total rod population). Single crystal HAP rods after long time.
7	No buffer	No additive	Immersion	No rods.
8	No buffer	Polyaspartic acid	Immersion	Low yield (10% of pores filled), polycrystalline HAP and single crystal OCP rods rods (5% of total rod population).
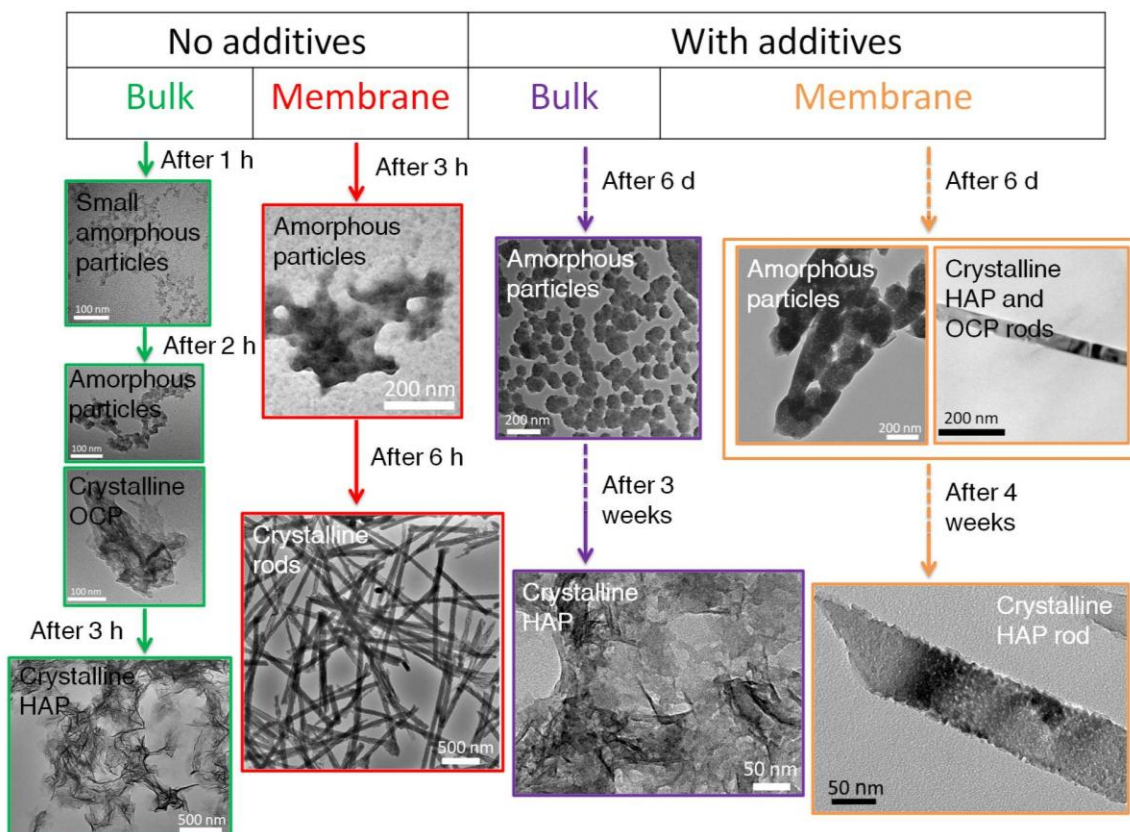
Figure 37: Overview of the results of the different reaction conditions for the buffered solutions.

3.6 Discussion

These above stated results demonstrated calcium phosphate rods were successfully precipitated in alumina and track-etched membrane pores. Using U-tubes gave the highest yield of rods, which could be expected since this system allowed precipitation to occur more easily within the pores, where the Ca^{2+} and PO_4^{3-} ions ideally meet. Most rods were about 1 to 2 µm long and it is thought this is due to the fact that at some point pore blocking occurred, disabling the supply of ions.

The results with and without buffer were quite similar and didn't seem to have much influence on the formation mechanism of the rods. In the presence of the buffer, the amorphous phase was stabilised for a longer time (In the absence of PAsp, 1 day instead of less than 1 h for respectively with and without the presence of the buffer). This is expected since it has been shown previously that the lifetime of ACP can be increased by the inclusion of simple inorganic ions[208]. Since it is hard to quantify how the pH

changed in the absence of the buffer system, and how this influenced the precipitation, the discussion will principally focus on the results obtained with the buffer system.

3.6.1 Discussion of results in absence of PAsp

Considering first CaP precipitation in the absence of PAsp, comparison of the precipitates formed in the bulk solution with those which were produced in the membrane pores, demonstrated that confinement on the length scales used here (30-300 nm) had a number of significant effects on the precipitation of CaP, influencing the size, morphology, orientation, type of mineral and the rate of crystallization. While only bundles of nanoplatelets of HAP were found in bulk solution, by growing the crystals in TE and PAM pores, morphologically distinct polycrystalline rods of HAP with aspect ratios of up to 20-40 times were generated. Imaging the precipitates with SEM and TEM revealed an internal structure comprising HAP platelets, although the ability of the rods to remain completely intact during isolation from the membrane suggests significant intergrowth. This was further supported by both the SEM and TEM images, which reveal that the rods are dense, and exhibit large, smooth areas on their surfaces. The rods were thought to be formed by filling of the pores with an amorphous phase first. In this way, the whole pore was filled or only the pore surface was covered. With time it was assumed, that crystallisation occurred at multiple nucleation sites, leading to polycrystalline rods, both hollow and filled. Very often, additional amorphous material was seen covering the rod. This covering was seen on many rods in almost all the conditions, and is likely to be caused by of the track-etched membrane not being sufficiently dissolved in DCM. However, this is very unlikely considering the rigorous cleaning procedure. Extrusion of the polymer during the transformation to a crystalline phase might also provide an explanation for this amorphous layer.

3.6.1.1 Orientation by confinement

What was very interesting though, is that although polycrystalline, the rods also showed a preferred crystallographic orientation, where the [001] axis of the HAP crystallites was preferentially aligned with respect to the long axes of the rods, and therefore the membrane pores. This was especially true for smaller pore sizes, where growing the crystals in pore sizes of 300 nm yielded polycrystalline rods (angular spread of the (002) reflection is almost 90 degrees) with almost no orientation, while pores of 30 nm

supported the formation of polycrystalline rods with a strong preferential orientation along the rod (angular spread of slightly more than ± 10°). The fact that the pore dictates the morphologies of the CaP precipitates is not surprising, and was consistent with templating studies which have been widely used to demonstrate that by the use of an appropriate reaction volume, it is possible to mould the morphology of inorganic solids[32, 162, 166]. The fact that we were able to influence the orientation was more surprising however, considering that the only factor which could define this is the shape of the pores since the functional groups on the membrane surface will be randomly oriented and thus could not define the in-plane orientation of the HAP crystals. Intuitively, it would be expected that the orientation of the crystals would be set at nucleation forcing the crystals to align in a certain way. However, since the curvature of a 200 nm pore can be considered negligible as compared with a 2-5 nm crystal nucleus, the crystal will effectively see this as an isotropic, flat surface. Therefore, it was assumed that the preferred orientation observed is likely to be the product of competitive growth of the individual crystallites (see Figure 38). As demonstrated in the previous results (Figure 20 and 22), HAP typically forms as elongated plates or needles, where the [001] axis is coincident with its direction of most rapid growth[243, 291]. Imagining the crystals growing within the membrane pores, it can be easily understood that if the HAP crystals impinge on the membrane walls, their growth will be retarded, while those whose [001] axis lies closer to the long axis of the pore will be able to grow unrestricted. This effect, which often leads to the texturing of a polycrystalline material[292, 293], will clearly be more significant the smaller the pore diameter, as was observed here.
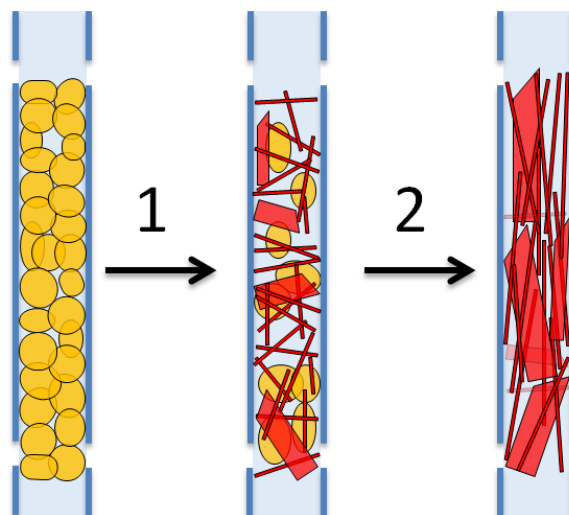
Figure 38: Schematic representation of the formation of HAP crystals inside the membrane pores. The ACP particles in the membrane pore (yellow spheres left Figure) dissolve and HAP (red) reprecipitates inside the membrane pores (Step 1). At first crystals are oriented in random directions since nucleation happens randomly. With time, the small crystals that can't grow due to membrane restrictions redissolve (step 2) while those whose [001] axis lies closer to the long axis of the pore will be able to grow unrestricted.

The fact that we can achieve such a strong orientational control over an array of HAP crystallites, by using such a simple technique as precipitating them a confined reaction volume, is intriguing and may further provide some insight into the mechanism of control over the orientation of the HAP crystallites in bone and dentin. As mentioned in section 3.1.2, the HAP crystals in bone are preferentially oriented such that there is reasonable alignment of the *c*-axes of the crystals with the long axis of the collagen fibrils[153, 198, 237, 290] giving similar results as obtained here. The typical angular spreads in the HAP orientation are $\pm$ 15° both in bone[3, 96, 290, 294] and for mineralised collagen fibrils generated through *in vitro* remineralisation of collagen fibrils[96, 196, 247] as compared with $\pm$ 15 in our system. It has to be stated though that the HAP crystallites in bone are also morphologically co-aligned, in such a way that the crystals exhibit plate-like morphologies (where the faces are (100) planes), a result which could not be directly observed for the HAP crystals precipitated in the pores of our membranes. Whether this orientation effect is also present for HAP crystals nucleated on the surface of the collagen[3] and not inside the collagen gaps is not entirely clear[295].

Considering bone and dentin, the origin of this orientation effect has been much discussed and is generally believed to be due to an epitaxial match between the HAP nanocrystals and the amino acid groups on the collagen[196, 198, 199] which was widely accepted. Previous investigation with FT-IR has revealed that the carboxyl groups on the surface of collagen molecules are able to bind Ca^{2+} ions, and therefore promote the nucleation of HAP[296]. Furthermore, modelling studies of the collagen peptide showed that a collagen-like peptide could arrange the calcium ions in a similar structure to that found in the HAP lattice[297]. The suggestion that the structural match between an organic matrix and the HAP lattice was responsible for an oriented precipitation of HAP was further supported by experiments where HAP was precipitated in the presence of nanofibers and bundles of nanofibers, including the use of structures based on supramolecular assembly[198, 298], a filamentous phage[299, 300] and spider dragline silks[301]. In all of these systems orientation was observed, where the [001] axis of HAP was typically co-aligned with the long axis of the fibers or fiber bundles[198, 298-300]. The spider dragline silk was particularly effective in directing the HAP as it composes an assembly of protein crystallites, on which the HAP crystals grow epitaxially orientated with their [001] axes at an average angle of 73° to the fiber axis[301]. In another example an epitaxial structural relationship was also suggested to drive the oriented growth of HAP on peptide-amphiphile nanofibers[198]. To gain more insight into the orientational control this latter system was further investigated by comparing HAP precipitation on aligned bundles of nanofibers which all exhibited a β-sheet secondary structure, but varied in morphology from cylindrical to flattened tape[298]. It was found that only the cylindrical structures exerted control over the HAP orientation, which suggested that a strict epitaxial match may actually not be required to achieve this alignment effect.

With our experiments we were able to demonstrate that an organised organic matrix is not required to direct the orientation of HAP crystals along their [001] axes and that this alignment can actually be achieved by the effect of confinement alone. It is therefore suggested that the alignment is actually caused by the geometry of the gaps in collagen. The collagen gaps have a certain size and shape, and it is believed that they significantly contribute in this way to the orientation of the HAP crystallites and to a lesser extent the protein sequence of the collagen. It also needs to be pointed out that this result is the consequence of the characteristics of the HAP crystals themselves, which have a strong anisotropy in their crystal lattice self, and a [001] axis as the axis of fastest growth[243,]

[291]. Given that the HAP crystals in bone form in collagen gaps of only a few nanometers thick, it is actually surprising that a better control over orientation of the crystals is not observed in the natural systems. The fact that the HAP crystals in bone also all exhibit (100) faces which are co-aligned over the collagen fibrils[302], is actually unsurprising, given that this is the most stable, and therefore also commonly displayed crystal face of HAP[291]. It is therefore concluded that no real selection of this face has to be made during the formation of the bone, and the co-alignment of the crystals in the collagen is only just defined by the geometry of the gaps in the collagen fibrils in which the crystals form.

3.6.1.2 Stabilisation of ACP and formation of single crystal OCP rods

In addition to the effect on the orientation of the crystallites, a further very interesting effect of confinement was on the rate of crystallisation and on the type of mineral observed. While only crystalline HAP was found in additive-free bulk solutions after 3 hours, only amorphous CaP was isolated from the membrane pores after the same time. Interestingly, hollow rods were frequently observed after 6 hours, suggesting that amorphous material may first coat the walls of the membrane pore, before filling in the volume. The effect of confinement in stabilising ACP is consistent with previous studies of calcium carbonate precipitation in confinement, which demonstrated that amorphous calcium carbonate (ACC) is stabilised in an annular wedge when the walls of the wedge are separated by distances of less than a micron thick[152] and also within the pores of TE membranes[29]. In this work the stabilisation of the amorphous phase was attributed to kinetic factors rather than a thermodynamic stabilisation of ACC with respect to the other polymorphs of $CaCO_3$, and due to the fact that in confinement there is a limited contact of ACC particles with the solution resulting in its stabilisation. A similar mechanism might have taken place in the membrane pores for calcium phosphate.

The obtained results also demonstrated that it was possible to form large single crystal rods of OCP and HAP in the pores of the track-etched membranes. These single crystals were entirely distinct from any crystal observed in bulk in control reactions. Similar results were found when calcium phosphate was crystallised within crosslinked gelatine nanoparticles with sizes of a few 100 nm[270]. The results showed that a similar pathway occurred where HAP was formed through an amorphous phase which

eventually transformed into single crystal HAP via an OCP intermediate. Many previous studies have also described the formation of single crystal OCP rods, although the vast majority were formed under hydrothermal conditions and in the presence of organic additives[303, 304]. It has been shown large single crystal rods of HAP can be formed from similar conditions[305-309], and in some cases form via similarly-sized OCP rods as an intermediary phase[303, 304, 310, 311]. The transformation of OCP to HAP has been studied previously by titration and high resolution TEM, which implied the transformation occurred by two different mechanisms. In one mechanism OCP dissolves whereafter HAP precipitates, while in a second, a direct solid-state transformation can occur, where hydrolysis of an OCP unit cell leads to a two unit cell thick layer of HAP[138, 312]. In the latter case, the formed HAP crystallites would be pseudomorphs of the parent OCP crystals, where the [001] axis of the parent OCP crystal will correspond with the [001] axis of the HAP product[313, 314]. This kind of transformation was also stated to be responsible for the so-called dark line inclusion due to the inherent lattice mismatch between OCP and HAP during the transformation of OCP to HAP[214, 216, 217].

3.6.2 Discussion of the results in presence of PAsp

3.6.2.1 Effect of PAsp on infiltration and discussion of PILP phase

By addition of PAsp it was hoped to get a better infiltration of CaP into the membrane pores and to increase the orientation and single crystallinity of the rods. This was not observed. Instead, addition of PAsp actually produced fewer rods, a result which can be attributed to the inhibitory effect of PAsp on CaP precipitation[258]. Particle sizes remained unchanged at lengths of about 1 to 2 μm with no change in the orientation effect observed, and although the single crystal OCP rods were a higher part of the overall rod population than in the absence of PAsp (about 10 times more), they were still at low number. These results came as a surprise considering the results obtained on precipitating $CaCO_3$ in the pores of track-etched membranes which showed that the presence of a PILP phase, as generated in the presence of PAsp or poly(acrylic acid) (PAA), significantly enhances the ability of the mineral to infiltrate into the membrane pores[29]. Due to this effect particles precipitated in a much higher fraction of the membrane pores and a significant increase in efficiency of filling of small membrane pores was also observed. These effects were attributed to the liquid-like properties of

the so-called PILP phase of $CaCO_3$, where the mineral phase had the ability to be drawn into the pore via capillary action and fill the entire membrane pore[29].

Emanating from the observation that in the CaP system the PAsp was unable to enhance filling of the membrane pores as compared to the additive-free system, it was considered that CaP seemed to behave quite differently in the presence of PAsp than from the $CaCO_3$/ PAsp system and might not form a liquid-like PILP phase at all. Previous research showed that the formation of a PILP phase can be attributed to a microphase separation[28, 85, 95], driven in this case by the association of the PAsp polyelectrolyte and Ca^{2+} ions[12, 28]. In the calcium carbonate system, it was believed that subsequent addition of carbonate ions resulted in the generation of Ca^{2+}/ CO_3^{2-}/ PAsp species which with time would gradually convert to amorphous $CaCO_3$, before ultimately crystallising[85] forming crystals with extraordinary morphologies such as films and fibers[12, 76]. It can easily be presumed that the ability of the system to behave in this way must rely upon a subtle balance between the strength of the Ca^{2+}/ PAsp interaction on the one hand, and the driving force for precipitation of the mineral product on the other hand. Therefore if the cation/ polyelectrolyte interaction is very strong, immediate precipitation of these complexes will occur. When on the contrary a strong cation/ anion interaction is present, the formation of this Ca^{2+}/ anion/ PAsp species which characterises the PILP phase will be limited, and $CaCO_3$ will nucleate from solution without any strong effect of the polyelectrolyte.

Since it was never properly proven before that CaP/PAsp is able to form extensive thin films or other unusual morphologies such as fibers, which in addition to effective infiltration, can be taken as a key signature of a PILP phase[12, 28], we therefore must question whether a PILP phase actually really forms in the CaP system. The principal evidence for CaP PILP comes from the effective infiltration of CaP into the nanometer sized gaps in collagen fibers. This infiltration could only be achieved in the presence of PAsp, where it had been suggested that due to the formation of liquid-like droplets of CaP/PAsp, the CaP was able to be drawn into the collagen fibers by capillarity action[96] as discussed before in section 3.1.4. Further research on collagen infiltration with cryogenic electron tomography and molecular modelling has shown that filling of the pores in the collagen fibers is simply driven by the molecular interactions between the net negative surface charge of the stabilised PAsp/ACP complex and the positively

charged regions in the collagen fibril[196], which counteracted the requirement for infiltration simply based on capillary action. From this idea we therefore suggest that the PAsp is effective in stabilising ACP particles, by the adsorbing of the polymer to the particle surfaces, as has been mentioned before in other papers[247], but that these do not induce the formation of "liquid-like" character which leads to film formation or effective infiltration into nanosized pores, and which is typical for a PILP phase. The fact that this PILP phase doesn't exist for CaP may be due to the lower solubility of CaP, and therefore thus higher driving force for the precipitation of CaP as compared with $CaCO_3$ (with values for the solubility products of ACP and amorphous calcium carbonate (ACC) being 10^{-25} and 10^{-6} respectively)[202, 203, 315].

3.6.2.2 Effect of PAsp on the formation of different mineral types of CaP

Despite this, the addition of PAsp to the solution had some effects on the intra-membrane precipitation process and a number of differences in the mineral type of the crystal products were noted. In addition to polycrystalline HAP rods identical to those formed in the additive-free system and which were most abundantly present, single crystal OCP and amorphous rods were also isolated in the membrane pores after 6 days reaction time, where the OCP rods were about 10 times more abundant than in the absence of PAsp. This effect is entirely consistent with the ability of PAsp to retard the transformation of OCP to HAP by absorption on the (100) face of the OCP crystals[254]. Keeping the membranes in solution allowed all amorphous material to crystallise, and resulted in the conversion of the OCP rods to single crystal rods of HAP which maintained the morphology and orientation (where topotactic transformation of OCP to HAP leads to [100] OCP with respect to [100] HAP)[313, 314] of the OCP single crystals. Considering the formation process of the rods it is thought that at the early stages of the reaction most material inside the pores is amorphous. With time, these rods crystallised to single crystal OCP rods or polycrystalline HAP rods. The low amount of single crystal OCP rods are believed to be formed by local dissolution/reprecipitation and partial solid state transformation from ACP rods to OCP as was discussed before for single crystal rods of calcite formed in TE membranes[29]. The polycrystalline rods must have formed by a dissolution-reprecipitation mechanism.

However, the greatest effect of PAsp was surprisingly seen together with confinement, where in comparison with the control experiments, no crystalline material was present

after 6 days suggesting that the crystallization of the CaP crystals proceeded more rapidly within the membrane pores than in bulk solution. This peculiar result was surprising and intriguing and one possible explanation might originate from the ability to obtain different barriers to nucleation of crystalline materials within the amorphous phase. Previous research on the influence of environmental factors such as pH, additive molecules and ions, ionic strength and temperature on ACP crystallization has shown that although these factors can induce significant differences in the time taken for initial nucleation of the crystalline phase to occur, crystallization of the amorphous phase subsequently proceeds at a similar rate for all samples[231]. It has also been shown that poly(L-glutamate) and poly(L-aspartate) can act as strong inhibitors for HAP when present in solution, but promote HAP and OCP nucleation when adsorbed onto inorganic surfaces like germanium[258]. It is therefore possible that in our case, PAsp might act to promote crystallization when it is located on a solid surface provided by the membrane pores, while acting as an inhibitor when present in bulk solution. This mechanism also has been discussed for non-collagenous proteins adsorbed into collagen[197].

3.7 Conclusion

The results showed that by the use of nanosized pores of track-etched membrane and porous alumina membranes, we were successful in fabricating rods in pores with pore sizes of 30 nm to 200 nm. The rods were in general 1 to 2 μm long giving aspect ratios of around 5 and 20 for pores of 200 nm and 50 nm respectively. The use of a double diffusion method gave the highest yield of rods. Growing the crystals inside the membrane pores had a large effect on the crystallisation rate and morphology of the formed crystals. Polycrystalline HAP, together with some single crystal OCP rods were generated, particularly in the smaller pore sizes of 50 nm, with similar sizes and aspect ratio's of 5 to 20. The polycrystalline rods were also oriented with their *c*-axes along the length of the rod, similar to the structure of mineralised collagen in bone and dentin. Although our experimental system employed was rather simple so it cannot be considered as a direct mimic of HAP precipitation in collagen, we do believe the above discussed results provide insight into the control mechanisms which may operate *in vivo*. In contrast to previous assumptions where the orientation of the HAP crystallites in bone was attributed to a structural match between hydroxyapatite and the collagen

matrix, we believe our experiments demonstrated this orientation was the mere effect of confinement. In this way we pointed out that the role of physical confinement originating from the collagen fibril structure should not be neglected when trying to understand the mechanism of formation of the mineralized collagen fibrils of bone and dentin.

Furthermore this research investigated the effect of additives. It was found that addition of PAsp had no effect on the infiltration of CaP into the pores, but did inhibit the formation of material and increased the ratio by 10 of single crystal rods to polycrystalline rods. In addition it was also observed that crystallization proceeds more rapidly within the pores of the membrane than in the bulk solution in the presence of PAsp. It is thought this observation is due to the ability of PAsp to promote nucleation when it is located on a substrate, while behaving as an inhibitor in solution. The absence of a strong effect of PAsp raised questions about the existence of the CaP PILP phase, held responsible for the infiltration of the collagen fibrils by capillary action during bone formation. This challenges the idea that a PILP phase forms in the CaP/ PAsp system, and it is therefore suggested it is actually a specific interaction between the collagen matrix and ACP/PAsp precursor particles[196] or PAsp molecules[247] which is responsible for an effective mineralisation.
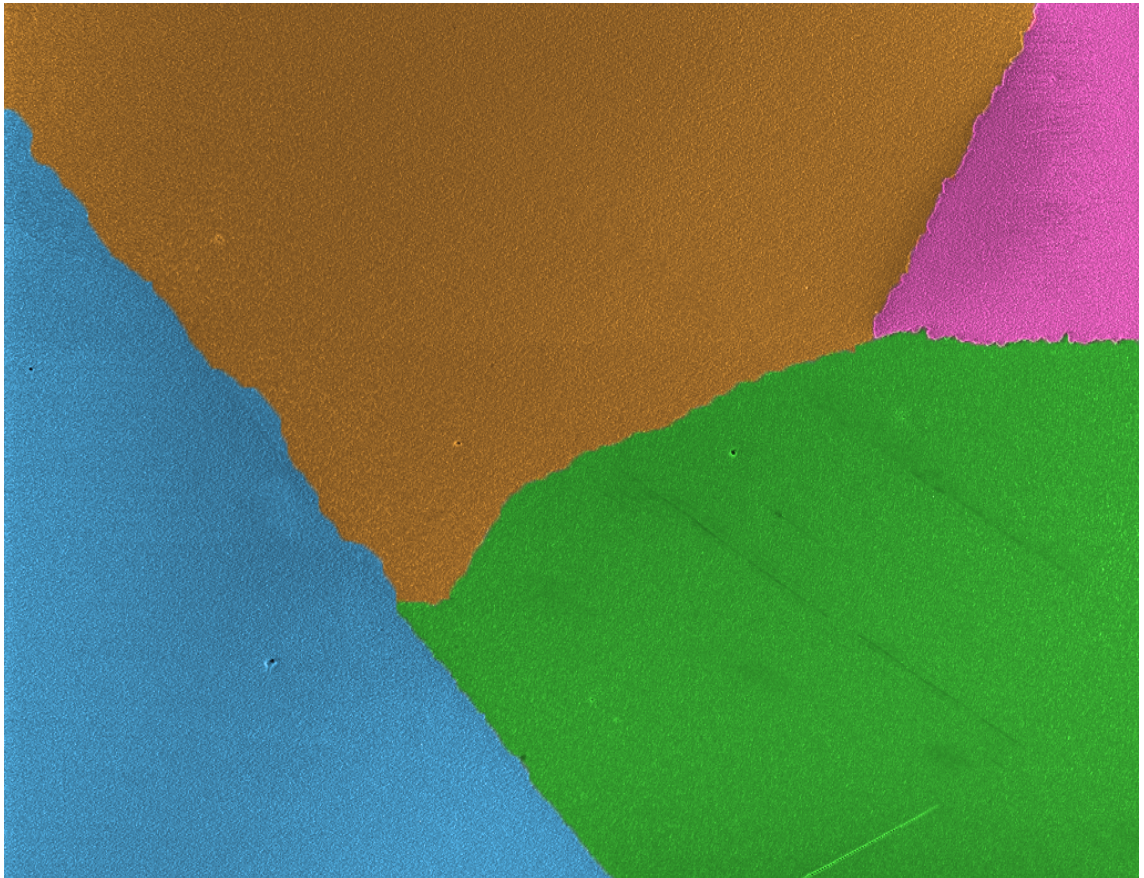
Chapter 4: Concerning Positively Charged Additives and their Effect on Crystallization

This chapter deals with the effect of positively charged polymer additives on the crystallization of calcium carbonate. Inspired by previous findings that the biomacromolecules occluded within calcium carbonate biominerals are highly acidic, most research on the effect of additives was based on the use of negatively charged additives. In this chapter though, we demonstrate that the addition of the positively charged additive poly(allylamine hydrochloride) (PAH) can also have a dramatic effect on the crystallization of $CaCO_3$, forming unusual structures such as films and fibers. Raman and optical microscopy analysis combined with TEM showed that these fibers were single crystals of calcite, micrometers long, while the films generally comprised mainly single crystal and polycrystalline calcite domains, in addition to small amounts of polycrystalline vaterite. To understand the mechanism by which PAH induces these effects, a range of techniques was used, which demonstrated that hydrated $Ca^{2+}/PAH/CO_3^{2-}$ droplets initially form in the solution, which subsequently coalesce and then crystallise, to give calcite patches and fibers, together with small quantities of vaterite. It was therefore suggested that the initial formation of hydrated $Ca^{2+}/PAH/CO_3^{2-}$ droplets is key to this process, rather than a specific interaction between the polymer and the growing crystal. The formation mechanism of the fibers, in contrast, appears to rely on an oriented attachment mechanism of the charged anisotropic $Ca^{2+}/PAH/CO_3^{2-}$ particles formed at low Ca^{2+}/PAH ratio. These findings therefore demonstrate that positively charged polyelectrolytes can have a dramatic effect on the crystallization of calcium carbonate crystals.

4.1 General overview of calcium carbonates.

$CaCO_3$ makes up 4% of the earth's crust and is one of the most abundant biomineral being present in sea shells, sea urchins, coral and coccoliths. It therefore plays a significant role in the chemistry of ocean water and in the understanding of the geological CO_2 cycle[316]. In addition to the fact that $CaCO_3$ is present in large quantities in Nature, it is also very important industrially and has a huge relevance to daily life including scale formation, carbon sequestration and many applications in plastics, paints, paper and coatings industry[4, 25, 68, 317].

During its fabrication, control over the crystal habit of the $CaCO_3$ crystals is very important since certain crystal habits are highly undesirable in industrial processes[39] as

they can affect in many ways the appearance and characteristics of the powder, the flow characteristics, and the handling or packaging of the material. Depending on the application where $CaCO_3$ is needed, cubes, prisms, flakes, granules or needles may be the targeted morphology and it is therefore of general interest to find ways to control the morphology and shape of $CaCO_3$ crystals. In addition, calcium carbonate is often used as a model system to investigate the fundamentals of crystal growth since it is non-toxic, abundant and essentially uncomplicated to grow under ambient conditions[14, 30]. In this way, the approaches which are developed with $CaCO_3$, can then often also be applied directly to other materials in many different ways.

Considering $CaCO_3$, there are three anhydrous polymorphs (calcite, vaterite and aragonite), and two hydrated forms (calcium carbonate hexahydrate ($CaCO_3.6H_2O$) and calcium carbonate monohydrate ($CaCO_3.H_2O$)). Calcite and aragonite have similar thermodynamic stabilities under standard conditions and are both common in biological and geological samples[318]. Vaterite is thermodynamically unstable with respect to calcite and aragonite and is consequently extremely rare in Nature, being discovered as a minor component of only a few biominerals (for example in the inner ear of salmon[319]. Calcium carbonate hexahydrate ($CaCO_3.6H_2O$) and calcium carbonate monohydrate ($CaCO_3.H_2O$)) are extremely rare in Nature and only a few examples can be found[320, 321]. Recently, amorphous calcium carbonate (ACC), another form lacking long range order, has gained increasing interest, as it has been shown to act as a precursor for the formation of some crystalline phases during biomineralisation[4, 22, 25, 98].

4.1.1 Calcite

Calcite is the most thermodynamically stable and abundant polymorph of calcium carbonate under ambient conditions, and is the main constituent of shells and most limestones in sedimentary rocks[4, 14]. It has a rhombohedral lattice structure, and its unit cell can be considered in terms of the face-centred cubic unit cell of NaCl, where the Ca and CO_3 groups replace the Na and Cl groups respectively. Due to the larger size of the CO_3 groups, the unit cell is somewhat distorted along a triad axis, resulting in a face-centred rhombohedral cell. For convenience, it is also possible to use a hexagonal unit cell with the same height as the rhombohedral cell, containing six $CaCO_3$ units, as shown in Figure 1[4, 318]. This model clearly shows the organisation of the calcite

structure with the alternating position of the Ca^{2+} and CO_3^{2-} ions perpendicular to the c-axis, where they are spaced at intervals of $c/12$. The CO_3 groups are oriented identically within a layer, in such a way that the orientation reverses between adjacent layers. Each Ca^{2+} ion is surrounded by six immediate CO_3^{2-} neighbours, oriented in such a way that one oxygen from each CO_3^{2-} neighbours calcium. In this way each calcium occupies an octahedral environment of O atoms[4, 98, 322].
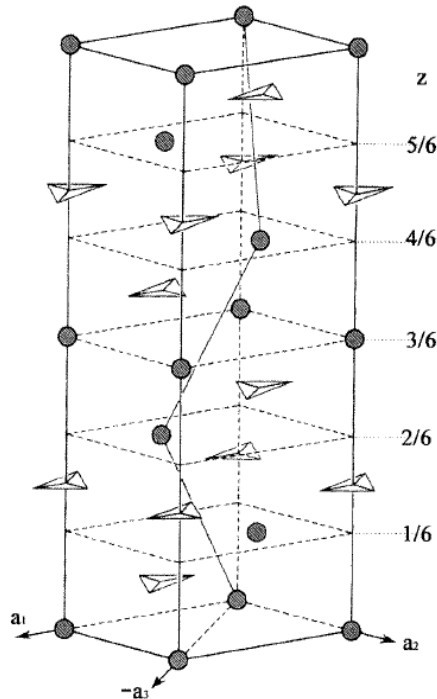
Figure 1: Schematic representation of the hexagonal unit cell of calcite   Image reproduced from ref. 318.

4.1.2 Aragonite

Aragonite is the second most abundant calcium carbonate biomineral with the difference in standard free energy between calcite and aragonite being 1.14 ± 0.01 kJ/mol[36]. The crystal structure of aragonite (Figure 2a) can be described by an orthorhombic unit cell, where the ions are arranged in a pseudohexagonal arrangement[4]. In common with the calcite structure, the Ca^{2+} and CO_3^{2-} are arranged in alternate layers perpendicular to the c-axis, with the plane of the CO_3 groups lying perpendicular to the c-axis. In aragonite, however, the CO_3 layers are split into two layers parallel to the a-axis. Each Ca^{2+} ion is again surrounded by six immediate CO_3^{2-} neighbours, but this time the first three CO_3^{2-} neighbours are bonded by two oxygen ions while the other

116

three are bonded by one oxygen each, leading to nine immediate oxygen neighbours. Although all the Ca-O bonds are longer in aragonite than in calcite, aragonite has a higher density due to its more effective packing.
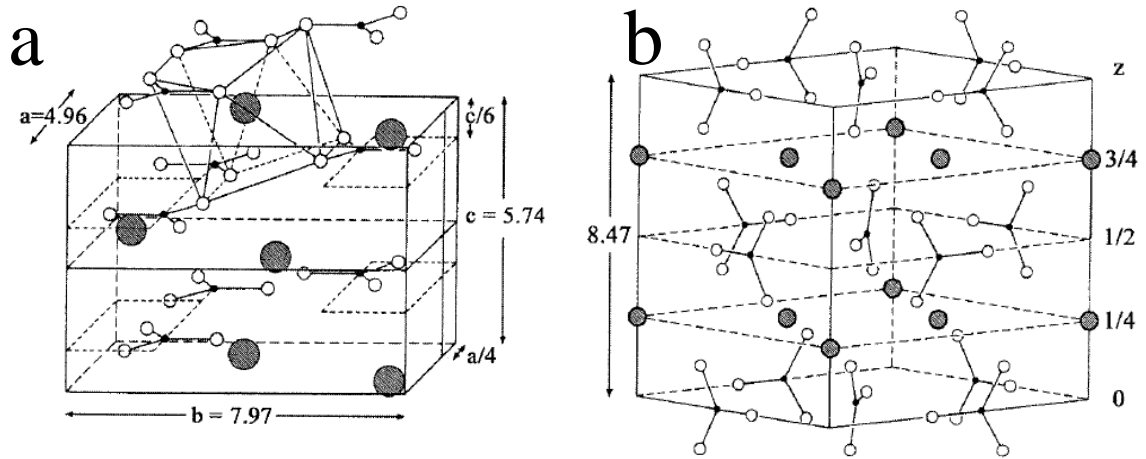
Figure 2: (a) Unit cell of aragonite demonstrating orthorhombic unit cell with the additional CO_3^{2-} groups outside the cell showing the Ca^{2+} ion coordination, and (b) subcell of vaterite. Image reproduced from ref. 318.

4.1.3 Vaterite

Although rare in Nature, vaterite often occurs as a product of precipitation reactions, being kinetically favoured under certain conditions.

The structure of vaterite (Figure 2b) can be described by a hexagonal unit cell in which the Ca and CO_3 groups are again organised in alternating layers parallel to the c-axis. Yet in this case, the plane of the CO_3 groups is parallel to the c-axis[323]. Due to the loosely packed structure, vaterite is less dense then calcite and under ambient conditions would gradually transform into the more stable calcite or aragonite polymorphs.

4.1.4 Amorphous calcium carbonate (ACC).

Recent developments showed the presence and importance of an amorphous calcium carbonate (ACC) phase practicing a big role as precursor phase during biomineralisation[25, 324]. According to Addadi et al.[25], the first mention of ACC was made in the beginning of the twentieth century[325], yet it was until 1997 that ACC was first shown to be a precursor of other $CaCO_3$ polymorphs in biominerals during a study

of the development of sea urchin larval spicule[22]. This was originally believed to be a single crystal of calcite, yet this research proved ACC was also present in the spicule which transformed into calcite with time.

When synthesised, ACC is formed as aggregates of spherical particles around 100 nm in size[326] and is shown to have composition of $CaCO_3. H_2O$[25]. Under ambient conditions, ACC is the least stable form of $CaCO_3$ and readily transforms into more stable forms such as calcite and vaterite with time. Nature has the ability to stabilise ACC under atmospheric conditions, and under lab conditions it has been found to be possible to stabilise ACC by the addition of organic additives and ions such as magnesium[4, 25]. Recent findings also demonstrated that confinement can have a strong effect on the crystallization of ACC, due to its isolation from the surrounding solution[152].

Although ACC has no long range order, work done with X-ray absorption spectroscopy demonstrated short range atomic order can be found in ACC around the calcium ion in the first and second coordination shell, which reflects the final structure of the product polymorph[25, 327-330]. Short range structures of proto calcite and proto vaterite were also reported by Gabauer et al. in their study of prenucleation structures[331].

How ACC transforms into more stable polymorphs is not entirely clear but two different transformation mechanisms have been proposed: a solid state transformation and a dissolution/reprecipitation mechanism. According to Addadi et al.[25] the mechanism of transformation involves a solid state rearrangement in which the locally-ordered ACC acts as the basic unit and subsequently reorganizes into the corresponding crystalline form. This was based on their findings on the crystallization of the amorphous precursor phase of sea urchin larval spicules, which occurred uniformly throughout the biomineral by development of a network of crystalline domains in the absence of a defined crystallization front[22]. According to their argument, this preservation of local structure could not have occurred under the alternative "dissolution and reprecipitation" route. The "dissolution and reprecipitation" route[332-335] on the other hand, describes a transformation occurring by dissolution and recrystallization of ACC into a more stable phase. This was demonstrated by Aizenberg et al.[27, 336] using self-assembled monolayers (SAMs) to stabilize ACC and enable a single nucleation point. By the use of organically modified micropatterned templates, the formation of metastable ACC film was induced, whereafter a nanoregion of calcite nucleation sites were imprinted in certain specific areas. Their research showed that the crystallization of the synthetic ACC on a surface proceeds from the nucleation site, and that the crystal phase grows

from this point with a well-defined crystallization front, expelling water from the structure during crystallization. The crystallization process was suggested to occur by mass transport between the amorphous and crystalline phases, rather than by a solid-state transformation. This was demonstrated by the increase of the pore diameters in the forming crystal as compared with the original ACC film.

4.1.5 Influence of Mg on the crystallization of $CaCO_3$.

Investigation of biogenic $CaCO_3$ has shown that calcite biominerals often contain substantial amounts of magnesium[129, 337]. Occupation of the Ca^{2+} sites of the calcite lattice by Mg^{2+} ions gives rise to high-magnesium calcite which is generally defined as containing at least 4% $MgCO_3$, although in biological systems examples of calcite crystals where about 40% of the sites have been replaced by Mg^{2+} ions have been found[338]. Until now it hasn't been possible to obtain a similar result in synthetic systems due to the inevitable formation of aragonite instead of calcite at high Mg^{2+} concentrations. This is because Mg^{2+} ions have the ability to stabilise aragonite since they are less affected by the incorporation of the highly hydrated Mg^{2+} ions than calcite[4]. The incorporation has no effect on the rate of crystal growth of aragonite, but has a retarding effect on that of calcite since the denser aragonite structure cannot incorporate partially dehydrated magnesium ions. The incorporation of Mg^{2+} inside the calcite structure induces strain in the crystal lattice, increasing the internal free energy of the crystal and the crystal solubility[26]. The thermodynamic limit for Mg incorporation into calcite crystals was determined to be 10 mol% since at this value calcite reaches a similar solubility to aragonite[129]. The mechanism of how biological calcite achieves such a high level of Mg^{2+} incorporation remains unclear but measurement of the amount of Mg^{2+} incorporated appears to largely depend on the present environmental levels of Mg^{2+} in the growth solution[339, 340]. It is known that high levels of Mg^{2+} are able to contribute significantly in stabilising the amorphous phase and it is possible this is one of the reasons such high Mg^{2+} contents are found. Mg^{2+} ions are clearly an important component in the formation of ACC *in vivo*, since they appear to be present in all biogenic ACC samples characterized to date[4, 129, 132]. Previous research showed that a Mg^{2+} content of up to 21 mol% Mg^{2+} could be generated synthetically via an amorphous phase[129] which can be increased to up to 34

mol% when macromolecules are additionally present[129, 337]. These synthetically formed high-Mg calcites are invariably formed as polycrystalline material though.

4.1.6 Influence of soluble additives on the morphology of $CaCO_3$.

Since applications of $CaCO_3$ strongly depend on the morphologies of the crystals, the production of particles with well-defined morphologies and uniform size distributions is a necessity and has been investigated intensively before[11, 12, 30, 48, 98, 104, 341]. As discussed in the introduction, inspired by Nature, soluble macromolecules are often used to manipulate the morphology[28, 30, 98, 103, 104] and since this process is much easier to mimic then the use of confinement or templates, a much higher focus in research was therefore on this method[28, 30, 98, 103, 104].

4.1.6.1 Effect of positively charged additives

Based on previous observations that the amino acids associated with $CaCO_3$ were highly acidic, being rich in aspartic and glutamic acid[113-117], negatively charged additives have principally been considered important in controlling the morphologies of biominerals. Yet the potential importance of other amino acids present in the extracted biomacromolecules was largely overlooked. For example, in addition to aspartic and glutamic acid, the basic amino acids lysine and arginine are also common in the sequences of these macromolecules[112] and the terminal sequences of nacre macromolecules, can exhibit either a net negative or positive charge[112]. Recent modelling results with biogenic macromolecules have also shown that arginine residues are the most important binders of the chicken eggshell protein ovocleidin-17 to calcite[342]. Work done by Helmut et al. with the positively charged polyelectrolyte poly(allylamine hydrochloride) (PAH) and a N-trimethylammonium derivative of hydroxylethyl cellulose, showed an influence over the morphology of $BaCO_3$[341] and $CaCO_3$[343] forming spherical and dumbbell $BaCO_3$ shapes and hexagonal vaterite mesocrystals respectively. Other positively charged additives include dodecyltrimethylammonium bromide (DTAB), whose addition resulted in six-petal-flower-shaped, coral-shaped, dendrite-shaped and multi-antenna-shaped $CaCO_3$[344] while adding poly(L-lysine) formed twin-sphere $CaCO_3$ with an equatorial girdle[345]. Although not crystalline, work done on silicates also showed that a set of polycationic peptides called silaffins, isolated from the cell wall of a diatom, formed networks of

silica nanospheres within seconds when added to a solution of silicic acid[346]. The cell wall also contained large quantity of long chained polyamines (LCPAs), which induced rapid precipitation of silica and controlled the silica sphere size in vitro[347]. Similar results were found for synthetic polyamines, such as polyallylamine and LCPAs, and aggregation and aggregate size were found to be directly correlated with the presence and concentration of multivalent anions, such as phosphate, sulfonate, or citrate ions. These negatively charged ions act to cross-link LCPAs through the establishment of hydrogen bond and ionic interactions. Silicic acid species may absorb onto the LCPA aggregates, forming a liquid precipitate which then polymerize into silica[348, 349].

4.2 Aims of the project.

All the work stated above demonstrates that positively charged polyelectrolytes can have some an effect on the morphology of crystals, yet the research on the effect of the additives has never been done thoroughly and systematically. In this chapter, the effect of the positively charged polyelectrolyte poly(allylamine hydrochloride) (PAH) on the precipitation of $CaCO_3$ is investigated over different additive concentrations and pH ranges. This molecule has previously been shown to influence the crystallization of $BaCO_3$[341], and features a similar structure to the negatively charged polyelectrolyte PAA (poly(acrylic acid)).

PAH it is a cationic polyelectrolyte, manufactured by the polymerization of allylamine (Figure 3). It consists of functional amino groups and has a pKa value of 8.5, and is therefore protonated at the applied starting pH of 6 ($CaCl_2.2H_2O$ solution).
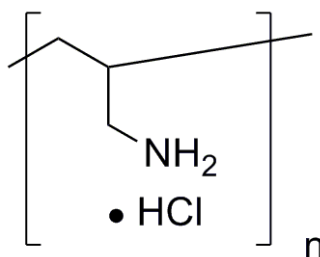
Figure 3*: Structure of PAH.*

4.3 Experimental procedures

Calcium carbonate was precipitated in the presence of poly(allylamine hydrochloride) (PAH) with and without purification under a range of solution concentrations. The progress of the reaction was also investigated with time and pH.

4.3.1 Crystallization Process.

$CaCO_3$ was precipitated in the presence of PAH (Mw 56.000 Da and 15.000 Da available from Aldrich) using the ammonium carbonate diffusion method (See 2.1.2). A $CaCl_2.2H_2O$ solution of 20 mM was prepared and variable amounts of PAH were added to the solution. PAH concentrations ranged from 5 μg/mL to 2 mg/mL. The initial pH of the solution ranged between 4.16 and 7 depending on the PAH concentration, and raised to about 9.5 after a couple of hours. Variable amounts of a 100 mM $MgCl_2 \cdot 6H_2O$ and 10 mg/mL PAH stock solution were added to a Petri dish containing $CaCl_2.2H_2O$ solution to give the required Ca^{2+}/Mg^{2+} ratio and PAH concentrations. Glass slides were used as substrates, and put upright into the Petri dish to avoid sedimentation of crystals onto the glass slides. The petridish was then placed in an ammonia desiccator whereafter crystallisation occurred. The glass slides were removed from solution after variable times (1 hour to 6 days), washed with ethanol and allowed to dry at room temperature.

4.3.2 Control experiments.

Control experiments were performed using identical procedures to those described below but in the absence of PAH.

4.3.3 Characterization of the calcium carbonate precipitates.

The precipitated $CaCO_3$ particles were investigated using both FEGSEM, TEM and optical microscopy, with analysis between crossed polars in the optical microscope providing information on the crystallinity of the film (single crystal/polycrystalline/amorphous structures). Micro-Raman spectroscopy and electron diffraction were used to determine the $CaCO_3$ polymorphs present in the samples. To investigate the early stages of the reaction, a carbon-coated Cu TEM grid was dipped in a solution which was taken out at variable times. Alternatively, to avoid oxidation of

the Cu-grids during the ammonia diffusion method, a carbon-coated Ni TEM grid was placed in a solution and removed from the solution at variable times. Afterwards both grids were washed with ethanol and left to dry. Investigation of the fibers with TEM was also accomplished by scraping the fibers off the supporting glass slide and transferring them to a carbon-coated Cu TEM grid.

4.3.4 Compositional analysis

After a certain reaction time the solution was filtered through Millipore track-etched membranes (0.45 µm) and washed 3 times with ethanol. The precursor phase was then scraped off the membrane, and analysed with infrared, TGA, AA and Raman microscopy. The obtained data was compared with those obtained from a control sample which had been prepared in the absence of Ca^{2+} ions by mixing a solution of 10 mM Na_2CO_3 with 1 mg/mL PAH, and adjusting the pH level to 9.0 with HCl.

4.3.5 Cryo-TEM

The Cryo-TEM measurements were carried out in collaboration with Dr. Fabio Nudelmann of Nico Sommerdijk's group in Eindhoven University.
A vitrification robot (FEI Vitrobot Mark III) which was equipped with a humidity- and temperature-controlled glove box was used to prepare the samples. Cryo-TEM grids, R2/2 Quantifoil Au Jena grids, were surface plasma treated using a Cressington 208 carbon coater before the vitrification procedure. 3 µl of the solution was taken out of the petridish after variable times and put on an Au grid inside the vitrobot chamber (at 100% humidity and 20 ° C), which was subsequently blotted for 2 sec with filter paper and immersed in liquid ethane cooled by liquid nitrogen. The samples were kept in liquid nitrogen and then loaded into the Cryo-TEM holder.

4.3.6 DLS measurements

DLS measurements were conducted by taking out 2 mL of the solution after 30 min and 3 hours placed in an ammonium carbonate desiccator and pipetting the sample into a cuvette. DLS-measurements and zeta potential measurements were subsequently conducted on the samples.

4.3.7 Investigation of effect of pH by slow addition experiment:

A slow addition or dripping method experiment was set up where the effect of the solution pH on the precipitation of $CaCO_3$ was investigated in the presence of PAH (Figure 4). This technique allowed us to recreate the slow build up and continuous repletion of carbonate ions characteristic of the gas diffusion technique (see Chapter 2.1.2) but with a control of the pH. Therefore, a 20 mM $CaCl_2.2H_2O$ solution was slowly added over a period of time to a 20 mM Na_2CO_3 containing 1 mg/mL of PAH by drop wise addition of the $CaCl_2.2H_2O$ solution, to give final concentrations of 10 mM Na_2CO_3, 0.5 mg/mL PAH, and 10 mM $CaCl_2.2H_2O$. The initial pH of the solutions was varied from 4 to 12 to allow the precipitation to happen at different final pH values.
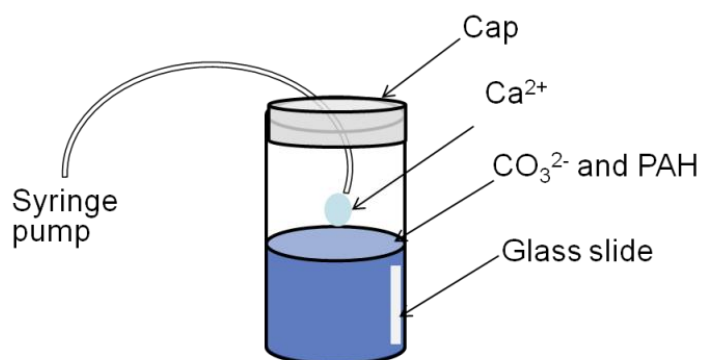
Figure 4: Experimental set-up for the slow addition experiment of Ca^{2+} to a CO_3^{2-} and PAH solution.

4.3.8 Track-etched membrane experiment

A track-etched (TE) membrane (membrane pore 50 nm) was put in a Petri dish filled with 10 mM $CaCl_2.2H_2O$ and 1 mg/mL PAH placed in an ammonia desiccator. At the end of the reaction, the TE membranes were removed from the reaction solution and dissolved in DCM

4.4 Results

4.4.1 Effect of PAH on the morphology of calcium carbonate

For the control experiments, in the absence of PAH, calcite rhombohedra (Figure 5a) with an average size of 50 μm were distributed over the glass substrate as expected.

Examination of the crystals under crossed polarisers shows that they were single crystals (Figure 5b).
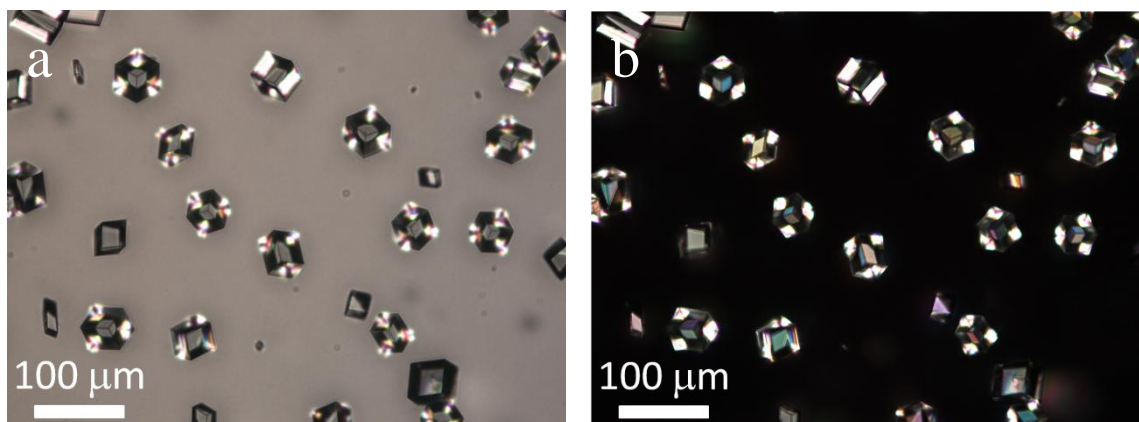
Figure 5: Optical microscope image under crossed polarisers (b) of calcite crystals precipitated on a glass slide after 1 day from a 10 mM $CaCl_2$ solution.

The polymorph was confirmed using Raman microscopy (Figure 6), which showed characteristic peaks at 1085 cm^{-1} (υ_1 internal CO_3 symmetric stretch), 711 cm^{-1} (υ_4 internal in-plane-bending), 280 cm^{-1} (rotational) and 154 cm^{-1} (translational) corresponding to literature values for calcite[350, 351].
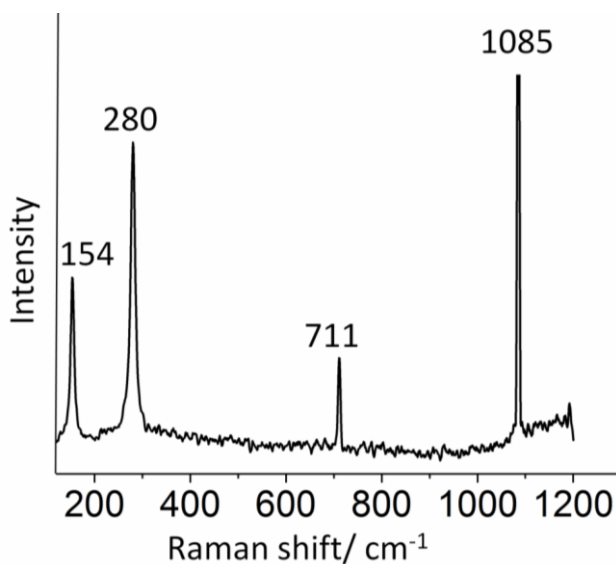
Figure 6: Raman spectrum of crystals precipitated on a glass slide after 1 day from a 10 mM $CaCl_2$ solution, corresponding to calcite.

Subsequently, the effect of the addition of PAH was investigated at concentrations of 10 mM CaCl$_2$.2H$_2$O. Firstly it was found low that concentrations of 5 to 10 μg/mL PAH had little effect on the crystallization. Rhombohedral calcite crystals were formed, where some of them were slightly deformed, showing rounded faces and geometric cavities in their centres (Figure 7). This relatively minor modification in crystal morphology could be expected and was easily ascribed to interaction of the polymer with the edges and faces of the crystal[14, 38, 102] influencing the growth rate of the faces and edges.
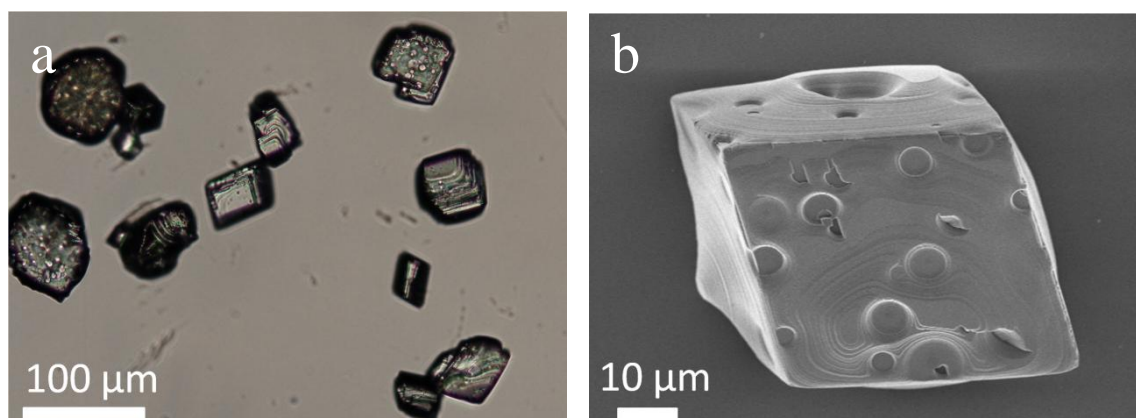
Figure 7: Optical microscope image (a) and FEGSEM image (b) of crystals formed in the presence of PAH at [CaCl$_2$] = 10 mM and [PAH] = 0.01 mg/mL.

By further addition of PAH to concentrations of 50 to 80 μg/mL a much bigger effect was observed. In addition to deformed crystals as observed before, the presence of PAH also led to the formation of some remarkable fibrous particles growing out of distorted rhombohedral calcite crystals (Figure 8). Most of the fibers grew out of the crystals, perpendicular to the crystal surface, often changing direction abruptly. The fibers were almost always attached to the glass slide and were only a couple of nm thick, but typically a few μm long. Small bobbles were also sometimes observed at the ending of the fibers (Figure 8d).
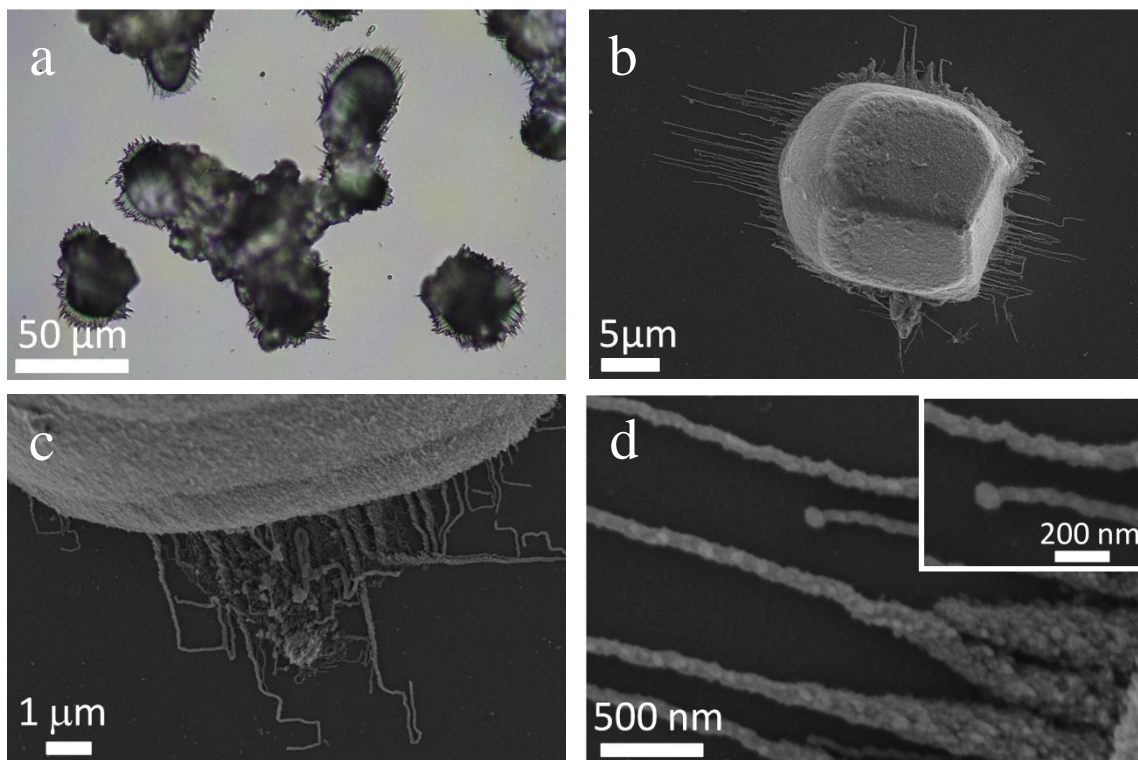
Figure 8: Optical microscope image (a) and FEGSEM images (b, c, d) of CaCO$_3$ crystals precipitated in the presence of 0.08 mg/mL PAH after 3 days reaction time. Inset of (d) shows a small bobble at the end of a fiber.

An even more remarkable result was the formation of a crystalline film at this PAH concentration, which was highly birefringent under the crossed polars of the optical microscope (Figure 9). The occurrence of these films became more profound when polymer with lower molecular weight was used (15.000 Da instead of 56.000 Da). Some of the films looked polycrystalline (Figure 9a, b) under crossed polarisers, while others consisted out of single crystal patches, around 100 μm in size (Figure 9c, d)
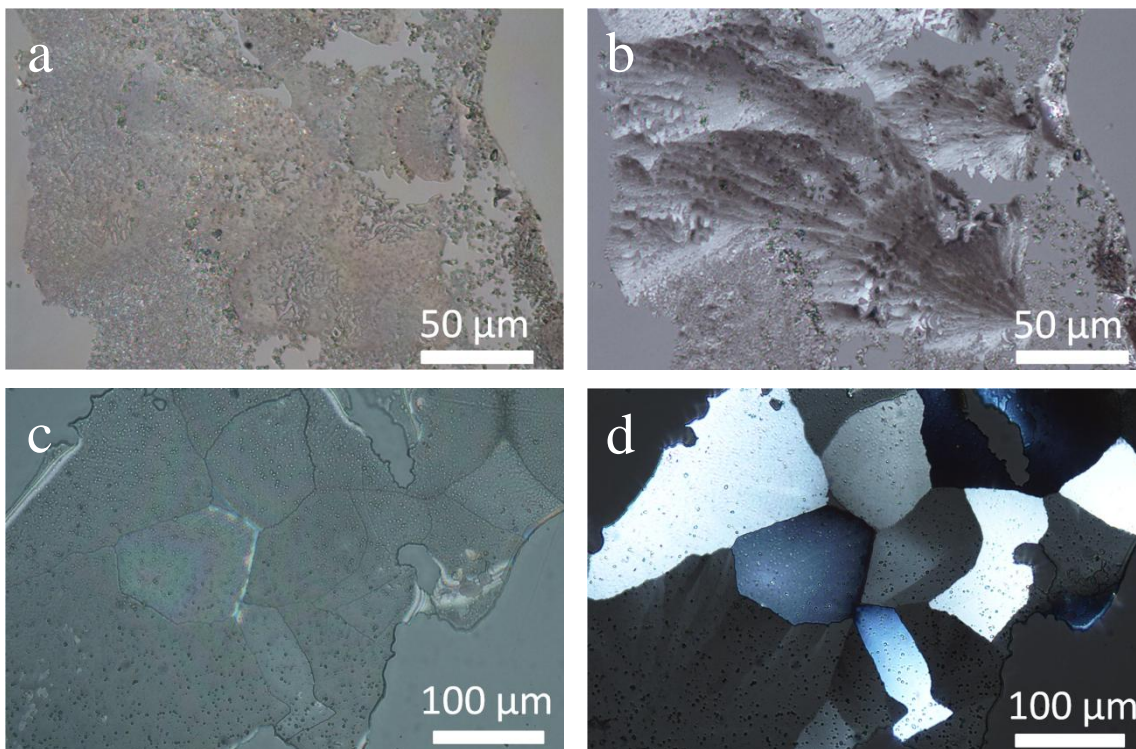
Figure 9: Optical microscope images after 3 days reaction time of a vaterite film (a, b) and calcite film (c, d) under crossed polars (b and d), covering the top parts of the glass slide after addition of 0.08 mg/mL PAH to the solution.

Raman analysis showed that the polycrystalline film was constructed from vaterite (with characteristic peaks at 1079 cm^{-1} and 1093 cm^{-1} from the internal CO_3 symmetric stretching υ 1 and a lattice mode peak at 300 cm^{-1})[352], while the single crystal ones were calcite (with characteristic peaks at 1085 cm^{-1}, 713 cm^{-1}, 280 cm^{-1} and 152 cm^{-1})[350, 351] (Figure 10). These films were only present at the point of the water-air interface.
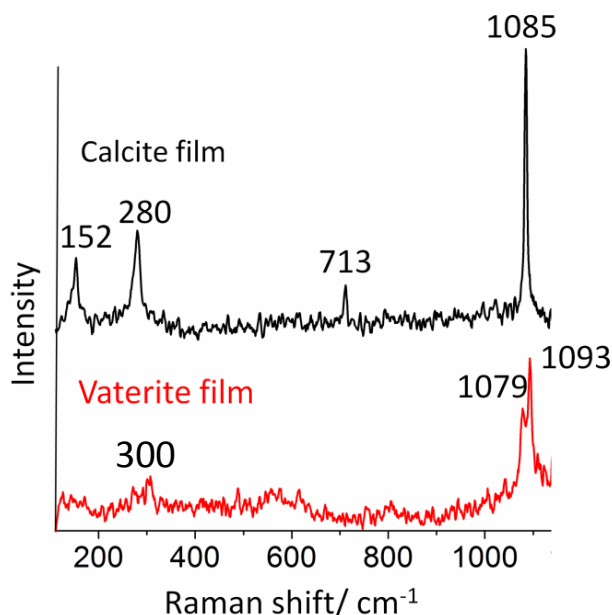
Figure 10: Raman spectra of a single crystal calcite film (Figure 9c) and a polycrystalline vaterite film (Figure 9a) formed after 3 days on a glass slide in the presence of 0.08 mg/mL [PAH].

The formation of fibers and films became more profound at higher concentrations such that at concentrations of 0.2 mg/mL fibers with aspect ratio's of over 20 (60 μm long) were produced growing out of a central core (Figure 11a) or film (Figure 11c, d). These fibers were identified as calcite using Raman microscopy (Figure 12). The formation of film became more extensive at random positions on the glass slide (Figure 11b), and were often identified as calcite by Raman (Figure 12).
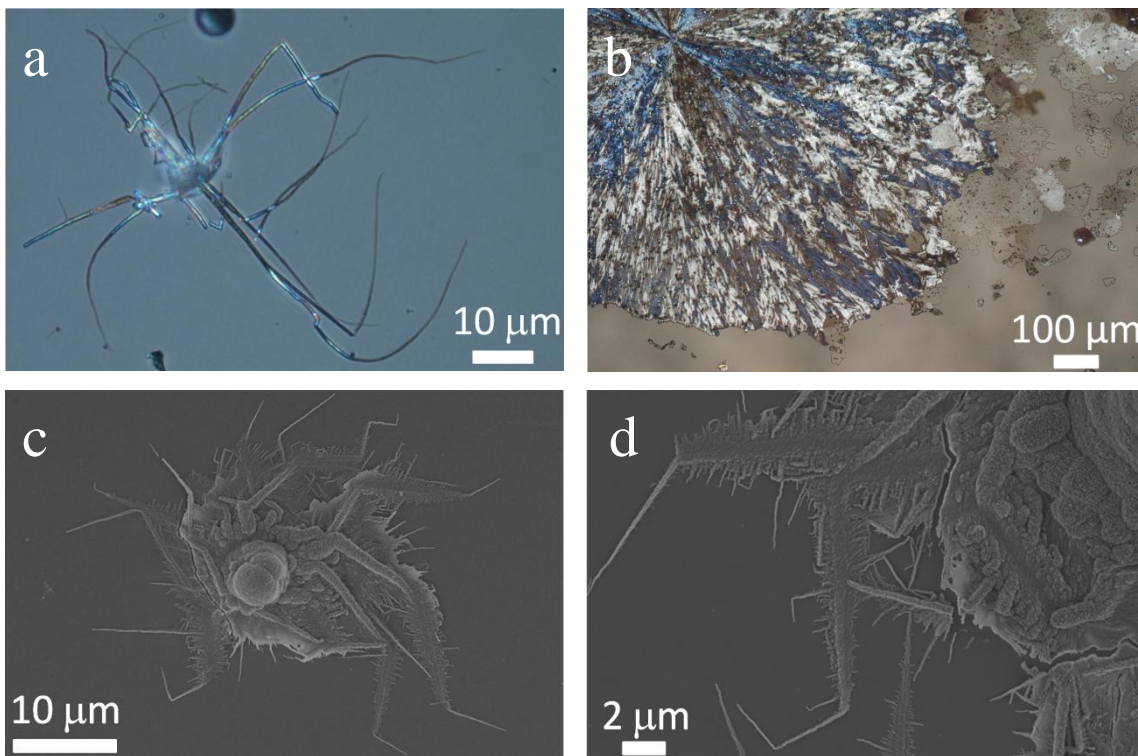
Figure 11: Optical microscope images taken under crossed polars of calcite fibers (a) and a crystalline calcite film (b) covering some parts of the glass slide after 1 day in the presence of 0.2 mg/mL PAH. (c) And (d) show FEGSEM images of the same sample.
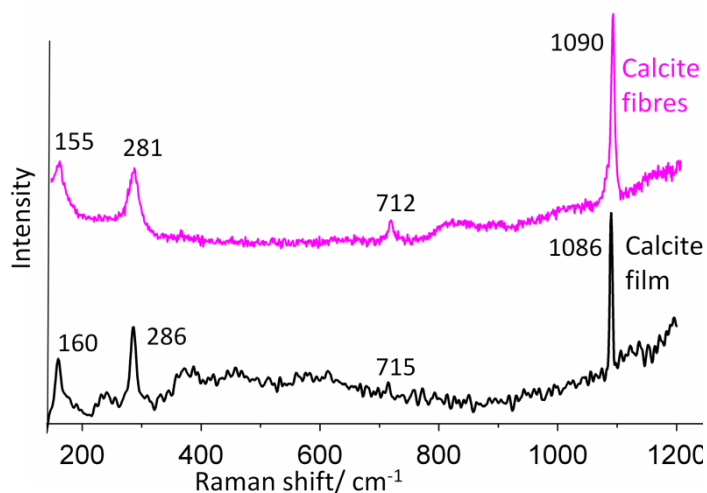
Figure 12: Raman spectra of fibers and film formed on a glass slide after 1 day after in the presence of 0.02 mg/mL PAH.

Increasing the concentration further to 0.5 mg/mL and 1 mg/mL led to the construction of polycrystalline calcite films which almost entirely covered the glass surface with fibers often associated with these films (Figure 13a and c arrowed and 14a and b). In

between the calcite film, small areas of vaterite film (about 10% of the total polycrystalline film) were also found (Figure 13c) as identified by Raman (Figure 15). In addition the polycrystalline calcite film more patches of single crystal calcite film were observed at the top of the glass slide, and in between the polycrystalline film (Figure 13d, e and f).
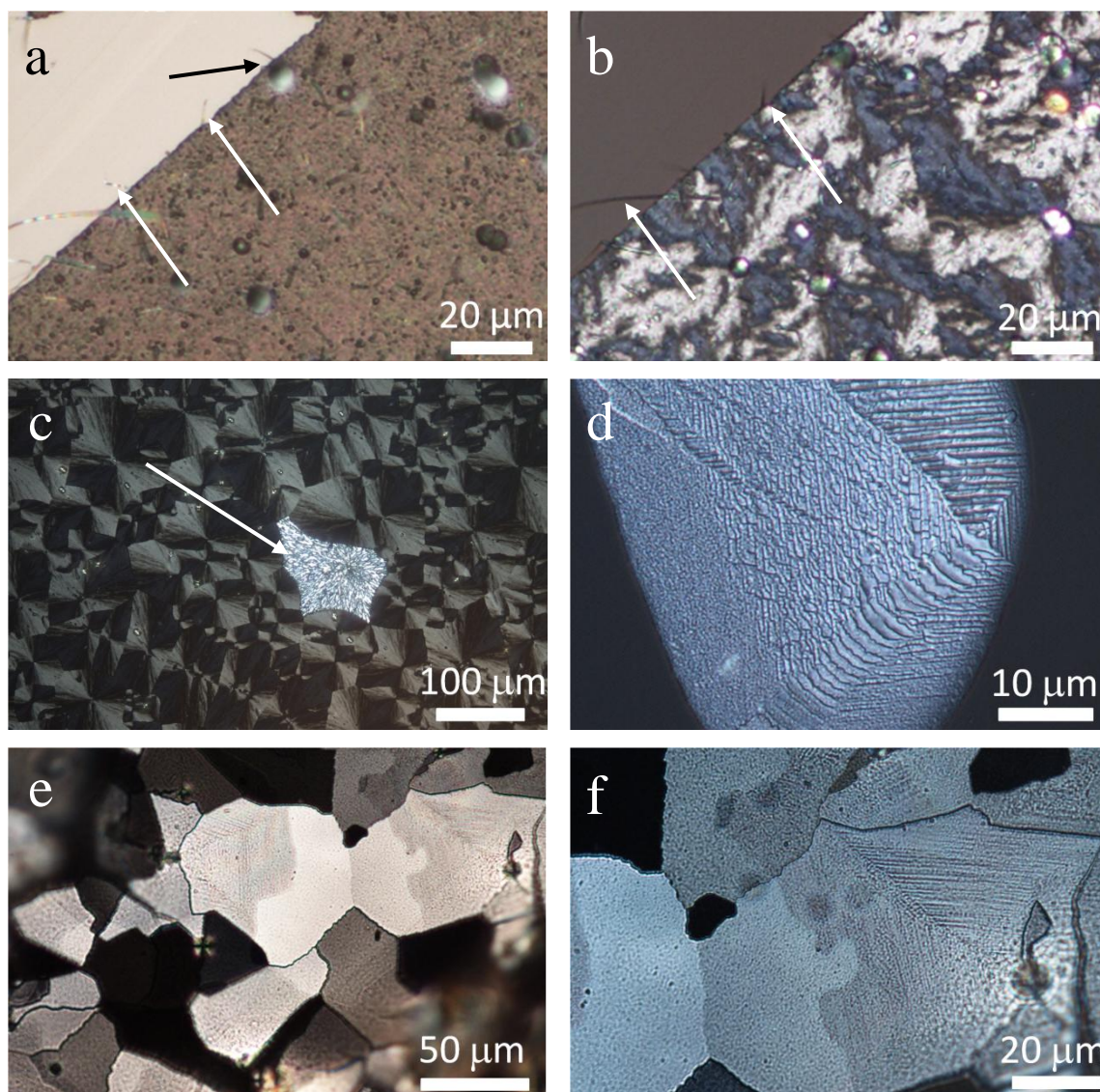
Figure 13: Optical microscopy images (a) under crossed polarisers (b-f) of crystalline films formed after 1 day by addition of 1 mg/mL PAH to the solution. (a) And (b) show images of a polycrystalline film with small fibers growing out (arrowed). (c): A calcite polycrystalline film with the white arrow denoting the vaterite patch. (d, e, f) Calcite single crystal film covering some parts of the glass slide. Transition bars are observed especially in (d) and (f).

FEGSEM imaging showed that the single crystal films had a thickness of about 0.5 µm (Figure 14f) and had quite a smooth surface as compared with the polycrystalline ones (Figure 14a, b in comparison with c, d, e).
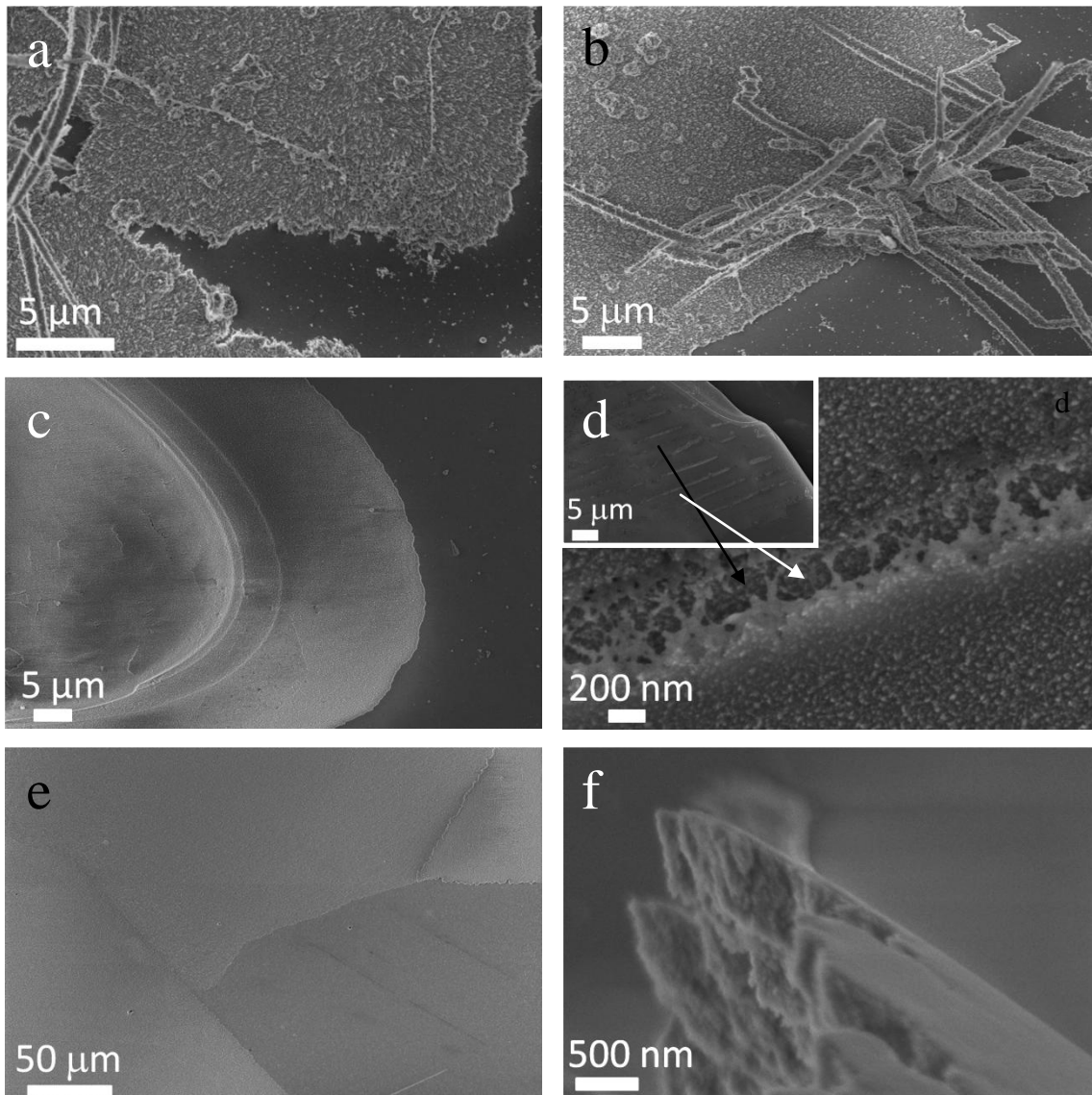
Figure 14: FEGSEM images of a polycrystalline (a, b) and single crystal (c, d, e, f) calcite film covering some parts of the glass slide formed after 1 day by addition of 1 mg/mL PAH to the solution. The polycrystalline film (a, b) is much rougher and fibers emerge from the film. The single crystal films are much smoother (c, d, e). The parallel striations on the single crystal patches (d) seem to be gaps in the surface.
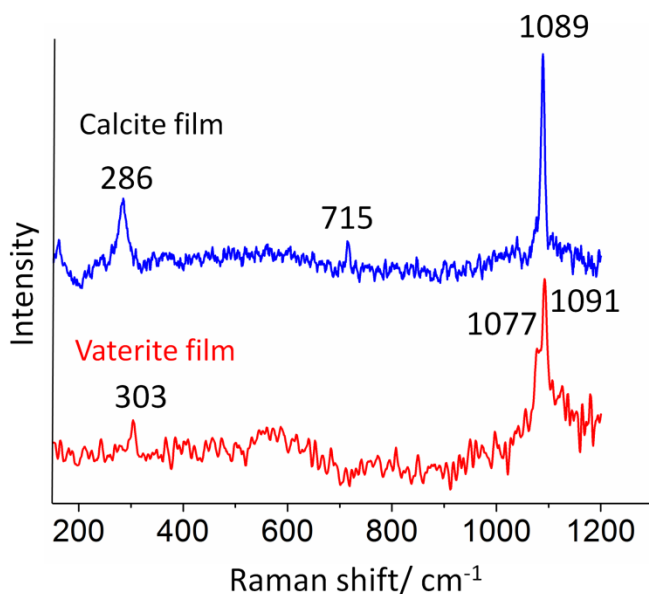
Figure 15: Raman spectra of a polycrystalline calcite film and vaterite film formed on a glass slide after addition of 1 mg/mL [PAH].

In agreement with the results obtained with the negatively charged polyelectrolytes PAsp/PAA, the single crystal films often featured also so called "transition bars" (Figure 13d, e, f and 14d), which were attributed before to exclusion of the polymeric impurity into diffusion limited zones as crystallization proceeds across the amorphous phase[89].

In time the transition bars on our samples seem to diminish, and FEGSEM images (Figure 14d) showed the transition bars were ridge-like regions with gaps in the film, delineated by material with an undefined shape.

Surprisingly, these single crystal patches could principally be observed at the air/ water interface, while the polycrystalline films were present where the glass slide was entirely dipped into the solution. Their single crystal structure was further confirmed by their uniform contrast and optical extinction under polarised optical microscopy (Figure 16). By rotation of the sample by 45 degrees it was seen the film went from completely bright (the crystal is perpendicular to the light beam) to dark when the crystal was parallel to the incident light.
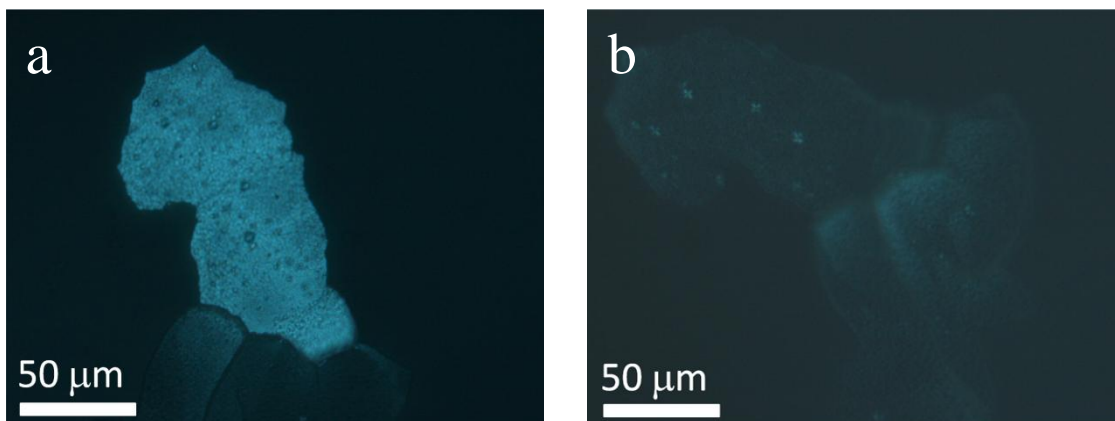
Figure 16: (a) Optical microscope of a single crystal calcite domain in a thin film deposited on the substrate adjacent to the air/water interface, viewed between crossed polarisers. (b) The same area viewed after rotation of the sample, demonstrating uniform extinction. Both were formed in a 10 mM $CaCl_2$ solution with 1 mg/ml PAH after 1 day.

The films and fibers formed were further investigated with TEM. Since it proved to be a challenge to remove film patches of the glass slide, thin enough to be investigated with TEM, Ni-grids were used as a substrate on which to deposit $CaCO_3$ films. They were put floating on top of the solution, with the carbon-covered formvar film in contact with the solution. Although the surface properties of the glass slides and the TEM grids are different, similar $CaCO_3$ films were obtained in both cases.
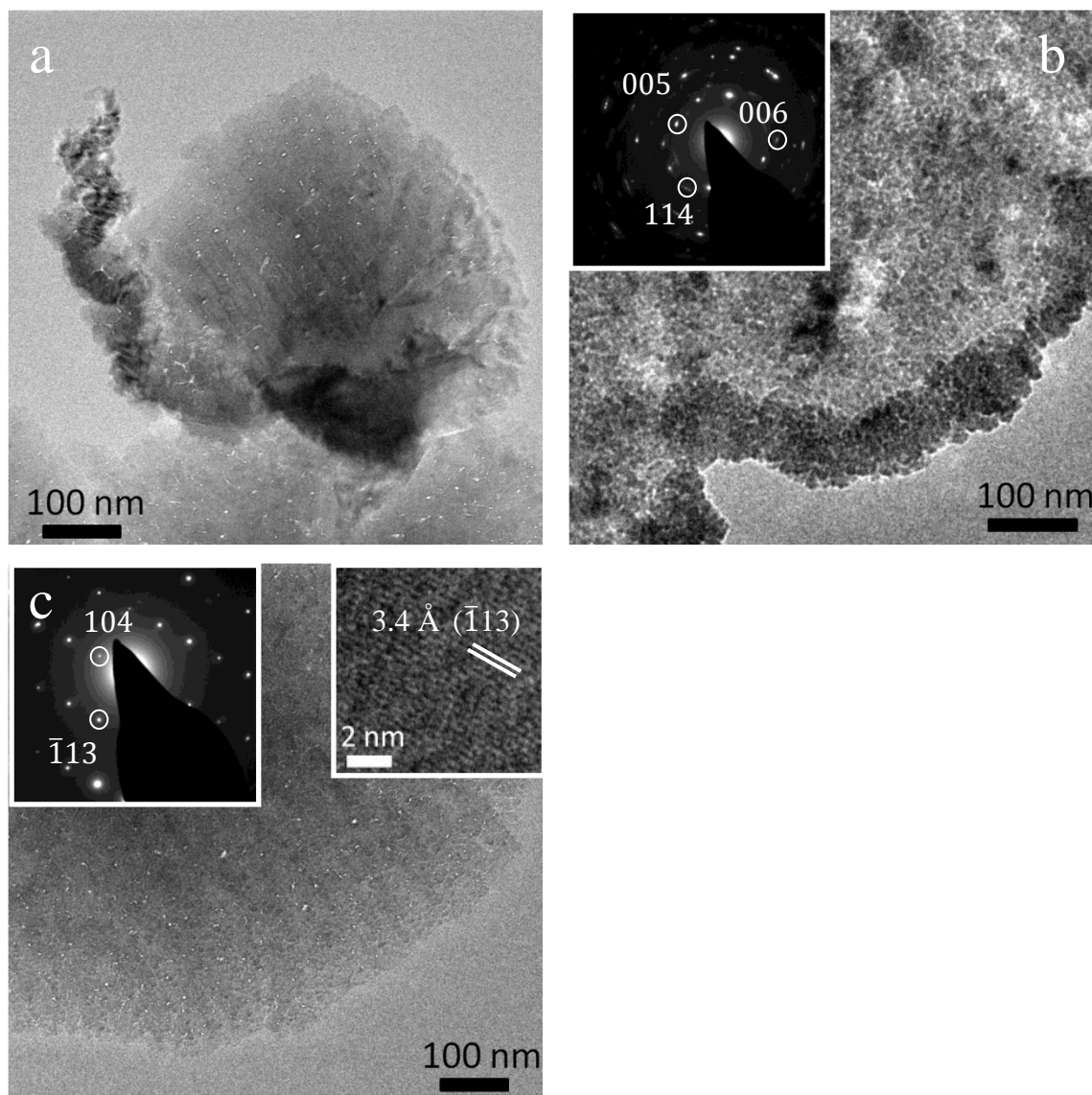
Figure 17a, b, c: TEM images of $CaCO_3$ films precipitated on a TEM grid in the presence of 1 mg/mL PAH after 1 day. (a) Shows a TEM image of a grid with a fiber growing out. Polycrystalline films (b) and single crystal (c) patches were found. Both crystalline films were identified as calcite.

Figure 17a shows a spherical patch with a fiber-like entity growing out of the patch. The shape of the fiber appears as if it is grown in a helical shape. Figure 17b shows a polycrystalline film of calcite and the patches appear to be built from smaller particles of about 10-30 nm in size. In addition to polycrystalline patches, patches with a single crystal diffraction pattern were also found (Figure 17c and inset). The distance between the fringes is 3.4 Å, corresponding to the diffraction pattern and the ($\bar{1}$13) plane of calcite. The films appear to be constructed from an agglomeration of smaller particles.

As described before, as well as supporting the formation of crystalline $CaCO_3$ films, the PAH also induced the growth of interesting fibers of $CaCO_3$. The fiber thickness and length varied from sample to sample with thicknesses from 10 nm to 10 μm and lengths a couple of nm to hundredths of μm. Characterisation of the thin fibers was carried out with TEM and selected area electron diffraction (SAED) and high resolution TEM (HRTEM) showed that each fiber was a single crystal of calcite. Figure 18a shows a TEM image of a fiber with corresponding SAED as inset. The SAED corresponds to calcite with a [4 5 $\bar{1}$] zone axis. An HRTEM image of the same fiber (Figure 18b) and inset) shows continuous fringes along the fiber which can be ascribed to {104} planes of calcite. The long axis of the fiber in Figure 18 was identified as corresponding to the [13 5 3] direction as indicated by the arrow, but analysis of a number of fibers showed no preferential direction. Interestingly, the TEM images of the fibers also showed that they are often covered with a less dense surface coating (Figure 18b). By observing the lattice fringes it was seen that these did not persist into this coating suggesting that the layer is amorphous. This would be consistent with an extrusion of polymer during the crystallization stage, thereby creating an ACC phase too rich in polymer to crystallise. A similar amorphous layer has also been observed surrounding the aragonite platelets comprising the nacre of molluscs, an effect which was in this case attributed to their formation via a polymer-stabilised ACC phase[353].

Unfortunately, efforts to determine the elemental composition of the coating on the fibers using EDX were unsuccessful, due to its small thickness.
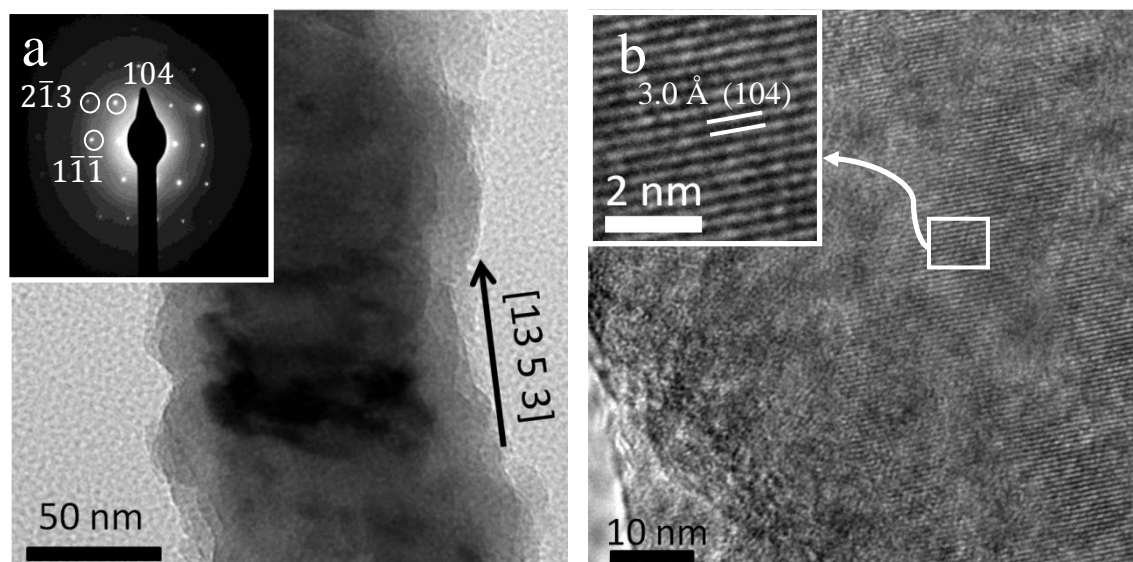
Figure 18: TEM images of a fiber formed after 1 day in the presence of 1 mg/ml PAH. (a) TEM image with corresponding SAED pattern in the inset corresponding with a single crystal pattern of calcite with a zone axis of [4 5 $\bar{1}$]. An arrow indicates the [13 5 3] direction along the long axis of the fiber. (b) An HRTEM image of the fiber shown in (a) with an image of the continuous {104} lattice fringes in the inset.

4.4.2 Effect of Ca^{2+} concentration

To investigate the effect of the Ca^{2+} concentration, a 1.5 mM $CaCl_2.2H_2O$ solution was mixed with 0.5 mg/mL PAH and was placed in a saturated ammonium carbonate desiccator to precipitate calcium carbonate crystals. The initial pH of the solution was 4.60 which rose to 9.5 after 1 day.

In contrast with the polyhedral prismatic rhombohedral calcite crystals, which are precipitated in the absence of additives, remarkable fibrous particles formed in the presence of PAH, growing from one centre point (see Figure 19 and 20). In contrast to the higher Ca^{2+} concentrations, no film formation was observed expect in some very small patches. These patches were always associated with fibers and had a very rough appearance (Figure 20e). The fibers grew out of previously deposited spherical particles or thick films covering the surface. Reaction times of more than 1 day were necessary such that material could be observed with the optical microscope. Since almost no film formation was observed in this case, it appears that low Ca^{2+}/PAH ratios favour fiber formation.
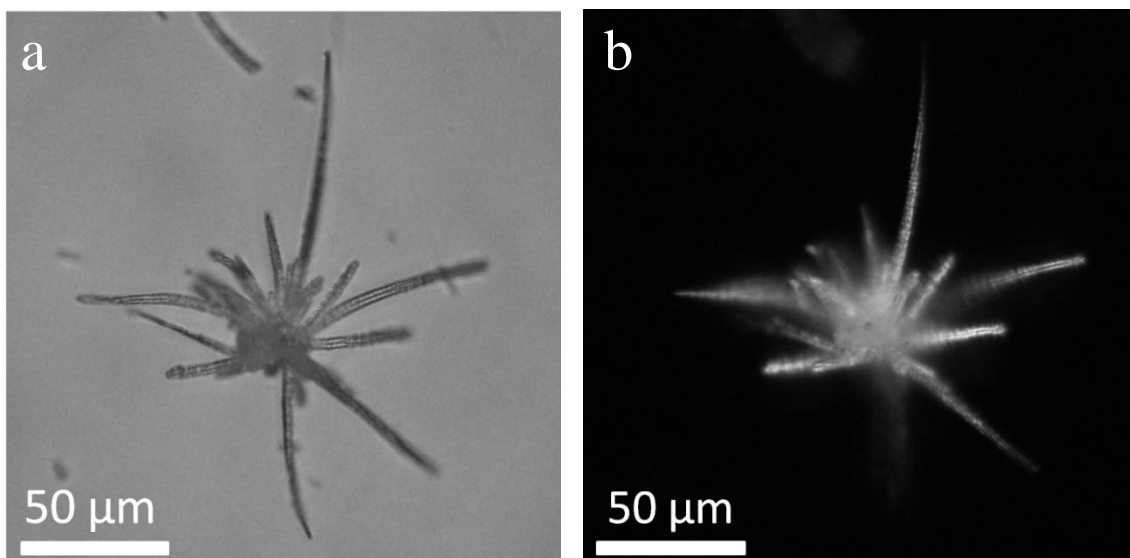
Figure 19a: Optical microscope images of fibrous structures formed 6 days after mixing 1.5 mM $CaCl_2$ solutions with 0.5 mg/mL PAH. (b) Analysis between crossed polars of the fibers shows that they are single crystals.

These fibers were again single crystals (Figure 19b and 20f) and solid fibers with lengths of 50 µm to 120 µm and thicknesses of 60 nm to 200 giving average aspect ratio's of ≈ 400 (Figure 20e) were observed. The diameter of the fibers varied from 5 µm at the base to a few nanometres at the top (Figure 20a) and the fibers were constructed out of nanometre sized building blocks. Some of the fibers showed the formation of branches (Figure 20d inset) and a double growth of fibers was also observed occasionally (Figure 20a, b and c), which evolved into a single fiber at the end. The growth direction was quite random where as well as straight fibers (Figure 20a), curly fibers (Figure 20c) and fibers abruptly changing direction (Figure 20d) were observed. Usually, the abrupt change of direction occurred at angles of around 70-100 degrees, although this differed a lot and no real trends were seen. Raman and TEM with SAED confirmed about 90% of fibers were calcite (Figure 21 and 20f) while the remaining fibers were vaterite (Figure 22). The orientation of the fiber in Figure 20f is in the [330] direction along the long axis of the fiber, but this wasn't always the case for other investigated fibers.
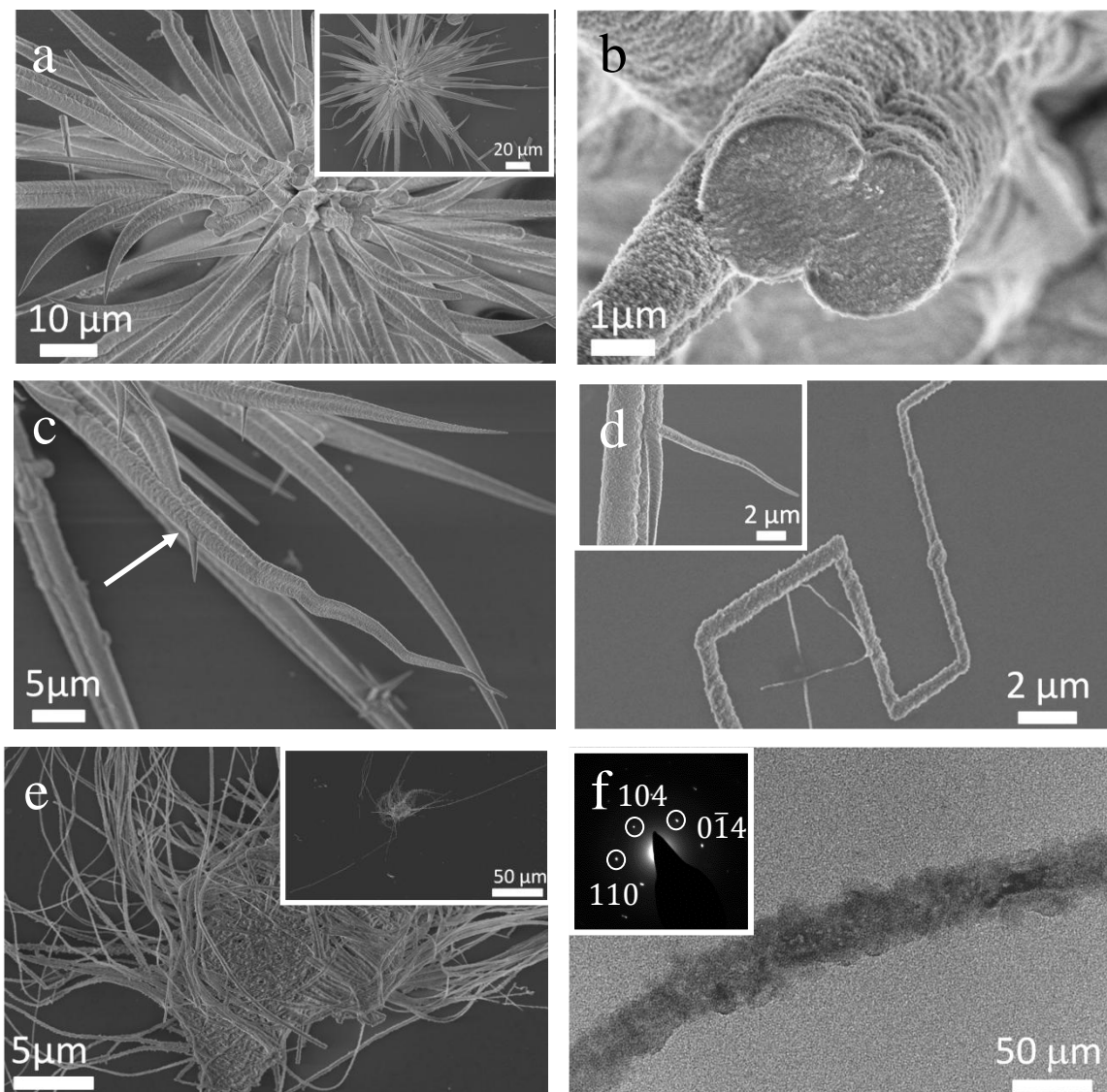
Figure 20: FEGSEM images of calcium carbonate fibers precipitated from 1.5 mM CaCl$_2$ solutions containing 0.5 mg/mL PAH after 3 days. (a) Shows CaCO$_3$ fibers growing out of a central core with a lower magnification in the inset of the same crystal. (b) Is a higher magnification of (a). (c) And (d) show higher magnification images of a single fiber, demonstrating the different growth behaviour. (e) Shows fibers growing out of a patch on the surface. A TEM image of a fiber with corresponding calcite SAED is shown in (f) oriented according to the [330] direction.
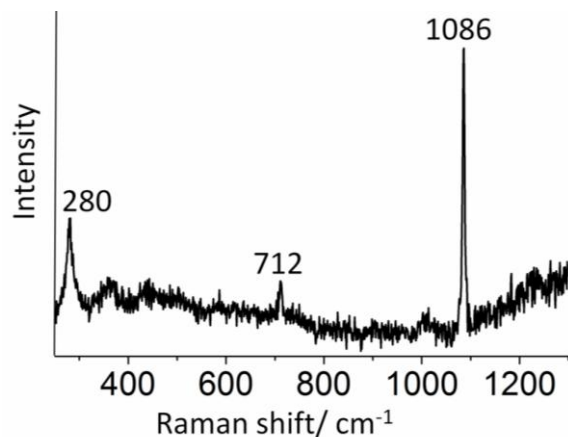
Figure 21: Raman spectrum of produced fibers grown in the presence of 0.5 mg/mL PAH after 3 days, corresponding with calcite.

Although the vast majority of the fibers were calcite, a number of short vaterite fibers were also observed. These fibers were almost the same morphology as the calcite fibers except that they had smaller aspect ratios, constant thicknesses, were more curly and tended to grow alone instead of in group (Figure 22).
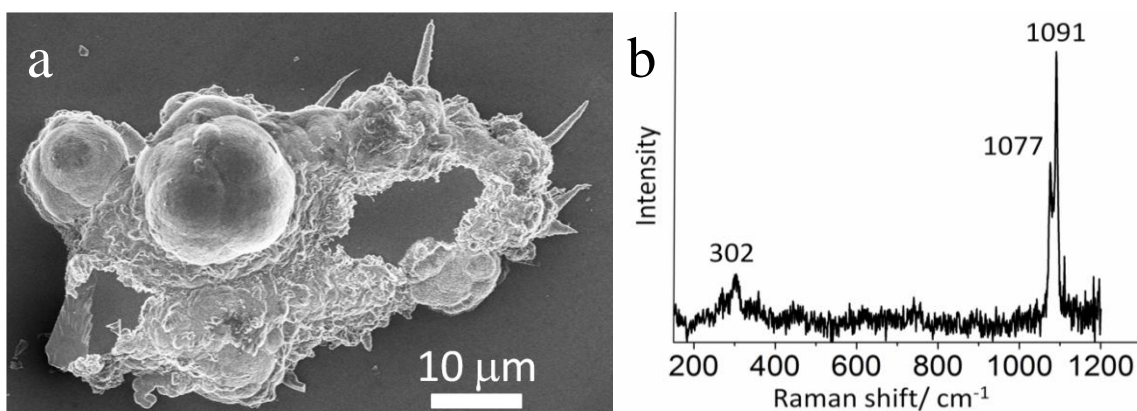
Figure 22a: SEM images of fibers grown in the presence of 0.5 mg/mL PAH after 6 days. (b) Raman spectrum of the produced fibers corresponding with vaterite

Variation of the PAH concentration had a small effect on the fiber morphologies. As can be seen in Figure 23a, at higher PAH concentrations of 4 mg/mL, the fibers were quite smooth and thin forming a bundle of fibers, and were covered with some globular material without a defined shape (Figure 23a, b). Lowering the PAH concentration to conditions of 0.5 mg/mL (Figure 23b, c and Figure 20) led to rougher, shorter fibers where the constituent particles were very clearly visible. Lowering the concentration

further to 0.01 mg/mL led to the construction of fewer, but thicker fibers which seemed to grow out of films deposited on the glass slide. Very few fibers formed at concentrations of 0.005 mg/mL such that these were small and only were observed growing out of spherical aggregates (Figure 23g). Holes were found inside the crystals and in some cases (Figure 23h), large spiral pits formed in the centres of the crystal faces, comparable with previous results[76]. No fibers formed at lower concentrations, and only calcite and some vaterite crystals were observed (Figure 23i and j).
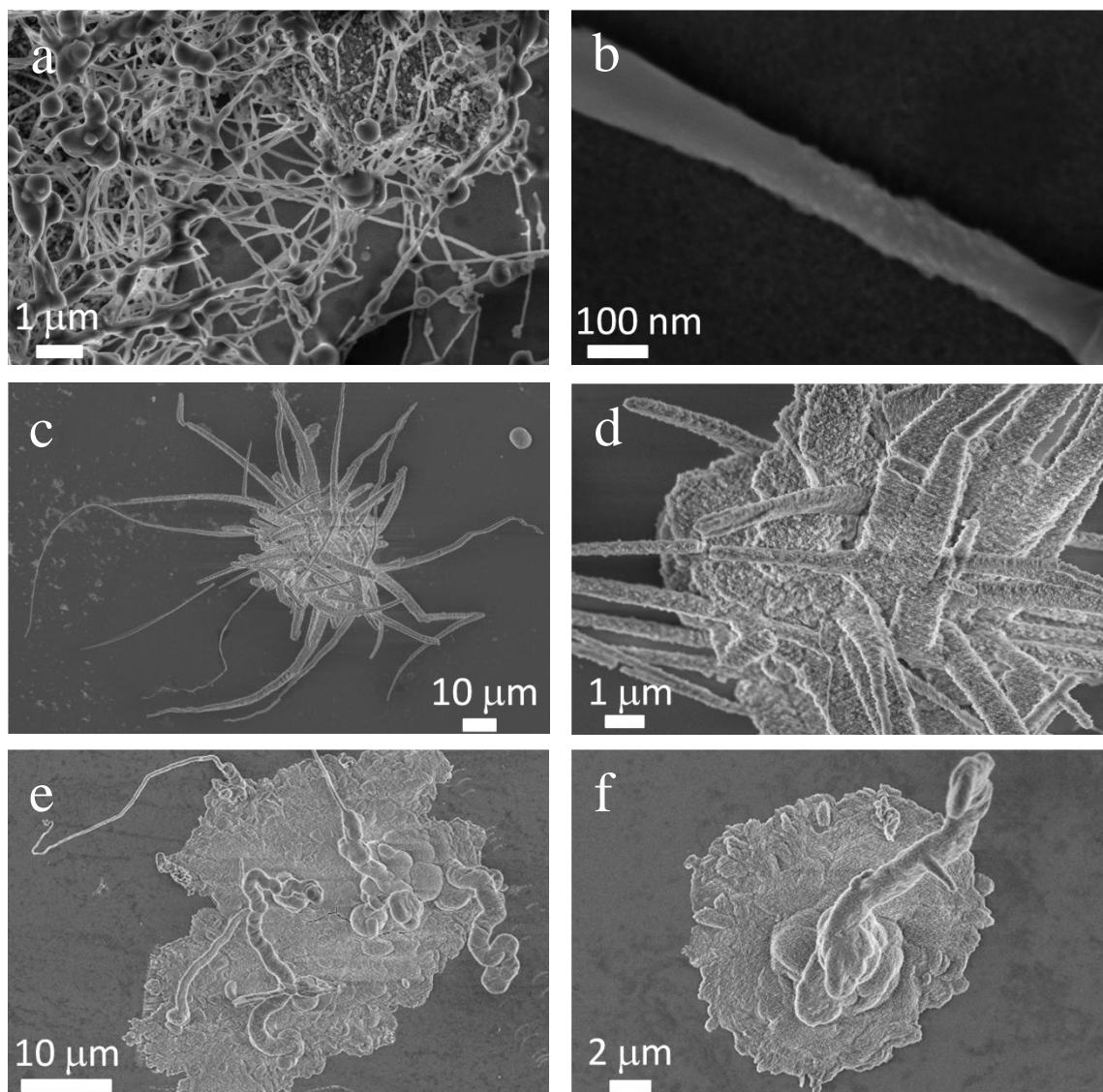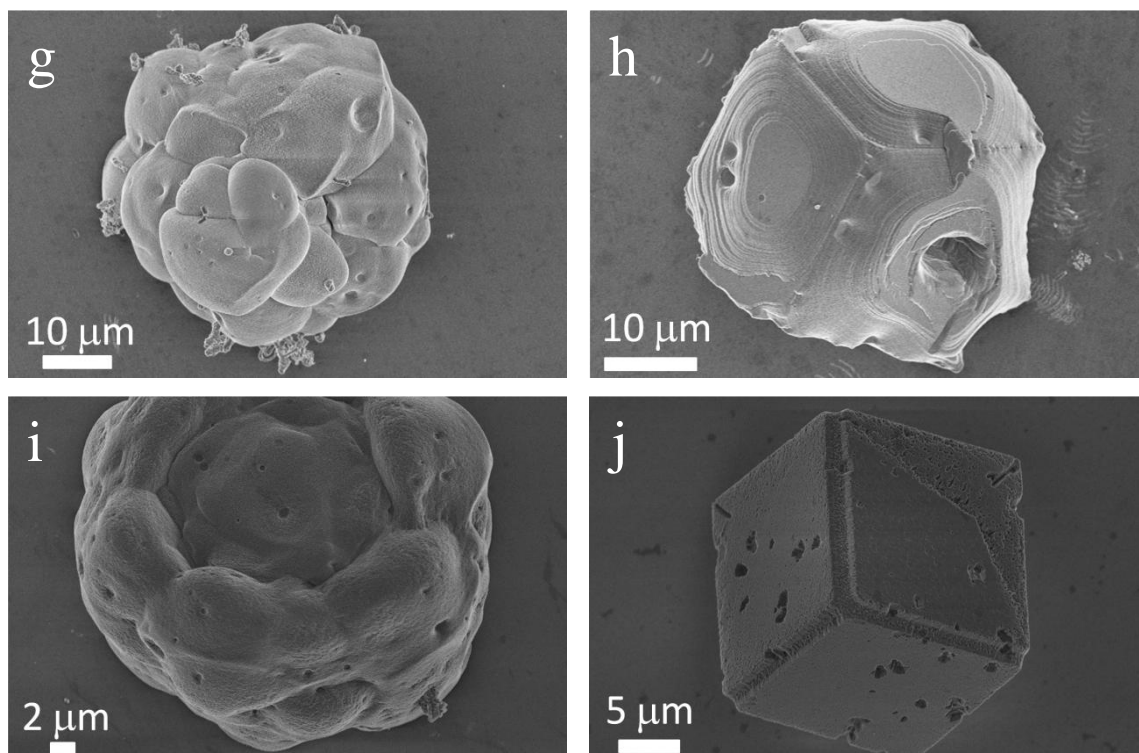
Figure 23: CaCO$_3$ particles precipitated in the presence of PAH at [CaCl$_2$] = 1.5 mM and [PAH] = 4 g/L (a, b,), 0.5 g/L (c, d), 0.01 mg/mL (e, f), 0.005 mg/mL (g, h,), 0.001 mg/mL (i) and 0.0005 mg/mL (j) after 6 days reaction time.

4.4.3 General film formation mechanism

The results of the previous experiments were rather surprising, especially given that most positively charged organic additives exert little influence on calcium carbonate precipitation[344,345]. To understand the formation mechanism of the films better, we investigated the early stages of precipitation process of calcium carbonate in the presence of PAH using a range of methods.

4.4.3.1 Indications of a phase separation mechanism: Optical microscopy and SEM.

PAH is known to undergo a microphase separation in the presence of carbonate ions (and also in the presence of other anions[354]) due to the formation and co-existence of R-NHCO$_2^-$ and R-NH$_3^+$ groups in the pH range of 7.4 to 10[355]. Since at the working pH of our experiments (9.5), the amine groups on the PAH molecule are expected to be 50% protonated[356], a microphase separation should occur, which was also confirmed here visually, even in the presence of Ca^{2+} cations in the reaction solution. This phase

separation started at the top of the solution and gradually penetrated into the solution. By the use of optical microscopy it was possible to distinguish the formation of droplets at early reaction times of 3 h, which were seen to condense together later on, providing some evidence for liquid-like behaviour (Figure 24).
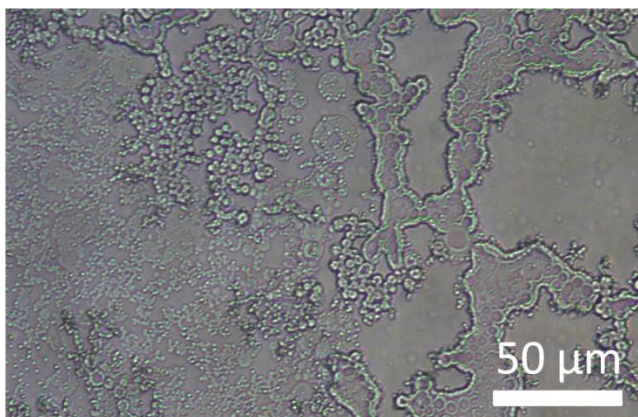
Figure 24: Optical microscope image of material formed in a solution of composition $[CaCl_2]$ = 10 mM and [PAH] = 1 mg/mL after exposure to ammonium carbonate vapour for 3h.

To investigate this further, glass substrates were placed in solution for 6 h to investigate the formation of the various morphologies on the glass slides. Analysis with optical microscopy showed large patches of amorphous films were formed (Figure 25a). These crystallised after heating in an oven to 400°C (Figure 25b). Looking at these glass slides with FEGSEM revealed that in addition to large big amorphous patches, assemblies of small spherical particles were also found on the surface (Figure 25c, d). These seemed to coalesce into films, indicating they might be highly hydrated and can exhibit some liquid-like behaviour.
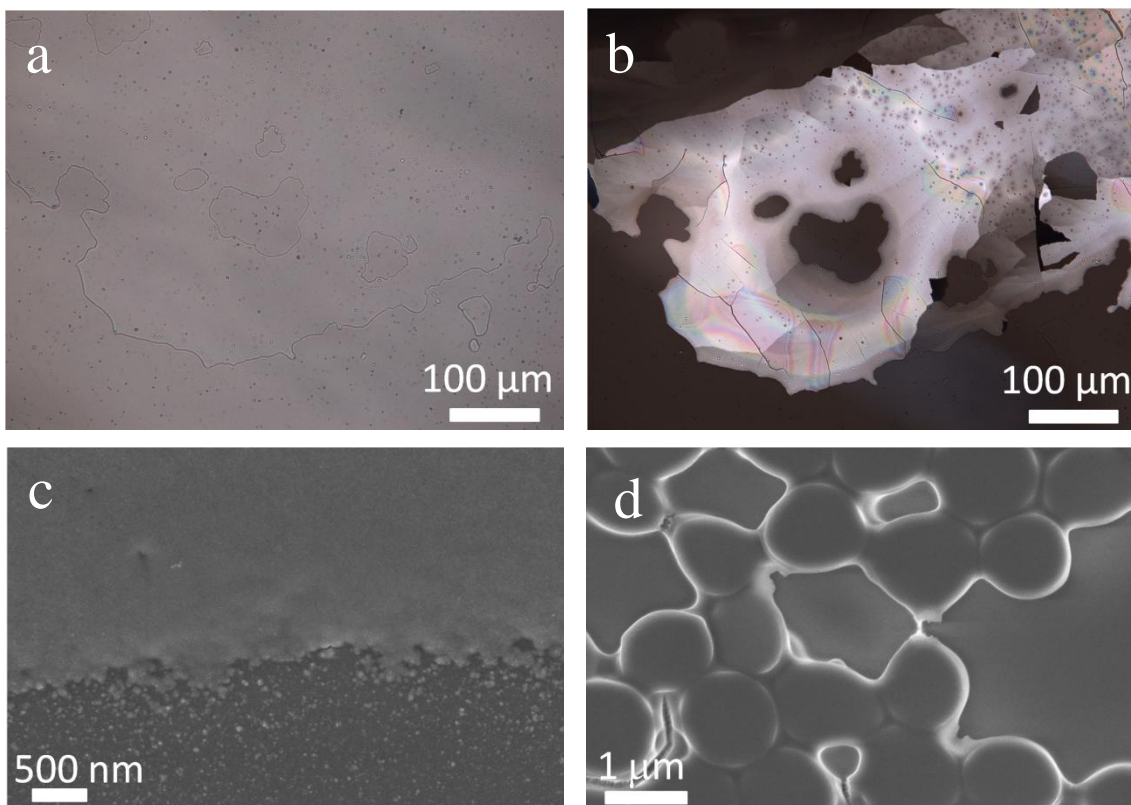
Figure 25: Optical microscope (a, b) and FEGSEM images (c, d) of amorphous (a, c, d) CaCO$_3$ films precipitated in the presence of PAH at [CaCl$_2$] = 10 mM and [PAH] = 1 mg/mL after 6 h. Figure (b) shows an optical image of (a) under crossed polarisers after heating to 600° C, indicating that the amorphous film had crystallised.

It was further observed that the starting solutions of Ca^{2+} and PAH became turbid both on diffusion of ammonium carbonate vapour into a Ca^{2+}/PAH solution, but also stayed turbid when Ca^{2+} ions were slowly added to a Na$_2$CO$_3$/PAH solution by the use of a pump system (Figure 4).

This experiment was set up to avoid the buffering activity of the ammonia in the ammonia diffusion method with final pH of 9.5. Therefore a 20 mM Na$_2$CO$_3$ solution containing 1 mg/mL PAH (pH 11), was slowly mixed with 20 mM CaCl$_2$ (pH 6.3) by dropwise addition of the solution, to give final concentrations of 10 mM Na$_2$CO$_3$, 0.5 mg/mL PAH and 10 mM CaCl$_2$. The initial pH of the solutions was varied from 4 to 12 to investigate the effect of pH and therefore the charge of the NH$_2$ group on the PAH molecule.

When the final solution pH was 9.3 (Figure 26a, b), similar morphologies as with the ammonia diffusion method were obtained and thick films were deposited from a cloudy

solution. In some cases small fibers growing out of spherical particles were also observed (Figure 26b).
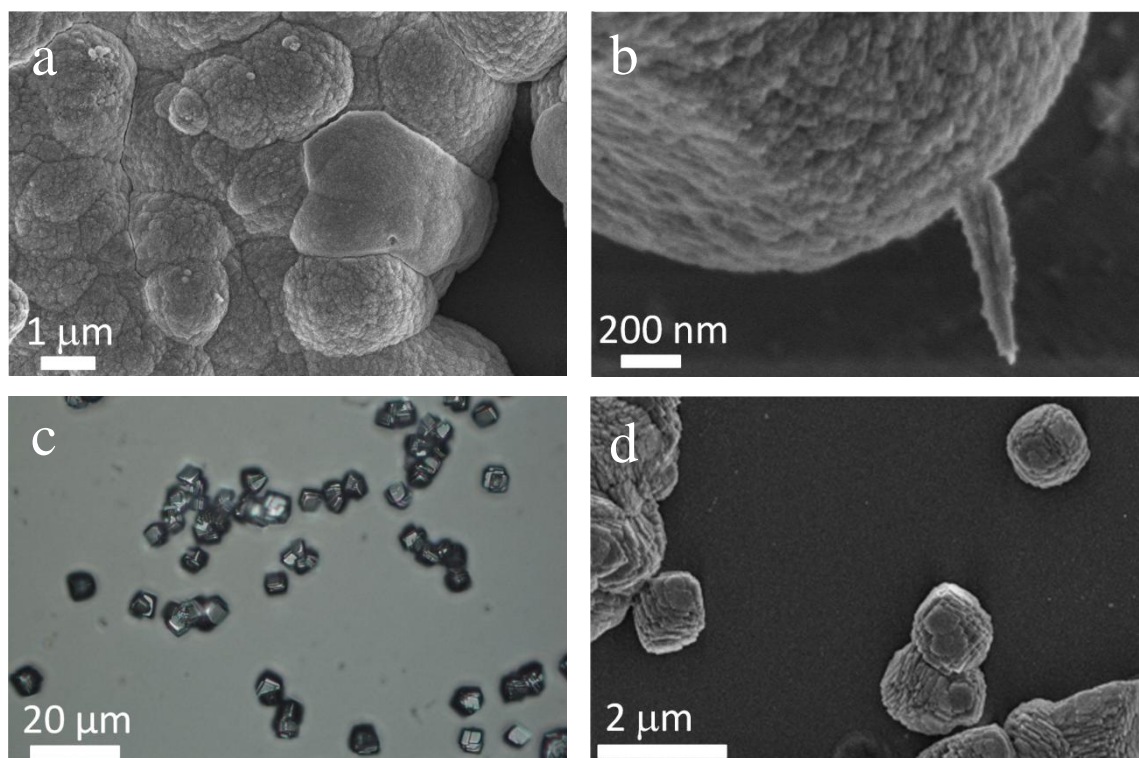
Figure 26: FEGSEM (a, b, d) and optical microscope image (c) of calcium carbonate crystals obtained on drop-wise addition of a 20 mM $CaCl_2$ solution to a solution containing 20 mM Na_2CO_3 and 1 mg/mL PAH. (a, b) The starting pH of the $CaCl_2$ was ≈ 6.3 and $Na_2CO_3 \approx 11.3$ to give a final pH of 9.36 after 1 h reaction time. Thick film patches and spherical particles were formed from which fibers grew. In the case of (c) and (d) the starting pH of both solutions was ≈ 12.5 while the final pH was ≈ 12.2 after 1 h 15 min reaction time. Only distorted calcite crystals were observed under these conditions.

When the same experiment was repeated, but this time with the initial and final pH values of the solution ≈ 12, only distorted calcite crystals were obtained (Figure 26c and d). In this case, no phase separation occurred due to the deprotonated amine group

4.4.3.2 TGA, Raman and IR analysis of the phase separation

In order to rule out that the solutions comprising $Ca^{2+}/PAH/CO_3^{2-}$ became visibly cloudy simply due to the precipitation of $CaCO_3$, thermogravimetric analysis (TGA), Raman investigations and IR of the precipitates formed at early reaction times were

carried out. These strongly supported the model of phase separation. Figure 27 shows the Raman spectrum of a precipitate obtained from exposure of a solution of composition $[CaCl_2] = 10$ mM and $[PAH] = 1$ mg/mL to ammonium carbonate vapour for 3 h, which was compared with that of the PAH molecule alone, and of a polycrystalline calcite film generated under the same reaction conditions after 1 day. The Raman spectrum of the precursor PAH/$CaCO_3$ (Figure 27B) species showed broad peaks at 1084 cm^{-1} (v_1, internal CO_3^{2-} symmetric stretch mode), 720 cm^{-1} (v_4, CO_3^{2-} symmetric bending mode) and 158 cm^{-1} (translational lattice mode) which can clearly be attributed to ACC[350], while peaks at 830 cm^{-1} (Cl-NH$_2$ stretch mode) and 1165 cm^{-1} (C=C bending mode) corresponded to the PAH molecules[355, 357] (Figure 27C).
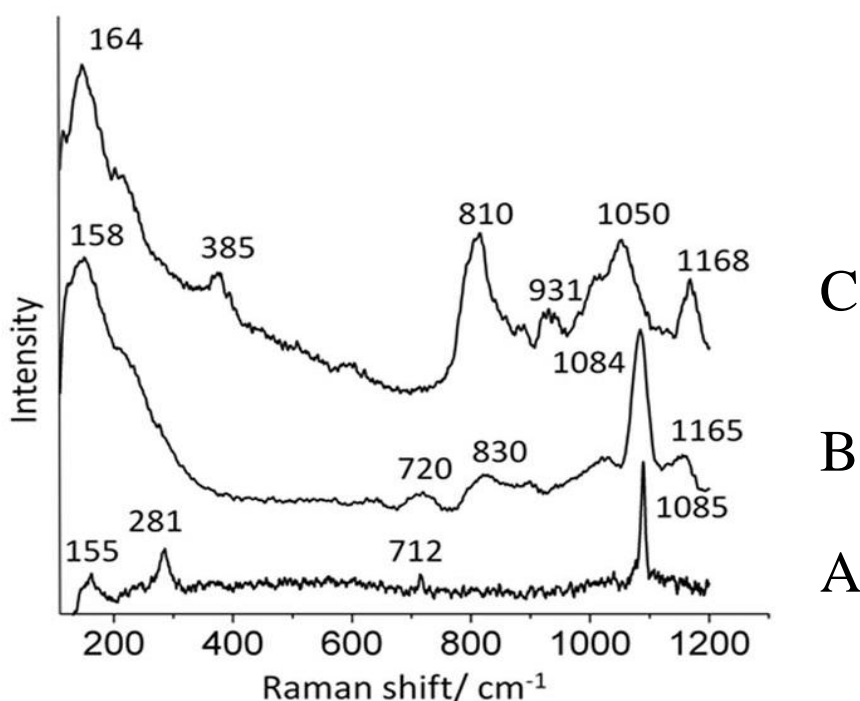
Figure 27: Raman spectra of (A) a polycrystalline calcite film, (B) precipitate obtained from exposure of a solution of composition $[CaCl_2] = 10$ mM and $[PAH] = 1$ mg/mL to ammonium carbonate vapour for 3 h and (C) PAH.

With IR (Figure 28) a similar result was obtained where the bands around 1500–1600 cm^{-1} originate from the so-called amide II of the PAH molecule and are attributed mainly to the distortion oscillations of N-H and the stretching oscillations of C–N in the carbamate. The band around 1300 cm^{-1} is called the amide III band and is attributed to the carbamate[358]. An N-stretching band from the PAH molecule at 814 cm^{-1} can be seen

in both curves. The precipitate from the reaction solution show two extra peaks at 1393 cm^{-1} and 862 cm^{-1} originating from the CO_3 asymmetric stretch and the CO_3 out-of-plane bend of amorphous calcium carbonate respectively[330] (Figure 28A). The PAH peaks are also shifted to higher wavenumbers from 1552 cm^{-1} to 1567 cm^{-1} and from 1479 cm^{-1} to 1484 cm^{-1}.
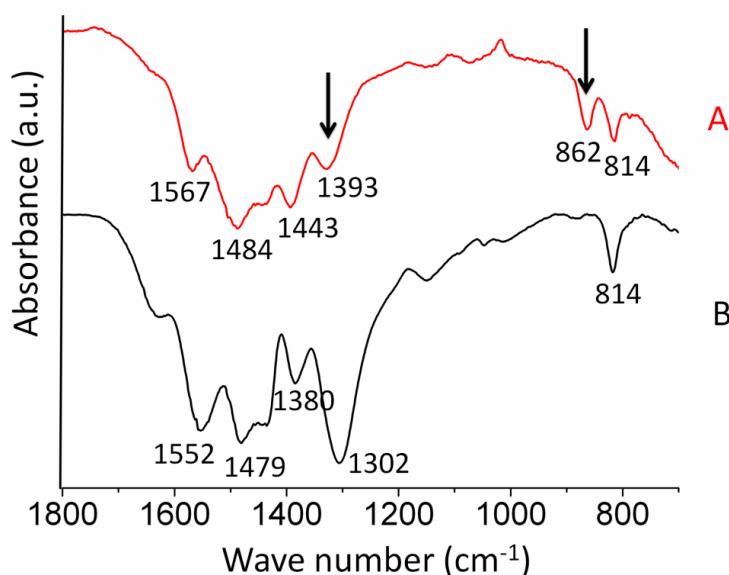
Figure 28: Spectra of (A) precipitate from solution of $[CaCl_2]$ = 10 mM, [PAH] = 1 mg/mL after 3 hour reaction (pH 8.8) (B) PAH control. The precipitate show two extra peaks at 1393 and 862 originating from ACC.

Further investigation of the composition of this phase was carried out using TGA which revealed that the early stage precipitates contained 20.68 wt% water, 37.80 wt% PAH and 41.52 wt% $CaCO_3$ (Figure 29). The 20.68 % loss in weight which is seen up to 200 °C was attributed to the loss of water and further dehydration, while the subsequent 37.80 % weight loss lasting till about 600 °C was attributed to the degradation of the PAH molecules. The complexation of the polymer delays the thermal decomposition up to 600 °C (thermal decomposition of PAH occurs only before 450 °C). Finally, above ≈ 650 °C, the characteristic decomposition of calcium carbonate (18.36 % weight loss) to calcium oxide (23.16 wt%) can be seen.
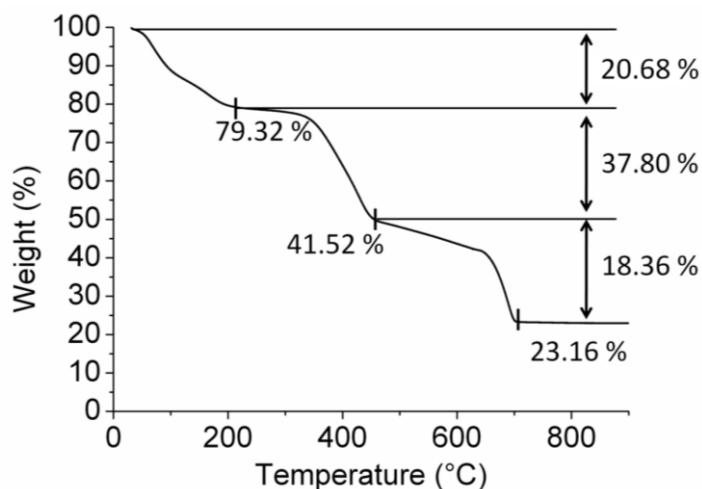
Figure 29: TGA data of material obtained after 3 h at Ca = [10 mM], [PAH] = 1 mg/mL.

Comparison with precipitates formed in the PAH/ carbonate system alone, shows that these comprise 37.10 wt% water and is therefore more hydrated than the precipitates from the PAH/CaCO$_3$ system (Figure 30A). The decomposition profile of pure PAH was also investigated (Figure 30B), which proved that the PAH polymer can be stabilised in the presence of carbonate/calcium ions, as can be seen by an increase in the decomposition temperature from $\approx 250\ ^oC$ to $\approx 450\ ^oC$.
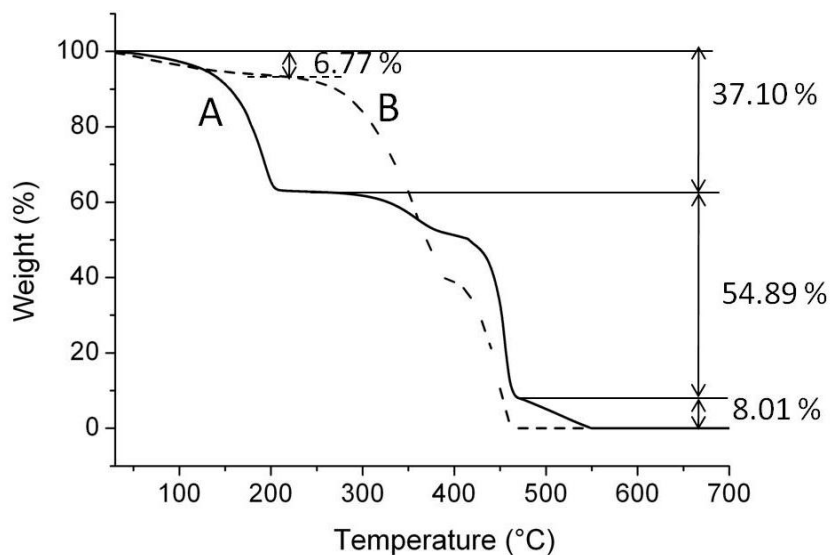
Figure 30: Thermogravimetric analysis (TGA) data of (A) a precipitate obtained from a solution of composition $[CO_3^{2-}]$ = 10 mM and [PAH] = 1 mg/mL and (B) pure PAH.

4.4.3.3 Conclusive results by Cryo-TEM

Cryo-TEM was used to investigate the formation mechanism of the PAH-CaCO$_3$ phase at early stages without having to dry out the sample. A 30 min sample (Figure 31a, b)

showed the presence of small particles, only a few nm in size (50 nm-100 nm), which were prone to radiation damage. These developed voids in their structure and faded away upon exposure to an electron dose of 400-1200 electrons/ $Å^2$, indicating that these particles were hydrated and contained high amounts of organic material. Proof that this wasn't ice originating from the vitrification process is shown in Figure 32 where ice-particles are shown which disappear and are not damaged by the electron beam. After 3 hours (Figure 31c and d), round structures with sizes ranging from 300 nm to 1 μm were observed, which were again sensitive to the electron beam. Low-dose selected-area electron diffraction (LDSAED) showed that these calcium carbonate structures are amorphous (Figure 31c, inset), while high resolution Cryo-TEM suggested that they might comprise clusters 1 nm in size (Figure 31d, inset red circles). The morphology of the material suggested that it shows liquid-like behaviour, particularly where several of these structures seemed to have merged together prior to freezing of the sample, like droplets coalescing (Figure 31e). After 6 h, structures of over 10 μm in diameter were found which were still amorphous, as shown by LDSAED. These structures were often composed of a denser core surrounded by a more diffuse material, covering the TEM grid like a film (Figure 31f). Similar structures were found after 20 h, but at this stage most of the material was no longer amorphous, but had already transformed into calcite, as seen by LDSAED (Figure 31g, inset). In addition, smaller particles of 500 nm in size were also present, where prolonged exposure to the electron beam induced the transformation of ACC into calcite (Figure 31h).
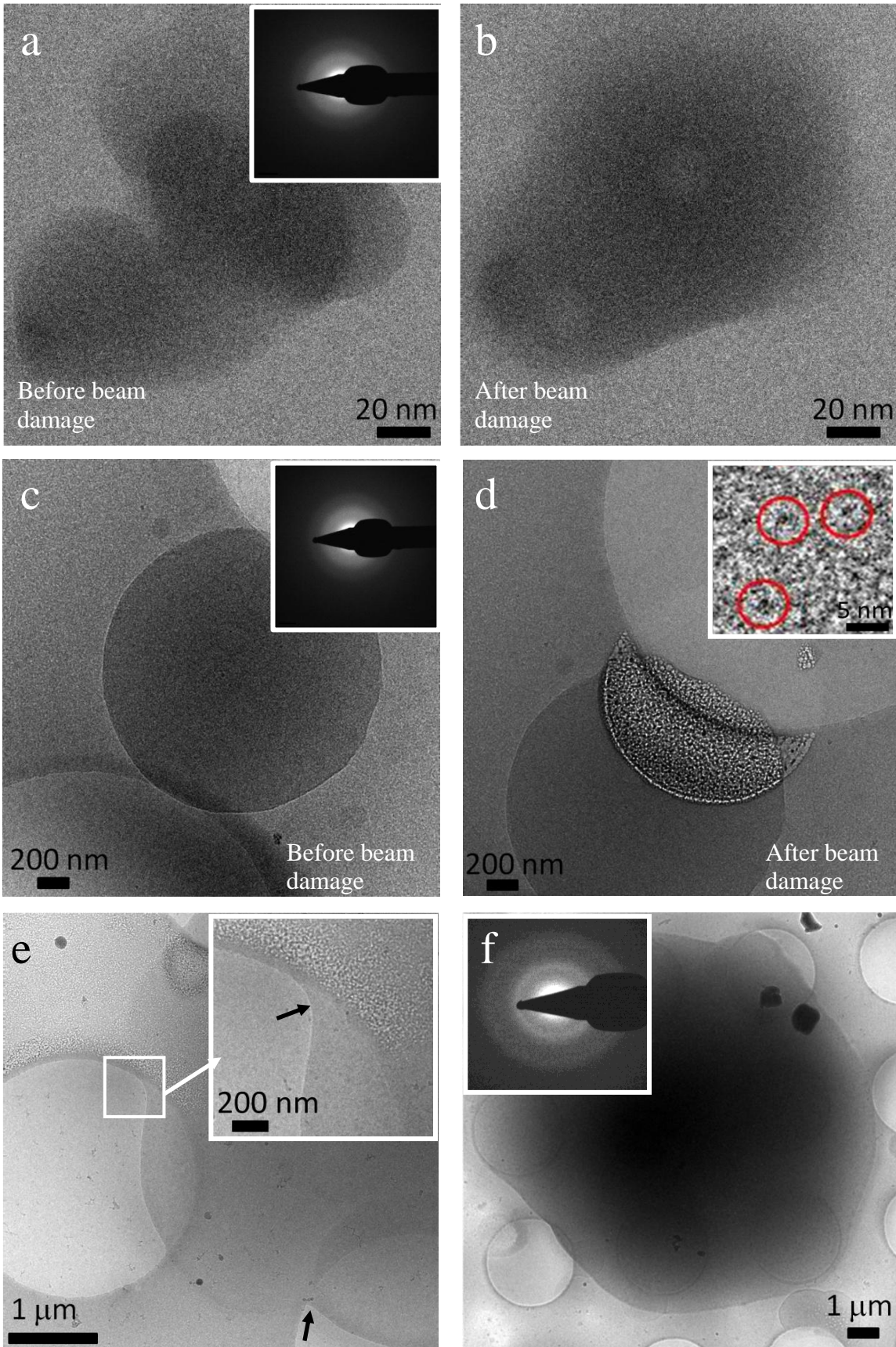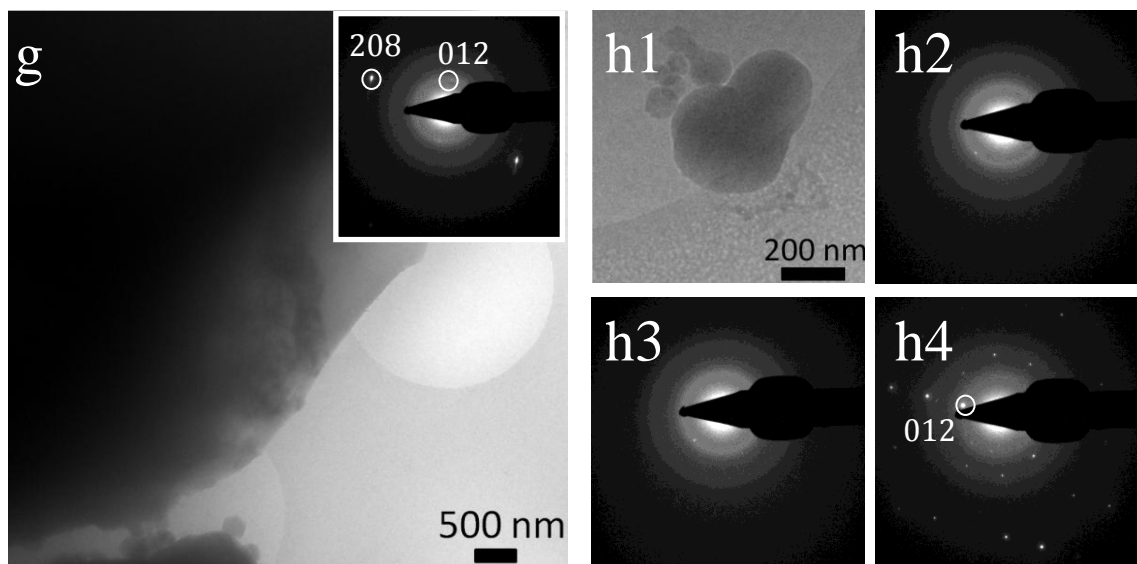
Figure 31: Cryo-TEM images of particles precipitated on a TEM grid with [PAH] = 1 mg/mL after 30 min (a, b), 3 h (c, d, e) 6 h (f), 20 h (g, h). Inset of (d) shows a high resolution image of the area. (e) Shows an image after 3 h, where several droplet-like structures are fusing together (black arrows). The inset shows a high magnification image of the area marked by the square. The insets in (f) and (g) show the corresponding diffraction patterns both corresponding with calcite. (h2, 3, 4) Shows diffraction patterns subsequently taken of the particle in (h1).
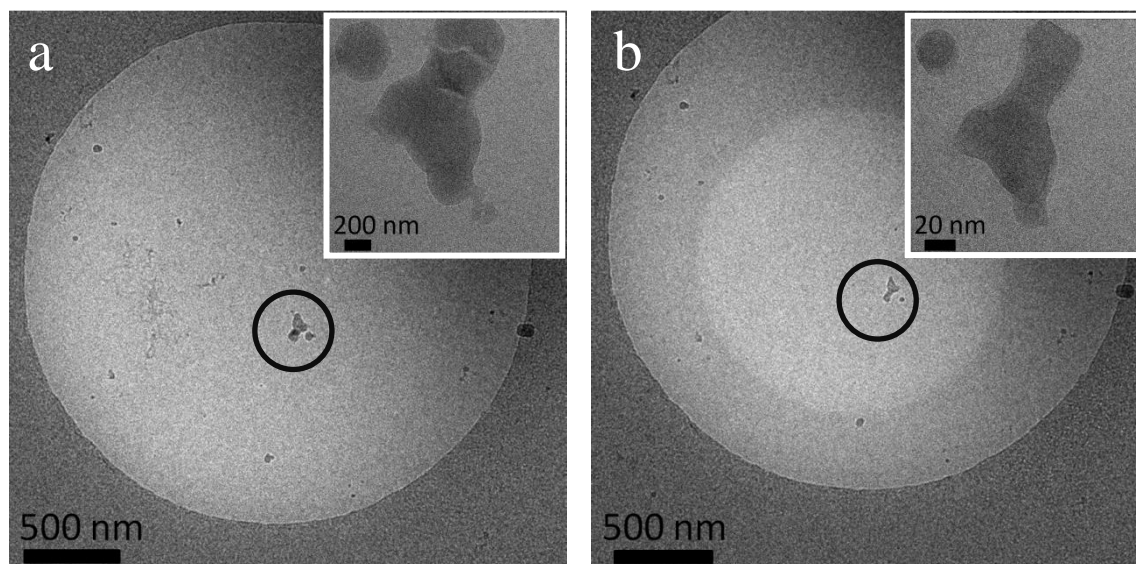
Figure 32: (a) And (b) show low magnification Cryo-TEM images of a typical ice particle contaminant (black circle) before (a) and after (b) prolonged exposure to the electron beam. The inset shows the corresponding high magnification images.

In order to confirm these results, control experiments were carried out in the absence of Ca^{2+} or CO_3^{2-}. In control experiments containing solutions of PAH, or PAH with $CaCl_2$, only diffuse structures with sizes of about 20 nm to 50 nm were present (Figure 33a and d). These quickly faded away and disappeared upon exposure to the electron beam.
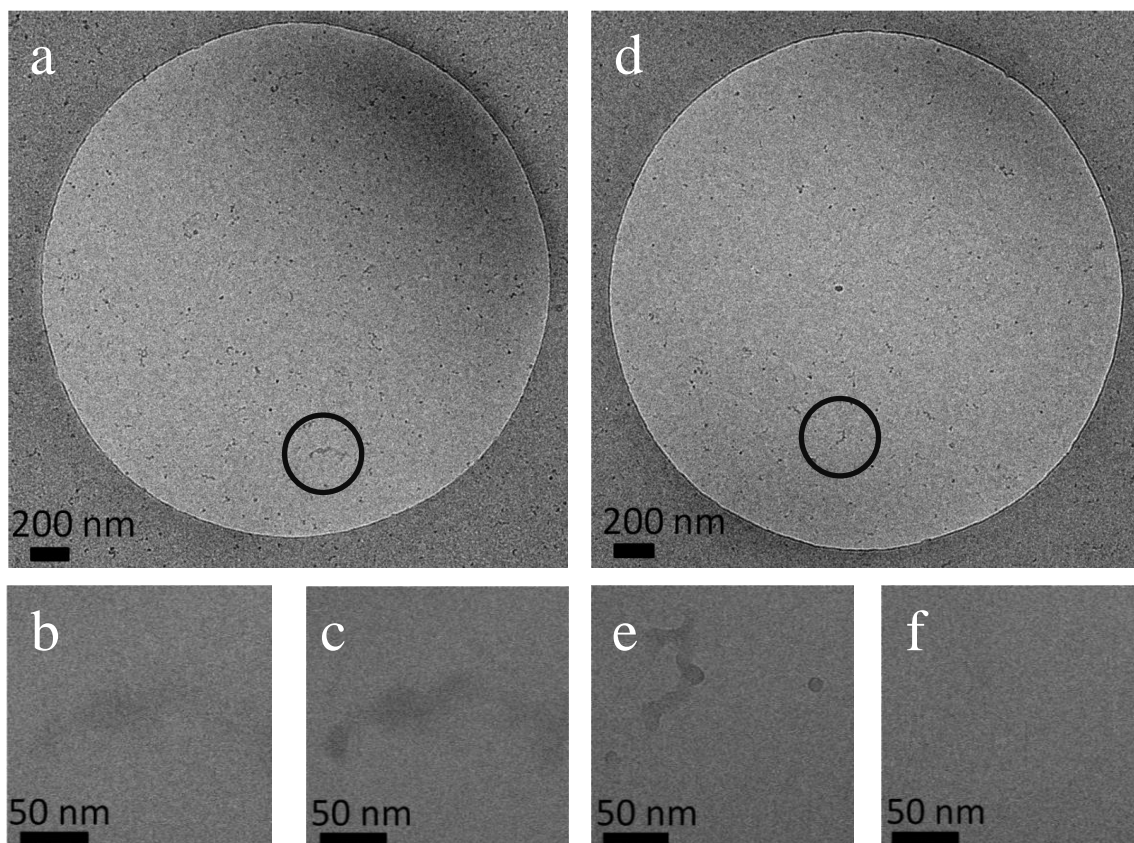
Figure 33: (a) Cryo-TEM image of a solution containing only PAH. Only 20-50 nm diffuse structures are present. (b, c) Show the high magnification images of the area marked by the black circle, indicating that the particles quickly fade away upon exposure to the electron beam. (d) Shows Cryo-TEM image of PAH + $CaCl_2$. Only diffuse structures of 20 nm -50 nm could be found. (e, f) Show again the high magnification images of the area inside the black circle

In contrast, Cryo-TEM image of PAH and Na_2CO_3, showed that the polymer phase-separates in the presence of carbonate, forming droplet-like structures $1 - 2$ μm in size, covering the grid with a network-like structure (Figure 34). These structures were also prone to radiation damage by the electron beam (Figure 34c).
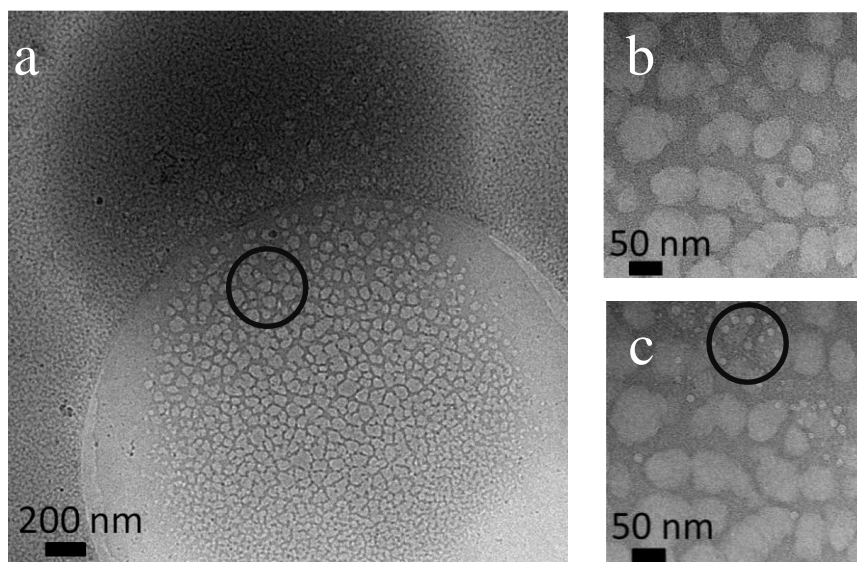
Figure 34: (a) Shows a Cryo-TEM image of PAH + Na_2CO_3, demonstrating that in this case the polymer has the ability to phase-separate in the presence of carbonate. (b, c) Show some high magnification images of the area marked by the black circle in (a). The black circle in (c) marks an area with electron beam-induced radiation damage

4.4.3.4 Supportive experiments by DLS and Zeta potential measurements

By DLS, particles were measured after 30 min with sizes of 20 to 150 nm corresponding with the Cryo-TEM observations. After 3 h bigger particles with sizes of 1-2 μm were formed (Figure 35).
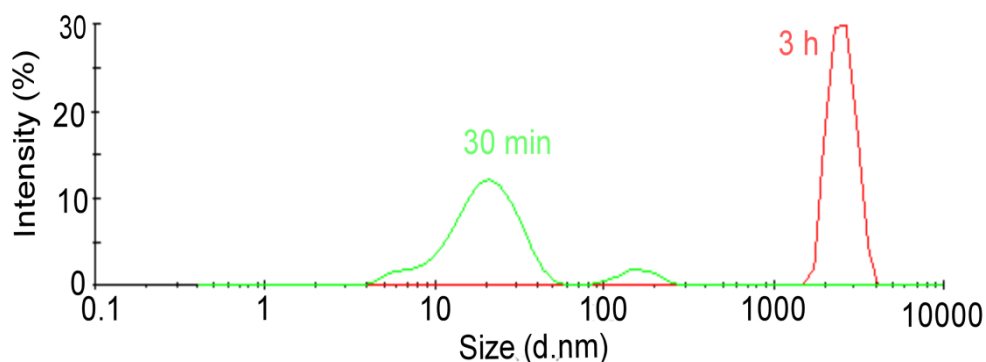
Figure 35: Mean hydrodynamic diameter by DLS measurements of samples taken from a reaction solution ([$CaCl_2$] = 10 mM, [PAH] = 1 mg/mL) obtained after 30 minutes (green curve) and 3 hours (red curve). Two peaks are seen after 30 minutes (one at 20 nm and one at 150 nm), and one after 3 hours at 2500 nm.

Zeta potential measurements (Figure 36) gave a positive potential of 12 indicating that the droplets are electrostatically stabilized by an outer excess layer of adsorbed PAH in accordance with previous research[93].
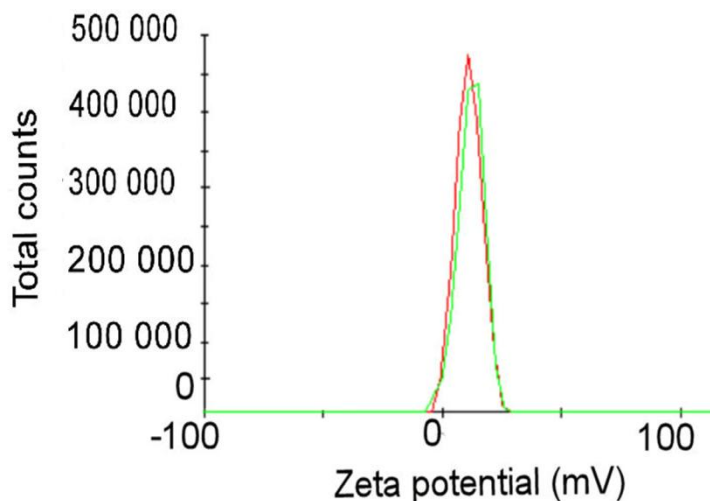
Figure 36: Zeta potential measurement of droplets taken from a reaction solution ($[CaCl_2]$ = 10 mM, [PAH] = 1 mg/mL) formed after 3 hours reaction time. The results from two repeated experiments are shown

These data demonstrated the construction of films by the formation of an initial amorphous PAH/calcium/carbonate phase which grows to micron sizes after a couple of hours. This phase is highly hydrated and exhibits liquid-like character, allowing the particles to coalescence and form film-like structures. With time this amorphous calcium carbonate phase crystallises to form crystalline domains.

4.4.3.5 Liquid-like characteristics of PAH/calcium/carbonate phase.

Given the similarities between the stabilisation of ACC by polyacrylic acids in the PILP (polymer-induced liquid-precursor) phase, and the results obtained with PAH, experiments were carried out to investigate if liquid-like properties such as pore infiltration could also be observed in the PAH system[29] . Similar experiments were therefore performed as with CaP (see chapter 3), where $CaCO_3$ was precipitated in the pores of track-etched membranes by immersion of a membrane in the $CaCO_3$/PAH reaction solution. Isolation of the material obtained in the pores showed that these were filled with material, which crystallised to rod-shaped single crystals of calcite (Figure 37). The rods were 5 to 10 μm long, almost all were single crystals, but no preferred

orientation of the rods was found. This again demonstrated, liquid-like properties such as capillary action and pore infiltration could be characterised to the CaCO₃/PAH system
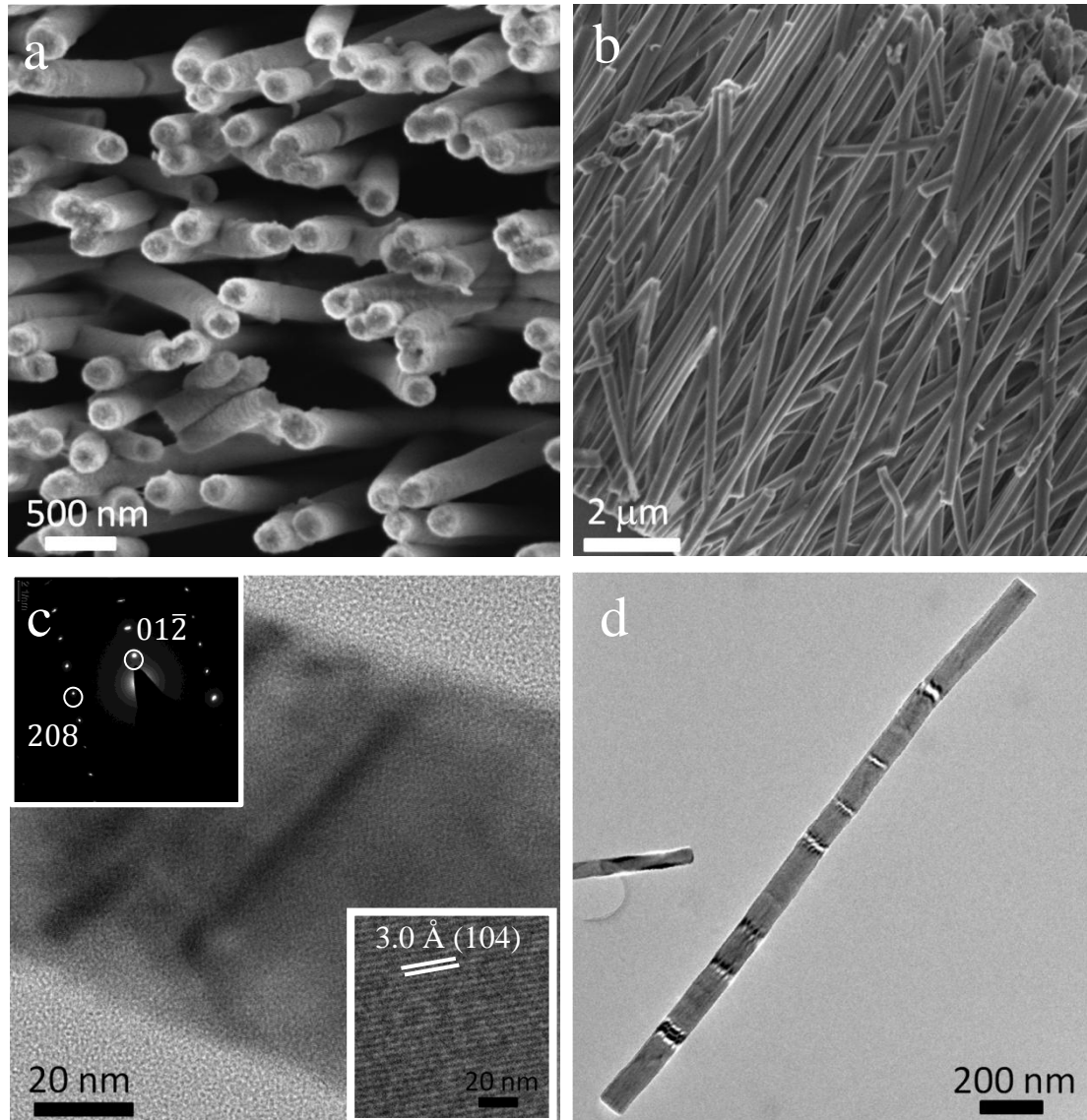
Figure 37: FEGSEM image (a) and TEM images (b, c, d) of CaCO$_3$ rods formed inside track-etched membrane pores of 50 nm after addition of 1 mg/mL PAH in a 10 mM CaCl$_2$ solution. The diffraction pattern corresponds to calcite. The inset in (c) shows a high resolution image of the lattice fridges corresponding to the {104} plane.

Repeating this experiment with PAH for calcium phosphate gave similar results as discussed in Chapter 3 (no improvement of infiltration by addition of polymer), contributing to the theory that no PILP phase exists for calcium phosphate.

4.4.4 Formation mechanism of fibers.

Experiments were performed to investigate the mechanism of fiber formation. Therefore, the fiber samples were exposed to bleach to attempt to selectively remove the polymer component (Figure 38b, c, d), hoping that this would provide more information about the fiber formation process. The bleaching principally resulted in a smoothing of the fibers (compare Figure 38a and b) and the small building blocks of the fibers also became much more visible. Some of the bleached fibers also showed a porous structure (Figure 38c and d) demonstrating a considerable loss of the polymer from inside the fibers (white circles in Figure 38d).
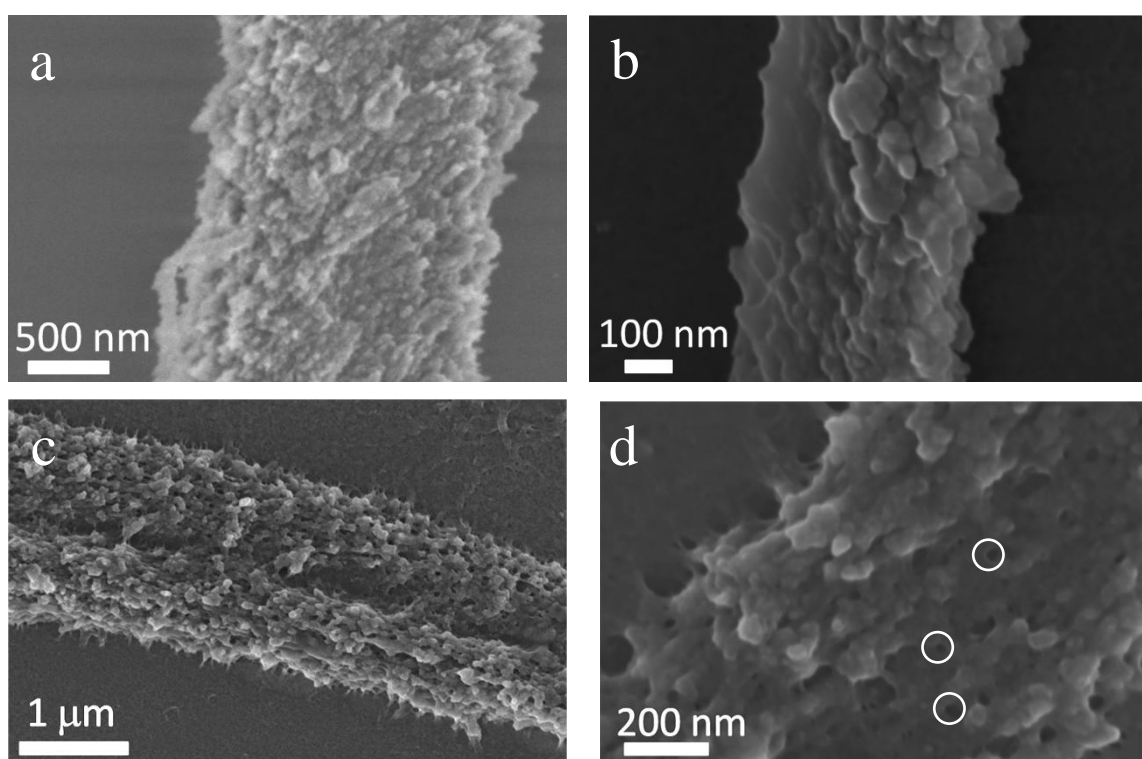
Figure 38: SEM images of $CaCO_3$ fibers precipitated in the presence of PAH at $[CaCl_2]$ = 1.5 mM and [PAH] = 0.5 mg/mL after reaction times of 6 days (a) and bleaching for 1 day (b, c, d). Bleaching resulted in a smoothing of the fiber surface (b) and appearance of a porous-like structure (c, d white circles).

To investigate the formation of the fibers with time, Ni grids were placed in a $CaCl_2$ solution to allow the fiber formation to occur on the TEM grids. The grids were taken out of the solution at different time points (3h, 6h, 8h, 12h, 24h). After 8 h (Figure 39a) the whole grid was covered with an amorphous film which had started to crystallise at

some positions. After 12 h, extrusions were observed from the crystalline film (Figure 39b arrowed) and after 14 h these had evolved into small fibers (Figure 39c arrowed). After 24 h, the fibers had grown into hundreds of nanometers (Figure 39d). These results therefore suggested that film formation proceeds fiber formation. Fibers form from the crystallised films and then grow longer and longer out of the film by addition of crystalline particles.
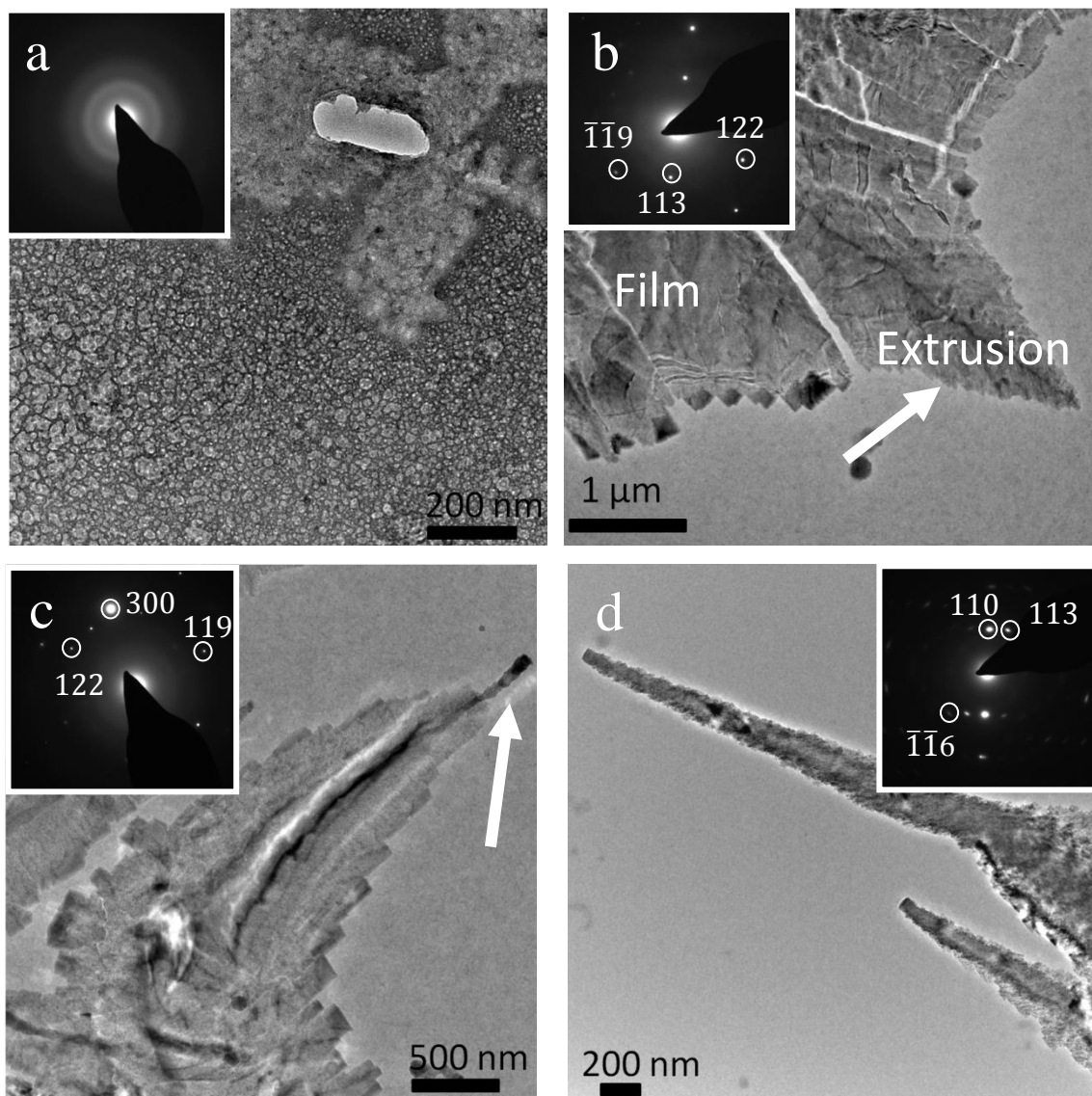
Figure 39: TEM images with corresponding diffraction patterns of $CaCO_3$ films and fibers precipitated on a Ni TEM grid from 10 mM $CaCl_2$ solutions containing 1 mg/mL PAH after (a) 8 h, (b) 12 h, (c) 14 h and (d) 24 h. The corresponding diffraction patterns all correspond to calcite.

TEM imaging enabled investigation of how the orientation of the fibers changed, with different growth directions (Figure 40). Surprisingly, the crystallographic orientation stayed the same along the different growth directions of the fibers. Figure 40a shows a TEM image of a fiber abruptly changing direction with diffraction patterns taken along the fiber.
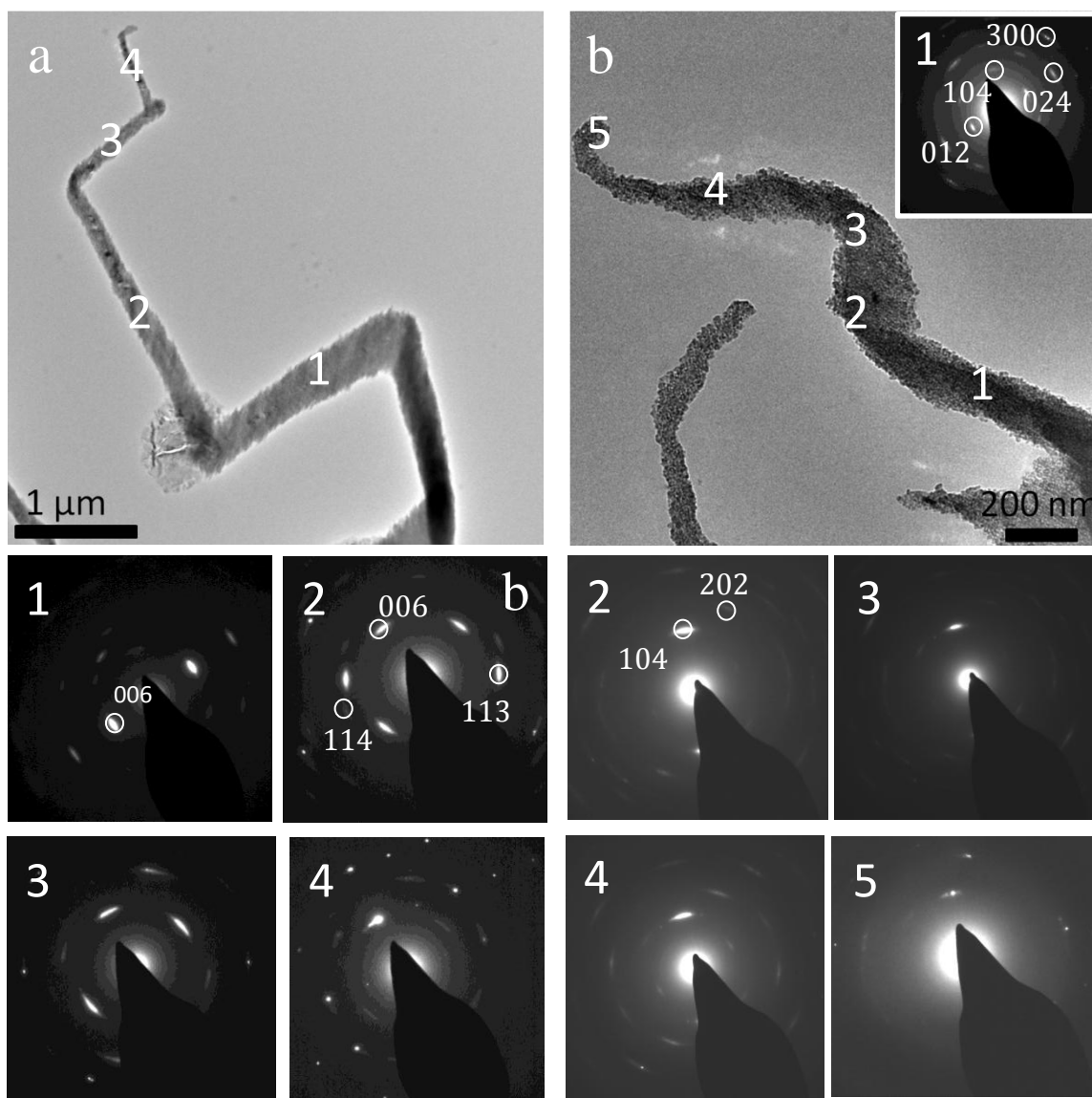
Figure 40: TEM images with corresponding diffraction patterns of calcite fibers precipitated on a Ni TEM grid from 10 mM $CaCl_2$ solutions containing 1 mg/mL PAH after 1 day. (a) Shows an image of a fiber, changing direction abruptly, (b) shows an image of a curly fiber. Diffraction patterns were taken along the fibers demonstrating little change in crystallographic orientation along the fiber

Interestingly, it can be seen the diffraction patterns are all very similar, and have a strong reflection of the (006) plane at similar positions. Notably though, there is a small shift for position 2 to 3 which is about 15 degrees clockwise. The same kind of orientation is true for curly fibers (Figure 40b), where the position of the (104) reflection almost stays the same along the whole fiber.

4.4.5 Influence of Mg^{2+} ions on $CaCO_3$ precipitation in presence of PAH

In common with PAsp/PAA PILP, the structure of the films could be further controlled through the addition of Mg^{2+} ions. These are a common component of biogenic $ACC^{[129]}$ and they retard the crystallization of synthetic ACC such that thin films can be formed in the PAsp/PAA PILP system at lower polymer concentrations than in Mg-free solutions[337, 359].

Control experiments were performed in which the influence of Mg^{2+} on $CaCO_3$ precipitation in the absence of PAH was investigated (Figure 41). As expected, polycrystalline calcite crystals with a spherical morphology were formed[129, 132].
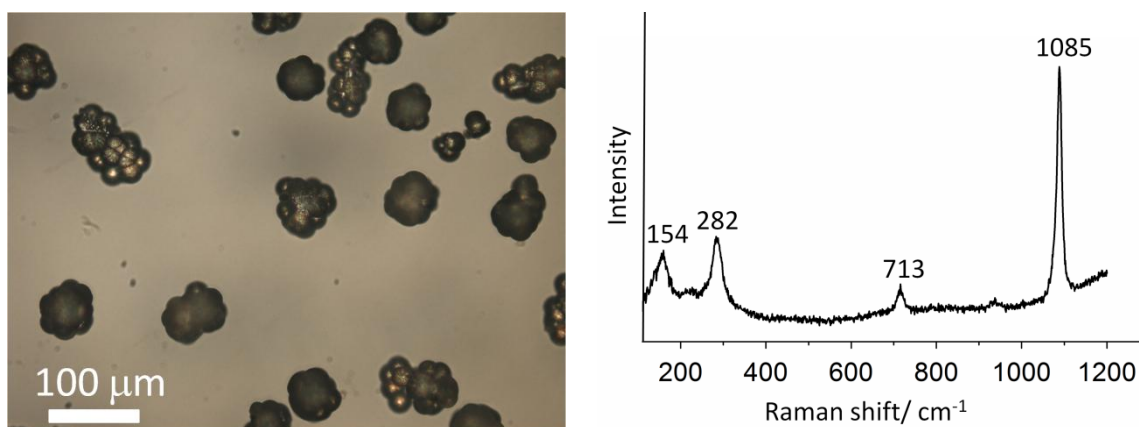
Figure 41: Optical microscope image (a) and Raman (b) of polycrystalline calcite particles precipitated from a solution containing 10 mM $CaCl_2$, 10 mM $MgCl_2$ after 1 day.

Addition of Mg^{2+} at a 10 mM concentration to a 10 mM $CaCl_2$ solution (such that [Ca] = [Mg]) containing 20 µg/mL PAH led to the formation of polycrystalline films (Figure 42 and 43) of $\approx$ 300 nm thick (Figure 43c) which covered the entire glass surface. This is significantly lower than the 0.5 – 1.0 mg/mL PAH required in the absence of Mg (Figure 13). No areas with single crystal domains were observed, nor the formation of

fibers. After 3 days only 30% of the film (as judged by area) was crystalline (Figure 42a) while after 14 days in the solution the whole glass slide was covered with crystalline film (Figure 42b). Raman analysis showed that the crystalline films were calcite (Figure 42c). By increasing the Mg^{2+} concentration to 3 times and 5 times more the Ca^{2+} concentration, even lower amounts of 5 µg/mL of PAH were able to produce films. In this case the amorphous phase was stabilised for longer times and more time in solution was necessary for crystallization.
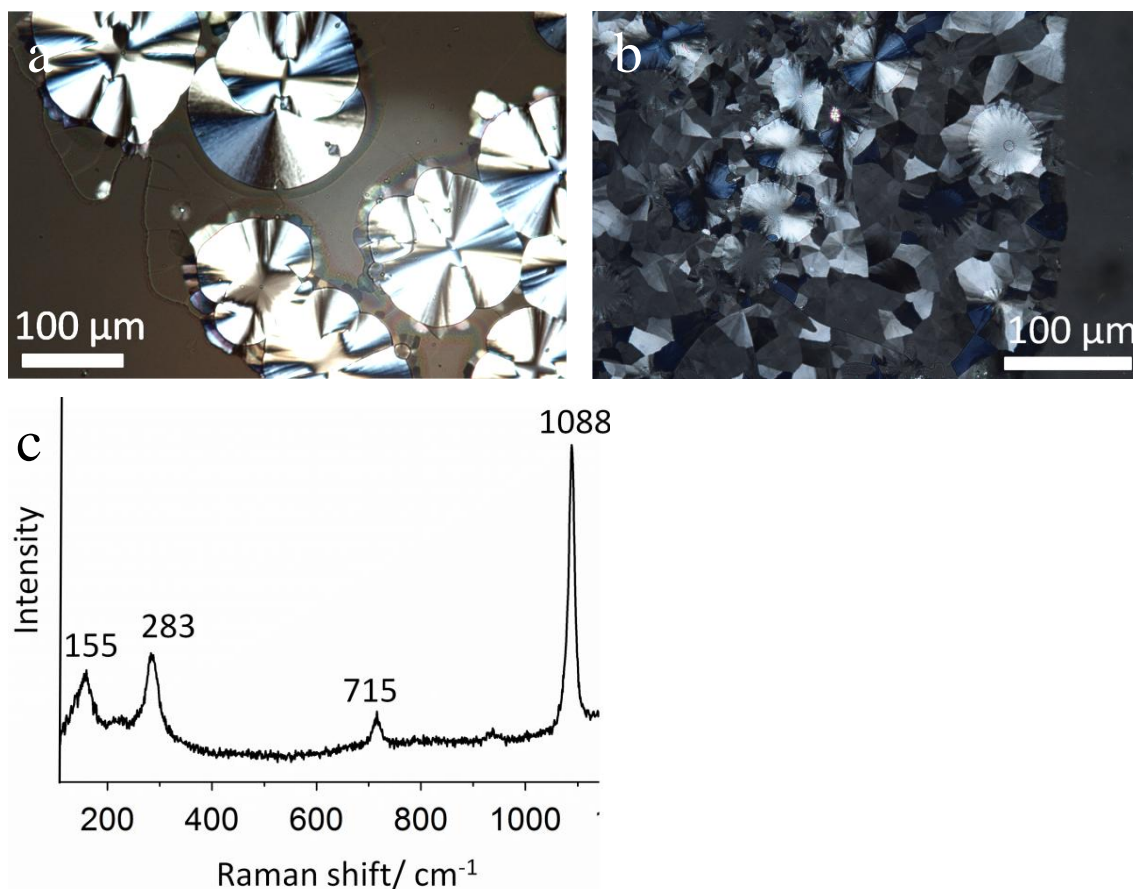
Figure 42: Optical microscope image under crossed polarisers (a, b) and Raman spectrum (c) of polycrystalline calcite thin films precipitated from a solution containing 10 mM $CaCl_2$, 10 mM $MgCl_2$ and 20 µg/mL PAH after 3 days (a) and 14 days (b).

Investigation with FEGSEM showed that the films were much smoother and thinner than those formed with PAH alone (Figure 43a and b and Figure 14). They also varied in density, presumably due to different states of crystallization (Figure 43d). The more porous film is assumed to be crystallised while the more dense is still amorphous. EDX analysis showed that the film contained about 2 atomic weight % of Mg^{2+} (Figure 43b).
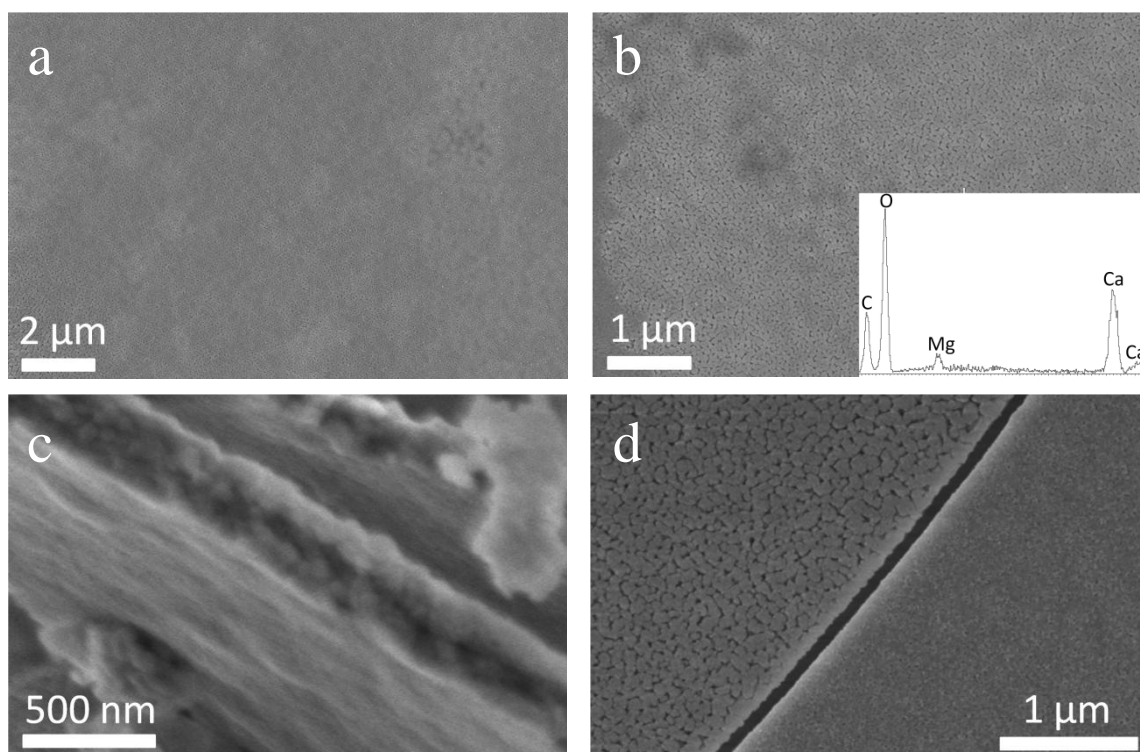
Figure 43: FEGSEM images of films with EDX (b) formed from solutions of composition of 10 mM $CaCl_2$; 10 mM $MgCl_2$ and 20 µg/mL PAH after 2 weeks. The thickness of the film is about 200 nm (c). The porosity of the film varies from area to area as shown in (d).

Investigation of the films with AA and TGA (Figure 44) (10 mM [$CaCl_2$], 10 mM [$MgCl_2$], 20 mg/mL PAH) showed that at early stages (3 h) 2 wt% Mg was present as measured with AA, together with 6.65 wt% of PAH as shown by TGA (Figure 44a). After a weight loss of water of 15.52 wt% till 200 °C, a weight loss of 6.65 wt% is seen between 200 °C and 600 °C which originates from the decomposition of the polymer. At later stages (3 weeks) where almost all of the film had crystallised, 2 wt% Mg was still present, as measured with AA, while only 3.32 wt% of PAH remained (Figure 44b).
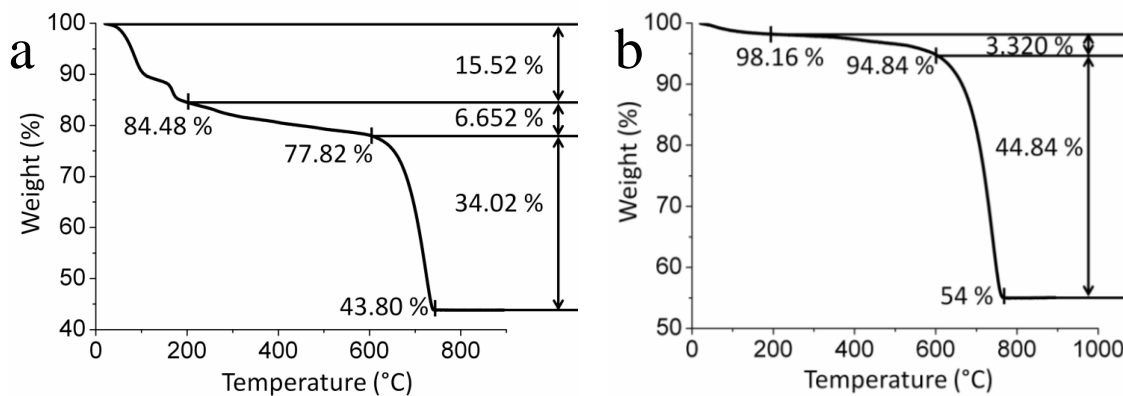
Figure 44: TGA data of precipitate obtained from exposure of a solution of composition 10 mM CaCl$_2$, 10 mM MgCl$_2$ and 20 µg/mL PAH after 3 h (a) and (b) after 3 weeks.

Another interesting observation was that absolutely no fiber formation was observed. However, on lowering the Mg^{2+} and Ca^{2+} from concentrations of 7.5 mM to 1.5 mM, fibers formed again (Figure 45).
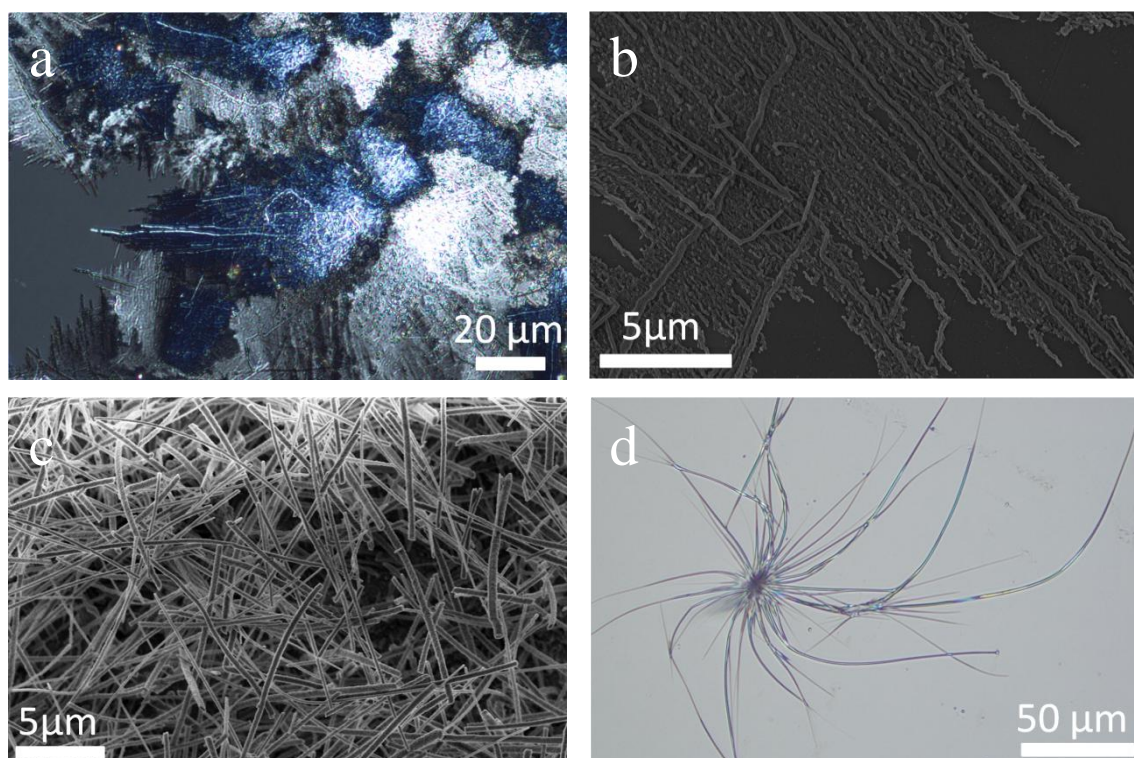
Figure 45: Optical microscope images under crossed polarisers (a and d) and FEGSEM (b and c) images of calcium carbonate fibers precipitated after 3 days from 1.5 mM CaCl$_2$ solutions containing 0.5 mg/mL PAH and 1.5 mM MgCl$_2$ (a, b and c) or 3.5 mM CaCl$_2$ containing 0.02 mg/mL PAH and 3 mM MgCl$_2$ (d).

These fibers had a similar structure to those formed without Mg^{2+} (Figures 18, 19, 20), growing on and from films, micrometers long. Analysis of these fibers with TEM showed they were again calcite but had more a tendency to be a mixture of polycrystalline and single crystal (Figure 46). EDX showed that they contained Mg^{2+}.
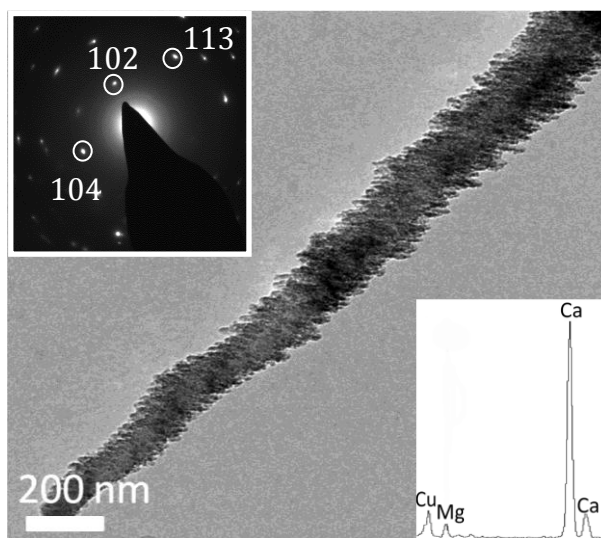
Figure 46: TEM image of a calcite fiber precipitated after 3 days from 1.5 mM $CaCl_2$ solutions containing 0.5 mg/mL PAH and 1.5 mM $MgCl_2$ with corresponding polycrystalline diffraction pattern. The EDX pattern demonstrates the presence of Mg within the fibers.

4.5 Discussion

Although it was previously assumed positively charged additives only had a minor effect on the morphology of calcium carbonate[345], the results stated above clearly contradict this idea. By the addition of the positively charged additive poly(allylamine hydrochloride) (PAH), we have demonstrated it is possible to obtain a strong effect on the crystallization of calcium carbonate, changing its morphology dramatically, forming fibers and crystalline films, proving this is not unique to negatively charged polyelectrolytes.

Given the industrial interest and many applications[4, 67] in producing $CaCO_3$ with different morphologies, it is surprising to see how few studies of additive-directed calcium carbonate growth have been reported before with positively charged additives, as compared with their negatively charged counterparts. A few examples exist where positively charged additives played a role, for example with lysine[319], poly-L-lysine[345, 360] or with a positively-charged 16-residue peptide[361], but these additives always tended

to show relatively minor changes in the morphology. One of the minor effects discovered, however, was that amine side-groups have a tendency to stabilize the vaterite polymorph with respect to calcite[343, 362]. A much stronger effect has been found for aggregates of poly(propylene imine) dendrimers that were modified with octadecylamine and were active in stabilising ACC, a behaviour which was later attributed to their structural rigidity[363]. We therefore question ourselves what was so special about PAH, enabling it to achieve such a massive effect on the morphology, and how can we relate this to formation of $CaCO_3$ in biominerals.

4.5.1 Previous formation of $CaCO_3$ films

Formation of $CaCO_3$ films is not a rare phenomenon. Continuous $CaCO_3$ films have been deposited before under Languir monolayers in coorperation with polyacrylic acid (PAA) as a soluble inhibitor[364]. Later on, monolayers of stearic and arachidic acid were also found to be successful in the formation of $CaCO_3$ films[365, 366]. Depending on the side of the substrate, different surface textures were distinguished where the side facing the monolayer was smooth and featureless, while the side facing the liquid was covered with particles, showing considerable intergrowth. A similar colloidal structure was found on the $CaCO_3$ films formed with PAH as described above, although in this case a difference was seen depending on how deep the glass slide was dipped in the reaction solution. ACC films have also been formed by the addition of the synthetic acid polysaccharide, maleic chitosan[367]. As a construction mechanism, a colloidal nanoparticle self-organisation mechanism was proposed, starting from particles of 10 nm in size, self-organising into larger particles of 2 µm by aggregation, finally leading to the formation of continuous ACC films[367]. Other films have been constructed in Kato's group by combination of soluble acidic polymers[368, 369] or peptide structures[88] with biomimetic polysaccharide substrates such as chitosan. Another interesting result by this group was the fabrication of high purity aragonite thin films, by the addition of Mg^{2+} ions in the presence of an acidic polymer and chitosan[370]. Later on it was found this was also possible without Mg^{2+} by the use of crystalline polyvinyl alcohol (PVA) substrates, where even vaterite films could be deposited[371].

Formation of comparable crystalline films have also been accomplished on addition of negatively charged polyelectrolytes, such as polyaspartic acid (PAsp) and polyacrylic acid (PAA), by the so-called polymer-induced liquid precursor (PILP) process[77] (See

1.2.4.3). In this case the solution underwent a liquid-liquid phase separation process forming PILP droplets. These droplets settled and adsorbed to the substrate after which they coalesced into a film or coating. This initial amorphous film then crystallised into a birefringent film of $CaCO_3$, retaining the shape of the precursor phase[12].

4.5.2 Formation mechanism of CaCO$_3$ films by PAH

Because of the similarities in the results obtained with PAH, with those observed for PAA and PAsp in the crystallization of calcium carbonate[76], a similar mechanism is likely to occur. It is thought that the effect of PAH can be attributed to the fact that it undergoes a microphase separation in the presence of carbonate ions, rather than there being a strong interaction of the amine groups with the growing $CaCO_3$ crystal. PAH solutions have been known before to undergo microscopic phase separation in the presence of sulphate and phosphate ions[354]. Furthermore this was also demonstrated for a Na_2CO_3 solution, where PAH is broken down into colloidal particles of carbamate ions ($R\text{-}NHCOO^-$) and amino ions ($R\text{-}NH_3^+$) in the pH range of 7.5 to 9[355, 358]. These results were confirmed by our own experiments and we have further shown that the positively charged PAH molecules not only sequester the CO_3^{2-} anions forming a complex, but this complex further also associates with the positively charged Ca^{2+} ions, forming a positively charged entity which phase separate out of the aqueous solution. This phase is highly hydrated and exhibits a liquid-like character, allowing the particles to coalesce. Since our measurements show the zeta potential of the particles after 3 h is only about 12, it is not implausible that the particles aggregate together forming a bigger entity. It is expected that these complexes, just as observed for the negatively charged PILP droplets[83], attach preferentially onto pre-existing minerals and materials, in our case especially onto the negatively charged surface of the glass slides. The droplets formed in solution settle and subsequently wet the substrate and spread into a film. With time, this amorphous calcium carbonate phase crystallises, generating crystalline domains. Since the carbonate enters the calcium solution at the gas-liquid interface, this phase separation will occur firstly at the top of the glass slide, as was also observed experimentally. At this point the droplets are still highly amorphous, forming a smooth amorphous film, which crystallises to a single crystal film at the top of the glass slide. Deeper in solution, the droplets might already have started to crystallise before, forming a much rougher, polycrystalline film (Figure 47).
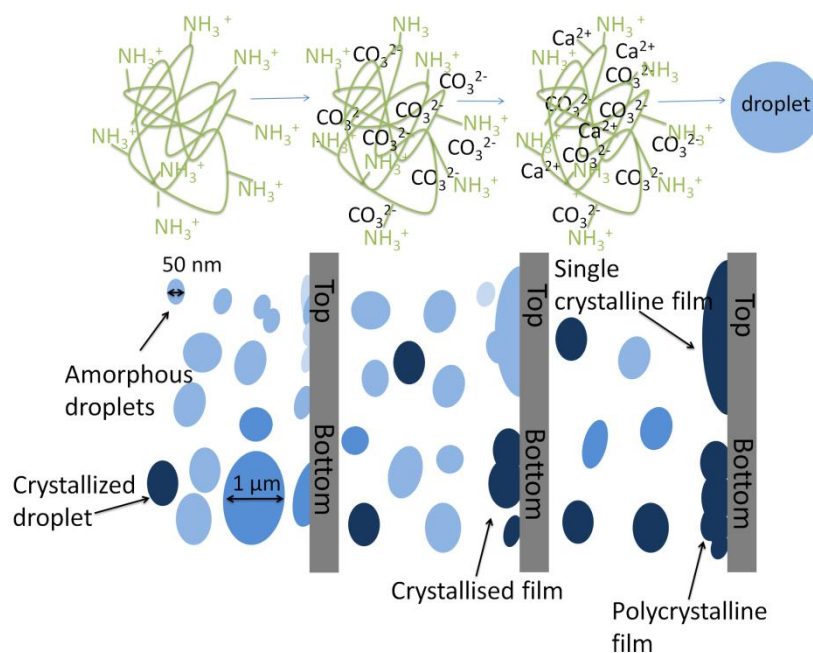
Figure 47: Formation mechanism of PAH/complex and successively crystalline films. At the top of the glass slide single crystal films are formed while at the bottom mostly polycrystalline films.

Further adding to the discussion, Wolf et al. have recently observed a formation of $CaCO_3$ thin films in the presence of the acidic protein ovalbumin. They suggested that a liquid amorphous calcium carbonate (LACC) phase must form in the presence of the negatively charged polymer[87]. The LACC is thought to be stabilised due to electrostatic and depletion factors as the "liquid droplets" are negatively charged, and their formation mechanism was seen to markedly reduce the free Ca^{2+} concentration in solution (depletion stabilisation), thereby reducing the rate of the crystallization process. It is thought that similar factors are likely to operate in the $CaCO_3$/ PAH system as indicated by the zeta potential measurements which show that the droplets produced in solution after 3 h exhibit positive surface charges of 12 mV (Figure 36).

In comparison with negatively charged polyelectrolytes, where amounts of about 20-50 µg/mL were necessary[77], 5 times more PAH was required to initiate film formation, which suggests a weaker polymer/ counter-ion interaction at the working pH of ≈ 9.5. This is probably due to the difference in the degree of protonation of the polymers as PAH is only 50% protonated at pH 9.5, while PAsp/PAA are completely deprotonated

and negatively charged at this pH value[356]. Since the ammonium diffusion technique was used to increase the $[CO_3^{2-}]$ concentration, it is hard to estimate how high the concentration was of the CO_3^{2-} ions at each time point, which might also explain the differences in effect of the positively and negatively charged additives. Another explanation of the formation process might be that instead of CO_3^{2-} the PAH interacts with the Ca^{2+} ions, encapsulating them, and as with the negatively charged ones forming a complex as CO_3^- enters the solution. Yet this does not seem to be the case since the slow addition experiment proved that the positive charge of the NH_2 molecule was necessary for the process.

4.5.3 Transition bars and the effect of magnesium

The appearance of transition bars on the single crystal calcite films, were explained before by diffusion-limited exclusion of the polymeric impurity during crystallization[89]. The results presented here agree with this suggestion and it seems at repeating distances, gaps are formed containing material with a less defined shape, which are presumably amorphous material. This might be due to PAH being expelled from the crystallising material at certain distances giving rise to a transition bar pattern. Further research with a fluorescently-labelled poly(allylamine) might give more conclusive results about this.

An interesting feature of the results is the production of very smooth films by addition of Mg^{2+} ions. Magnesium ions have been seen to have a similar effect in the PAA/ $CaCO_3$ and PAsp/ $CaCO_3$ systems, where thin films are formed at concentrations of 10-50 µg/ml at a Ca:Mg ratio of 1 and as low as 5 µg/ml at ratios of Ca: Mg = 1:3. These compare with typical polymer values of 20-100 µg/ml PAA/PAsp in the absence of Mg[337, 359]. In both these polymer systems, it was stated the small Mg^{2+} ions may facilitate the formation of polymer/ cation/ carbonate complexes, which enables them to form at lower polymer concentrations[337, 359]. In correspondence with those results, also the addition of Mg^{2+} to the PAH/ $CaCO_3$ system enabled formation of very smooth films of polycrystalline calcite. Instead of the usual values of 0.5 mg/mL PAH required to cover the entire substrate, crystalline films covering the entire glass slide were obtained with 20 µg/mL PAH at a Ca:Mg ratio of 1, and even 5 µg/ml PAH at a Ca:Mg ratio of 3. As compared with the negatively charged additives system though were

Mg^{2+} incorporating in the lattice with the addition of PAsp could go up to 26 wt%[337], TGA and AA investigation of the PAH system showed much lower amounts of Mg^{2+} (only 2 wt%) were incorporated. The difference between the positively charged and negatively charged system is assumed to be due to a charge effect of the positively charged PAH molecules, which will keep the positively charged Mg^{2+} ions out of the complex instead of inducing their incorporation.

4.5.4 Fiber formation process

Considering calcite fiber formation, calcite whiskers and rods are often found in geological samples where they are usually termed moonmilk[372]. $CaCO_3$ fibers have been synthesised in the lab before, where for example polycrystalline vaterite fibers formed on self-assembled monolayers in the presence of PAA[373], and hollow vaterite tubes precipitated on silicon substrates by the use of water-electrolysis[374]. Comparable fibers as the ones produced in our system have also been observed previously by precipitation of calcium carbonate in the presence of PAsp[82] and PAA[375]. Their formation was attributed to a growth mechanism analogous to the vapour-liquid-solid (VLS) and solution-liquid-solid (SLS) processes responsible for the catalytic formation of nanowires[82, 376]. This $CaCO_3$ fiber formation process was called the catalytic SPS (solution precursor solid) mechanism, where the growth of fibers is attributed to PILP droplets which provide a flux of reagents to the fiber. This process resulted in a remnant bobble on the tip of the fibers which is considered proof of float growth[82]. Yet, since this SPS mechanism was autocatalytic (no catalytic particles were added), the observation of these bobbles couldn't be considered as conclusive in this system[30]. Such a bobble was often observed in our research (see Figure 8d), yet this was not a necessity for fiber growth.

Another mechanism proposed in the literature is the growth of fibers by aggregation. Here, additives, such as low molecular mass polyelectrolytes and block copolymers, directed growth of crystalline fibers via aggregation. In this way, fibers were made out of small sub-units or nanocrystals, forming so-called mesocrystals[104, 377]. $BaSO_4$ fibers with random and curved morphologies were formed by Yu et al.[104] and the formation process was attributed to an oriented aggregation process of the nanoparticles, depending on the supersaturation level. $CaCO_3$ fibers with a helical morphology have

been described before which grow on glass and mica via the formation of a copolymer-stabilised amorphous calcium carbonate (ACC) phase[30]. Due to redistribution of the polymer chains by absorption of the amorphous particles on the glass slide, the adsorbed particles experienced a charge anisotropy resulting in attraction and absorption of particles to the fiber end resulting into fiber growth[30]. In this case the fibers were amorphous and partially transformed to vaterite after incubating in air for 3 weeks. Similar fibers grown on single crystals of calcite and aragonite proved to be single crystals of calcite, and in this case fiber formation was attributed to an oriented assembly process.

Furthermore, unidirectionally oriented fibrous vaterite crystals have been formed on the functional polymer poly(N-isopropylacrylamide)[375] by an aggregation process, while polymer micelles of poly(*N*-isopropyl acrylamide)-*b*-poly(L-glutamic acid) mediated the formation of aragonite fibers and vaterite particles by an SPS mechanism[378]. $SrCO_3$ fibers with aspect ratios of around 600 have been formed on self-assembled monolayers (SAM) of thiols in the presence of PAA[379] and the mechanism of formation was thought to be a template-induced crystallization process, due to coordination of the primary particles by the multidentate PAA ligands present in the solution and on the SAM surface, forming aggregates.

Previous reports where $SrCO_3$ and $BaCO_3$ fibers were observed, have suggested that these structures were constructed via a combination of colloidal aggregation and an SPS mechanism[12, 83]. $SrCO_3$ and $BaCO_3$ fibers were formed by addition of PAA and just as the calcite fibers shown above, the fibers featured a nanodomain texture. The formation of these fibers was explained by the PILP mechanism where the PILP droplets arise out of solution and absorb onto the glass slide forming a PILP film, becoming a new surface to promote fiber growth. It was suggested that the PILP nanodroplets (or nanoparticles, depending on the state of the precursor phase) that are still forming in solution, will deposit, and preferentially adsorb at points of high energy. These might be mineral surfaces with high curvature, such as lumpy mineral coatings. This process would lead to an autocatalytic effect for preferential adsorption of droplets at the tip of the protrusion. With longer time this would turn into and extend the tip of the fiber in a one-dimensional fashion. If the tip stays as a liquid-like droplet, it might follow the SPS mechanism and lead to the formation of more homogeneous fibers. But if the tip solidifies very rapidly, it would most likely lead to a more granular texture[83].

Considering our obtained results, it appears that fiber formation starts from deposited crystalline films. These films first precipitate on the glass slide as amorphous films and then crystallise. This lowers the Ca^{2+} concentration and since the polymer gets excluded during crystallization as seen with TGA, the Ca^{2+}/PAH ratio decreases. Other experiments with low Ca^{2+}/PAH ratio confirm that fiber formation and alignment effects are much more significant at a low Ca^{2+}/PAH ratios and it is assumed that at these conditions, the particles are less stabilized and contain some kind of charge anisotropy, resulting in fiber formation. Since the $[CO_3^{2-}]$ is assumed to remain constant during the crystallization process due to the continuous source of ammonium carbonate[182], it is hard to isolate its role, but it is reasoned that charged anisotropic Ca^{2+}/PAH/CO_3^{2-} particles formed at low Ca^{2+}/PAH ratio are responsible for the formation process. Interestingly, the particles maintain their orientation even during growth. Since amorphous fibers were not observed in any case, fibers must get constructed, piece by piece, by a continuous supply of polarised amorphous or crystalline particles attaching to preformed fibers in an oriented way, and crystallising directly.

It is therefore suggested that a similar mechanism took place as for the formation of the above described $SrCO_3$ and $BaCO_3$ fibers: After film formation, a rough coating is formed (as shown in Figure 14a, b), and it is expected that the anisotropic Ca^{2+}/PAH/CO_3^2 droplets falling from solution will preferentially absorb to these protrusions and irregularities on the substrate due to their higher surface energies (Figure 48). The absorption at the specific charged sites on the substrate could give rise to charged anisotropy in the absorbed particle, due to redistribution of the polymer chains causing polarisation effects as has been shown before[30]. Precursor particles moving close to the charged tip of the developing fiber will be further polarised, resulting in their attraction and adsorption to the fiber end. Repetition of this process would lead to fiber growth, with depletion of starting materials at the tip leading to narrower sizes (see Figure 20). The images obtained with FEGSEM and HRTEM, which show small units, 100 nm in size, and respectively continuous crystalline areas support this idea (Figure 18 and 20). It is not entirely clear though if the droplets attach by oriented attachment as crystalline particles or as amorphous polarised droplets crystallising when they attach.
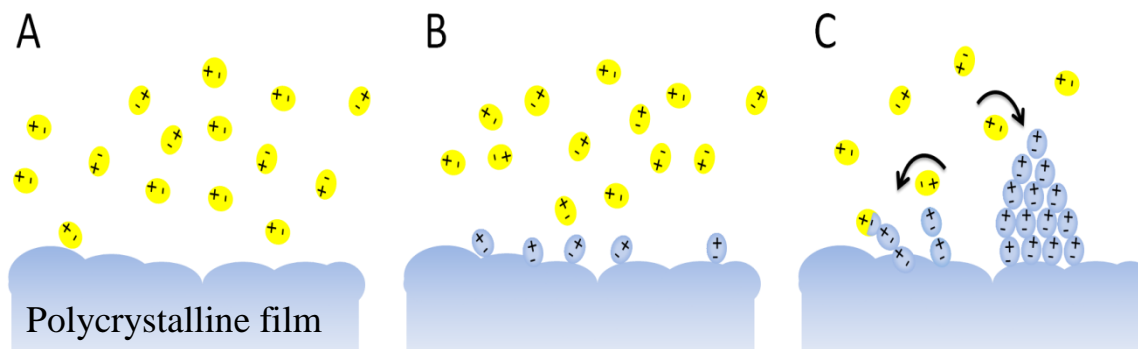
Figure 48: Proposed fiber formation process. Anisotropic particles (yellow) approach the polycrystalline film (a) and absorb to irregularities on the substrate (b). Other precursor particles moving close to the charged tip of the developing fiber, will be attracted and adsorbed to the fiber end (c).

4.5.5 Relevance to biomineralisation

Although the results and discussion above demonstrated that a microphase separation can provide a route to producing $CaCO_3$ with remarkable structures, a significant question remains: is this relevant to calcium carbonate biomineralisation, as has been suggested before[12], and could an analogous effect be achieved with the proteins present within the $CaCO_3$ biominerals?

Soluble proteins, as found in biological systems, only represent one type of biological polyelectrolyte, and actually often display many differences in their structure and phase behaviour as compared with simple polyelectrolytes such as PAA and PAH[380]. Since they are constructed from both hydrophilic and hydrophobic groups, soluble proteins usually prefer to form into well-defined 3D structures, which are characteristically significantly more robust against changes in solution conditions and in particular ionic strength, in comparison with simple polyelectrolytes. Also, while simple polyelectrolytes are uni-charged and have their charge distributed uniformly along the molecule, proteins are more amphoteric in character, with many of the constituent amino acids being either strong acids or bases. Consequently, positive and negative charges are present simultaneously in the protein structure, and are usually heterogeneously distributed over the protein surface as negative and positive domains[381].

Chapter 4: Concerning Positively Charged Additives and their Effect on Crystallization

The macromolecules which are usually associated with $CaCO_3$ biominerals represent a special class of proteins. Generally, they are classified as "highly acidic", containing from $\approx$ 20% up to even 40-50 mol% of glutamic and aspartic acid[107, 382-384]. These residues are present in the structure as negatively charged domains which are heterogeneously distributed along the chain of the protein, and exist together with small domains of positively charged amino acids and also a range of other polar or hydrophobic groups. It is therefore possible that, in common with simple polyelectrolytes, proteins which comprise 50% glutamic and aspartic acid would be able to strongly associate with Ca^{2+} ions, which could, if possible, conceivably lead to microphase separation if they were sufficiently flexible. This concept has recently been further investigated by the fabrication of a series of random copoly(amino acid)s which were constructed from 20–80%, 50–50% and 80–20%, aspartic acid and serine residues where their effect on the precipitation of $CaCO_3$ was determined. It was found that a strong correlation existed between the composition and function of the polypeptide, where the polypeptides with the highest amount of aspartic acid had the biggest effect[99]. Knowing this, it is therefore possible that based on their chemistry alone, highly acidic biomacromolecules could be active in driving a phase separation, thereby changing crystal morphologies and textures. The positively charged residues lysine and arginine, which are of low abundance in these proteins, are unlikely to support phase separation, and no evidence exists for the phase separation of poly-L-lysine in the presence of carbonate ions[385].

Although a PILP formation process seems plausible, many studies have been carried out in which $CaCO_3$ has been precipitated in the presence of macromolecules extracted from $CaCO_3$ biominerals[101, 127, 386] and no evidence for a PILP phase in the reaction solution or the crystal products has been reported. Also running counter to this suggestion, are some observations of crystallization in biological systems, where it appears that amorphous calcium carbonate (ACC) and also amorphous calcium phosphate (ACP) are actually present as well-defined granules prior to the transfer to the mineralisation site[22, 239, 327]. Therefore, although some of the unusual features arising from crystallization of a $CaCO_3$ "PILP" phase make it tempting to ascribe the formation of $CaCO_3$ biominerals to this mechanism, the above discussion sheds some doubt on this.

4.6 Conclusions

This work demonstrated that poly(allylamine hydrochloride) (PAH) has a dramatic effect on the crystallization of calcium carbonate, challenging the current understanding that positively charged additives have little influence on $CaCO_3$ growth. By the mechanism of a microphase separation in the presence of carbonate and calcium ions, droplets of complexes with liquid-like character are formed which subsequently wet the substrate and spread into a film. In this way crystalline films are formed, which are comparable to those formed with the negatively charged additives PAA and PAsp. Once crystalline films are formed, it is thought fiber formation occurs on the polycrystalline rough films at low Ca^{2+}/PAH ratio's, by an oriented attachment mechanism of anisotropic particles due to unequal distribution of charge. Addition of Mg^{2+} to the PAH/ $CaCO_3$ system enabled formation of very smooth films of polycrystalline calcite at much lower PAH concentrations. In comparison with negatively charged additives such PAsp where high-Mg calcites were obtained, the amount of Mg incorporation in the presence of PAH wasn't much increased.

These results provide a strong indication that positively charged additives, can be valuable for the production of $CaCO_3$ structures with complex morphologies. Synthetically, it will certainly not be possible to translate this process to all positively charged additives, but it is believed that other positively charged polyelectrolytes may have the same effect on crystallization. Future work will investigate this topic.

The relevance of such a phase separation in the biomineralisation of $CaCO_3$ is however unclear. Although the acidic proteins characteristic of some $CaCO_3$ biominerals could direct a similar phase separation, it is still not clear how this can fit with previous observations of calcification *via* amorphous precursor phases *in vivo*.

Chapter 5: Templating Calcium Carbonate into Nanoscale Plate-shaped Crystals by the Use of Collagen
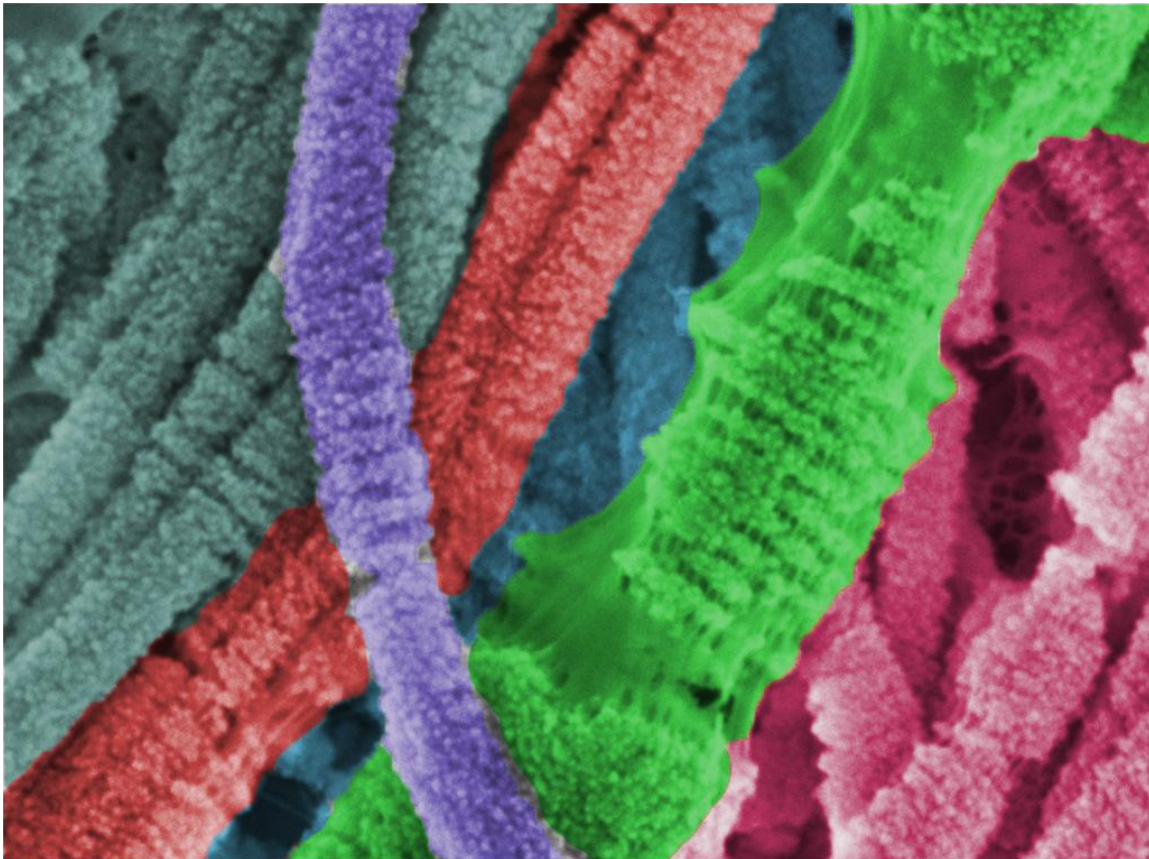
Chapter 5: Templating Calcium Carbonate into Nanoscale Plate-shaped Crystals by the Use of Collagen

This chapter deals with the infiltration of collagen with $CaCO_3$. Based on bone formation, where HAP crystals are formed inside collagen as nanoscale platelets, it was investigated whether collagen is specifically and exclusively tailored to control HAP formation, or whether it is possible to use it as a template for the precipitation of different minerals. To investigate this, SAXS and WAXS techniques, combined with TEM, were used, and it was proven that calcium carbonate was able to infiltrate into the collagen gaps in the presence of additives, which directed the mineralization according to a phase separation mechanism involving the formation of a liquid-like amorphous phase of $CaCO_3$. These liquid-like amorphous particles of $CaCO_3$ got infiltrated into the collagen structure due to capillary action, followed by their crystallisation, reducing the molecular spacing of the collagen from the initial 1.5 nm to 1.1 nm. Due to the moulding effect of the collagen, the amorphous particles transformed into nanoscale crystals of calcite and vaterite (10-20 nm long and a 2-6 nm thick), randomly oriented.

5.1 Introduction

Inorganic/organic hybrids have attracted much attention in recent years due to their potential as new functional materials[10, 14, 387, 388]. A great source of inspiration are biominerals, which are almost all composite materials, made out of an inorganic solid phase surrounded by an organic insoluble matrix phase and/or soluble organic molecules, forming a ductile, tough, and lightweight material. One interesting example is that of bone, which consists of about 30% organic matrix (collagen) and 70% inorganic material (calcium phosphate) giving rise to its remarkable strength, and the fracture toughness that the bodies of vertebrates need. By embedding the hydroxyapatite (HAP) crystals inside an organic matrix of collagen fibrils, the high stiffness and toughness of HAP is much improved, being more than 1000 times higher than in the absence of this matrix[389-392]. Although the high toughness of bone is due to the hierarchical organization of the mineralized collagen fibrils[232], its remarkable fracture resistance arises from the nanometer size of the HAP crystals. Previous research done by Gao et al.[393] demonstrated that below a length scale of around 30 nm, the HAP crystals become insensitive to cracks and defects, which allows them to maintain their strength despite pre-existing flaws or cracks. In other words, by being

only 3-5 nm thick, the HAP crystals in bone are optimized to serve in their role in the human body with a high fracture strength and good tolerance of flaws.

This level of optimization of crystal morphology and size in relation to the required mechanical properties and hence the function of the material, suggests that biogenic crystals must be formed under a tight biological control[105]. This control is mainly exerted by the corresponding organic matrix, serving as a scaffold for mineral formation and templating the crystals size and morphology. Considering bone formation, this scaffold is made from collagen and due to its biocompatibility and interesting properties this organic compound is often used in hybrid biominerals synthesis and finds its application as stress-bearing scaffolds for bone repair[394]. However, the question remains whether the fibrils are specifically tailored to control HAP formation, or if they can also template different minerals, producing analogous arrays of oriented crystals with morphologies and sizes similar to those of HAP.

5.1.1 Introduction to collagen

Collagen type I is the major constituent not only of bone (see chapter 3) but of many biological tissues, including tendon, ligaments, skin or cornea and is therefore the most abundant fibril forming protein in our body[395, 396]. Type I collagen molecules are assembled from supercoiled assemblies of three polypeptide chains, each containing over 1000 amino acid residues. The amino acid sequence of the protein is highly repetitive based on –Gly-X-Y- units (where Gly is glycine and X and Y are often proline and hydroxyproline) which allows the three polypeptide chains (two α_1 and one α_2 chains, similar but not the same) to fold into a triple-helical structure. The side groups of the proline and hydroxyproline residues form bonds with the nitrogen on the polypeptide chain, thus hindering the rotation between adjacent residues in the chain and stiffening the molecule. Prior to the final collagen molecule, procollagen is formed which is a full length collagen molecule containing two large pro-domains on both N and C terminal ends of each polypeptide chain, preventing any spontaneous self-assembly within the cells[197]. The procollagen molecules are assembled within the cell to form triple helices, where after excretion, the globular pro-domain ends are cleaved off by enzymes, and the 300 nm long and 1.5 nm thick triple helical molecules remain. The latter are called tropocollagen and as mentioned previously in chapter 3 (see 3.1.2),

these molecules undergo a self-assembly process into a microfibril in which they are staggered with a periodicity of D= 67 nm[237]. The molecular packing of the collagen molecules is such that the packing neighbours are arranged in such a way that they form a super-twisted (discontinuous) right-handed microfibril that interdigitates with neighbouring microfibrils[396]. The length of the molecules (300 nm) is not an integer multiple of the staggering period D, and therefore gap regions appear due to the staggered arrangement of the collagen molecules within the fibrils. The individual molecules are shorter than 5D periods (5 times 67 nm = 335 nm), leaving a gap of about 40 nm to the next molecule and thus generating an overlap zone of 27 nm length within the fibril (see Figure 1)[3, 141].
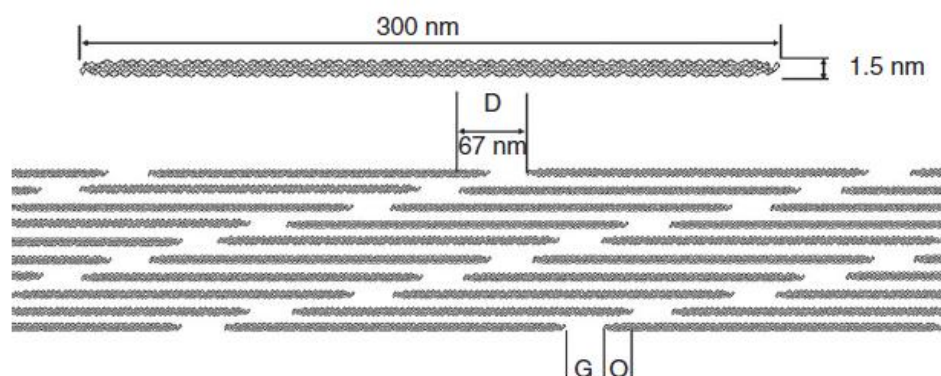
Figure 1: Schematic representation of the structure of collagen adapted from ref. 197. Each collagen molecule, 300 nm long and 1.5 nm thick, is shifted with respect to its neighbour 40 nm in the axial direction, giving rise to the 67-nm periodic pattern or D-period (D), consisting of gap (G) zones of 35-40 nm length and overlap (O) zones of 27-32 nm length.

5.1.1.1 Collagen in bone

As discussed before, bone is a composite material, consisting of inorganic HAP crystals and collagen, the latter acting as a scaffold for a highly organized arrangement of uniaxially oriented mineral crystals[3, 180]. Mineralisation of collagen with HAP has been studied *in vitro* previously using SAXS and WAXS techniques. These experiments have demonstrated a co-orientation of the HAP crystals inside the collagen structure with their crystallographic *c*-axes parallel to the long axis of the collagen fibril. It was further shown that the crystals took the shape of platelets 30-50 nm wide, 60-100 nm

long and a mere 2-6 nm thick[3, 397], making the HAP crystals in bone the smallest biogenic crystals known. They are understood to nucleate mainly within the less dense 40-nm-long and 2 nm thick gap zone of the collagen[3, 197, 237]. As discussed in chapter 3, the exact infiltration mechanism of the calcium phosphate particles into the nanoscopic spaces within the collagen fibrils[96, 196, 197, 253] has not yet been completely unravelled.

5.1.1.2 The effect of HAP formation on the collagen structure

Neutron scattering experiments on collagen revealed the existence of an equatorial spacing, d, between the collagen molecules (Figure 2). This parameter measured about 1.6 nm in non-mineralized wet fibrils, whereas in dried conditions the spacing of the molecules was reduced to 1.1 nm[398]. In a mineralized wet bone structure, an intermediate value of 1.25 nm was found. By computer modelling studies and comparison with SAXS experiments, a process of closer packing of the collagenous molecules was identified and confirmed when water was replaced by mineral clusters within the fibril[399]. This effect is illustrated in Figure 2.

It can be seen that when dried, the packing density of the molecules increases and the typical lateral spacing between the molecules in the fibrils decreases from about 1.6 nm to 1.1 nm (Figure 2a to c). If the water (a) is replaced by mineral, the growing mineral particles compress the molecule packets that are between them and in this way effectively reduce the molecular spacing to the value of dry fibrils (1.1 nm) (Figure 2d). The SAXS peak (Figure 2c) is in this case however, much lower and broader than in the case of dry fibril, since the size of the islands with a dense packing of the collagen molecules is much smaller. Therefore, it can be seen that the mineralized fibril has an average density of collagen molecules similar to the case of the wet fibrils, but a molecular spacing similar to the dry fibril.
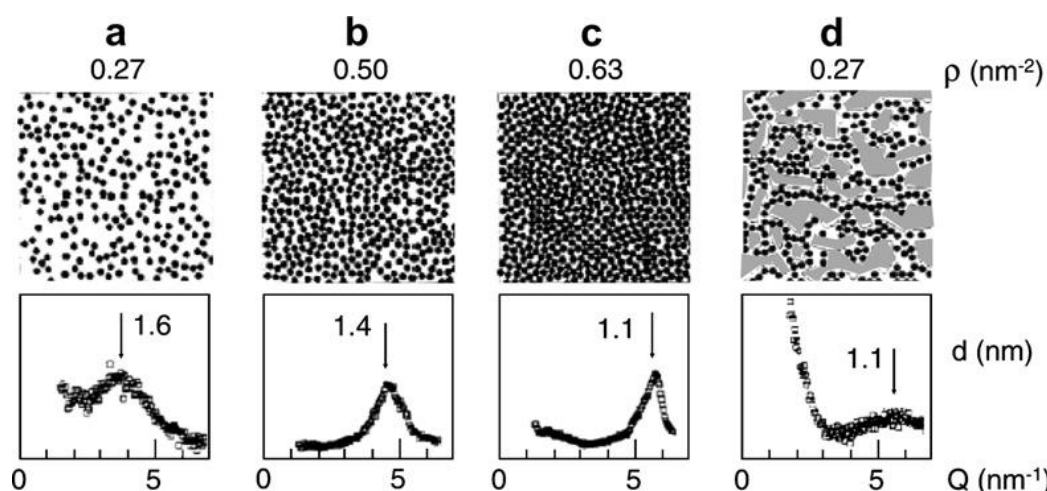
Figure 2: Four Equatorial diffuse X-ray scattering peaks representing the lateral spacing of collagen molecules as a function of water content. The water content decreases from fully wet in (a) to fully dry in (c). The black circles in the figures symbolize the collagen molecules in the cross-section of a fibril with on top the number of collagen molecules per unit surface of the fibril cross-section. Mineralized collagen is represented in (d). It is shown that the peak of the average lateral spacing between the molecules shifts from (a) to (c), at which point it is equal to the mineralized collagen. It has to be noted that the number of molecules in (d) is about the same as in the fully wet case (a). Image reproduced from ref. 3, 399.

5.1.1.3 Collagen as a template material

Type I collagen has been widely used in hybrid biominerals synthesis due to its biocompatibility and interesting properties. Yet since highly porous, nonmineralized collagen matrices have an inherent lack of mechanical resistance, their applications as stress-bearing scaffolds for bone repair are limited though[394, 400]. Therefore, to overcome this problem, attempts have been made to introduce different kinds of minerals inside the collagen structure. In addition to infiltration with calcium phosphate[96], collagen has also been infiltrated with silica *in vivo*[401] as *in vitro* as well[394], suggesting that collagen may act as an universal template. Also by using $CaCO_3$, it was claimed to be possible to infiltrate collagen, although this was never clearly proven[126]. In the case of silica, the introduction of the mineral phase was achieved by the use of polyamine-enriched collagen. By stabilization of polysilicic acid, it acted as a fluidic precursor phase, which infiltrated the collagen by capillary action[394]. The polyamine-

enriched collagen acted then as a template and catalyst for polymerization of the precursor phase into silica[394].

In the case of calcium carbonate, a similar mechanism was proposed where the addition of polyacrylic acid (PAA) enabled the formation of an amorphous polymer-induced liquid-precursor (PILP) phase of $CaCO_3$, infiltrating the collagen by capillary action[126]. An interesting periodic banding pattern of calcite disks was also observed, with a spacing of about 6 times that of the banding pattern observed for native type I collagen. By removing the organic part, indications were found that the mineral had been deposited throughout the fibers and not solely as disks. Based on this it was hypothesised that the liquid-precursor phase was drawn into the collagen fibers by capillary action, which would preferably occur at the hole-zones of the collagen, leaving those regions of collagen more fully entrenched with the mineral. Since this research was mainly carried out by SEM and bleaching methods, a conclusive proof of the infiltration could not be provided, and the proposed mechanism of capillary action infiltration was merely based on the observation of the PILP phase to seep into cracks and crevices due to capillary forces acting on the phase boundaries of the precursor phase[126]. Furthermore the morphology of these $CaCO_3$ crystals, as well as the crystallographic orientation of the crystals formed inside the collagen (if formed) was never described or discussed.

Subsequent research based on the previous results, provided a better proof of infiltration of reconstituted type I collagen fibrils with $CaCO_3$, using magnetic resonance microscopy[402]. The fibrils were infiltrated using conditions similar to the experiments described above[126] by the use of a $CaCO_3$ PILP phase, and were investigated by means of SEM, XRD and magnetic resonance microscopy (MRM). It was found that the water proton MRM properties and the hydration state of the collagen changed with the onset of mineralization. These two events were thought to be a result of the infiltration of the mineral inside the collagen. Firstly, the reduced hydration state was attributed to displacement of water by the amorphous material when infiltrating the collagen. Secondly, the reduction in the proton MRM properties, and more precisely the water proton T_2 values, was linked with the immobilization of water molecules through ionic or dipolar interactions at the surface of crystalline mineral deposits. Further, this reduction was explained by the enhanced field heterogeneities caused by the different

bulk magnetic susceptibility of the mineral from that of water. Interestingly, an increase in collagen content could also be observed, which was ascribed to an indirect effect of collagen fusion during mineral formation. XRD showed that crystallisation into the calcite polymorph occurred after 12 days, and the crystalline mineral content increased substantially from days 13 and 15. The X-ray diffraction peak appearing at 10.607° in the diffractogram of collagen (lateral molecular spacing of 1.67 nm) was also observed and remained constant throughout the PILP experiment, which was in contrast with previously published X-ray diffraction studies[402, 403]. An exact explanation for this could not be given. As a mechanism for infiltration it was proposed that the amorphous $CaCO_3$ PILP phase is taken up by the collagen, displacing the water within the matrix structure. In a second phase, the amorphous $CaCO_3$ droplets begin to coalescence within the intrafibrillar space of collagen. Since this doesn't influence the MRM properties, they plateau in this region. Finally the amorphous phase crystallises, thereby increasing the rigidity of the collagen molecules.

5.1.1.4 Precipitation of $CaCO_3$ in collagen matrices

Precipitation of calcium carbonate in oriented and non-oriented collagenous matrices, has previously demonstrated that the microenvironment in which crystallisation occurs can define the polymorph and orientation of the crystals formed[4, 404]. This was shown by precipitation of $CaCO_3$ on crosslinked and uncrosslinked gelatin films containing adsorbed polypeptides such as poly-L-glutamate (poly-G) or polyaspartic acid (PAsp) and Ca^{2+} ions[405, 406]. Gelatin itself is a complex structure consisting of denatured and degraded collagen molecules[404]. Depending on the degree of deformation of the gelatin films, and the type and concentration of the polypeptide used, different kinds of polymorph selectivity and crystal orientation were obtained. In unstretched gelatin films containing PAsp or poly-Glu, non-oriented crystals were almost exclusively formed. As an exception, lower concentrations of PAsp (less than 0.5 µg per gram of gelatin), allowed the formation of oriented calcite crystals on the surface of the film with their *c*-axes being oriented perpendicular to the film surface[404]. This ability of PAsp to influence the orientation of calcite nucleation was possibly due to its ability in adopting a β-sheet conformation on absorption to the collagen matrix while poly-Glu adopts a random orientation. Increase in the concentration of the additive from 0.5 to 10 mg per g of gelatin resulted first in the precipitation of non-oriented aragonite while

higher concentrations formed non-oriented vaterite[404, 405]. This observation was in accordance with Ostwald's rule of stages where the least stable polymorph is formed under kinetically controlled conditions.

By uniaxially deforming the films, a different behaviour could be observed. In this case a significant increase in the degree of crystal orientation occurred accompanied by a polymorph switch. In the presence of PAsp it was now possible to observe oriented crystals of all three anhydrous crystalline polymorphs of calcium carbonate, whereas in the presence of poly-Glu, oriented aragonite and vaterite crystals were obtained[404]. Interestingly, the oriented aragonite crystals produced within the films had their morphologies dictated by the initial shape of the sites in which they grew and were therefore rod-shaped with their long axis parallel to the direction of elongation and *c*-axis perpendicular to the longitudinal axis of the rod[405]. Besides enabling polymorphic control by increasing the concentration of polypeptide, polymorphic selection also depended on the degree of uniaxial deformation. This was due to reduction of the average cavity size by stretching, increasing the local supersaturation and the concentration of the negatively charged polyelectrolytes, favouring formation of the least soluble polymorph being vaterite[407].

5.2 Aims of the project

The aim of this project was to investigate the possibility of using collagen to template different materials. The mineralization of collagen fibrils with calcium carbonate was chosen as a model system for this work and SAXS and WAXS, in combination with electron microscopy, were selected as analytical techniques. An introduction to $CaCO_3$ is given in Chapter 4. Since collagen is a highly organized matrix, controlling the organization and orientation of hydroxyapatite nanocrystals in bone, it provides an appropriate confined environment to template crystal growth and morphology. By the use of SAXS and WAXS, we will be able to study the deformations on the collagen template caused by mineral formation. These characteristics are relevant for the understanding of biogenic calcification processes, focussing on the role of confinement in ACC stabilisation.

Chapter 5: Templating Calcium Carbonate into Nanoscale Plate-shaped Crystals by the Use of Collagen

5.3 Experimental

The synchrotron experiments were performed at the European synchrotron radiation facility (ESRF), utilising the setup at the SAXS/WAXS Dutch/Belgian BeamLine (DUBBLE) BM26. For the execution of the experiments, a liquid flow cell was used, equipped with Kapton or mica windows. As a substrate, two different types of collagen were used: type I collagen extracted from horse tendon, and collagen sponges.

5.3.1 Construction of the flow cell.

To investigate the infiltration of the collagen fibrils *in situ*, a flow cell had to be developed to pump $CaCO_3$ solution into a reaction environment containing collagen. The flow cell consisted of a metal frame (Figure 3) with an inlet and outlet.
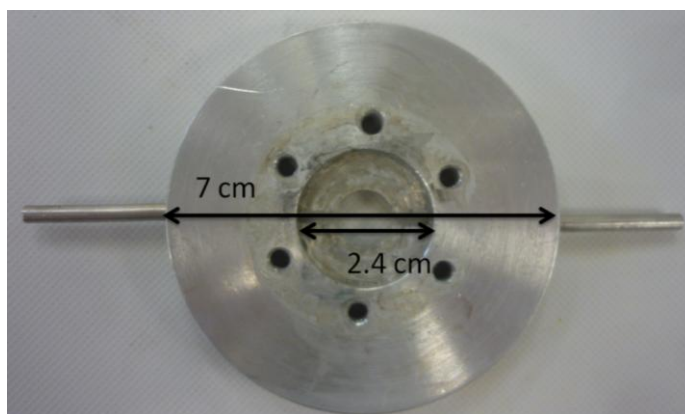
Figure 3: Metal framework of the flow cell. Bottom and top look the same.

In this framework, two mica windows or two pieces of Kapton were put in the centre, forming the two windows. Two teflon pieces were screwed in (Figure 4) with the help of a rubber O-ring to keep the windows in place and close the flow cell liquid thightly to avoid leaking. The bottom and top pieces had different conical openings (Figure 4a) on the outer side of the cell to avoid interference between the scattered beam and the cell. The inner surface of both pieces were identical (Figure 4b). Figure 5 illustrates the fully assembled flow cell.

Chapter 5: Templating Calcium Carbonate into Nanoscale Plate-shaped Crystals by the Use of Collagen
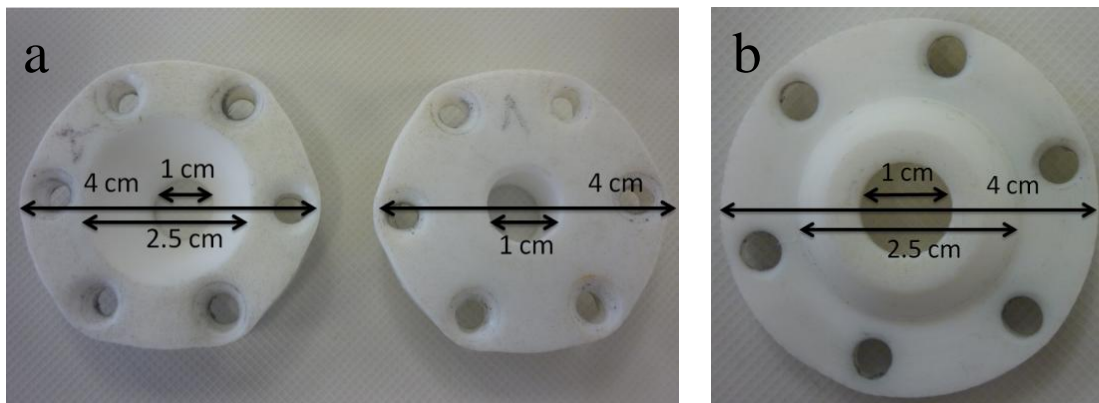
Figure 4: Teflon pieces to close the metal frame flow cell. (a) Shows the outside of the top and bottom part of the cell while (b) shows the inside of both pieces.
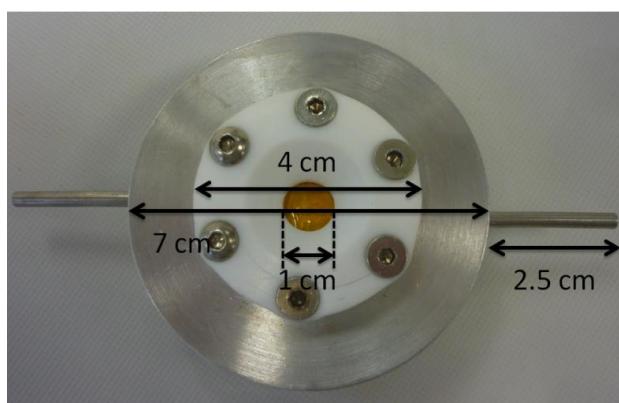
Figure 5: Assembled liquid flow cell.

In order to be able to put the flow cell in the path of the beam, a holder was fabricated (Figure 6a). This holder had two screw holes at the bottom, which allowed it to be screwed to the robotic platform. The flow cell itself was fixed with two screws to keep it stationary during the experiments (Figure 6b).
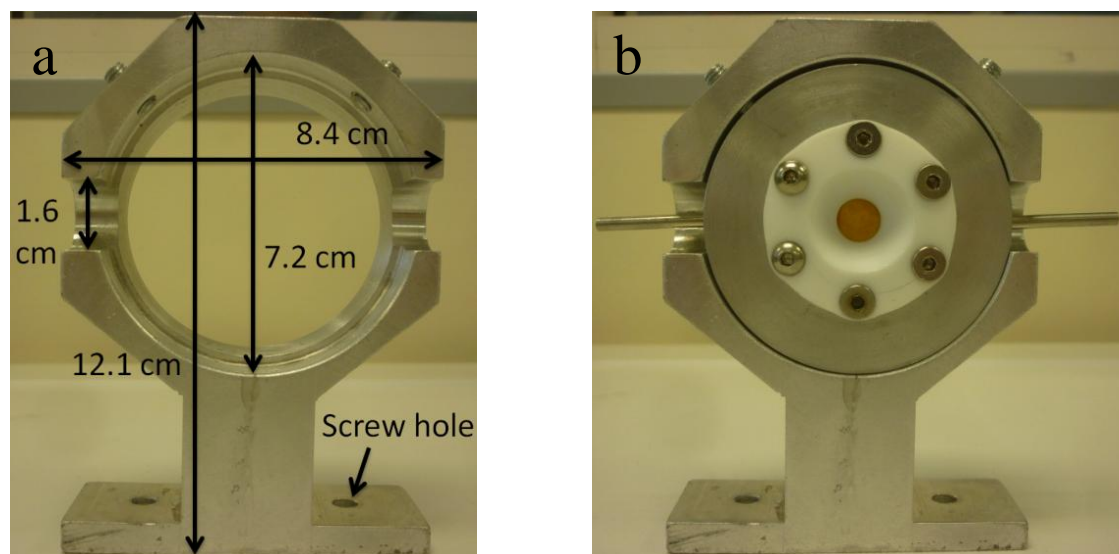
Figure 6: Holder with dimensions (a) and flow cell screwed in (b).

5.3.2 Preparation and experiments with horse tendon type I collagen

The horse tendon collagen was prepared as follows: 1 gram of horse tendon extract (Opocrin, Corlo, Modena, Italy) was mixed with 10 mL of aqueous acetic acid (50 mM, pH 2.5) and was left to stir overnight at room temperature. Under these conditions, the collagen fibrils remained dispersed in solution. Subsequently, the mixture was centrifuged at 5000 rpm for 10 min and the supernatant was collected and stored at 4 ° C in the fridge. In the next step, the collagen fibrils were formed on a Kapton film or mica window to be put into the flow cell. Prior to the investigations at the synchrotron beamline, similar experiments were carried out in the laboratory where horse tendon collagen was formed on glass slides or C-coated formvar covered Ni TEM grids as substrates. The fibrils formed in this way were infiltrated with $CaCO_3$ and studied by TEM and SEM. To form the collagen on the substrates, 10 μL of the supernatant solution was put on a piece of parafilm, and the top side of the substrate was placed on the collagen solution for 10 sec. It was then removed and excess collagen was disposed with a filter paper. The substrates were then put on a droplet of DI water, which triggered the assembly of collagen fibers and their subsequent precipitation[80, 179]. After 10 min, the substrates were washed with ethanol and left to dry. Optical microscopy was used to determine whether collagen fibrils had formed on the substrate.

Chapter 5: Templating Calcium Carbonate into Nanoscale Plate-shaped Crystals by the Use of Collagen

To study the infiltration of the collagen fibrils with $CaCO_3$ by TEM and SEM, the glass slides or Ni-TEM grids were put in a 10 mM solution of $CaCl_2.2H_2O$ with 1 mg/mL poly(allylamine hydrochloride) (PAH) or 50 µg/mL of polyaspartic acid (PAsp) with the side of the collagen fibrils on top. This solution was put in an ammonia desiccator and samples were collected after variable times, washed with ethanol and left to dry.

At the synchrotron beamline, the collagen covered Kapton and mica sheets were inserted as windows for the flow cell. Subsequently, a solution of 10 mM $CaCl_2.2H_2O$ containing either 1 mg/mL of poly(allylamine hydrochloride) (PAH) or 50 µg/mL of polyaspartic acid (PAsp) was placed in an ammonia desiccator. The reactant solution was pumped through the flow cell with an addition rate of 2.5 mL/min. The flow cell containing the collagen was placed in front of the SAXS and WAXS detectors in the X-ray beam. While the Ca^{2+}/PAH solution was pumped through the flow cell, the WAXS and SAXS signal was recorded from the sample at intervals of 5 min with an acquisition time of 3 min, for a total time of 8 h.

5.3.3 Preparation and experiments with collagen sponges

The collagen sponges were prepared as follows. Fragments of collagen sponge were cut into cubes of 0.125 cm^3 which were hydrated and degassed in a vacuum oven for 30 min, as described in previous research[126]. The collagen sponges were then incubated in a flow cell between two mica or Kapton windows. Subsequently as described before, a solution of 10 mM $CaCl_2.2H_2O$ containing the additives was placed in a desiccator containing ammonium carbonate and was pumped through the flow cell with an addition rate of 2.5 mL/min. The WAXS and SAXS signal was acquired from the collagen sponge in intervals of 5 min for an acquisition time of 3 min, for a total time of 8 h. Control experiments were carried out in the absence of additives (PAH or PAsp). After the experiments, the sponges were removed from the flow cell, crushed in liquid nitrogen, resuspended in ethanol and dispersed on a C-coated formvar covered Cu TEM grid which was allowed to air dry. Alternatively, collagen sponges were incubated in $CaCl_2.2H_2O$ solution containing either 1 mg/mL of PAH or 50 µg/mL of PAsp inside a desiccator containing ammonium carbonate, and at designated times specimens were collected for analysis with TEM and SEM. After 8 h of measurements, the sponges

were removed from the solution, briefly washed in water and air dried. For TEM measurements, the sponges were crushed again in liquid nitrogen, resuspended in ethanol, and dispersed on a C-coated formvar covered Cu TEM grid which was allowed to air dry. Figure 7 shows an overview of the experimental set-up.
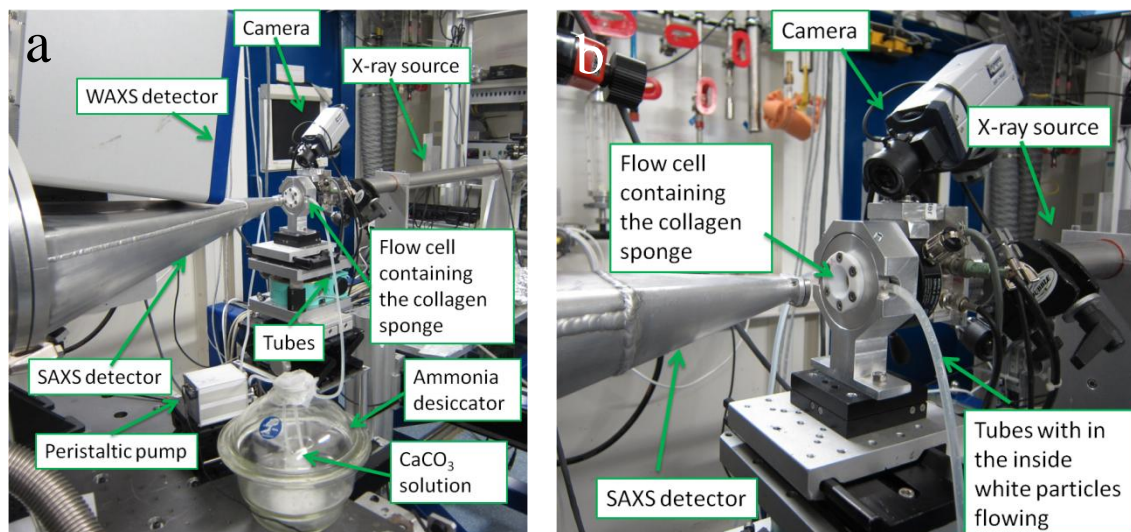
Figure 7: Experimental set-up at the European Synchrotron Research Facility (ESRF), Grenoble, France, Dutch/Belgian beam line BM26.

5.4 Results:

Unless otherwise stated, all experiments were conducted in collaboration with Dr. Fabio Nudelman from the University of Eindhoven. Background subtraction of all the synchrotron data and data analysis of the SAXS spectra were done by Dr. Daniel Hermida Merino and Dr. Guiseppe Portale from the ESRF. Figures 16 and 18 were prepared by Dr. Daniel Hermida Merino and Dr Giuseppe Portale. TEM and SEM for Figure 19, 22, 25 were done by Dr. Fabio Nudelman at the University of Eindhoven.

5.4.1 Preparative studies with electron microscopy on the infiltration of $CaCO_3$ in horse tendon collagen fibrils

Before the experiments at the synchrotron were preformed, the horse tendon collagen fibrils were investigated with TEM. Figure 8 shows TEM images of the collagen. The diameter of collagen molecules ranged from 70 nm to 660 nm and they were tens of

micrometers long. The typical collagen structure with an overlap zone of 27 nm and a gap zone of about 40 nm can be seen in Figure 8b.
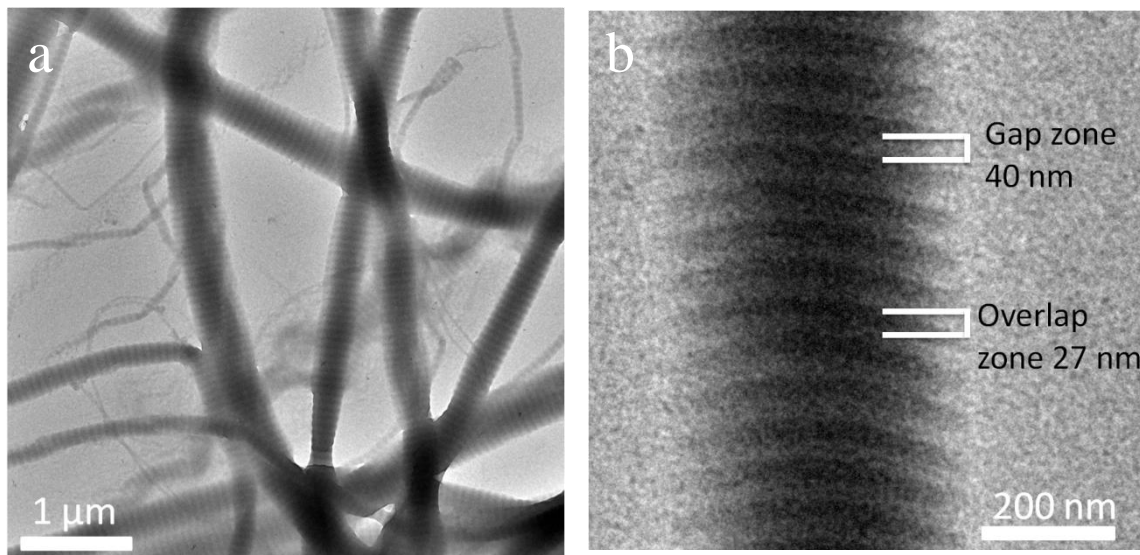
Figure 8: TEM image of collagen fibril of horse tendon collagen. The overlap and gap zone of the collagen can be distinguished (b).

In the next step, the collagen infiltration in the presence and absence of PAH was investigated with SEM and TEM. In the absence of PAH, FEGSEM showed that rhombohedral calcite crystals formed, growing on top or even including the collagen fibrils (Figure 9). The calcite crystals were distributed along the collagen fibrils and had sizes ranging from 20 to 40 µm which is the characteristic morphology of calcite crystals in the absence of any additives.
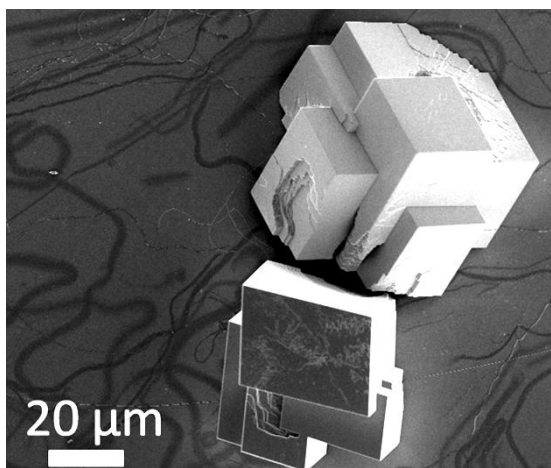
Figure 9: FEGSEM image of glass slide covered with horse tendon collagen. The glass slide was put in a $CaCO_3$ solution (10 mM $[Ca^{2+}]$) for 1 day. $CaCO_3$ crystals were formed on top of the collagen fibrils.

Repeating the experiments in the presence of PAH, FEGSEM images showed that the collagen fibers were covered with a patchy film-like coating of $CaCO_3$ after one day reaction (Figure 10). Interestingly, the $CaCO_3$ was organised in a banded pattern of disks around the collagen. The disks were about 50-100 nm thick and spaced about 20-30 nm apart, with the disks oriented perpendicular to the *c*-axis of the collagen fibrils.
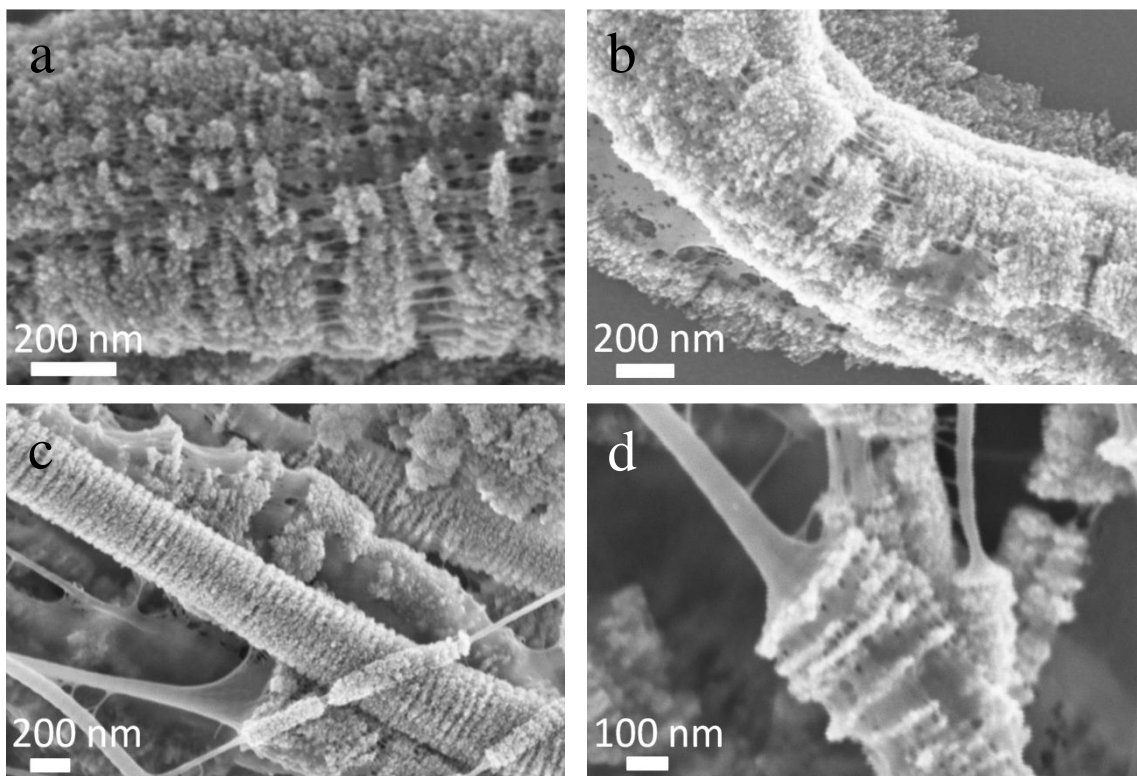
Figure 10: FEGSEM images of collagen fibrils formed on a Kapton film, put in a $CaCO_3$ solution (10 mM $[Ca^{2+}]$) for 1 day in the presence of 1 mg/mL PAH. The collagen fibrils are covered with $CaCO_3$ in a banded pattern.

TEM was used to further investigate the collagen fibrils. For this, collagen fibrils were formed on C-coated Ni-TEM grids, which were put in a $CaCO_3$ solution for times between 6 h to one day (Figure 11 and 12). After 6 h, it was seen that round amorphous particles with sizes of 100 nm to 450 nm had formed (Figure 11a), similar to the particles formed in a $CaCO_3$/PAH bulk solution (See Chapter 4). EDX also showed that they contained Ca^{2+}, while no crystalline material was found. Interestingly, these amorphous particles were mainly associated with the collagen fibrils, covering and sticking to the side of the collagen. The particles also covered large areas of the collagen, which contrasts previously obtained results with calcium phosphate, where amorphous calcium phosphate droplets seemed to bind to certain preferential sites of the collagen[196].

Further investigation showed that the collagen had become very electron dense at different positions, which might be due to the presence of calcium carbonate. Interestingly, at some positions on the collagen fibril, small particles associated with the collagen fibrils could be distinguished (see Figure 11b, c, d). These particles were still

amorphous, 5 to 10 nm thick and around 20 nm long, but whether these particles were covering the collagen or were inside was not clear from the images, especially because similar looking structures were also found next to the collagen (Figure 11b).
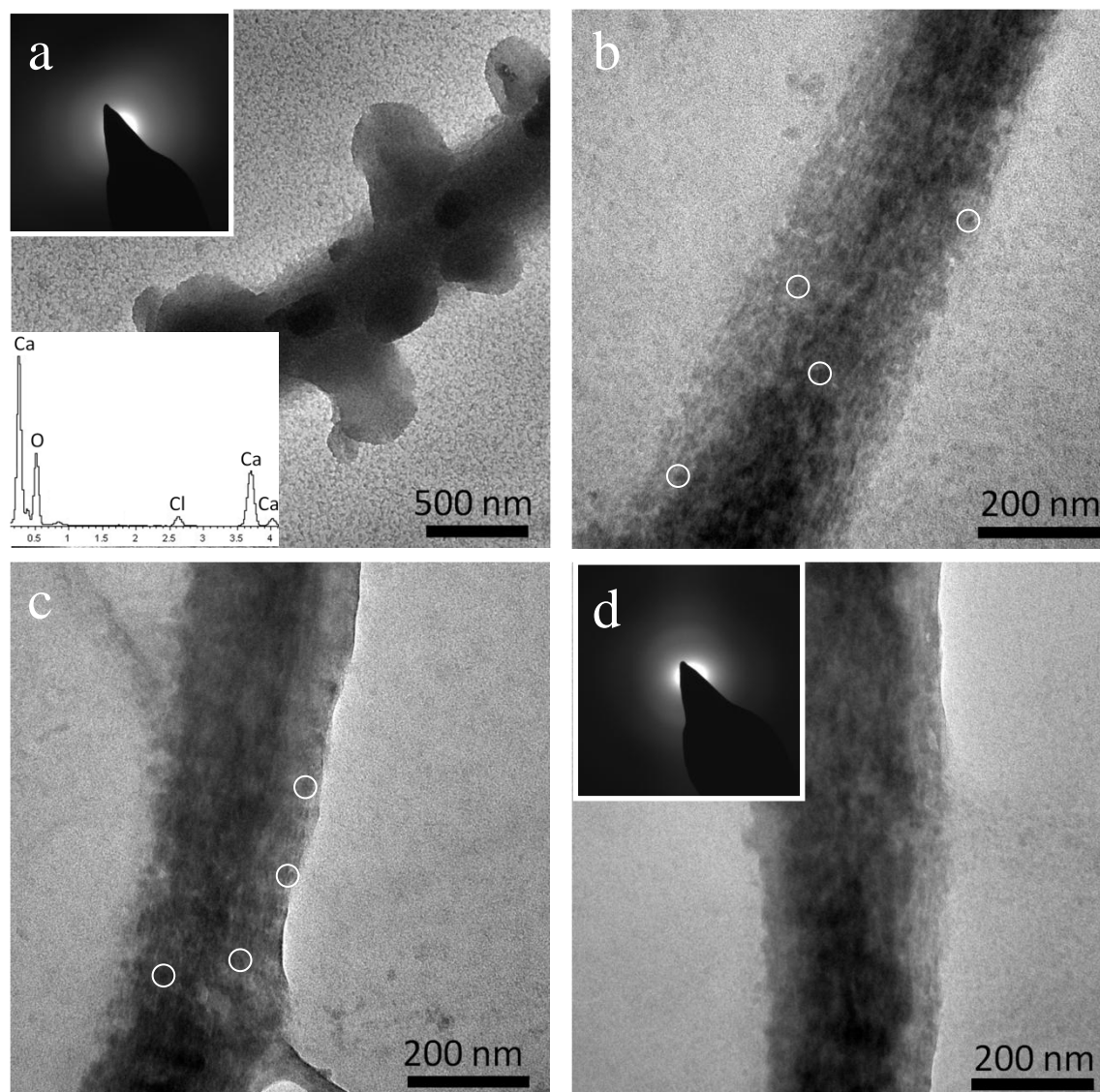
Figure 11: TEM images of collagen fibrils on a Ni TEM grid put in a $CaCO_3$ solution (10 mM [Ca^{2+}]) with 1 mg/mL PAH after 6 h. Small particles 10 nm thick and 20 nm long were found inside or on top of the collagen fibrils (white circles in b, c, d).

After 12 h to one day, the collagen fibrils were completely covered with $CaCO_3$ which had crystallised into calcite and vaterite (Figure 12b). It was therefore difficult to obtain a clear image of the infiltration of $CaCO_3$. The covering of the collagen fibrils with disk shaped $CaCO_3$ particles as shown before with SEM is demonstrated here again (Figure

12a). Some parts of the collagen were not completely covered though (Figure 12c) and interestingly, after beam damage, small electron dense particles were visible inside the collagen, but only at the overlap zone of the collagen (Figure 12d). The particles had a needle-like appearance, were 30 nm long and between 5 to 10 nm thicknesses. Unfortunately, this event only occurred once and no diffraction was obtained. The arrow in Figure 12d indicates the place of beam damage
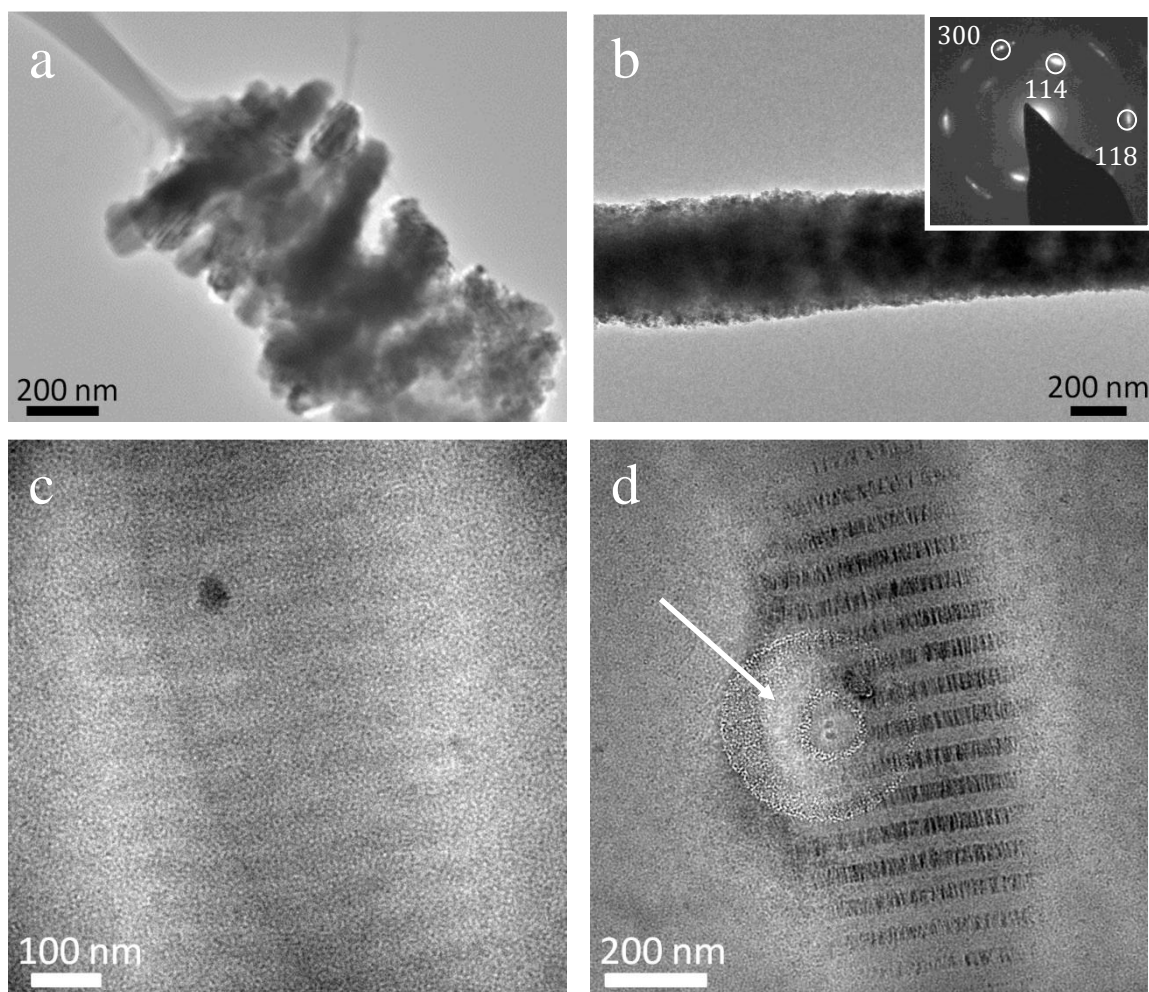
Figure 12: TEM images after 1 day of collagen fibrils on a Ni TEM grid put in a $CaCO_3$ solution (10 mM $[Ca^{2+}]$) with 1 mg/mL PAH. (a, b) Most collagen fibrils are covered now $CaCO_3$. The diffraction pattern in (b) corresponds to vaterite. Non-covered collagen fibrils before (c) and after (d) beam damage (arrowed) are also shown.

Chapter 5: Templating Calcium Carbonate into Nanoscale Plate-shaped Crystals by the Use of Collagen

5.4.2 Studies on the infiltration of collagen sponges with $CaCO_3$ in the presence of PAH

5.4.2.1 Studies with SAXS and WAXS

At the synchrotron beamline, SAXS and WAXS experiments were conducted. First the collagen was studied in aqueous solution. It was soon discovered that there were some problems with the set-up. First of all, the SAXS signal of the horse tendon collagen fibrils assembled on the windows wasn't strong enough since the sample volume illuminated by the beam was not sufficient. Therefore, it was decided to do all experiments with collagen sponges put in the flow cell. In addition, measuring the collagen sponges with Kapton windows, showed a characteristic Kapton peak in the SAXS signal which would cover the signal of the collagen. Therefore, it was decided to work with mica windows instead of Kapton. This made the flow cell design rather complicated since the mica windows didn't fit in the flow cell. As a solution, mica windows were glued to a piece of Kapton containing a small hole in the middle to allow the X-ray beam to pass through the Kapton (Figure 13). The Kapton containing the mica window was then placed inside the liquid cell, and the cell was closed.
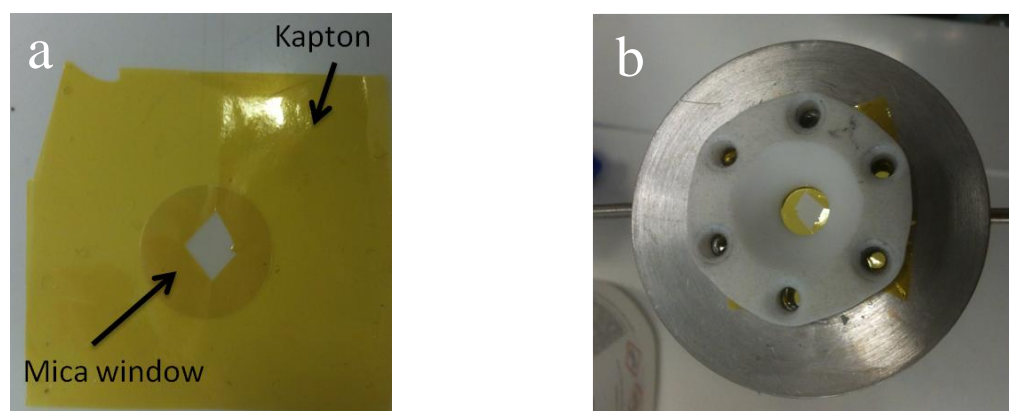
Figure 13. Kapton with a small hole in the middle with a mica window glued on. In this way it was possible to allow investigation of the collagen with the flow cell (right image).

After the flow cell with adapted windows had been assembled, the cell was filled with 10 mM $CaCl_2$ solution containing 1 mg/mL PAH and a collagen sponge was inserted between the two windows. SAXS and WAXS measurements were then performed. The SAXS signal of the unmineralized collagen showed the typical 3rd and 5th order peaks of the collagen, relating to the 67 nm periodic banding pattern of collagen (Figure

14). Importantly, a broad peak centred at 1.5 nm is also visible (arrow 2 in Figure 14), which corresponded to the intermolecular distances present between the collagen microfibrils exhibiting a liquid-crystal-like order[398, 399].
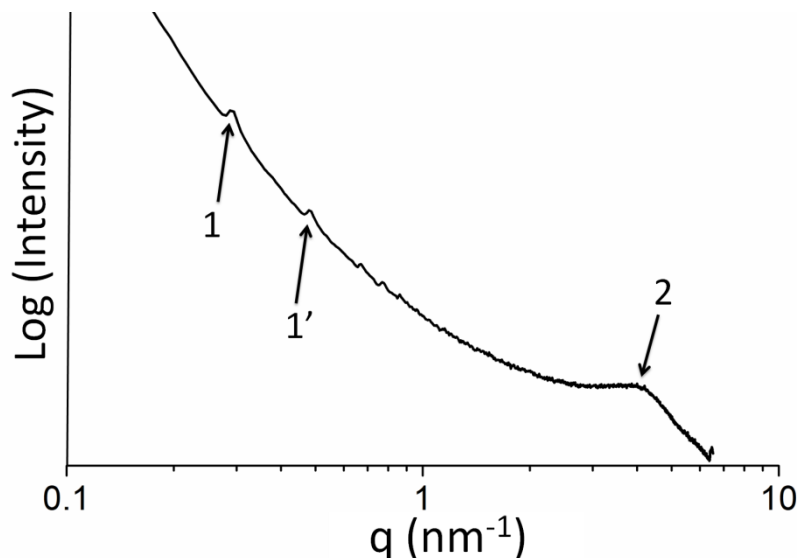
Figure 14: SAXS spectrum collected at the synchrotron of a collagen sponge in a 10 mM $CaCl_2$ solution in the presence of 1 mg/mL PAH. The two arrows 1 and 1' denote the 3rd and 5th order peaks of collagen while arrow 2 denotes a peak corresponding with the intermolecular distances between the collagen microfibrils.

The beaker containing the $CaCl_2$ + PAH solution was then placed in an ammonia desiccator to allow formation of $CaCO_3$, whereafter it was connected to the flow cell by a pump system. The pump was activated and 1 min later SAXS and WAXS measurements were taken simultaneously every 5 min with an acquisition time of 3 min. Figure 15 shows the development of the SAXS signal over time.
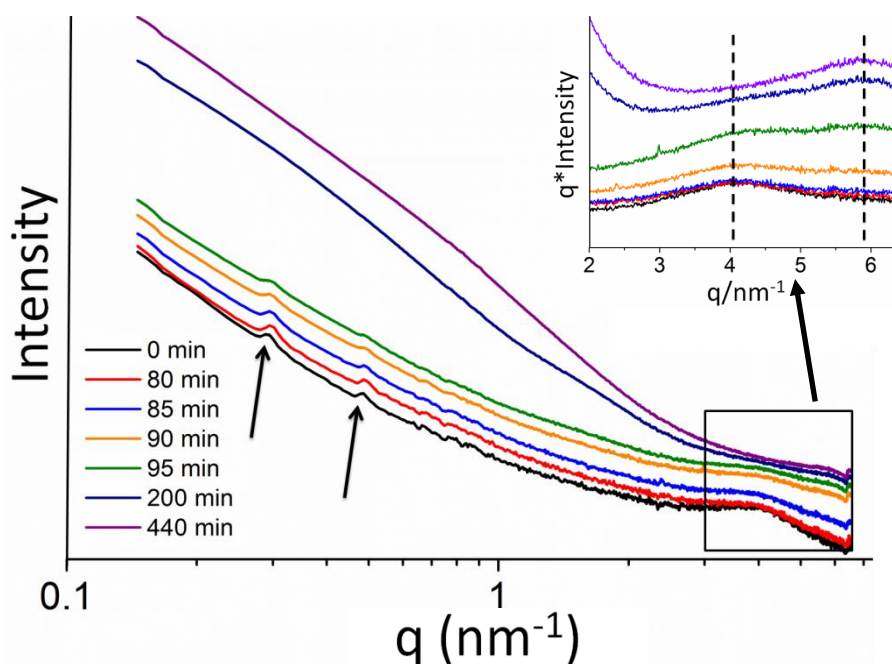
Figure 15: SAXS spectra collected of collagen mineralization with $CaCO_3$ (10 mM $[Ca^{2+}]$) in the presence of 1 mg/mL PAH at different time points. The two arrows denote the 3rd and 5th order peaks belonging to the axial organization of the collagen. The inset shows a plot of I(q)*q of the area marked by the black square. Left line shows the broad peak at 1.5 nm, corresponding to the intermolecular distances between the molecules of collagen. Right line marks the position of a peak at 1.1 nm demonstrating a more compact packing.

As can be seen from Figure 15 and Figure 17, the SAXS and WAXS signals were relatively constant during the first 80 min of the reaction. After 90 min though, the scattering intensity started to increase, which can be attributed to the formation and deposition of calcium carbonate inside or possibly on the surface of the collagen fibrils (Figure 15). Due to this, the 3rd and 5th order peaks of the collagen started to disappear due to masking by the intense signal of the mineral particles. Interestingly though, the peak at the Bragg spacing of $q = 4.08$ nm^{-1} in the SAXS spectrum, (intermolecular spacing of 1.5 nm between the collagen molecules) started to broaden further, which suggested an increase in the disorder in the lateral packing of the molecules. Remarkably, no crystalline peaks were observed in the WAXS spectrum (Figure 17), indicating only amorphous calcium carbonate (ACC) was forming in the reaction solution at this stage. These results therefore suggested that ACC infiltrated the collagen, causing a loss in order in the lateral packing of the collagen molecules. The

fact that this was taking place before crystallisation occurred made it even more interesting. Crystallinity then started to develop after 95 min of reaction, as can be seen in the WAXS pattern by the progressive appearance of a Bragg reflection corresponding to the (104) lattice planes of calcite at 19.64° (Figure 17). Simultaneously, the peak in the SAXS spectrum at $q = 4.08$ nm^{-1} started to decrease further, while at the same time a new shoulder was appearing at $q = 5.68$ nm^{-1}. This is ascribed to the reordering of the molecules, with the intermolecular distances decreasing from the initial 1.5 nm to 1.1 nm (Figure 15 inset). By fitting of the first peak with a Gaussian profile, it was demonstrated that the axial arrangement of the microfibrils didn't change. During the further development of the experiments this reflection was mostly unchanged in shape, with only a small, non-significant change in q value (Figure 16). These results are entirely consistent with previous experiments on *in situ* mineralization measurements with hydroxyapatite of turkey tendon[399], showing that the *in vivo* mineralization of collagen with calcium carbonate induced the same changes on the collagen structures.
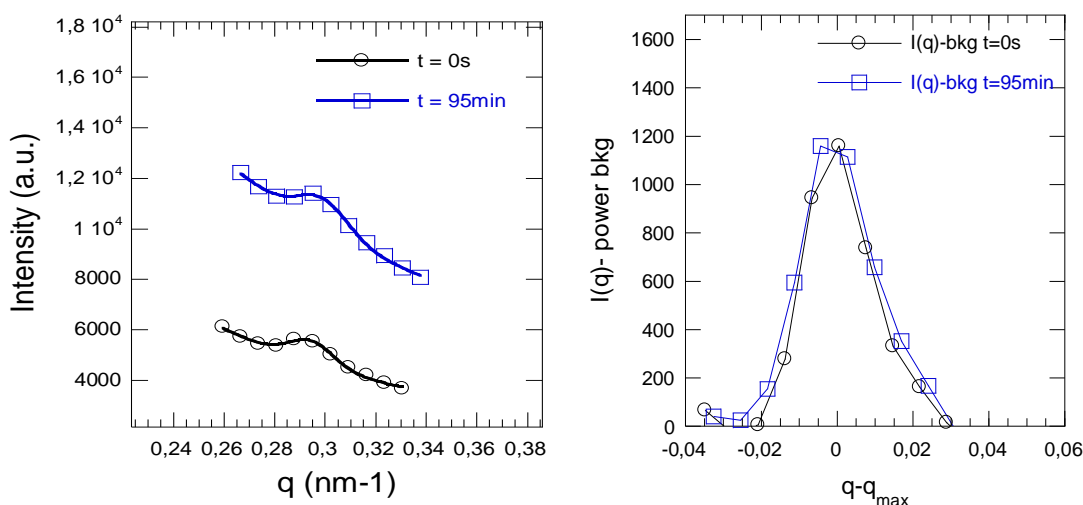
Figure 16: Gaussian (a) and power-background fit (b) of the first peak in the SAXS spectrum in Figure 15, at time = 0 min and time = 95 min. Figure prepared by Dr. Daniel Hermida Merino and Dr Giuseppe Portale from the ESRF

After 200 minutes of reaction, the 3rd and 5th order peaks of collagen could no longer be distinguished anymore as the scattering intensity of the SAXS spectrum was completely dominated by the scattering of the incipient crystals. The crystallinity continued to develop as shown in the WAXS pattern which also indicated that in addition to the

presence of calcite peaks, vaterite was detected, as shown by the characteristic vaterite peak of the (112) plane at 18.20° (Figure 17).
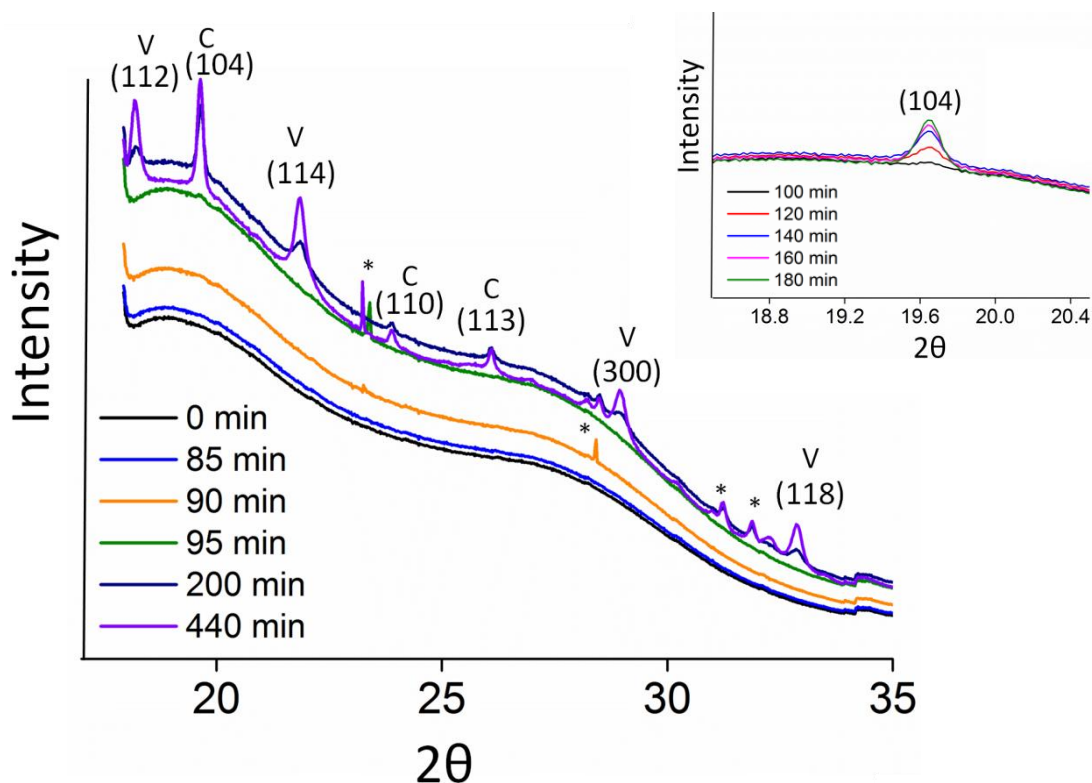
Figure 17: WAXS spectra of collagen mineralization with $CaCO_3$ (10 mM [Ca^{2+}]) in the presence of 1 mg/mL PAH at different time points. At the end of the reaction a mixture of calcite (noted by C) and vaterite (noted by V) peaks were found. The asterisk * indicates the background peaks due to cosmic X-rays or scattering of the mica window. The inset shows an expansion of the (104) calcite peak, demonstrating the gradual appearance of the peak.

After almost 7.5 h (440 min), the crystalline phase completely dominated the SAXS pattern, and the collagen was assumed to be completely covered with calcite and vaterite crystals. It was also observed that the peak at q = 4.08 nm^{-1} had disappeared at this time, being replaced by one at q = 5.68 nm^{-1} (Figure 15).

Further analysis of the SAXS pattern after 150 minutes of mineralisation showed that the mineral particles were plate-shaped, with a thickness of 5.4 nm and a polydispersity of ≤ 0.05, which is similar to the hydroxyapatite crystals found in bone (Figure 18).
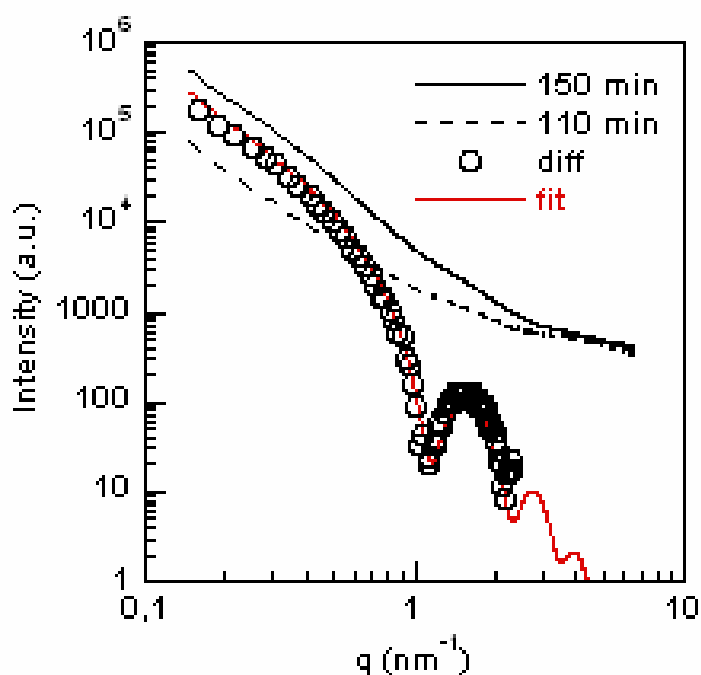
Figure 18: SAXS profile of Figure 15 after 440 minutes of mineralization of the collagen $CaCO_3$ (10 mM [Ca^{2+}]) in the presence of 1 mg/mL PAH. The q^{-2} slope at low q-values is indicative of flat mineralized particles, 5.4 nm in size with low polydispersity. Figure prepared by Dr. Daniel Hermida Merino and Dr Giuseppe Portale.

By analysis of the peak width in the WAXS spectrum it was possible to obtain information about the lateral dimensions of the $CaCO_3$ crystals using the Scherrer equation:

$$\tau = \frac{K\lambda}{\beta \cos\,\theta}$$
Equation 4

where τ is the mean size of the nanocrystals or ordered crystalline domains, K is a dimensionless shape factor with a typical value of 0.9, λ the X-ray wavelength, β the line broadening at half the maximum wavelength and θ the Bragg angle[408].

By analysis of the broadening of the (114) peak of vaterite in the WAXS pattern (see Figure 17) the size of the crystals was determined to be 21.3 nm. This evaluation does not distinguish between particle length and width and caution has to be taken when interpreting the results since peak broadening can also originate from microstrain fluctuations and instrumental parameters.

5.4.2.2 Studies with TEM

Given the results from the synchrotron, the formation of the calcium carbonate crystals was investigated again in more detail with TEM in order to obtain more information about the orientation of the plate-like $CaCO_3$ crystals. Studies were done at the University of Eindhoven by Dr. Fabio Nudelman. Horse tendon collagen and collagen sponges were used in this case, and instead of using a flow cell, the sponges were directly incubated in a 10 mM $CaCl_2$ solution containing 1 mg/mL PAH in an ammonia desiccator. In this case, collagen fibrils were found that were not covered with $CaCO_3$. Figure 19a shows a fibril mineralised with calcite where the crystals are orientated in the direction of the (104) plane, 28 degrees in correspondence with the collagen fibril axis. The orientation of the collagen fibril with respect to this plane was fibril specific and often a large angular spread of around 30° was seen. When vaterite was formed, the crystals in a single fibril were co-oriented, with a smaller angular spread, although the orientation was still fibril-specific (Figure 19b).
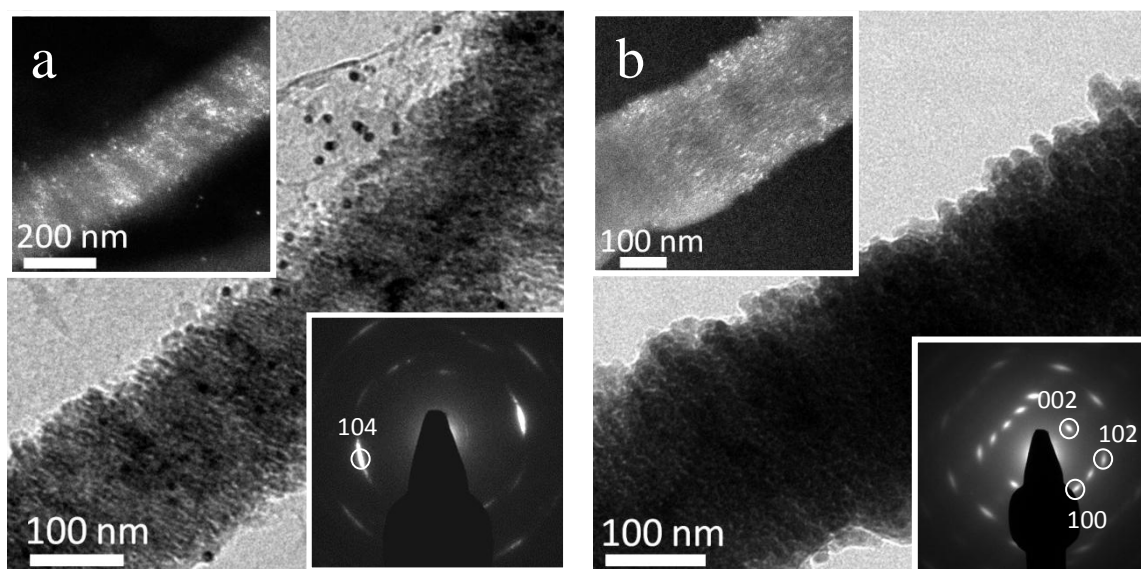
Figure 19: TEM images of collagen mineralized with $CaCO_3$ (10 mM $[Ca^{2+}]$) after 6 h in the presence of 1 mg/mL of PAH. (a) A horse tendon collagen fibril mineralized with calcite. In the inset a dark field image is seen showing the crystalline domains that contribute to the (104) reflection in the electron diffraction pattern. (b) A collagen fibril of a collagen sponge mineralized with vaterite. The inset shows the corresponding diffraction pattern and dark field image, highlighting the plate-shaped crystalline domains contributing to the (002) reflection. TEM done by Dr. Fabio Nudelman.

5.4.3 Studies on the infiltration of collagen sponges with $CaCO_3$ in the presence of PAsp

5.4.3.1 Studies with SAXS and WAXS

When the experiments were repeated with PAsp as an additive, similar results were obtained, although with a slightly faster crystallisation rate. In this case, almost no change in the SAXS spectrum was observed until 30 min, after which time the scattering intensity significantly increased (Figure 20). WAXS showed no crystalline material was present in the reaction until about 30 min, whereafter crystallisation started as shown by the progressive development of a Bragg peak corresponding to the (104) plane of calcite (Figure 21).
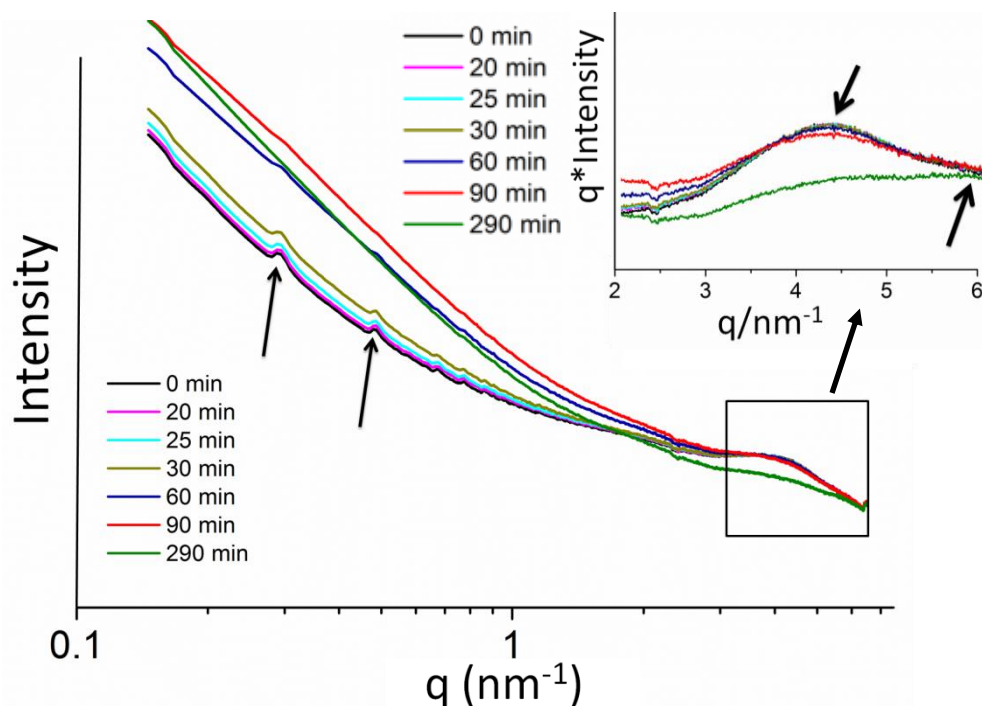
Figure 20: SAXS spectra collected at different time points of collagen mineralization with $CaCO_3$ ([10 mM $CaCl_2$]) in the presence of 50 µg/mL PAsp. The two arrows denote again the 3rd and 5th order peaks belonging to the axial organization of the collagen. The inset shows a plot of I(q)*q of the area marked by the black square. The left arrow shows the broad peak at 1.5 nm. The right arrow shows a peak at 1.1 nm demonstrating a more compact packing.

After 60 min, the mineral phase was predominantly crystalline and the 3rd and 5th order peaks had disappeared completely in the SAXS pattern, as the scattering was dominated

completely by the formation of the mineral phase. Further analysis of the pattern showed that it was only possible to observe broadening of the peak at 1.5 nm after 90 minutes of reaction, indicating the increase in disorder in the lateral packing of the microfibrils (see Figure 20 inset). In contrast to the experiments performed in the presence of PAH, this peak was still present in the pattern even after 290 minutes, but was now much broader. After this time, a broad peak at 1.1 nm also started to develop in the SAXS pattern (Figure 20 inset), suggesting that the microfibrils had reorganised into a more compact packing. At the end of the reaction, the WAXS pattern showed that the mineral phase consisted of a mixture of calcite and vaterite (Figure 21).
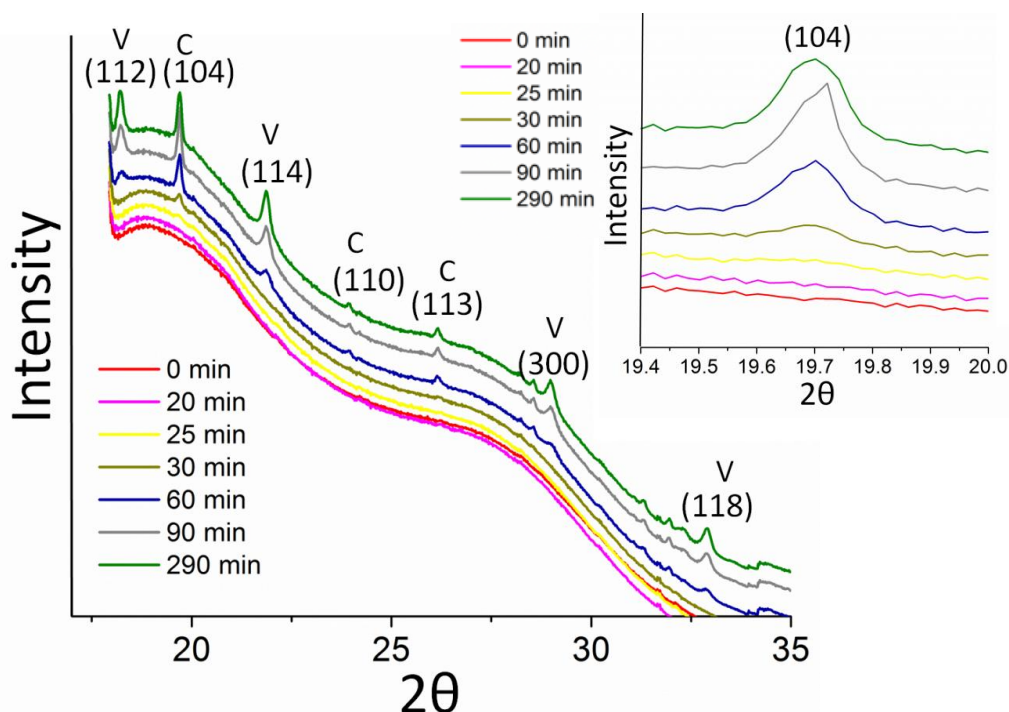
Figure 21: WAXS spectra collected at different time points of collagen mineralization with $CaCO_3$ ([10 mM $CaCl_2$]) in the presence of 50 μg/mL PAsp. When the reaction was finished, a mixture of calcite (noted by C) and vaterite (noted by V) peaks was found. The respective planes are indicated in the graph. The inset shows an expansion of the (104) peak of calcite.

5.4.3.2 Studies with TEM

TEM measurements were done again by Dr. Fabio Nudelman on collagen sponges and showed that after 3 hours of reaction, the collagen fibril were covered with droplet-like

structures, sticking to the collagen fibril (Figure 22a). It is assumed that these structures likely consisted of liquid-like ACC-PAsp complexes, infiltrating into the collagen. Interestingly, vaterite crystals of around 10 nm in size were only observed to start forming inside the collagen after 17 hours reaction time, which is comparable to the PAH system (Figure 22b). The orientation of the crystals with respect to the collagen fibril was again fibril specific.
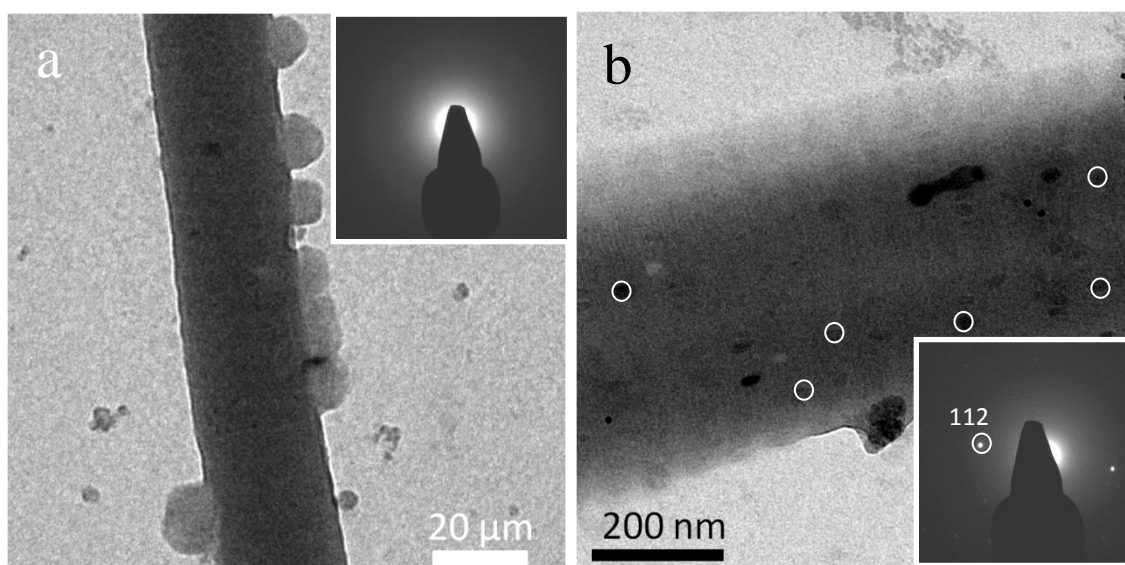
Figure 22: TEM images of collagen mineralized with $CaCO_3$ (10 mM $[Ca^{2+}]$) in the presence of 50 μg/mL of PAH, after 3 h (a) and 17 h (b). The insets show the corresponding amorphous (a) and vaterite (b) diffraction pattern of the fibrils. (b) Shows very small particles are visible within the collagen fibril (white circles). TEM done by Dr. Fabio Nudelman.

5.4.4 Studies on the infiltration of collagen sponges with $CaCO_3$ in the absence of additives

To determine whether PAH and PAsp are necessary for the infiltration of the collagen fibrils, collagen was mineralized with $CaCO_3$, in the absence of additives (Figure 23, 24). In this case, no $CaCO_3$ was found inside or on the surface of the individual fibers. Almost no change was observed in the SAXS spectrum until 150 min reaction time, when the scattering became completely dominated by the mineral particles, and the peaks corresponding to the collagen structure could no longer be observed (Figure 23). The results revealed that there was no change in the fibrillar structure of the collagen,

and the axial and lateral packing of the molecules didn't change during the mineralisation event.
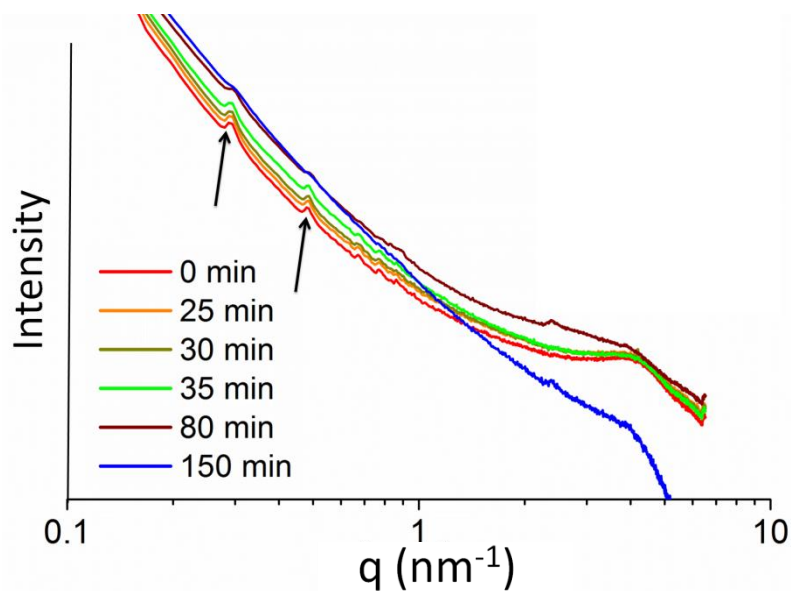
Figure 23: SAXS pattern collected of a collagen sponge in a 10 mM $CaCl_2$ solution put an ammonia desiccator, collected at different reaction times. The arrows show the 3rd and 5th order peaks belonging to the axial organization of the collagen.
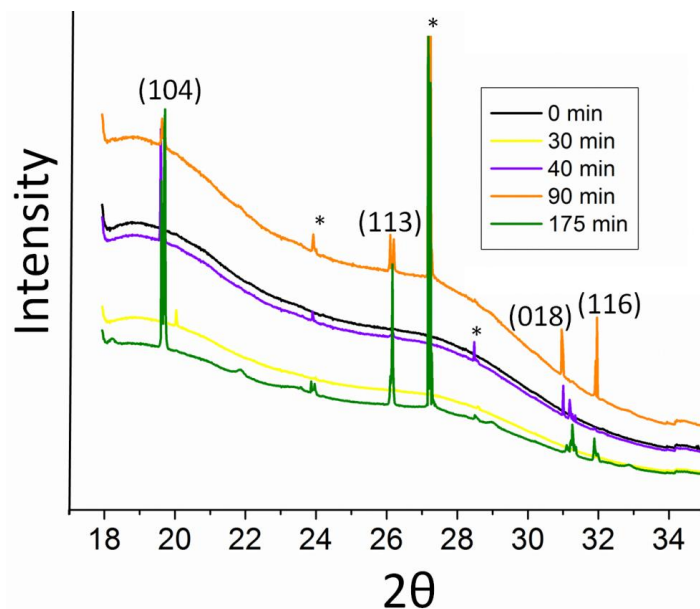
Figure 24: WAXS spectrum of a collagen sponge in a 10 mM $CaCl_2$ solution put in an ammonia desiccator, collected at different reaction times. All the diffraction peaks were appointed to calcite. The asterisk* sign indicates the background peaks.

WAXS measurements which were done in parallel with the SAXS measurements. showed that crystalline calcite particles started to develop after 30 min of reaction. Characteristic peaks of the (104), (113), (018) and (116) planes of calcite were distinguished (Figure 24).

After the SAXS and WAXS experiments were done, the sponges mineralized with $CaCO_3$ were taken out of the flow cell and analysed with SEM. In the control sample, where the sponges were mineralized without additives, the collagen fibrils stayed almost completely clean and only a few rhombohedral calcite crystals were found, scattered on the surface of the fibrils (Figure 25a). In the presence of additives, no calcite crystals were present on the collagen and the fibrils had the appearance of being mineralised (Figure 25b).
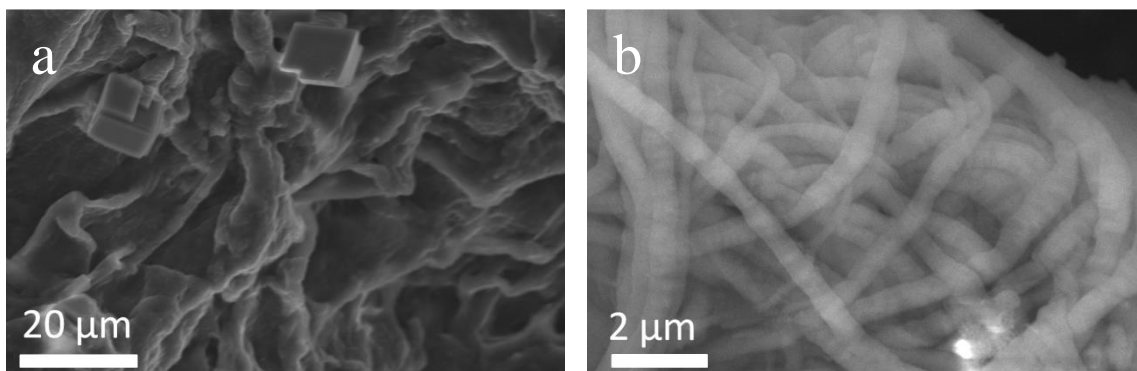
Figure 25: FEGSEM images of sponges mineralized with $CaCO_3$ after the SAXS and WAXS measurements in the absence of additives (a) and with PAH (b). SEM done by Dr. Fabio Nudelman.

5.5 Discussion

5.5.1 Comparison with previous observations

As discussed in the introduction, infiltration of collagen fibrils with calcium carbonate crystals has been investigated before in the presence of PAA with SEM[126], where it was proposed that an amorphous polymer-induced liquid-precursor (PILP) phase of $CaCO_3$ infiltrated the collagen fibrils by capillary action. Collagen fibrils covered with $CaCO_3$ were found and an interesting periodic banding pattern of calcite disks was observed, with a spacing of about 6 times that of the banding pattern observed for native type I

collagen. However, the morphology of these $CaCO_3$ crystals, and the crystallographic orientation of the crystals formed inside the collagen (if formed) was never described or discussed.

The results described here, show that similar results are obtained using PAH and PAsp. In the light of previous results described in chapter 4, this can be expected as PAH and PAsp are able to stabilise a liquid-like amorphous phase of $CaCO_3$[28, 77]. Different from the results with PAA is the time frame of crystallisation. Previous results suggested that crystallisation in the presence of PAA takes days, while in our experiments, crystallisation occurred after a couple of hours. This was most probably due to the set-up (use of a liquid cell and pumping system, different kinds of preparation of collagen), different polymer, and also the reduced amount of polymer used (50 µg/mL PAsp instead of 200 µg/mL PAA) which might have influenced the kinetics. The disks formed on the collagen itself in the presence of PAH were also much closer together then discussed in the presence of PAA (20 nm instead of 250 - 500 nm apart), although this was most probably due different type of collagen substrate (in our study we used horse tendon type I collagen instead of reconstituted bovine collagen).

5.5.2 Infiltration mechanism and effect on collagen

To obtain some more information about the infiltration mechanism and its influence on the crystallisation of the $CaCO_3$ crystals, the infiltration in the presence of PAsp and PAH was investigated with TEM and synchrotron X-ray scattering techniques. In this way we were able to demonstrate collagen does indeed get infiltrated by $CaCO_3$, influencing the structure of the organic template. This could be seen in the broadening of the Bragg peak at spacing of q = 4.08 nm^{-1}, corresponding to an intermolecular spacing of 1.5 nm. The broadening of the Bragg peak at q = 4.08 nm^{-1} was related to an increase in the disorder in the lateral packing of the molecules, due to displacement of the water molecules[399]. At the same time, an increase in intensity of the SAXS scattering was also observed, which was attributed to the formation calcium carbonate around the collagen fibrils. Since at this time point no crystalline peaks were observed in the WAXS spectrum, only amorphous calcium carbonate could have formed. Infiltration of liquid-like amorphous calcium carbonate into the collagen was therefore responsible for the increase in disorder of the lateral packing of the collagen molecules.

Chapter 5: Templating Calcium Carbonate into Nanoscale Plate-shaped Crystals by the Use of Collagen

The liquid-like properties of this amorphous calcium carbonate phase stabilised by PAsp or PAH has been discussed in previous papers[12, 28] and its infiltration into nanoporous templates has been demonstrated before[29, 84] (see also chapter 4). The subsequent decrease of the peak at $q = 4.08$ nm^{-1} and appearance of a new peak at $q = 5.68$ nm^{-1} was linked to the reordering of the molecules during crystallisation since at that time crystalline peaks for calcite and later vaterite also appeared in the WAXS spectrum. The formation of the crystalline particles reduced the molecular spacing of the collagen from the initial 1.5 nm to 1.1 nm by compressing the molecule packets that are between them. A similar phenomenon has been observed for collagen mineralised with HAP, as studied with SAXS[399]. It has to be noted the axial arrangement of the microfibrils didn't change during the course of the experiments, as was demonstrated by fitting of the 1st peak with a Gaussian.

During the reference experiments in the absence of additives, crystallisation is much quicker than in the presence of PAH and PAsp, which has been observed before and can easily be explained due to the inhibiting effect of the polymers[28, 80]. Whether collagen also has an influence on stabilisation of the amorphous phase is not entirely clear, but collagen is known to inhibit HAP nucleation[409] and calcite growth[131]. Mineralisation of CaCO$_3$ in collagen hydrogels showed that 18% of the calcium carbonate could be stabilized as amorphous calcium carbonate[410]. This stabilization could last till 6 weeks when the gel containing the CaCO$_3$ was stored in deionised water. The exact reason for this stabilization was not addressed, although the results suggested that the fiber diameter, fiber spacing, and the amphoteric nature of the collagen fibers were important. It is also not clear from our results whether confinement itself had an effect on the crystallisation, but is expected, taken into consideration previous results where ACC was stabilized by confinement[152].

5.5.3 Comparison with calcium phosphate in collagen

TEM and SAXS data showed further that the infiltration of CaCO$_3$ inside the collagen allowed moulding of the shape of the crystals, resulting in the formation of remarkable calcite and vaterite crystals of 5 nm thick. These crystals are therefore only about 13 unit cells thick, which is very intriguing, taken into account that at this size they should

not be able to crystallise[71, 152, 411, 412]. The moulding of the ACC phase leading to crystals with remarkable morphologies has been demonstrated before[12, 29, 31, 162] and it is thought that this stabilisation of thin crystals must be achieved by strong interactions between the collagen and the mineral. Looking at the formation of hydroxyapatite (HAP) during bone formation, both the morphology and crystallographic orientation of the crystals are well controlled by the collagen[3, 180, 397]. In the case of calcium carbonate, the morphology of the crystals was also well controlled while the crystallographic orientation was not. It therefore seems that two different mechanisms are involved by which collagen controls the mineral formation. In a first mechanism, the morphology is templated by providing a confined environment in which the crystals nucleate and grow. This has been demonstrated to be possible before where next to $CaCO_3$[171], porous single crystals of $SrSO_4$, $PbSO_4$, $PbCO_3$, $NaCl$ and $CuSO_4.5H_2O$ were formed by moulding the crystal shape by the use of a template[32] even without the necessity of an amorphous phase. It seems therefore, also for the case of collagen, the templating mechanism is not specific to HAP, and can be extended to other minerals as well.

The control over crystal orientation and alignment, on the other hand, appears on the first hand to be specific to HAP. One possible explanation is that the surface chemistry of the collagen interacts differently with calcium carbonate and calcium phosphate crystals. Previously it was thought that the orientation of the HAP crystals in collagen is influenced by the 3-dimensional architecture of the nucleation sites, formed by the charged amino acids of collagen, effecting the coordination of the calcium and phosphate ions[196, 198, 199]. For calcium carbonate this effect might be different.

Yet, taking into account the results of chapter 3 where it was proven that an alignment effect of HAP can be achieved purely by a confinement effect, it might be that the surface chemistry of the collagen might not play such a large role in the orientation of the crystals at all. HAP nucleates as plate-shaped crystal 200 nm in size and has a strong anisotropy in its crystal lattice self with the [001] axis as the axis of fastest growth[243, 291]. It is therefore not much of a surprise, when HAP nucleates inside the collagen gaps, the crystals are oriented with their [001] axes coincident with the long axis of the collagen fibrils. Calcite on the other hand, generally forms rhombohedra 20-40 micrometers in size and doesn't have a strong axis of fastest growth[413]. The effect of confinement on the orientation is therefore expected not to be as significant and the

crystals are randomly oriented. Considering vaterite, stronger orientations than for calcite are expected, since at our working pH of 9.5, vaterite often forms disk-like structures[414-416], with a (001) zone axis and the (110) face as fastest growing face[415]. From the above shown results, the vaterite crystals seem to be more oriented with respect to the fibril although this is very fibril specific (Figure 22). More TEM research will be performed to investigate this further.

The results discussed in chapter 3 also raised doubt about the calcium phosphate PILP theory. As discussed before, filling of the collagen fibers with calcium phosphate, might be driven by a molecular interaction between the net negative surface charge of the stabilised PAsp/ACP complexes and the positively charged regions in the collagen fibril[196]. In the $CaCO_3$ system though, a PILP phase has been clearly demonstrated[28, 29, 77] and allows infiltration of the nanosized pores of collagen by capillary action. Whether these different infiltration mechanisms are connected to the differences in orientation of the crystals is not clear.

5.6 Conclusion:

This chapter investigated the infiltration of collagen with calcium carbonate. It was shown that calcium carbonate precipitates within collagen fibrils when the reaction is carried out in the presence of PAsp and PAH. The additives induce the formation of a liquid-like amorphous phase of $CaCO_3$, which infiltrates the collagen due to capillary action, increasing the disorder in the lateral packing of the collagen molecules. This is followed by crystallisation of the amorphous particles, which reduces the molecular spacing of the collagen from the initial 1.5 nm to 1.1 nm by compressing the molecule packets between them. Due to the moulding effect of the collagen, remarkable 5 nm thick crystals of calcite and vaterite are formed, randomly oriented with respect to the collagen fibril. The origin of this random orientation is not entirely clear. This study therefore demonstrates that collagen has the ability to template different type of minerals than calcium phosphate, and is already being investigated for other materials such as iron oxide.

Chapter 6: Formation of Hollow Calcium Carbonate Rods
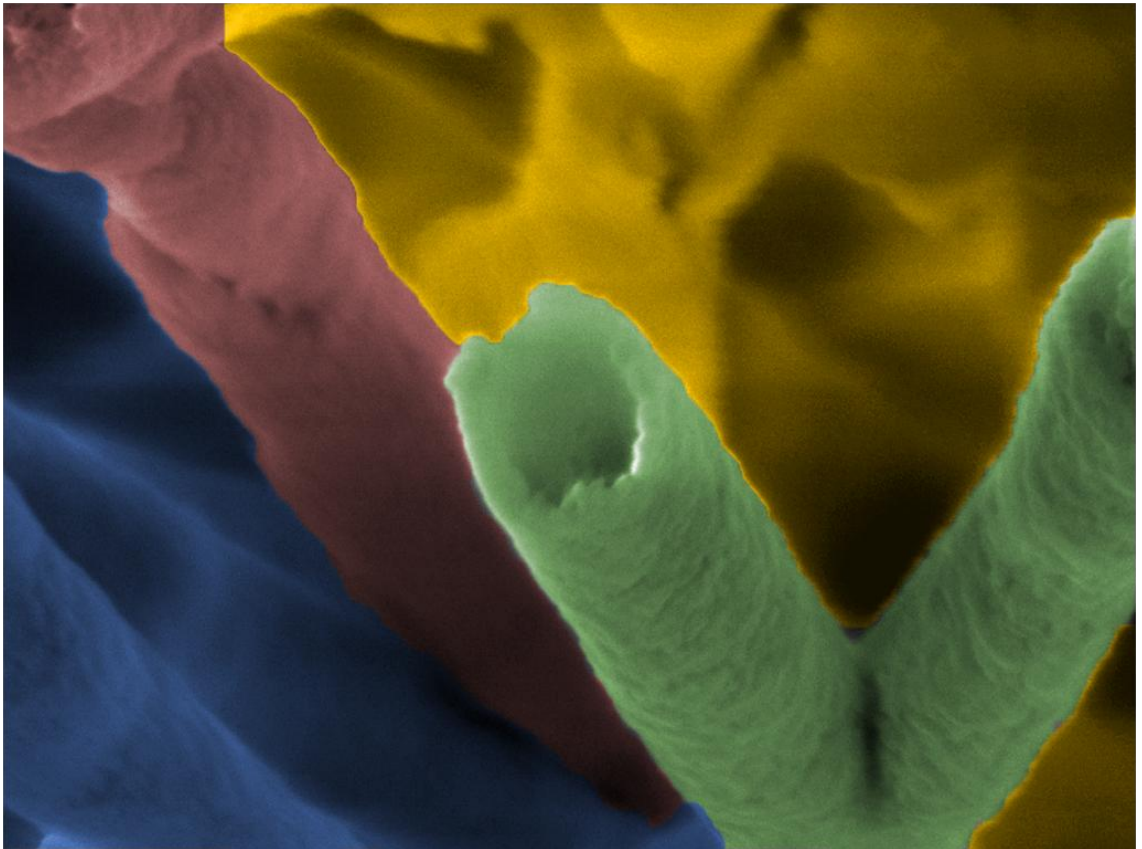
Chapter 6: Formation of Hollow Calcium Carbonate Rods

This chapter deals with the formation of hollow $CaCO_3$ rods, templated in the pores of track-etched membranes. Previous research already demonstrated the production of solid, rod-shaped single crystals of calcite by the use of nanosized track-etched membrane pores as templates[29, 31, 172]. With the formation process and crystallinity of these rods investigated, further research is carried out in this chapter to investigate different ways of controlling the morphology of the rods. Therefore track-etched membranes with nanosized and micron sized pores were used, and the effect of the pore size and surface morphology of the membranes was investigated. In addition to solid rods which had been observed before, hollow rods of $CaCO_3$ were also detected. These hollow rods formed in small pore sizes at early timescales and remained hollow in the case of bigger pore sizes. By changing the surface chemistry of the track-etched membrane pores, the amount of hollow rods increased, especially in the case of the 200 nm pores.

6.1 Introduction

6.1.1 Formation of hollow structures

Over the past two decades, formation of hollow structures became a hot topic in the material science area, due to their many applications in drug delivery, catalysis, coatings and the formation of composite materials[417, 418]. Commonly, nanostructures with hollow interiors, can be prepared by coating the surface of colloidal templates (such as gold or silver particles or silica beads) with thin layers of the desired material, followed by a selective removal of the colloidal template through calcination or chemical etching[419]. In this way, hollow nanostructures such as nanoshells and tubes of gold, platinum and palladium were prepared, from silver nanostructures as templates[419].

Another successful technique is the use of porous membrane templates such as alumina and polycarbonate track-etched membranes[178, 420, 421]. By the use of this technique, hollow rods of silica were deposited in polycarbonate track-etched membranes by interactions of silica particles with the polycarbonate surface[420]. After formation of the hollow rods, the tubes were progressively filled from the initial shell to the core with silica nanoparticle aggregates. Due to the absence of direct contact with the polycarbonate surface, these particles were loosely packed within the tube interior, in contrast to the dense coating deposited on the pore internal surface. Furthermore, silica

nanotubes could also be obtained in gels[422] and by a reversible micelle sol-gel method[423]. Nanotubular structures of other types of oxide materials were additionally formed by coating of templates such as carbon nanotubes, polymer and metal nanorods and nanowires, polycarbonate membranes and anodic aluminium oxide membranes, followed by removal of the template materials by dissolution, chemical etching and/or pyrolysis[178].

Hollow organic microtubules of polymers were prepared within the pores of track-etched membranes by preferential absorption of the polymer chains on the pore walls. The adsorption of the nascent polymer chains to the pore walls yielded a thin polymer "skin" which became thicker and thicker with time[421]. Depending on the polymer, the tubes could then completely fill to form solid fibers[424], or in some cases remained tubular even after long periods of time[425]. This was later thought to be due to the surface layers growing completely across the membrane surface and blocking the pore ends so tubes remained empty[425]. It was further reasoned that a strong electrostatic interaction between the pore wall and the depositing polymer material promoted the formation of hollow tubes rather than solid rods.

6.1.2 Track-etched membrane technique.

Previous research demonstrated the production of rod-shaped single crystals of calcite by the use of track-etched membrane pores as template material[29, 31, 172]. This was achieved by the deposition of amorphous calcium carbonate (ACC) within membrane pores of 50 nm to 10 μm, by the use of a double diffusion method. Polycrystalline rods with their shape dictated by the surrounding membrane pore were formed at bigger pore sizes of 10 μm, while the use of smaller sizes (200 nm) even allowed formation of single crystal rods of calcite, especially where ACC was stabilised at low temperatures[31].

In later research this system was further optimized by addition of polyacrylic acid (PAA)[29]. This resulted in the formation of an amorphous precursor phase, which infiltrated into the pores and subsequently crystallised to give single crystals of calcite with rod-like morphologies and aspect ratios of up to 100. These rods were randomly oriented, and the infiltration was thought to be achieved by capillary action of a polymer stabilised ACC phase (PILP phase, see section 1.2.2.3) with liquid-like properties. Once infiltrated, the amorphous phase crystallised and due to limiting contact of the

mineral with the bulk solution in the membrane pores[29], single crystals were formed. Since the transformation of the amorphous phase to the crystalline phase was accompanied by a loss of water, a reduction in the volume of the mineral phase of 26% was expected[29].

6.1.3 Layer-by-Layer deposition (LBL) techniques

In this chapter, the effect of the surface chemistry during the crystallisation of calcium carbonate in confinement has been investigated by functionalization of the pore walls of track-etched membranes using a layer-by-layer (LBL) technique. The concept of LBL techniques was first utilised in 1992[426] where it was demonstrated that layers of cations and anions could be built up by exposure of a substrate to alternating solutions of positively and negatively charged polyelectrolytes (eg PAA or PAH) (Figure 1). The procedure proved to be very versatile and useful for incorporating of charged compounds and nano-objects[427-429] and formation of hollow spheres[417].
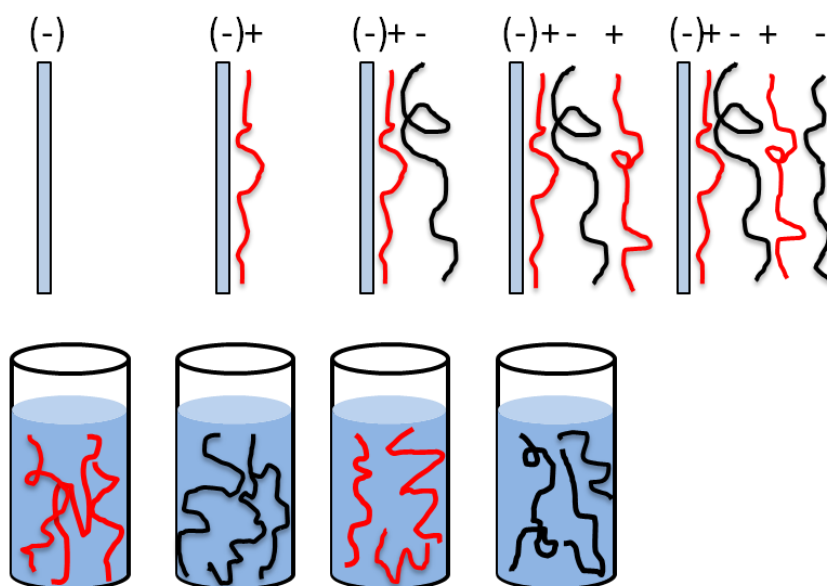
Figure 1: Schematic representation of the LBL technique, showing polycations (red) and polyanions (black) adhering to a negatively charged substrate.

Figure 1 shows a schematic diagram of the process, but it has to be noted that the representation of the distinct layers in an LBL multilayer assembly has to be considered as a simplified view of the formation mechanism[430]. The LBL layers are usually very stable in solution, due to the large number of electrostatic bonds involved in their

formation. In addition to electrostatic interactions, secondary interactions such as hydrophobic attraction and other intermolecular forces between the electrolytes, are considered as the driving force for the formation of LBL films. Furthermore, the increase in entropy associated with the release of counterions and solvent molecules from the hydration shell during the formation of an LBL film also plays a role in its stabilisation. It was found before that the diffusion of the polyelectrolyte chains themselves through the LBL assembly is extremely slow (undetected after 1 year), yet the equilibration by chain rearrangement of the outer layer takes place on the time scale of hours[431, 432]. The LBL films can often be viewed as dense hydrogels with strong hydration and swelling properties.

Previous studies investigated the deposition of $CaCO_3$ on metal substrates functionalized by LBL films of chitosan and poly(acrylic acid) (PAA)[433]. The LBL layers were assembled in such a way that the first and last layers were PAA, deposited from a 10 mM solution of $CaCl_2$. From the water containing Ca^{2+} counterions which were trapped within the LBL structure, $CaCO_3$ films were precipitated by the ammonia diffusion method, under conditions of high humidity. By not immersing the substrate in bulk solution during growth, $CaCO_3$ film was also forced to form within the gel-like structure of the LBL. In this way a dense homogenous and continuous film of $CaCO_3$ nanocrystals assembled on the substrates.

6.2 Aims of the project

The aim of this research is the investigation of the formation of hollow calcium carbonate rods when infiltrated inside track-etched (TE) membranes. Hollow structures of $CaCO_3$ gained much interest during the last decade due to interesting applications, such as encapsulation and controlled release of inks, flavours and other chemical reagents[434, 435]. Due to its biocompatibility and biodegradability, hollow structures of $CaCO_3$ are also of great interest for drug delivery[434, 436]. Hollow micron-sized tubes of $CaCO_3$ have been prepared under various conditions[434, 435, 437], however, they were often prepared under complex reaction conditions and were limited to small batch productions.

In this chapter, we investigated the possibility of forming hollow rods by templating them in TE membranes. By the use of a layer-by-layer (LBL) technique, the effect of

the surface chemistry of the pore walls of the TE membranes on the formed product was also investigated.

6.3 Experimental

Calcium carbonate crystals were precipitated inside track-etched (TE) membranes with pore sizes of 50 nm (Millipore polycarbonate membrane filters), 200 nm; 800 nm, and 3 μM and 10 μm (Sterlitech polycarbonate membrane filters). The TE membranes were 10 to 15 μm thick. A track-etched membrane was put in a Petri dish filled with 10 mM $CaCl_2.2H_2O$ solutions containing variable amounts of polyacrylic acid (PAA) and placed in an ammonia desiccator. The membranes were then removed from the reaction solution after different amounts of time. As mentioned in chapter 3, analysis of the track-etched membranes with FEGSEM (see 3.5.2) showed that the sizes of the pores ranged ± 20% from the size on the pack. This was especially the case for the smaller pore sizes so 200 nm pores were actually 150 nm to 250 nm and 50 nm pores were ≈ 40 nm to even 100 nm.

6.3.1 LBL method.

To alter the surface chemistry of the membranes a layer-by-layer (LBL) method was used. After cleaning of the membranes with the plasma cleaner, they were placed immediately in chitosan solution (0.1% w/w) and degassed under a reduced pressure (5-10 mbar) for 40 minutes. The chitosan solution was prepared by dissolving chitosan (molecular weight 161 g/mol) in 1% acetic acid and filtering though 0.45 μm syringe filter whereafter the pH was adjusted to 5.4 with NaOH. After 40 min under reduced pressure, the pressure was brought back to ambient and the membranes were allowed to soak in the chitosan solution for another 20 min. The membranes were then taken out of solution and the surface was wiped clean with a filter paper and washed by placing it in DI water for 5 min. In the next step, the membranes were transferred to a 0.1% w/w Ca/PAA solution (10 mM $CaCl_2.2H_2O$, 8000 g/mol PAA) followed by degassing and wiping clean as described above. Instead of using DI water, the membranes were washed in 10 mM $CaCl_2.2H_2O$ for 5 minutes. To obtain the desired number of layers, the chitosan and PAA deposition steps were repeated as necessary. In this way, membranes with either a positively charged chitosan outer layer or negatively charged

PAA outer layer were formed. Finally, the membranes were soaked in the relevant crystallization solutions overnight before initiating crystal growth by exposure to NH_3/CO_2 vapours. It has to be pointed out though that although the chitosan was positively charged under the deposition conditions, it might become less positively charged under conditions of $CaCO_3$ growth by the ammonia diffusion method.

6.4 Results:

A summary of the results is given in following table:

Table 1: Overview of results

Pore size	In absence of PAA	In the Presence of PAA	Surface modified by LBL
50 nm	no rods	Solid calcite rods (pores 90% filled)	No effect
200 nm	Few rods (pores 10% filled), some hollow appearance (5% of total rod population).	Many calcite rods (Pores 90% filled), some hollow at early times (50% of total rod population).	Many hollow vaterite rods which remained hollow after long time (80% of total rod population).
800 nm	Few rods (pores 10% filled), some hollow	More rods (90% filled), some hollow at early times (50-60%)	No effect
3 μm	Some solid rods (pores 10% filled)	Hollow rods (60%) and solid rods at later times	No effect
10 μm	No rods	Hollow rods (50%) and solid rods (60%) at later times	No effect

6.4.1 Precipitation of $CaCO_3$ in native TE membranes

6.4.1.1 Precipitation within nanoscale pores (50 nm, 200 nm and 800 nm)

Formation of material in 50 nm pores produced solid rods (pores 90% filled) after 6 h with lengths of 500 nm to 5 μm giving rods with aspect ratios of 100 (Figure 2). This is

much smaller than the thickness of the membrane but the rods might have been broken during the filtering process. Without PAA, almost no rods were found.
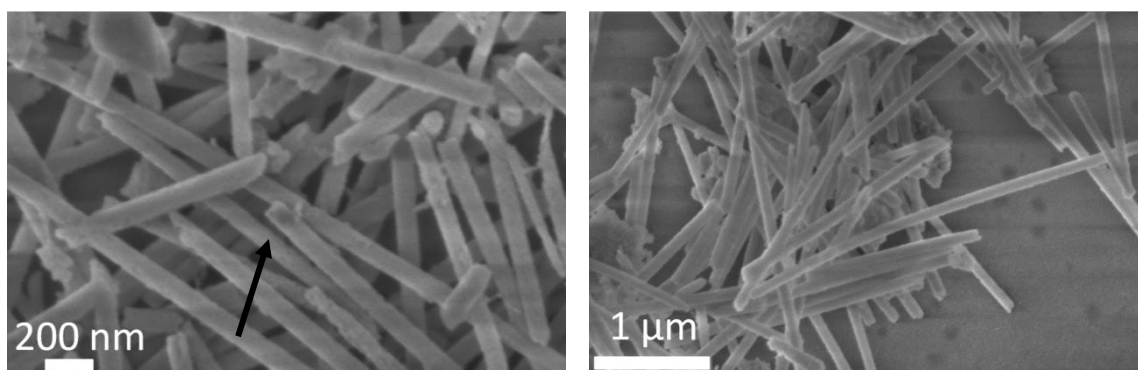
Figure 2: FEGSEM images of rods formed in 50 nm pores after 6 h from a 10 mM $CaCl_2$ solution containing 50 µg/ml PAA. No hollow rods were found. Arrow denotes a clear solid rod.

TEM analysis together with selected area electron diffraction (SAED) shows that these rods were single crystals of calcite (Figure 3).
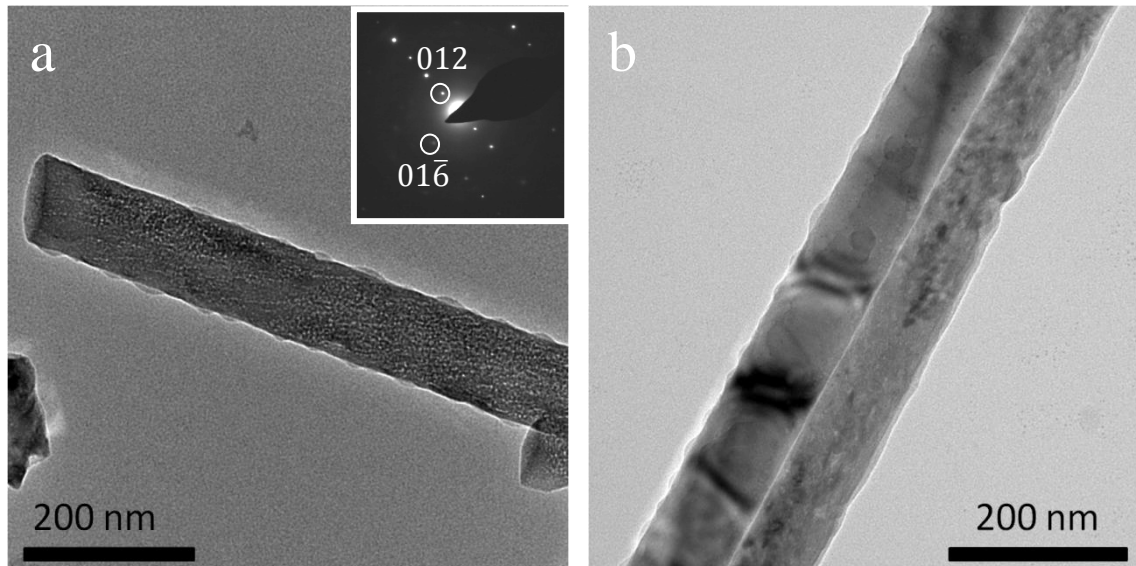
Figure 3: TEM images of rods formed in 50 nm pores after 1 day from a solution containing 50 µg/ml PAA.

In addition to solid rods, small hollow rods (5% of total material present) were found at early timescales of 6 h (Figure 4). These rods were usually only a couple of nm long

and were constructed from smaller particles 35 nm in size. Strangely the diameter of these rods was ≈ 200 nm.
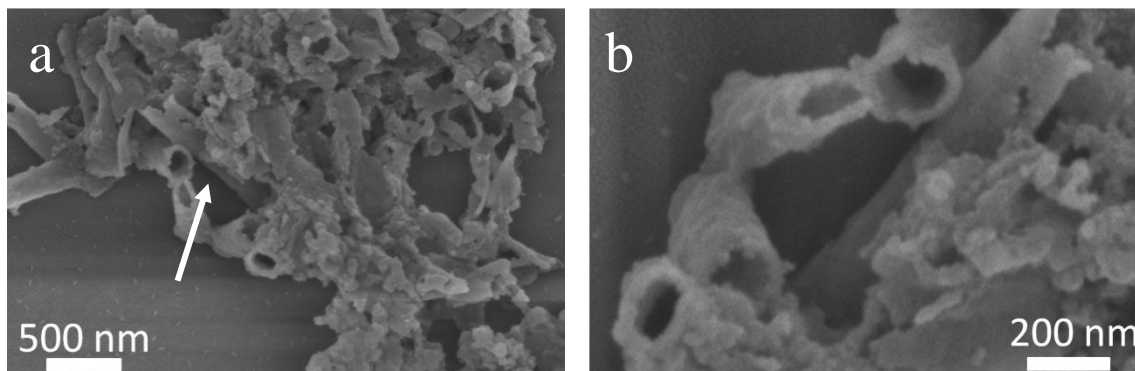
Figure 4: FEGSEM images of rods formed in 50 nm pores after 6 h from a solution containing 50 µg/ml PAA. Very small rods were formed with diameters of ≈ 200 nm and 500 nm long. The arrow denotes the side view of a rod.

In 200 nm pores, a significant amount of hollow rods (50% of the total rod population) were formed at early timescale in the presence of PAA (Figure 5a, b). Some rods also existed out of a shell surrounding particles inside (Figure 5b). The thickness of the shell varied from 50 nm (Figure 5b) at early timescales to 100 nm at later stages (Figure 5f). The nanoparticles were 10-15 nm in size and filled up the rods (Figure 5b).
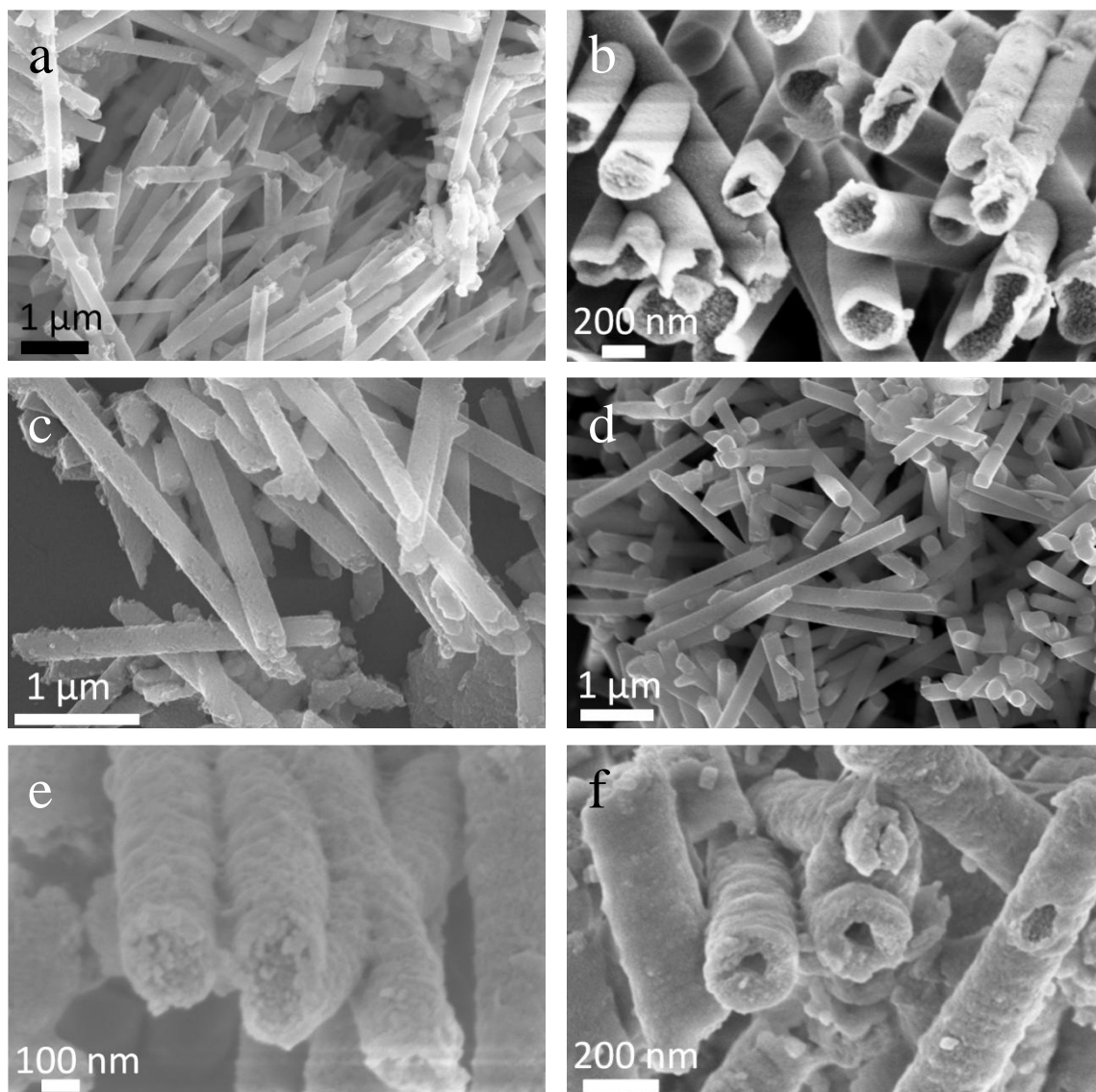
Figure 5: FEGSEM images of rods formed in 200 nm pores after 6 h (a, b, c), 1d (d, e) and 3 days (f) from a solution by addition of 50 µg/ml PAA (a, b, d, e, f) and in the absence of additives (c).

In the absence of PAA far fewer rods were formed (10% of the pores were filled) and almost none were hollow (5% of total rod population) (Figure 5c). The rods themselves were also much more granular. After 1 to 3 days almost no hollow rods were left in any condition and most rods were filled (90% of the rods) (Figure 5d, e). Some of the rods had stayed hollow but contained a much thicker shell wall (Figure 5f). The rods had an average length of 4 µm.

Investigation with TEM didn't provide any proof that the rods were hollow and all had a solid appearance (Figure 6). Selected area electron diffraction (SAED) allowed us to

identify the rods as calcite. Both single as polycrystalline rods were found, where addition of additives produced more single crystals.
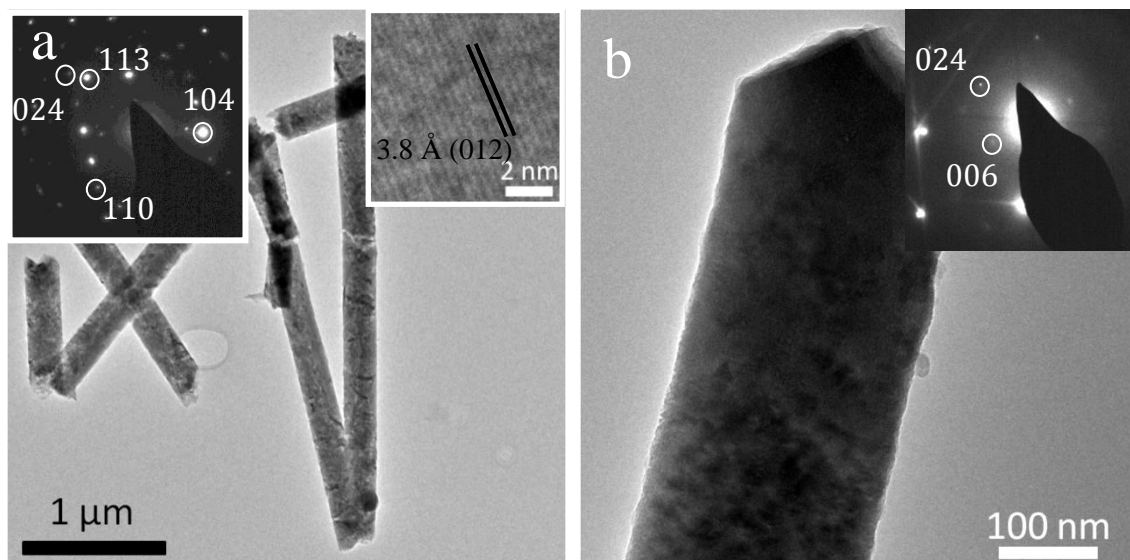
Figure 6: TEM images of rods formed in 200 nm pores after 1 day from a solution containing 50 µg/ml PAA. The diffraction patterns corresponded to calcite.

In the case of 800 nm (Figure 7), a substantial amount of hollow rods were found in the presence of PAA (about 50-60% of total rod population). The rods themselves were 4-5 µm long. After 1 day, almost all rods were solid except for a few which were still partially hollow (about 10%) (Figure 7d). The shell of the hollow rods was much thicker at later stages then at early stages (From 100 nm to 270 nm) (Figure 7b and d).
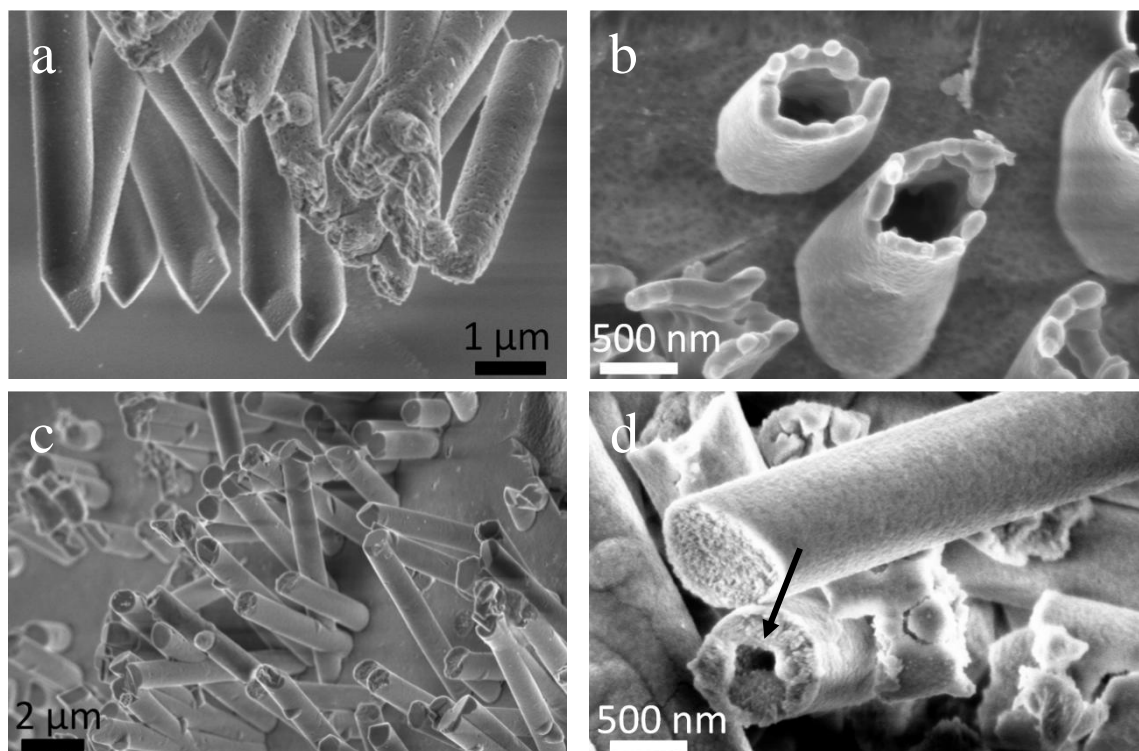
Figure 7: FEGSEM images of rods formed in 800 nm pores after 6 h (a, b) and 3 days (c, d) from a solution containing 20 µg/ml PAA (a, b, d) and no PAA (c). Mostly solid but some hollow rods were found (arrowed in d).

6.4.1.2 Precipitation within micron scale pores (3 µm and 10 µm).

When formed in the 3 µM pores, a lot of hollow rods were found at early timescales of 3 h in the presence of PAA (60% of total rod population) (Figure 8). These rods often consisted of small particles (50 nm) and were only about 500 nm long or thick (Figure 9a). The rods often had a rough surface on the outside. The yield of the rods (70% of the pores filled) was much smaller then when formed in the 50 and 200 nm nanoscale pores.
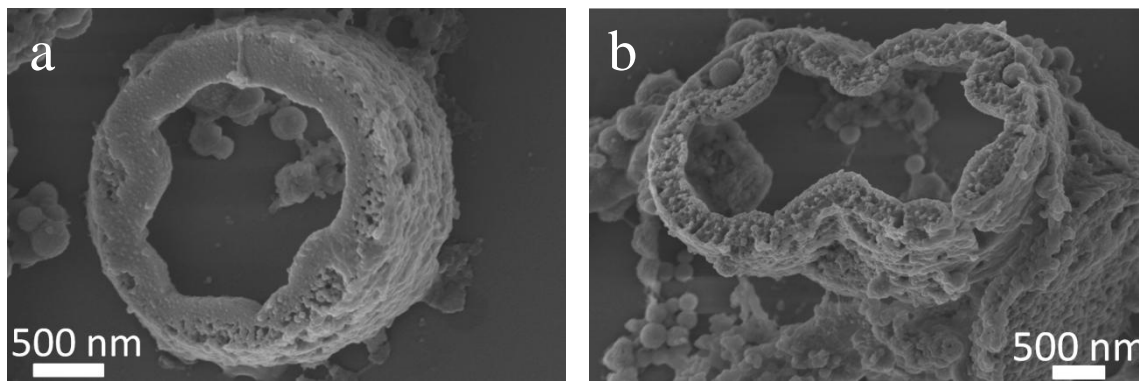
Figure 8: FEGSEM images of rods formed in 3 μm pores after 3 h from a solution containing 50 µg/ml PAA.
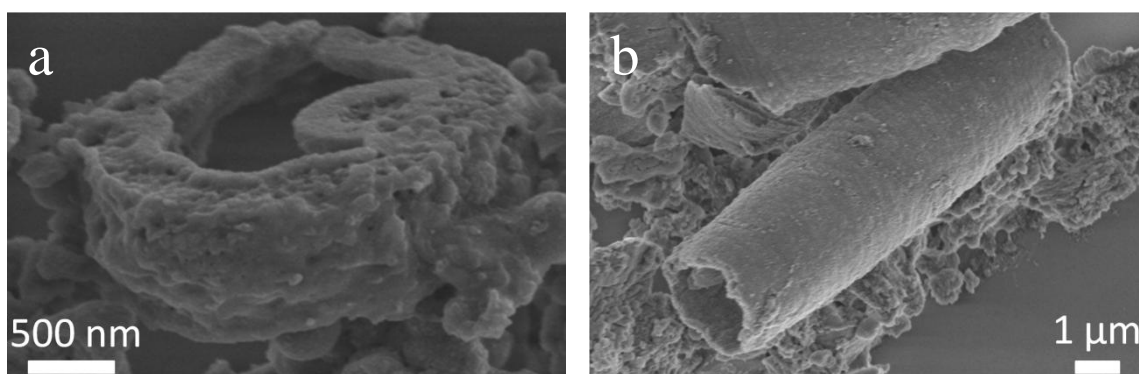
Figure 9: FEGSEM images of rods formed in 3 μm pores after 3 h (a) and 1 day (b) from a solution containing 50 µg/ml PAA, demonstrating the thickness of the rods. After 3 h hollow rods are formed only 500 nm thick (a), while after 6 days the rods got micron sized (b).

After longer reaction times (1 to 3 days), a few hollow (10% of rod population) but mostly filled rods were found (Figure 10). It appeared these rods were formed by filling of the hollow rods, since two different parts were found, one part acting as a shell covering the other part as inner solid rod. This shell was rather smooth and had a thickness of about 100 to 350 nm. The inside was quite rough and consisted of 30 nm to 50 nm particles (Figure 10d). Some partially filled rods were also found (Figure 10a)
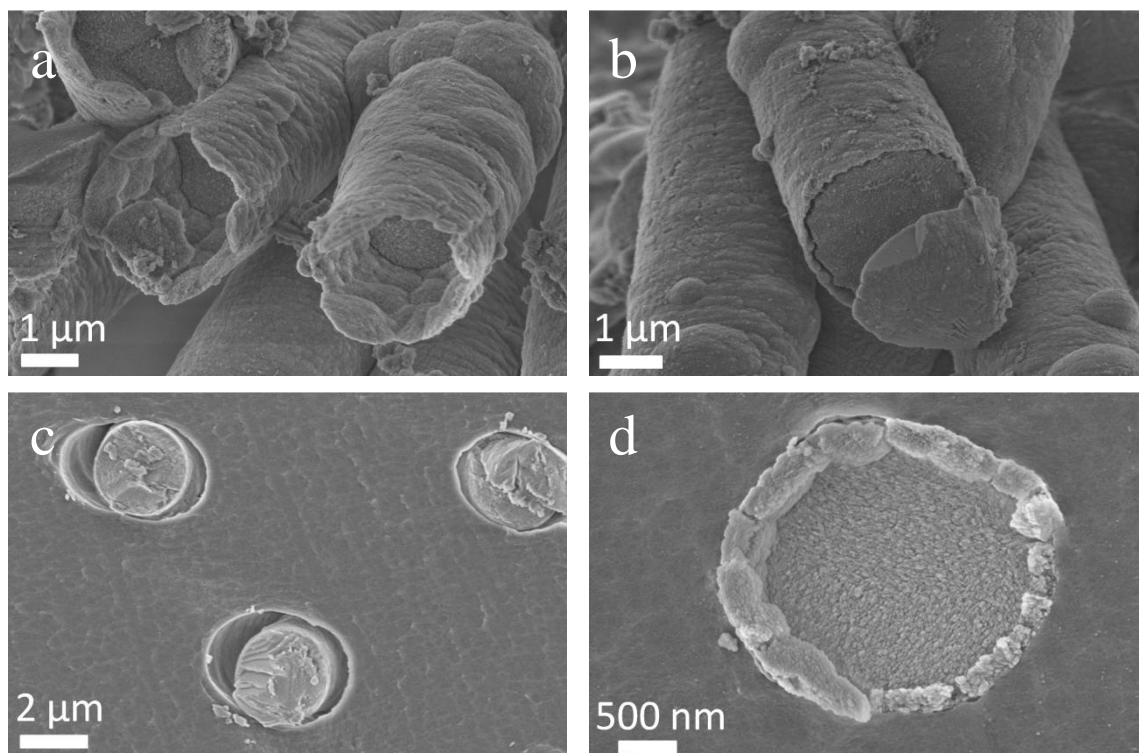
Figure 10: FEGSEM images of rods formed in 3 µm pores after 1 day from a solution containing 50 µg/ml PAA. The rods appear to exist out of a core and surrounding shell.

In comparison with the smaller pore sizes, it took longer time to fill the 3 µm and 10 µm pores. The rods were a couple of µm long (some even to 9 µm but most rods were rather short) (Figure 9b). Without PAA, a small amount of solid rods was found (pores 10% filed). These rods were rather short and incomplete (Figure 11)
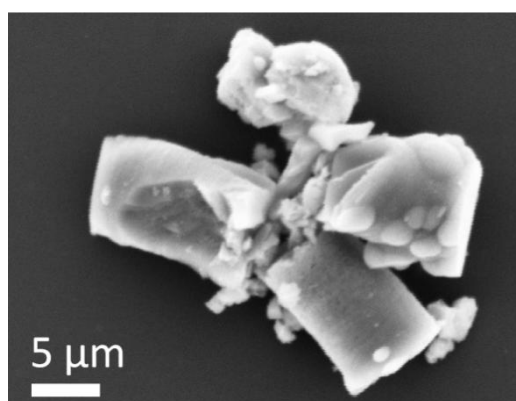
Figure 11: FEGSEM images of rods formed in 3 µm pores after 1 day from a solution containing no PAA. A small amount of solid, rod-like particles were formed.

In 10 μm pores (Figure 12), hollow (50% of total rod population) and filled "rods" were found in the presence of PAA but this time many rods remained hollow even after long times (40% of the rods). Without PAA no rods were found.
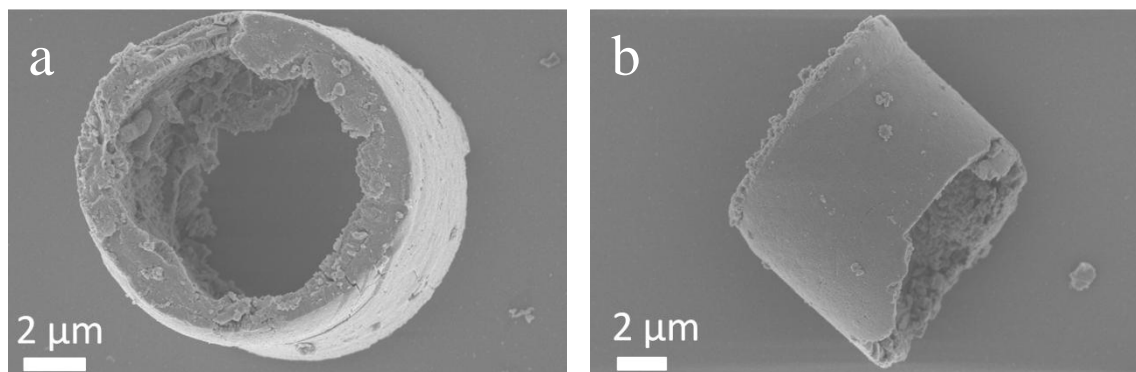
Figure 12: FEGSEM images of rods formed in 10 μm pores after 1 day from a solution containing 50 μg/ml PAA. Much hollow "rods" were formed and remained hollow after long times

Observation of the rods with optical microscopy under crossed polarisers, showed that they appeared polycrystalline (Figure 13).
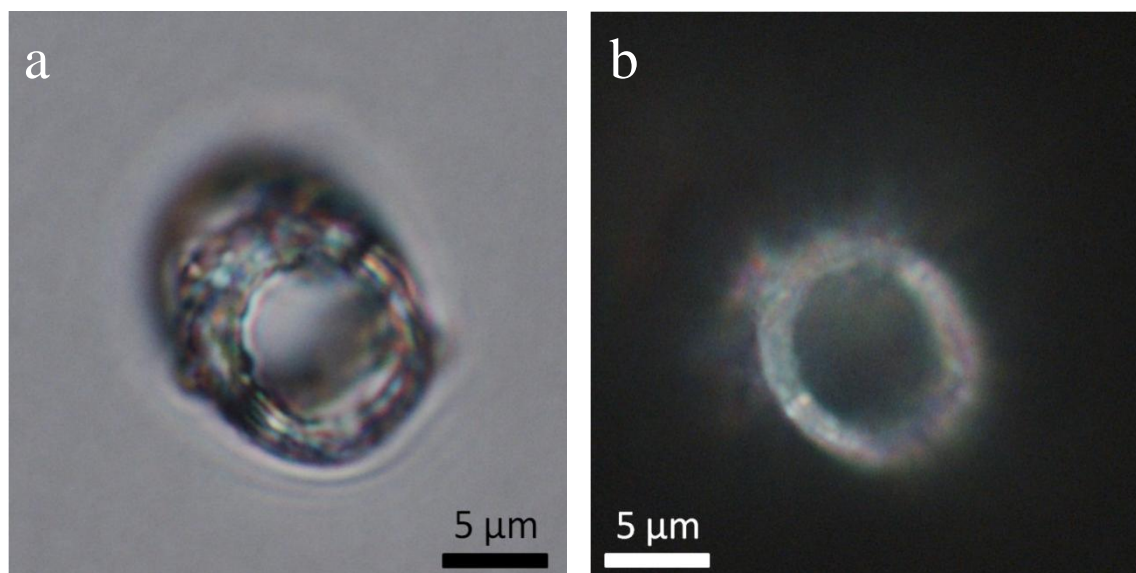
Figure 13: Optical microscope images (a) under crossed polarizers (b) of a particle formed in 10 μm pores after 1 day from a solution containing 50 μg/ml PAA. The particle appears hollow and polycrystalline under crossed polarisers (b).

6.4.2 Layer by layer techniques

6.4.2.1 50 nm pores

Changing the surface chemistry of the membranes had as good as no effect on the morphology of the crystals grown in the 50 nm pores. All rods were solid again and no hollow rods were found, as shown by SEM (Figure 14) and TEM (Figure 15). SAED showed the rods were single crystals of calcite (Figure 15).
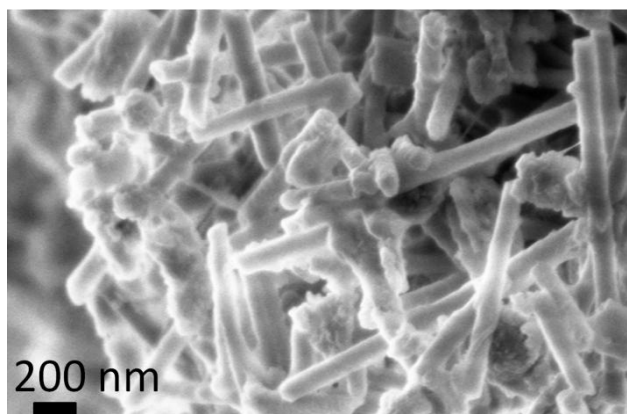
Figure 14: FEGSEM images of rods formed in 50 nm pores after 6 h from a solution containing 50 µg/ml PAA. The membranes were treated with 4 LBL layers (negative charge).
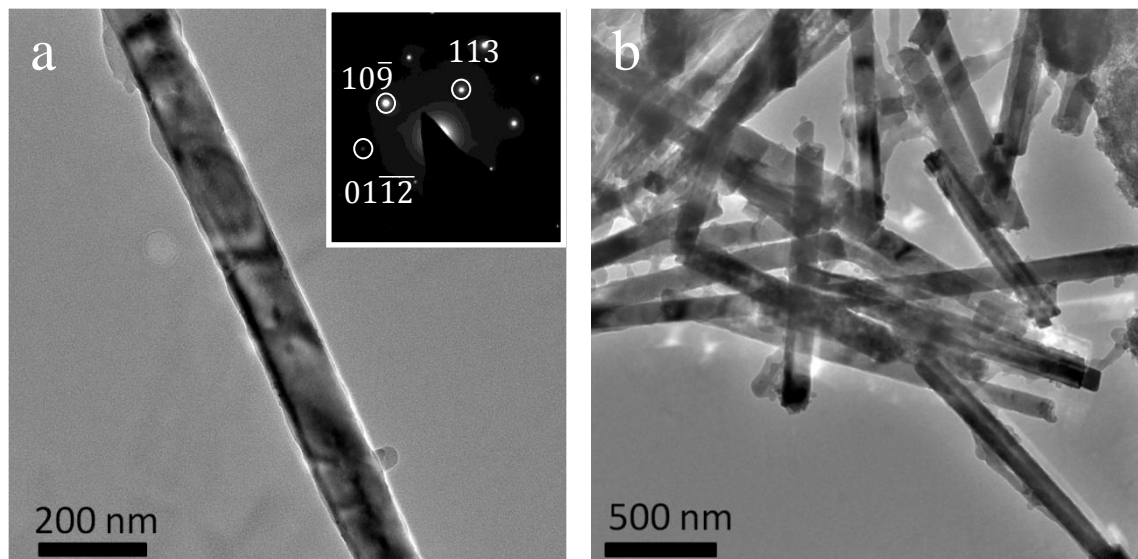
Figure 15: TEM images of rods formed in 50 nm pores after 3 h from a solution containing 50 µg/ml PAA. The membranes were treated with 5 LBL layers (positive charge)

6.4.2.2 200 nm pores

In the case of the 200 nm pores, the effect of the surface modification was much more pronounced. At early stages (6 h) most rods were hollow (80%) and had sizes of about 1 to 3 µm. Many of the rods looked rather fragile (Figure 16a, b) and were much more porous in surface structure as compared with the rods formed without the LBL method. It is thought this was due to the gel-like structure of the LBL film which might influence the crystal surface, becoming incorporated into the structure.
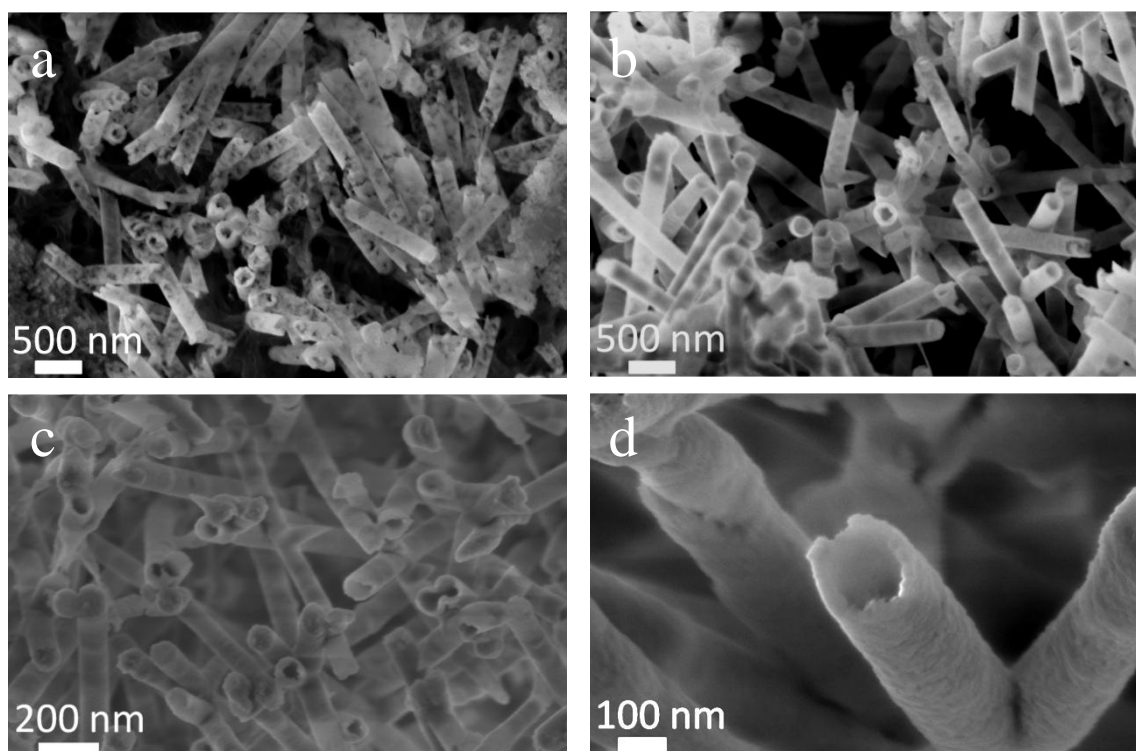
Figure 16: FEGSEM images of rods formed in 200 nm pores after 6 h (a, b) and 1 day (c, d) from a solution containing no PAA (a) and 50 µg/ml PAA (b, c, d). The membranes were treated with 4 LBL layers.

The presence of absence of PAA in the reaction solution didn't influence the results.. The yield of the rods was higher though than when no LBL layers were used (95% of the pores were filled now). After 1 day some of the rods were entirely filled, but most (50%) were still hollow (Figure 16c, d). The wall thickness of the hollow rods was 20 nm to 50 nm at early stages and did not change with further incubation. Identical results were obtained if the surface was either positively or negatively charged.

TEM (Figure 17) was used to investigate the rods in more detail. This revealed a large amount of rods were hollow (80% of the rods) even after 1 day, with the remainder solid (Figure 17c). Selected area electron diffraction of the hollow rods identified them as vaterite (Figure 17a) while the solid rods were mostly calcite, or a mixture of vaterite and calcite (Figure 17c).
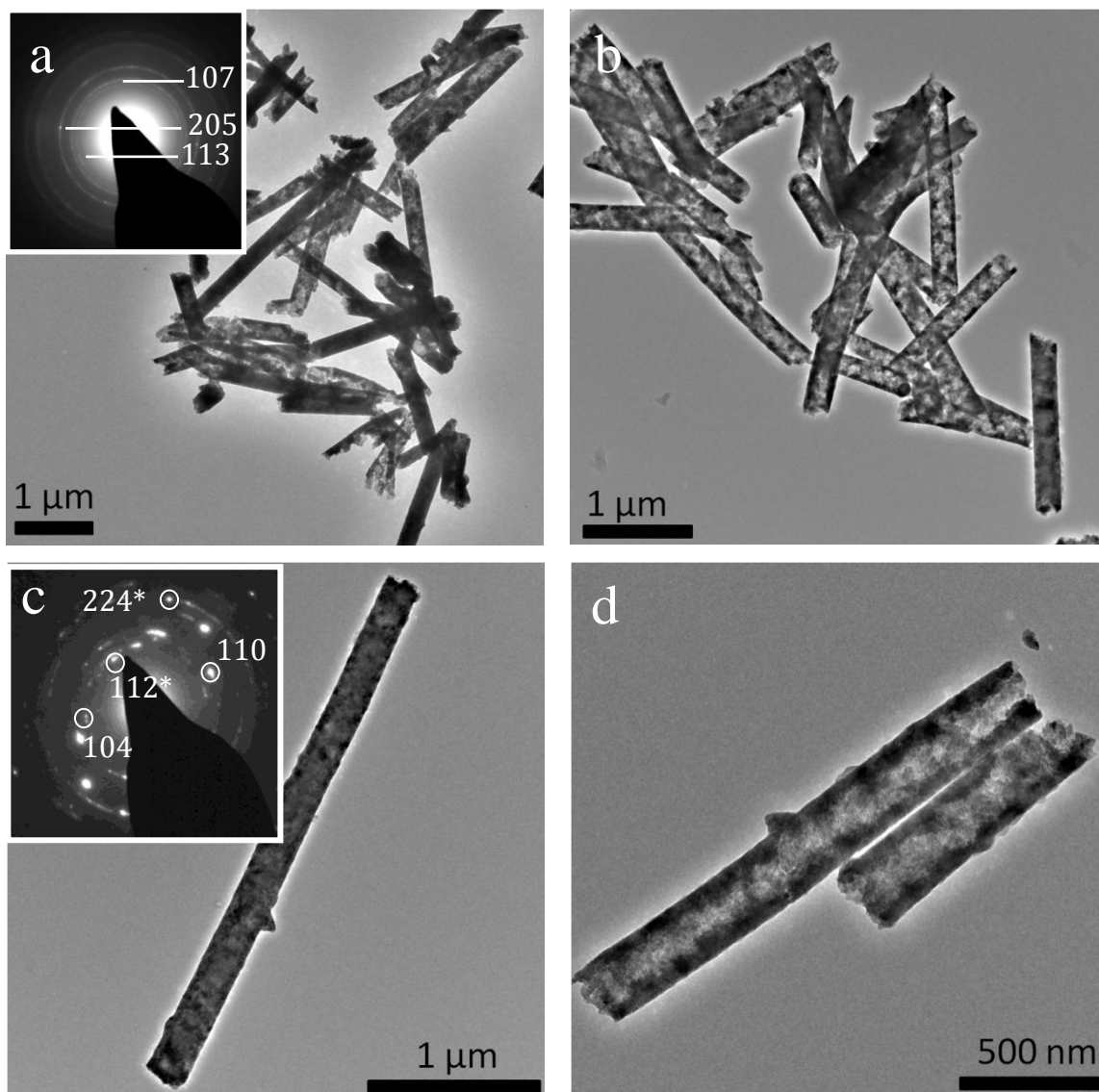
Figure 17: TEM images and corresponding SAED of rods formed in 200 nm pores after 1 day from a solution containing 50 µg/ml PAA (a, c, d) and no PAA (b). The membranes were treated with 4 LBL layers. Hollow vaterite and solid rods which were a mixture of vaterite and calcite were found. The * in the diffraction pattern in (c) indicates the diffraction pattern spots coming from vaterite.

With bigger pore sizes to 3 μm, no improvements in the formation of hollow rods were observed.

6.5 Discussion

The above results demonstrated the formation of $CaCO_3$ hollow rods in pores with sizes of 200 nm to 10 μm. In the case of 50 nm, no rods were formed in the absence of PAA, while in its presence, pores were filled quickly and only solid rods were found. With 200 nm pores, a small amount of hollow rods were formed at early timescales, especially in the presence of PAA, which got filled and became solid after 1 day. In the case of micron sized pores, many hollow rods were found at early timescales and half of the particles were still hollow after one to three days. A gradual trend was seen where more hollow rods were found, the bigger the pore size got. Filling up of the pore sizes was faster the smaller the pore size got, and therefore no hollow rods were found in the 50 nm pores.

6.5.1 Nanoscale pores

For the smaller pore sizes (50 nm to 800 nm) addition of PAA resulted in a much more effective filling of the pores. It is thought that by addition of PAA the rods are filled more effectively by the PILP phase due to capillary action. Due to limited contact with water in the 50 nm and 200 nm pores, most of these rods are single crystal[29]. It is reasoned that at first the surface of the membrane gets covered with $CaCO_3$, followed by the inside. At early stages it is therefore easier to find hollow rods. At later timescales most rods become solid and it was observed that the shell thickens with time in the 200 nm and 800 nm pores by continuously coating. It is thought that these pores get filled by successive layers of the PILP phase. A similar mechanism was found for the formation of hollow organic polymer rods[421]. It also appeared that the pores were sometimes filled with small particles, forming solid rods in an alternative way (Figure 5b). This is in correspondence with previous results for the formation of silica rods in TE membranes[420], where hollow rods of silica were progressively filled from the initial shell to the core with silica nanoparticle aggregates. Just as with the silica, a similar mechanism might take place, where the surface of the inner pores first gets covered again with a dense $CaCO_3$ layer due to attachment to the membrane surface. The tubes

are then progressively filled with nanoparticle aggregates depositing from solution. Since the particles are not in direct contact with the polycarbonate surface these will be loosely packed. In the absence of PAA, it is thought rods were formed by templating in the small 200 nm and 800 nm pores[29, 172] after nucleating on the membrane pore surface.

6.5.2 Micron scale pores

In the case of the larger pore sizes, addition of PAA was a necessity to achieve effective filling of pores and formation of the rods. Yet, since at bigger pore sizes the capillarity effect becomes negligible, the influence of PAA must be different. As mentioned in previous chapters (see 1.2.2.3 and 5.1.1.3) PAA can induce the formation of an amorphous polymer-induced liquid-precursor (PILP) phase of $CaCO_3$, forming thin films of calcium carbonate on a substrate[126, 364]. Taken into account the size of the pore, the pore wall can simply act as a substrate to deposit calcium carbonate films. Since in the bigger pore sizes there is much more contact with the environment, nucleation can happen anywhere, and polycrystalline hollow rods are formed. Once the initial layer is deposited, the tubes slowly get filled up by more and more particles depositing inside the pore. This can explain why an initial hollow rod is formed as a shell covering other particles in the inside. Since the membrane is placed flat on the bottom of the Petri dish, particles precipitating from the solution can easily fill up the pores. The small number of rods which formed in the 3 µm pores without additives; must have nucleated on the pore surface and then grown inside the pore, and get templated by the pore size, forming rough rod-like particles.

6.5.3 Layer by layer techniques

By using a LBL technique the quantity of hollow rods produced was tremendously increased for 200 nm pores. Here, the wall of the rods remained its thickness with time and it is suggested that $CaCO_3$ interacts with the positively and negatively charged surfaces and coats the wall, in the presence of a PILP phase. The coating of the membrane walls is therefore much more successful and many more hollow rods are formed. It is thought that the rods may stay hollow since no more material is left to fill the pores. Further research is necessary to investigate this. Due to the LBL layers, nucleation may be promoted, generating polycrystalline rods[438, 439].

In the case of 50 nm, 800 nm and 3 μm pores, coating the surface with the LBL technique did not enhance the formation of hollow rods. It is suggested that for the 50 nm rods, the LBL layers do not form well in the small pores. The fact that only single crystals were formed instead of polycrystals as in the case of 200 nm also supports this idea. For the bigger pore sizes it isn't exactly sure why the coating didn't have the desired effect. It is possible that five or four LBL layers weren't structurally stable enough in the big pore sizes. Since polymer mobility goes down in confinement[418] the LBL film might have been more stable in the 200 nm pores but not in the micron sized pores.

6.6 Conclusion:

The above results show that TE membranes can be used as an effective method to template hollow rods. It was observed that in addition to solid rods, hollow rods are formed at early timescales of less than 1 day. With time, they become filled with $CaCO_3$ particles or by successive layers of a $CaCO_3$ PILP phase. Larger pore sizes fill up more slowly and therefore more hollow rods are found. Addition of PAA was necessary to achieve efficient pore filling. Changing the surface chemistry of the membranes using LBL layers increased the yield of hollow rods, yet only in the case of 200 nm pores.

Chapter 7: Conclusions and Future Work

Final conclusions and future work

The content of this thesis dealt with the production of new materials by understanding and mimicking biomineralisation processes. In contrast to their synthetic counterparts, biominerals often feature some extraordinary morphologies, together with extreme hardnesses and strengths. Furthermore, biominerals are formed with these superior properties and characteristics under atmospheric pressure and temperature, something which is almost unachievable for most man-made synthetic materials[2, 4]. Inspired by Nature and biominerals, we endeavoured to unravel the mechanisms of biomineral formation, not only to understand but also to mimic, use, and even improve the material characteristics. Being able to mimic biomineral formation would allow us to produce extraordinary materials under atmospheric conditions, without the need for energy-consuming techniques based on high pressure or temperature. In this thesis, the effects of confinement and organic molecules, as used by Nature in the fabrication of biominerals, were investigated. Since calcium phosphate and calcium carbonate are the most abundant biominerals, they were used as model systems.

In the first experimental chapter, the production of calcium phosphate rods was demonstrated by nucleation of calcium phosphate crystals within nanosized pores of track-etched membranes made of polycarbonate and alumina. Based on previous observations of a liquid-like amorphous calcium phosphate PILP phase in the presence of PAsp[96], it was hoped to obtain a very effective infiltration inside the pores by addition of PAsp, to produce single crystals of calcium phosphate. This was not the case, which casted doubt on the liquid-like properties and existence of this calcium phosphate PILP phase. Interestingly, while amorphous calcium phosphate (ACP) was stabilised in confinement in the absence of PAsp, crystallization of ACP occurred faster in the membrane pores than in bulk solution in the presence of PAsp. It was considered that this effect could be attributed to the ability of PAsp to promote nucleation when located on a substrate, while behaving as an inhibitor in solution.

Growing the rods in confinement demonstrated that polycrystalline rods were produced with their *c*-axes oriented along the length of the rod, as is observed in mineralised collagen in bone and dentin[3]. Although our experimental set-up was simple, the results showed that the orientation of calcium phosphate in bone and dentin can be due to confinement alone. This contrasts with previous hypotheses, which have attributed the

orientation of the HAP crystallites in bone to a structural match between HAP and the collagen matrix[198, 199]. In this way, we emphasised that the role of physical confinement originating from the collagen fibril structure, might play a more significant role in the understanding of bone and dentin formation.

Future work will involve manipulation of the surface chemistry of the membranes in order to enhance infiltration into the membrane pores. By the use of a LBL technique or a direct chemical modification of the polycarbonate surface, positively and negatively charged layers can be deposited on the surface of the membrane pores, changing the surface chemistry. Further investigation of the generality of orientation mechanism will be investigated by inclusion of other materials with a one directional growth direction such as ZnO[440] or aragonite needles[413]. Also by infiltration of the pores with a gel structure (such as agarose gel) it will be attempted to obtain different composite materials with interesting characteristics. Finally, by filling up the free spaces formed by the calcium phosphate rods with different materials such as silica or tungstate[441], different composite materials can be prepared.

In chapter 4 the effect of the positively charged additive poly(allylamine hydrochloride) (PAH) on the crystallisation of calcium carbonate was investigated. Although a small effect was anticipated, the addition of the polymer gave rise to significant changes in morphology. Polycrystalline and single crystal films of calcite were formed which covered the substrate, together with single crystal fibers of calcite with aspect ratios of up to 400. Interestingly, similar morphologies had been observed by addition of the negatively charged additives PAsp or PAA to a $CaCO_3$ crystallising solution[12, 77, 82]. The formation processes of the fibers and films were investigated and it was demonstrated that hydrated $Ca^{2+}/PAH/CO_3^{2-}$ droplets initially formed in solution by phase separation. These coalesced and then ultimately crystallised to give crystalline films. By the help of Cryo-TEM this film formation process related with PILP was observed for the first time. Once the crystalline film had formed, fiber formation occurred on the polycrystalline rough films. These fibers formed at low Ca^{2+}/PAH ratios and it was proposed that they formed by oriented attachment of anisotropic particles due to unequal distribution of charge. Addition of Mg^{2+} to the $PAH/CaCO_3$ system enabled formation of very smooth films of polycrystalline calcite at much lower PAH concentrations. The amount of Mg^{2+} incorporated into the crystals did not

increase by addition of PAH, something which was observed though in previous research, using additives such as PAsp[337].

The obtained results challenged the current understanding that positively charged additives have little influence on $CaCO_3$ growth, although the relevance of such a phase separation mechanism in the biomineralisation of $CaCO_3$ is unclear and was discussed to be rather implausible.

Further research will involve other positively charged additives with different functional groups such as poly(vinylamine) and poly(2-aminoethyl methacrylate hydrochloride). The influence of PAH and other positively charged additives will also be investigated on other inorganic crystals such as calcium sulphate, calcium oxalate, cobalt carbonate and manganese carbonate. Furthermore it will be investigated, knowing that positively charged additives can induce a big morphology change on $CaCO_3$, what the effect is in combination with negatively charged additives? Do both additives contribute, achieving better or similar results at lower additive concentrations, or will they be obstructive to each other? A complete understanding of the fiber formation process is also not established yet. By the help of in situ TEM it is hoped we will be able to achieve some more information about their assembly process.

Based on the findings of chapter 3 and 4, the infiltration of $CaCO_3$ into confined spaces of collagen and TE membranes was further investigated, by formation of a $CaCO_3$ PILP phase.

Chapter 5 describes the investigation of the mineralisation of collagen by $CaCO_3$, to understand better the mechanism of bone formation. By addition of PAH or PAsp, an amorphous phase of $CaCO_3$ with liquid-like properties was formed, which infiltrated into the collagen gaps by capillary action. The infiltration was monitored by SAXS and WAXS techniques, demonstrating an increase in disorder in the lateral packing of the collagen molecules. This was followed by crystallization, where the molecular spacing of the collagen molecules decreased, by compressing the molecule packets in between. Analysis of the SAXS signal together with TEM showed 5 nm thick crystals of calcite and vaterite were formed, which were randomly oriented with respect to the collagen. Although the nanoscale $CaCO_3$ crystals are similar in size to the calcium phosphate crystals formed in bone[397], the orientation of the calcium phosphate crystals along the long axis of the collagen fibril was not reproduced. The origin of this random orientation is not entirely clear but it is thought to be due to a different interaction of the

crystals with the charged amino acids of the collagen or the lack of a strong fastest growth direction for the calcite and vaterite crystals.

Further research will involve deeper investigation of the orientation of the $CaCO_3$ crystals. Formation of needle-like aragonite crystals inside the collagen gaps might lead to a similar orientation effect as seen for HAP. Also the infiltration inside the collagen gaps of other more applicable materials such as iron oxide will be investigated, to create new composite materials.

Finally, chapter 6 finally dealt with the formation of hollow rods of $CaCO_3$ by infiltration into the pores of track-etched membranes[29]. In addition to solid rods, hollow rods were formed and the effect of the pore size, presence of additives, time, and surface morphology of the membranes was investigated. Hollow rods were formed at early timescales and often remained hollow in the case of larger pore sizes. By subsequent formation of $CaCO_3$ layers and filling up of the rods with particles, solid rods were formed at later timescales. By changing the surface chemistry of the track-etched membrane pores, the amount of hollow rods increased significantly in the case of the 200 nm pores.

Further research will involve the pursuit to solely produce hollow rods or try to isolate them from the solid rods. By altering the amount of LBL layers, we will also try to obtain exclusively hollow rods in the nano- and micron sized pores. Once this is established, further research will involve infiltration of the rods with drugs[436] or drug model chemical compounds such as rhodamin, or drug carrier proteins like albumin[442].

In general this thesis demonstrated that, inspired by biomineralisation, the use of simple techniques such as soluble additives and confinement, gives rise to some fascinating materials with interesting morphologies and characteristics. Figure 1 gives an overview of the covered topics and obtained results of the thesis.

Figure 1: Overview of the topics and results covered and obtained by this thesis.

References

1. J. Seckbach and P. Kociolek, *The Diatom World*, Springer, 2011.
2. S. Mann, *Biomineralization : principles and concepts in bioinorganic materials chemistry*, Oxford University Press, New York, 2001.
3. P. Fratzl and R. Weinkamer, *Progress in Materials Science*, 2007, **52**, 1263-1334.
4. F. C. Meldrum, *International Materials Reviews*, 2003, **48**, 187-224.
5. L. Addadi, D. Joester, F. Nudelman and S. Weiner, *Chemistry-a European Journal*, 2006, **12**, 981-987.
6. F. Nudelman, B. A. Gotliv, L. Addadi and S. Weiner, *Journal of Structural Biology*, 2006, **153**, 176-187.
7. J. D. Currey, *Proceedings of the Royal Society B-Biological Sciences*, 1977, **196**, 443-463.
8. R. Z. Wang, H. B. Wen, F. Z. Cui, H. B. Zhang and H. D. Li, *Journal of Materials Science*, 1995, **30**, 2299-2304.
9. Y. Y. Kim, K. Ganesan, P. C. Yang, A. N. Kulak, S. Borukhin, S. Pechook, L. Ribeiro, R. Kroger, S. J. Eichhorn, S. P. Armes, B. Pokroy and F. C. Meldrum, *Nature Materials*, 2011, **10**, 890-896.
10. F. Nudelman and N. Sommerdijk, *Angewandte Chemie-International Edition*, 2012, **51**, 6582-6596.
11. H. Colfen, *Current Opinion in Colloid & Interface Science*, 2003, **8**, 23-31.
12. L. B. Gower, *Chemical Reviews*, 2008, **108**, 4551-4627.
13. W. D. Callister, *Materials science and engineering : an introduction*, John Wiley & Sons, New York, 2007.
14. F. C. Meldrum and H. Colfen, *Chemical Reviews*, 2008, **108**, 4332-4432.
15. S. Weiner and L. Addadi, in *Annual Review of Materials Research, Vol 41*, eds. D. R. Clarke and P. Fratzl, Editon edn., 2011, vol. 41, pp. 21-40.
16. D. R. Askeland and P. P. Phulé, *The science and engineering of materials*, Thomson Learning, 2006.
17. Y. T. Cheng and W. L. Johnson, *Science*, 1987, **235**, 997-1002.
18. C. A. Tulk, C. J. Benmore, J. Urquidi, D. D. Klug, J. Neuefeind, B. Tomberli and P. A. Egelstaff, *Science*, 2002, **297**, 1320-1323.
19. Z. H. Stachurski, *Materials*, 2011, **4**, 1564-1598.
20. K. M. Towe and H. A. Lowenstam, *Journal of Ultrastructure Research*, 1967, **17**, 1-13.
21. S. E. Wolf, L. Mueller, R. Barrea, C. J. Kampf, J. Leiterer, U. Panne, T. Hoffmann, F. Emmerling and W. Tremel, *Nanoscale*, 2011, **3**, 1158-1165.
22. E. Beniash, J. Aizenberg, L. Addadi and S. Weiner, *Proc. R. Soc.*, 1997, **264** 461-465.
23. H. A. Lowenstam and S. Weiner, *Science*, 1985, **227**, 51-53.
24. Y. W. Wang, Y. Y. Kim, H. K. Christenson and F. C. Meldrum, *Chemical Communications*, 2012, **48**, 504-506.
25. L. Addadi, S. Raz and S. Weiner, *Advanced Materials*, 2003, **15**, 959-970.
26. J. W. Xiao and S. H. Yang, *Nanoscale*, 2012, **4**, 54-65.
27. J. Aizenberg, D. A. Muller, J. L. Grazul and D. R. Hamann, *Science*, 2003, **299**, 1205-1208.

28. B. Cantaert, Y. Y. Kim, H. Ludwig, F. Nudelman, N. Sommerdijk and F. C. Meldrum, *Advanced Functional Materials*, 2012, **22**, 907-915.
29. Y. Y. Kim, N. B. J. Hetherington, E. H. Noel, R. Kroger, J. M. Charnock, H. K. Christenson and F. C. Meldrum, *Angewandte Chemie-International Edition*, 2011, **50**, 12572-12577.
30. Y. Y. Kim, A. N. Kulak, Y. T. Li, T. Batten, M. Kuball, S. P. Armes and F. C. Meldrum, *Journal of Materials Chemistry*, 2009, **19**, 387-398.
31. E. Loste, R. J. Park, J. Warren and F. C. Meldrum, *Advanced Functional Materials*, 2004, **14**, 1211-1220.
32. W. B. Yue, A. N. Kulak and F. C. Meldrum, *Journal of Materials Chemistry*, 2006, **16**, 408-416.
33. N. B. J. Hetherington, A. N. Kulak, Y. Y. Kim, E. H. Noel, D. Snoswell, M. Butler and F. C. Meldrum, *Advanced Functional Materials*, 2011, **21**, 948-954.
34. D. J. Grant, *Polymorphism in pharmaceutical solids*, 1999, **95**, 1-33.
35. R. Hilfiker, *Polymorphism*, Wiley-VCH, 2006.
36. R. J. Davey and J. Garside, *From molecules to crystallizers*, Oxford University Press, 2000.
37. C. Hammond, *Basics of Crystallography and Diffraction*, Oxford, 2001.
38. J. A. Dirksen and T. A. Ring, *Chemical Engineering Science*, 1991, **46**, 2389-2427.
39. J. W. Mullin, *Crystallization*, Butterworth-Heinemann, Oxford, 2001.
40. C. F. Woensdregt, *Faraday Discussions*, 1993, **95**, 97-107.
41. D. Temkin, *Consultants Bureau, New York*, 1966, 15.
42. G. Wulff, *Zeitschrift Fur Krystallographie Und Mineralogie*, 1901, **34**, 449-530.
43. P. Rein ten Wolde and D. Frenkel, *Physical Chemistry Chemical Physics*, 1999, **1**, 2191-2196.
44. X. Yin and M. J. Stott, *The Journal of Chemical Physics*, 2003, **118**, 3717-3723.
45. A. S. Posner and F. Betts, *Accounts of Chemical Research*, 1975, **8**, 273-281.
46. A. Dey, P. H. H. Bomans, F. A. Muller, J. Will, P. M. Frederik, G. de With and N. Sommerdijk, *Nature Materials*, 2010, **9**, 1010-1014.
47. W. J. E. M. Habraken, J. Tao, L. J. Brylka, H. Friedrich, L. Bertinetti, A. S. Schenk, A. Verch, V. Dmitrovic, P. H. H. Bomans, P. M. Frederik, J. Laven, P. van der Schoot, B. Aichmayer, G. de With, J. J. DeYoreo and N. A. J. M. Sommerdijk, *Nat Commun*, 2013, **4**, 1507.
48. J. P. Andreassen, R. Beck and M. Nergaard, *Faraday Discussions*, 2012, **159**, 247-261.
49. J. Seto, Y. R. Ma, S. A. Davis, F. Meldrum, A. Gourrier, Y. Y. Kim, U. Schilde, M. Sztucki, M. Burghammer, S. Maltsev, C. Jager and H. Colfen, *Proceedings of the National Academy of Sciences of the United States of America*, 2012, **109**, 7126-7126.
50. H. Cölfen and S. Mann, *Angew. Chem. Int. Ed*, 2003, **42**, 2350-2365.
51. H. C. M. Antonietti, *Mesocrystals and Nonclassical Crystallization*, 2008.
52. M. Niederberger and H. Cölfen, *Physical Chemistry Chemical Physics*, 2006, **8**, 3271-3287.
53. E. J. H. Lee, C. Ribeiro, E. Longo and E. R. Leite, *The Journal of Physical Chemistry B*, 2005, **109**, 20842-20846.

54. H. Cölfen and M. Antonietti, *Mesocrystals and nonclassical crystallization*, John Wiley & Sons Inc, UK, 2008.

55. R. L. Penn and J. F. Banfield, *Geochimica Et Cosmochimica Acta*, 1999, **63**, 1549-1557.

56. J. F. Banfield, S. A. Welch, H. Z. Zhang, T. T. Ebert and R. L. Penn, *Science*, 2000, **289**, 751-754.

57. D. S. Li, M. H. Nielsen, J. R. I. Lee, C. Frandsen, J. F. Banfield and J. J. De Yoreo, *Science*, 2012, **336**, 1014-1018.

58. T. X. Wang, H. Colfen and M. Antonietti, *Journal of the American Chemical Society*, 2005, **127**, 3246-3247.

59. A. N. Kulak, P. Iddon, Y. T. Li, S. P. Armes, H. Colfen, O. Paris, R. M. Wilson and F. C. Meldrum, *Journal of the American Chemical Society*, 2007, **129**, 3729-3736.

60. S. H. Yu, H. Colfen, K. Tauer and M. Antonietti, *Nature Materials*, 2005, **4**, 51-55.

61. R. Q. Song, H. Colfen, A. W. Xu, J. Hartmann and M. Antonietti, *Acs Nano*, 2009, **3**, 1966-1978.

62. S. Deng, V. Tjoa, H. M. Fan, H. R. Tan, D. C. Sayle, M. Olivo, S. Mhaisalkar, J. Wei and C. H. Sow, *Journal of the American Chemical Society*, 2012, **134**, 4905-4917.

63. C. Lausser, H. Colfen and M. Antonietti, *Acs Nano*, 2011, **5**, 107-114.

64. Y. Oaki, A. Kotachi, T. Miura and H. Imai, *Advanced Functional Materials*, 2006, **16**, 1633-1639.

65. T. E. Schaffer, C. IonescuZanetti, R. Proksch, M. Fritz, D. A. Walters, N. Almqvist, C. M. Zaremba, A. M. Belcher, B. L. Smith, G. D. Stucky, D. E. Morse and P. K. Hansma, *Chemistry of Materials*, 1997, **9**, 1731-1740.

66. H. Colfen and M. Antonietti, *Angewandte Chemie-International Edition*, 2005, **44**, 5576-5591.

67. D. Gebauer and H. Coelfen, *Nano Today*, 2011, **6**, 564-584.

68. D. Gebauer, A. Volkel and H. Colfen, *Science*, 2008, **322**, 1819-1822.

69. E. M. Pouget, P. H. H. Bomans, J. Goos, P. M. Frederik, G. de With and N. Sommerdijk, *Science*, 2009, **323**, 1455-1458.

70. R. Demichelis, P. Raiteri, J. D. Gale, D. Quigley and D. Gebauer, *Nature Communications*, 2011, **2**, 590

71. F. C. Meldrum and R. P. Sear, *Science*, 2008, **322**, 1802-1803.

72. D. Erdemir, A. Y. Lee and A. S. Myerson, *Accounts of Chemical Research*, 2009, **42**, 621-629.

73. P. G. Vekilov, *Nanoscale*, 2010, **2**, 2346-2357.

74. A. Navrotsky, *Proceedings of the National Academy of Sciences of the United States of America*, 2004, **101**, 12096-12101.

75. A. F. Wallace, L. O. Hedges, A. Fernandez-Martinez, S. W. Paolo Raiteri, G. A. Waychunas, J. D. Gale, J. F. Banfield and J. J. D. Yoreo, *Submitted*.

76. L. A. Gower and D. A. Tirrell, *Journal of Crystal Growth*, 1998, **191**, 153-160.

77. L. B. Gower and D. J. Odom, *Journal of Crystal Growth*, 2000, **210**, 719-734.

78. M. J. Olszta, D. J. Odom, E. P. Douglas and L. B. Gower, *Connective Tissue Research*, 2003, **44**, 326-334.

79. L. Addadi, J. Moradian, E. Shay, N. G. Maroudas and S. Weiner, *Proceedings of the National Academy of Sciences of the United States of America*, 1987, **84**, 2732-2736.
80. L. J. Dai, E. P. Douglas and L. B. Gower, *Journal of Non-Crystalline Solids*, 2008, **354**, 1845-1854.
81. Y.-Y. Kim, E. P. Douglas and L. B. Gower, *Langmuir*, 2007, **23**, 4862-4870.
82. M. J. Olszta, S. Gajjeraman, M. Kaufman and L. B. Gower, *Chemistry of Materials*, 2004, **16**, 2355-2362.
83. S. J. Homeijer, R. A. Barrett and L. B. Gower, *Crystal Growth & Design*, 2010, **10**, 1040-1052.
84. X. G. Cheng and L. B. Gower, *Biotechnology Progress*, 2006, **22**, 141-149.
85. M. A. Bewernitz, D. Gebauer, J. Long, H. Colfen and L. B. Gower, *Faraday Discussions*, 2012, **159**, 291-312.
86. N. A. J. M. Sommerdijk, E. N. M. van Leeuwen, M. R. J. Vos and J. A. Jansen, *Crystengcomm*, 2007, **9**, 1209-1214.
87. S. E. Wolf, J. Leiterer, V. Pipich, R. Barrea, F. Emrnerling and W. Tremel, *Journal of the American Chemical Society*, 2011, **133**, 12642-12649.
88. A. Sugawara, T. Nishimura, Y. Yamamoto, H. Inoue, H. Nagasawa and T. Kato, *Angewandte Chemie-International Edition*, 2006, **45**, 2876-2879.
89. L. Dai, X. Cheng and L. B. Gower, *Chemistry of Materials*, 2008, **20**, 6917-6928.
90. M. Faatz, F. Grohn and G. Wegner, *Advanced Materials*, 2004, **16**, 996-+.
91. S. E. Wolf, J. Leiterer, M. Kappl, F. Emmerling and W. Tremel, *Journal of the American Chemical Society*, 2008, **130**, 12342-12347.
92. J. Rieger, T. Frechen, G. Cox, W. Heckmann, C. Schmidt and J. Thieme, *Faraday Discussions*, 2007, **136**, 265-277.
93. S. Wohlrab, H. Colfen and M. Antonietti, *Angewandte Chemie-International Edition*, 2005, **44**, 4087-4092.
94. Y. Jiang, L. Gower, D. Volkmer and H. Colfen, *Crystal Growth & Design*, 2011, **11**, 3243-3249.
95. Y. Jiang, L. Gower, D. Volkmer and H. Colfen, *Physical Chemistry Chemical Physics*, 2012, **14**, 914-919.
96. M. J. Olszta, X. Cheng, S. S. Jee, R. Kumar, Y.-Y. Kim, M. J. Kaufman, E. P. Douglas and L. B. Gower, *Materials Science and Engineering: R: Reports*, 2007, **58**, 77-116.
97. A. Dey, G. de With and N. Sommerdijk, *Chemical Society Reviews*, 2010, **39**, 397-409.
98. S. Weiner and L. Addadi, *Journal of Materials Chemistry*, 1997, **7**, 689-702.
99. A. S. Schenk, H. Zope, Y. Y. Kim, A. Kros, N. Sommerdijk and F. C. Meldrum, *Faraday Discussions*, 2012, **159**, 327-344.
100. G. Falini, S. Albeck, S. Weiner and L. Addadi, *Science*, 1996, **271**, 67-69.
101. A. M. Belcher, X. H. Wu, R. J. Christensen, P. K. Hansma, G. D. Stucky and D. E. Morse, *Nature*, 1996, **381**, 56-58.
102. L. Addadi and S. Weiner, *P. N. A. S.*, 1985, **82**, 4110-4114.

103. S. Mann, *Angewandte Chemie-International Edition*, 2000, **39**, 3393-3406.
104. S. H. Yu and H. Colfen, *Journal of Materials Chemistry*, 2004, **14**, 2124-2147.
105. H. A. Lowenstam and S. Weiner, *On Biomineralization*, Oxford University Press, New York, 1989.
106. N. A. J. M. Sommerdijk and G. de With, *Chemical Reviews*, 2008, **108**, 4499-4550.
107. B. A. Gotliv, L. Addadi and S. Weiner, *Chembiochem*, 2003, **4**, 522-529.
108. H. Endo, Y. Takagi, N. Ozaki, T. Kogure and T. Watanabe, *Biochemical Journal*, 2004, **384**, 159-167.
109. M. Michenfelder, G. Fu, C. Lawrence, J. C. Weaver, B. A. Wustman, L. Taranto, J. S. Evans and D. E. Morsel, *Biopolym.*, 2003, **70**, 522-533.
110. A. Sato, S. Nagasaka, K. Furihata, S. Nagata, I. Arai, K. Saruwatari, T. Kogure, S. Sakuda and H. Nagasawa, *Nature Chemical Biology*, 2011, **7**, 197-199.
111. T. Samata, N. Hayashi, M. Kono, K. Hasegawa, C. Horita and S. Akera, *Febs Letters*, 1999, **462**, 225-229.
112. J. S. Evans, *Chem. Revs.*, 2008, **108**, 4455-4462.
113. K. A. Piez, *Science*, 1961, **134**, 841-842.
114. P. E. Hare, *Science*, 1963, **139**, 216-217.
115. K. Simkiss, *Comp. Biochem. Phys.*, 1965, **16**, 427-428.
116. D. F. Travis, C. J. Francois, L. C. Bonar and M. J. Glimcher, *J. Ultrastruct. Res.*, 1967, **18**, 519-550.
117. S. Weiner, *Calc. Tiss. Int.*, 1979, **29**, 163-167.
118. J. M. Didymus, P. Oliver and S. Mann, *J. Chem. Soc. Faraday Trans.*, 1993, **89(15)**, 2891-2900.
119. D. Volkmer, M. Fricke, T. Huber and N. Sewald, *Chemical Communications*, 2004, 1872-1873.
120. S. Elhadj, E. A. Salter, A. Wierzbicki, J. J. De Yoreo, N. Han and P. M. Dove, *Crystal Growth & Design*, 2006, **6**, 197-201.
121. H. Colfen, *Macromolecular Rapid Communications*, 2001, **22**, 219-252.
122. H. Colfen and M. Antonietti, *Langmuir*, 1998, **14**, 582-589.
123. R. J. P. Williams, *Philosophical Transactions of the Royal Society of London Series B-Biological Sciences*, 1984, **304**, 411-424.
124. N. Gehrke, H. Colfen, N. Pinna, M. Antonietti and N. Nassif, *Crystal Growth & Design*, 2005, **5**, 1317-1319.
125. S. H. Yu, H. Colfen, J. Hartmann and M. Antonietti, *Advanced Functional Materials*, 2002, **12**, 541-545.
126. M. J. Olszta, E. P. Douglas and L. B. Gower, *Calcified Tissue International*, 2003, **72**, 583-591.
127. S. Albeck, S. Weiner and L. Addadi, *Chemistry-a European Journal*, 1996, **2**, 278-284.
128. S. Albeck, J. Aizenberg, L. Addadi and S. Weiner, *Journal of the American Chemical Society*, 1993, **115**, 11691-11697.
129. S. Raz, S. Weiner and L. Addadi, *Advanced Materials*, 2000, **12**, 38-42.
130. I. Leveque, M. Cusack, S. A. Davis and S. Mann, *Angewandte Chemie-International Edition*, 2004, **43**, 885-888.
131. F. H. Shen, Q. L. Feng and C. M. Wang, *Journal of Crystal Growth*, 2002, **242**, 239-244.

132. F. C. Meldrum and S. T. Hyde, *Journal of Crystal Growth*, 2001, **231**, 544-558.
133. J. O. Titiloye, S. C. Parker and S. Mann, *Journal of Crystal Growth*, 1993, **131**, 533-545.
134. S. B. Mukkamala, C. E. Anson and A. K. Powell, *Journal of Inorganic Biochemistry*, 2006, **100**, 1128-1138.
135. S. Mann, J. M. Didymus, N. P. Sanderson, B. R. Heywood and E. J. A. Samper, *Journal of the Chemical Society-Faraday Transactions*, 1990, **86**, 1873-1880.
136. E. Altay, T. Shahwan and M. Tanoglu, *Powder Technology*, 2007, **178**, 194-202.
137. Z. Amjad, *Calcium phosphates in biological and industrial systems*, Kluwer academic publishers, 1998.
138. L. J. Wang and G. H. Nancollas, *Chemical Reviews*, 2008, **108**, 4628-4669.
139. V. K. Sharma, M. Johnsson, J. D. Sallis and G. H. Nancollas, *Langmuir*, 1992, **8**, 676-679.
140. O. Prymak, V. Sokolova, T. Peitsch and M. Epple, *Crystal Growth & Design*, 2005, **6**, 498-506.
141. L. C. Palmer, C. J. Newcomb, S. R. Kaltz, E. D. Spoerke and S. I. Stupp, *Chemical Reviews*, 2008, **108**, 4754-4783.
142. S. Schweizer and A. Taubert, *Macromolecular Bioscience*, 2007, **7**, 1085-1099.
143. F. Nudelman, G. de With and N. Sommerdijk, *Soft Matter*, 2011, **7**, 17-24.
144. J. J. Diegmueller, X. G. Cheng and O. Akkus, *Crystal Growth & Design*, 2009, **9**, 5220-5226.
145. A. Bigi, B. Bracci, S. Panzavolta, M. Iliescu, M. Plouet-Richard, J. Werckmann and D. Cam, *Crystal Growth & Design*, 2004, **4**, 141-146.
146. A. Bigi, E. Boanini, D. Walsh and S. Mann, *Angewandte Chemie-International Edition*, 2002, **41**, 2163-2166.
147. A. Peytcheva, H. Colfen, H. Schnablegger and M. Antonietti, *Colloid and Polymer Science*, 2002, **280**, 218-227.
148. X. Yang, X. Gao, Y. Gan, C. Gao, X. Zhang, K. Ting, B. M. Wu and Z. Gou, *Journal of Physical Chemistry C*, 2010, **114**, 6265-6271.
149. Y. S. Wang, M. S. Hassan, P. Gunawan, R. Lau, X. Wang and R. Xu, *Journal of Colloid and Interface Science*, 2009, **339**, 69-77.
150. K. W. Wang, Y. J. Zhu, X. Y. Chen, W. Y. Zhai, Q. Wang, F. Chen, J. A. Chang and Y. R. Duan, *Chemistry-an Asian Journal*, 2010, **5**, 2477-2482.
151. A. Shkilnyy, J. Brandt, A. Mantion, O. Paris, H. Schlaad and A. Taubert, *Chemistry of Materials*, 2009, **21**, 1572-1578.
152. C. J. Stephens, S. F. Ladden, F. C. Meldrum and H. K. Christenson, *Advanced Functional Materials*, 2010, **20**, 2108-2115.
153. W. Traub, T. Arad and S. Weiner, *Proceedings of the National Academy of Sciences of the United States of America*, 1989, **86**, 9822-9826.
154. S. Mann, N. H. C. Sparks and R. P. Blakemore, *Proceedings of the Royal Society B-Biological Sciences*, 1987, **231**, 469-476.
155. C. C. Tester, R. E. Brock, C. H. Wu, M. R. Krejci, S. Weigand and D. Joester, *Crystengcomm*, 2011, **13**, 3975-3978.
156. H. K. Christenson, *J. Phys. Condens. Mat.*, 2001, **13**, R95-R133.

157. B. D. Hamilton, J. M. Ha, M. A. Hillmyer and M. D. Ward, *Acc. Chem. Res.*, 2012, **45**, 414-423.
158. M. Beiner, G. T. Rengarajan, S. Pankaj, D. Enke and M. Steinhart, *Nano Letters*, 2007, **7**, 1381-1385.
159. G. T. Rengarajan, D. Enke, M. Steinhart and M. Beiner, *Journal of Materials Chemistry*, 2008, **18**, 2537-2539.
160. H. K. C. Yun-Wei Wang, Fiona C. Meldrum, *Advanced Functional Materials*, 2013.
161. C. J. Stephens, Y.-Y. Kim, S. D. Evans, F. C. Meldrum and H. K. Christenson, *Journal of the American Chemical Society*, 2011, **133**, 5210-5213.
162. A. S. Finnemore, M. R. J. Scherer, R. Langford, S. Mahajan, S. Ludwigs, F. C. Meldrum and U. Steiner, *Advanced Materials*, 2009, **21**, 3928-3932.
163. J. Aizenberg, S. Weiner and L. Addadi, *Connective Tissue Research*, 2003, **44**, 20-25.
164. A. Stein and R. C. Schroden, *Current Opinion in Solid State & Materials Science*, 2001, **5**, 553-564.
165. S. Deville, E. Saiz, R. K. Nalla and A. P. Tomsia, *Science*, 2006, **311**, 515-518.
166. B. Wucher, W. B. Yue, A. N. Kulak and F. C. Meldrum, *Chemistry of Materials*, 2007, **19**, 1111-1119.
167. S. D. Sims, D. Walsh and S. Mann, *Advanced Materials*, 1998, **10**, 151-154.
168. S. R. Hall, H. Bolger and S. Mann, *Chemical Communications*, 2003, 2784-2785.
169. J. M. Ha, J. H. Wolf, M. A. Hillmyer and M. D. Ward, *Journal of the American Chemical Society*, 2004, **126**, 3382-3383.
170. R. J. Park and F. C. Meldrum, *Advanced Materials*, 2002, **14**, 1167-1169.
171. R. J. Park and F. C. Meldrum, *Journal of Materials Chemistry*, 2004, **14**, 2291-2296.
172. E. Loste and F. C. Meldrum, *Chemical Communications*, 2001, 901-902.
173. J. Dennis and H. K. Henisch, *Journal of the Electrochemical Society*, 1967, **114**, 263-266.
174. H. K. Henisch, J. Dennis and J. I. Hanoka, *Journal of Physics and Chemistry of Solids*, 1965, **26**, 493-496.
175. D. Yang, L. M. Qi and J. M. Ma, *Chemical Communications*, 2003, 1180-1181.
176. H. Y. Li and L. A. Estroff, *Advanced Materials*, 2009, **21**, 470-473.
177. H. Y. Li and L. A. Estroff, *Crystengcomm*, 2007, **9**, 1153-1155.
178. C. Bae, H. Yoo, S. Kim, K. Lee, J. Kim, M. A. Sung and H. Shin, *Chemistry of Materials*, 2008, **20**, 756-767.
179. P. S. Dobson, L. A. Bindley, J. V. Macpherson and P. R. Unwin, *Langmuir*, 2005, **21**, 1255-1260.
180. Y. Kitano, *Bulletin of the Chemical Society of Japan*, 1962, **35**, 1980-1985.
181. J. Aizenberg, G. Lambert, L. Addadi and S. Weiner, *Advanced Materials*, 1996, **8**, 222-226.
182. J. Ihli, P. Bots, A. Kulak, L. G. Benning and F. C. Meldrum, *Advanced Functional Materials*, 2013, **23**, 1965-1973.

183. W. Brown, *Dynamic light scattering: the method and some applications*, Oxford University Press, USA, 1993.
184. E. S. R. Facility, http://www.esrf.eu/AboutUs/GuidedTour).
185. P. Bots, L. G. Benning, J. D. Rodriguez-Blanco, T. Roncal-Herrero and S. Shaw, *Crystal Growth & Design*, 2012, **12**, 3806-3814.
186. J. Goodisman and H. Brumberger, Journal of Applied Crystallography, 1971, 4, 347-351.
187. O. Glatter and O. Kratky, *Small angle X-ray scattering*, Academic press London, 1982.
188. W. Bras, G. N. Greaves, M. Oversluizen, S. M. Clark and G. Eeckhaut, *Journal of Non-Crystalline Solids*, 2005, **351**, 2178-2193.
189. O. Glatter, *Journal of Applied Crystallography*, 1977, **10**, 415-421.
190. G. Porod, *Kolloid-Zeitschrift and Zeitschrift Fur Polymere*, 1951, **124**, 83-114.
191. H. D. Bale and P. W. Schmidt, *Physical Review Letters*, 1984, **53**, 596-599.
192. J. Teixeira, *Journal of Applied Crystallography*, 1988, **21**, 781-785.
193. P. D. Nellist, M. F. Chisholm, N. Dellby, O. L. Krivanek, M. F. Murfitt, Z. S. Szilagyi, A. R. Lupini, A. Borisevich, W. H. Sides and S. J. Pennycook, *Science*, 2004, **305**, 1741-1741.
194. D. B. Williams and C. B. Carter, *Transmission electron microscopy: a textbook for materials science*, Springer, 2009.
195. H. Friedrich, P. M. Frederik, G. de With and N. A. J. M. Sommerdijk, *Angewandte Chemie-International Edition*, 2010, **49**, 7850-7858.
196. F. Nudelman, K. Pieterse, A. George, P. H. H. Bomans, H. Friedrich, L. J. Brylka, P. A. J. Hilbers, G. de With and N. Sommerdijk, *Nature Materials*, 2010, **9**, 1004-1009.
197. E. Beniash, *Wiley Interdisciplinary Reviews-Nanomedicine and Nanobiotechnology*, 2011, **3**, 47-69.
198. J. D. Hartgerink, E. Beniash and S. I. Stupp, *Science*, 2001, **294**, 1684-1688.
199. M. Kikuchi, S. Itoh, S. Ichinose, K. Shinomiya and J. Tanaka, *Biomaterials*, 2001, **22**, 1705-1711.
200. S. V. Dorozhkin and M. Epple, *Angewandte Chemie-International Edition*, 2002, **41**, 3130-3146.
201. J. C. Elliott, *Structure and chemistry of the apatites and other calcium orthophosphates*, Elsevier, Amsterdam [The Netherlands]; New York, 1994.
202. J. L. Meyer and E. D. Eanes, *Calcified Tissue Research*, 1978, **25**, 59-68.
203. K. Onuma and A. Ito, *Chemistry of Materials*, 1998, **10**, 3346-3351.
204. L. C. Chow, *Dental Materials Journal*, 2009, **28**, 1-10.
205. M. I. Kay, R. A. Young and A. S. Posner, *Nature*, 1964, **204**, 1050-1052.
206. G. Boivin, *Medicographia*, 2007, **29**, 126-132.
207. W. E. Brown and L. C. Chow, *Annual Review of Materials Science*, 1976, **6**, 213-236.
208. L. C. Chow and E. D. Eanes, *Octacalcium Phosphate*, Karger, 2001.
209. M. S. A. Johnsson and G. H. Nancollas, *Critical Reviews in Oral Biology & Medicine*, 1992, **3**, 61-82.

210. N. J. Crane, V. Popescu, M. D. Morris, P. Steenhuis and M. A. Ignelzi, *Bone*, 2006, **39**, 434-442.
211. C. Rey, C. Combes, C. Drouet and M. J. Glimcher, *Osteoporosis International*, 2009, **20**, 1013-1021.
212. W. E. Brown, J. P. Smith, A. W. Frazier and J. R. Lehr, *Nature*, 1962, **196**, 1050-1055.
213. W. Brown, N. Eidelman and B. Tomazic, *Advances in dental research*, 1987, **1**, 306-313.
214. P. Bodier-Houlle, P. Steuer, J. C. Voegel and F. J. G. Cuisinier, *Acta Crystallographica Section D-Biological Crystallography*, 1998, **54**, 1377-1381.
215. E. Beniash, R. A. Metzler, R. S. K. Lam and P. Gilbert, *Journal of Structural Biology*, 2009, **166**, 133-143.
216. M. Iijima, D. G. A. Nelson, Y. Pan, A. T. Kreinbrink, M. Adachi, T. Goto and Y. Moriwaki, *Calcified Tissue International*, 1996, **59**, 377-384.
217. Y.-H. Tseng, C.-Y. Mou and J. C. C. Chan, *Journal of the American Chemical Society*, 2006, **128**, 6909-6918.
218. M. Daudon, R. Donsimoni, C. Hennequin, S. Fellahi, G. Lemoel, M. Paris, S. Troupel and B. Lacour, *Urological Research*, 1995, **23**, 319-326.
219. P. G. Werness, J. H. Bergert and L. H. Smith, *Journal of Crystal Growth*, 1981, **53**, 166-181.
220. P. W. Brown and B. Constantz, *Hydroxyapatite and related materials*, CRC, 1994.
221. E. D. Eanes, I. H. Gillesse and A. S. Gosner, *Nature*, 1965, **208**, 365-367.
222. J. Christoffersen, M. R. Christoffersen, W. Kibalczyc and F. A. Andersen, *Journal of Crystal Growth*, 1989, **94**, 767-777.
223. S. Weiner, *Bone*, 2006, **39**, 431-433.
224. J. Mahamid, B. Aichmayer, E. Shimoni, R. Ziblat, C. H. Li, S. Siegel, O. Paris, P. Fratzl, S. Weiner and L. Addadi, *Proceedings of the National Academy of Sciences of the United States of America*, 2010, **107**, 6316-6321.
225. T. Terada, S. Yamabi and H. Imai, *Journal of Crystal Growth*, 2003, **253**, 435-444.
226. M. L. Watson and R. A. Robinson, *American Journal of Anatomy*, 1953, **93**, 25-59.
227. F. Betts and A. S. Posner, *Materials Research Bulletin*, 1974, **9**, 353-360.
228. A. L. Boskey, *Journal of Dental Research*, 1997, **76**, 1433-1436.
229. A. S. Posner, F. Betts and N. C. Blumenthal, *Progress in Crystal Growth and Characterization of Materials*, 1980, **3**, 49-64.
230. L. C. Bonar, A. H. Roufosse, W. K. Sabine, M. D. Grynpas and M. J. Glimcher, *Calcified Tissue International*, 1983, **35**, 202-209.
231. J. D. Termine, R.A. Peckauskas. and A. S. Posner, *Archives of Biochemistry and Biophysics*, 1970, **140**, 318-325.
232. S. Weiner and H. D. Wagner, *Annual Review of Materials Science*, 1998, **28**, 271-298.
233. H. H. Roseberry, A. B. Hastings and J. K. Morse, *Journal of Biological Chemistry*, 1931, **90**, 395-407.

234. R. A. Robinson, *The Journal of bone and joint surgery. American volume*, 1952, **34-A**, 389-435.
235. D. A. Cameron, *Clinical orthopaedics and related research*, 1963, **26**, 199-228.
236. S. S. Jee, R. K. Kasinath, E. DiMasi, Y.-Y. Kim and L. Gower, *Crystengcomm*, 2011, **13**, 2077-2083.
237. W. J. Landis, M. J. Song, A. Leith, L. McEwen and B. F. McEwen, *Journal of Structural Biology*, 1993, **110**, 39-54.
238. S. Lees, *Connective Tissue Research*, 1987, **16**, 281-303.
239. J. Mahamid, A. Sharir, D. Gur, E. Zelzer, L. Addadi and S. Weiner, *Journal of Structural Biology*, 2011, **174**, 527-535.
240. R. Felix and H. Fleisch, *Calcified Tissue International*, 1975, **21**, 344-348.
241. R. E. Wuthier, *Clinical orthopaedics and related research*, 1982, 219-242.
242. H. C. Anderson, R. Garimella and S. E. Tague, *Frontiers in Bioscience-Landmark*, 2005, **10**, 822-837.
243. J. P. Simmer and A. G. Fincham, *Critical Reviews in Oral Biology and Medicine*, 1995, **6**, 84-108.
244. C. E. Smith, *Critical Reviews in Oral Biology & Medicine*, 1998, **9**, 128-161.
245. H. C. Margolis, E. Beniash and C. E. Fowler, *Journal of Dental Research*, 2006, **85**, 775-793.
246. H. C. Anderson, *Clinical orthopaedics and related research*, 1995, 266-280.
247. A. S. Deshpande and E. Beniash, *Crystal Growth & Design*, 2008, **8**, 3084-3090.
248. T. Saito, A. L. Arsenault, M. Yamauchi, Y. Kuboki and M. A. Crenshaw, *Bone*, 1997, **21**, 305-311.
249. A. Veis, in *Biomineralization*, eds. P. M. Dove, J. J. DeYoreo and S. Weiner, Mineralogical Soc Amer, Chantilly, Editon edn., 2003, vol. 54, pp. 249-289.
250. D. Toroian, J. E. Lim and P. A. Price, *Journal of Biological Chemistry*, 2007, **282**, 22437-22447.
251. F. Nudelman, P. H. H. Bomans, A. George, G. de With and N. Sommerdijk, *Faraday Discussions*, 2012, **159**, 357-370.
252. P. A. Price, D. Toroian and J. E. Lim, *Journal of Biological Chemistry*, 2009, **284**, 17092-17101.
253. Y. Wang, T. Azais, M. Robin, A. Vallee, C. Catania, P. Legriel, G. Pehau-Arnaudet, F. Babonneau, M.-M. Giraud-Guille and N. Nassif, *Nature Materials*, 2012, **11**, 724-733.
254. A. Bigi, E. Boanini, B. Bracci, G. Falini and K. Rubini, *Journal of Inorganic Biochemistry*, 2003, **95**, 291-296.
255. E. M. Burke, Y. Guo, L. Colon, M. Rahima, A. Veis and G. H. Nancollas, *Colloids and Surfaces B-Biointerfaces*, 2000, **17**, 49-57.
256. A. Peytcheva and M. Antonietti, *Angewandte Chemie-International Edition*, 2001, **40**, 3380-3383.
257. M. D. Sikiric and H. Furedi-Milhofer, *Advances in Colloid and Interface Science*, 2006, **128**, 135-158.
258. A. Tsortos and G. H. Nancollas, *Journal of Colloid and Interface Science*, 2002, **250**, 159-167.

259. H. K. Christenson, *Journal of Physics-Condensed Matter*, 2001, **13**, R95-R133.
260. S. Singh, P. Bhardwaj, V. Singh, S. Aggarwal and U. K. Mandal, *Journal of Colloid and Interface Science*, 2008, **319**, 322-329.
261. G. K. Lim, J. Wang, S. C. Ng, C. H. Chew and L. M. Gan, *Biomaterials*, 1997, **18**, 1433-1439.
262. Y. J. Wang, S. H. Zhang, K. Wei, N. R. Zhao, J. D. Chen and X. D. Wang, *Materials Letters*, 2006, **60**, 1484-1487.
263. S. Sadasivan, D. Khushalani and S. Mann, *Chemistry of Materials*, 2005, **17**, 2765-2770.
264. M. Antonietti, M. Breulmann, C. G. Goltner, H. Colfen, K. K. W. Wong, D. Walsh and S. Mann, *Chemistry-a European Journal*, 1998, **4**, 2493-2500.
265. D. Walsh, J. D. Hopwood and S. Mann, *Science*, 1994, **264**, 1576-1578.
266. M. Sauer, T. Haefele, A. Graff, C. Nardin and W. Meier, *Chemical Communications*, 2001, 2452-2453.
267. B. R. Heywood and E. D. Eanes, *Calcified Tissue International*, 1987, **41**, 192-201.
268. B. R. Heywood and E. D. Eanes, *Calcified Tissue International*, 1992, **50**, 149-156.
269. G. Falini, M. Gazzano and A. Ripamonti, *Journal of Materials Chemistry*, 2000, **10**, 535-538.
270. A. Ethirajan, U. Ziener, A. Chuvilin, U. Kaiser, H. Colfen and K. Landfester, *Advanced Functional Materials*, 2008, **18**, 2221-2227.
271. K. Teshima, M. Sakurai, S. Lee, K. Yubuta, S. Ito, T. Suzuki, T. Shishido, M. Endo and S. Oishi, *Crystal Growth & Design*, 2009, **9**, 650-652.
272. C. R. Martin, *Science*, 1994, **266**, 1961-1966.
273. G. E. J. Poinern, N. Ali and D. Fawcett, *Materials*, 2011, **4**, 487-526.
274. G. D. Sulka and K. G. Parkola, *Thin Solid Films*, 2006, **515**, 338-345.
275. X. H. Wang, C. Y. Li, L. J. Ma, H. Cao and B. H. Zhang, *Surface Review and Letters*, 2009, **16**, 73-78.
276. D. D. Li, R. S. Thompson, G. Bergmann and J. G. Lu, *Advanced Materials*, 2008, **20**, 4575-4578.
277. Y. Li, Z. Ling, S. Chen and J. Wang, *Nanotechnology*, 2008, **19**, 225604.
278. Z. Li and K. Huang, *Journal of the Brazilian Chemical Society*, 2007, **18**, 406-409.
279. N. V. Myung, J. Lim, J. P. Fleurial, M. Yun, W. West and D. Choi, *Nanotechnology*, 2004, **15**, 833-838.
280. A. Huczko, *Applied Physics a-Materials Science & Processing*, 2000, **70**, 365-376.
281. U. o. Bath, *Report on Self-ordered Porous Alumina Template Technology*, http://wiki.bath.ac.uk/download/attachments/1278052/N2T2+Deliverable+WP1.1D3.pdf?version=1&modificationDate=1169224479000.
282. W. S. Chae, S. J. Im, J. K. Lee and Y. R. Kim, *Bulletin of the Korean Chemical Society*, 2005, **26**, 409-412.
283. H. Masuda, M. Ohya, K. Nishio, H. Asoh, M. Nakao, M. Nohtomi, A. Yokoo and T. Tamamura, *Japanese Journal of Applied Physics Part 2-Letters*, 2000, **39**, L1039-L1041.
284. W. Lee, R. Ji, U. Gosele and K. Nielsch, *Nature Materials*, 2006, **5**, 741-747.

285. H. Masuda and M. Satoh, *Japanese Journal of Applied Physics Part 2-Letters*, 1996, **35**, 126-129.
286. H. Masuda and K. Fukuda, *Science*, 1995, **268**, 1466-1468.
287. J. H. Yuan, F. Y. He, D. C. Sun and X. H. Xia, *Chemistry of Materials*, 2004, **16**, 1841-1844.
288. L. F. Marsal, L. Vojkuvka, P. Formentin, J. Pallares and J. Ferre-Borrull, *Optical Materials*, 2009, **31**, 860-864.
289. S. Koutsopoulos, *Journal of Biomedical Materials Research*, 2002, **62**, 600-612.
290. S. Weiner, W. Traub and H. D. Wagner, *Journal of Structural Biology*, 1999, **126**, 241-255.
291. K. Makrodimitris, D. L. Masica, E. T. Kim and J. J. Gray, *Journal of the American Chemical Society*, 2007, **129**, 13713-13722.
292. Vanderdr.A, *Philips Research Reports*, 1967, **22**.
293. C. V. Thompson, *Annual Review of Materials Science*, 2000, **30**, 159-190.
294. D. Jaschouz, O. Paris, P. Roschger, H. S. Hwang and P. Fratzl, *Journal of Applied Crystallography*, 2003, **36**, 494-498.
295. W. J. Landis, K. J. Hodgens, M. J. Song, J. Arena, S. Kiyonaga, M. Marko, C. Owen and B. F. McEwen, *Journal of Structural Biology*, 1996, **117**, 24-35.
296. W. Zhang, Z. L. Huang, S. S. Liao and F. Z. Cui, *Journal of the American Ceramic Society*, 2003, **86**, 1052-1054.
297. B. Yang and F. Z. Cui, *Current Applied Physics*, 2007, **7**, e2-e5.
298. C. J. Newcomb, R. Bitton, Y. S. Velichko, M. L. Snead and S. I. Stupp, *Small*, 2012, **8**, 2195-2202.
299. F. K. Wang, B. R. Cao and C. B. Mao, *Chemistry of Materials*, 2010, **22**, 3630-3636.
300. T. He, G. Abbineni, B. R. Cao and C. B. Mao, *Small*, 2010, **6**, 2230-2235.
301. B. Cao and C. Mao, *Langmuir*, 2007, **23**, 10701-10705.
302. J. Moradianoldak, S. Weiner, L. Addadi, W. J. Landis and W. Traub, *Connective Tissue Research*, 1991, **25**, 219-228.
303. J. H. Zhan, Y. H. Tseng, J. C. C. Chan and C. Y. Mou, *Advanced Functional Materials*, 2005, **15**, 2005-2010.
304. N. Ito, M. Kamitakahara, S. Murakami, N. Watanabe and K. Ioku, *Journal of the Ceramic Society of Japan*, 2010, **118**, 762-766.
305. M. Jevtic, M. Mitric, S. Skapin, B. Jancar, N. Ignjatovic and D. Uskokovic, *Crystal Growth & Design*, 2008, **8**, 2217-2222.
306. J. H. Tao, W. G. Jiang, H. H. Pan, X. R. Xu and R. K. Tang, *Journal of Crystal Growth*, 2007, **308**, 151-158.
307. K. Teshima, S. Lee, M. Sakurai, Y. Kameno, K. Yubuta, T. Suzuki, T. Shishido, M. Endo and S. Oishi, *Crystal Growth & Design*, 2009, **9**, 2937-2940.
308. F. Z. Ren, Y. H. Ding, X. Ge, X. Lu, K. F. Wang and Y. Leng, *Journal of Crystal Growth*, 2012, **349**, 75-82.
309. Y. Zhang and J. Lu, *Crystal Growth & Design*, 2008, **8**, 2101-2107.
310. M. Iijima and J. Moradian-Oldak, *Journal of Materials Chemistry*, 2004, **14**, 2189-2199.
311. X. Lu, Y.-b. Wang, J.-x. Wang, S.-x. Qu, J. Weng, R.-l. Xin and Y. Leng, *Journal of Crystal Growth*, 2006, **297**, 396-402.

312. D. G. A. Nelson and J. D. McLean, *Calcified Tissue International*, 1984, **36**, 219-232.
313. M. J. Arellano-Jimenez, R. Garcia-Garcia and J. Reyes-Gasga, *Journal of Physics and Chemistry of Solids*, 2009, **70**, 390-395.
314. M. E. Fernandez, C. Zorilla-Cangas, R. Garcia-Garcia, J. A. Ascencio and J. Reyes-Gasga, *Acta Crystallographica Section B-Structural Science*, 2003, **59**, 175-181.
315. T. Ogino, T. Suzuki and K. Sawada, *Geochimica Et Cosmochimica Acta*, 1987, **51**, 2757-2767.
316. R. A. Feely, C. L. Sabine, K. Lee, W. Berelson, J. Kleypas, V. J. Fabry and F. J. Millero, *Science*, 2004, **305**, 362-366.
317. K. H. Büchel, H.-H. Moretto and D. Werner, *Industrial inorganic chemistry*, Wiley-Vch, 2008.
318. F. Lippmann, *Berlin: Springer-Verlag*, 1973.
319. A. J. Xie, Y. H. Shen, C. Y. Zhang, Z. W. Yuan, X. M. Zhu and Y. M. Yang, *Journal of Crystal Growth*, 2005, **285**, 436-443.
320. Y. Kojima, A. Kawanobe, T. Yasue and Y. Arai, *Nippon Seramikkusu Kyokai Gakujutsu Ronbunshi-Journal of the Ceramic Society of Japan*, 1994, **102**, 1128-1136.
321. A. M. Shaikh, *Journal of Applied Crystallography*, 1990, **23**, 263-265.
322. N. B. J. Hetherington, 2010.
323. E. Mugnaioli, I. Andrusenko, T. Schaler, N. Loges, R. E. Dinnebier, M. Panthfer, W. Tremel and U. Kolb, *Angewandte Chemie International Edition*, 2012.
324. J. H. E. Cartwright, A. G. Checa, J. D. Gale, D. Gebauer and C. I. Sainz-Diaz, *Angewandte Chemie-International Edition*, 2012, **51**, 11960-11970.
325. A. P. Vinogradov, Sears Foundation for Marine Research, Yale University, New Haven, CT, 1953.
326. J. Ihli, A. N. Kulak and F. C. Meldrum, *Chemical Communications*, 2013, **49**, 3134-3136.
327. E. Beniash, L. Addadi and S. Weiner, *Journal of Structural Biology*, 1999, **125**, 50-62.
328. Y. Levi-Kalisman, S. Raz, S. Weiner, L. Addadi and I. Sagi, *Advanced Functional Materials*, 2002, **12**, 43-48.
329. S. Raz, P. C. Hamilton, F. H. Wilt, S. Weiner and L. Addadi, *Advanced Functional Materials*, 2003, **13**, 480-486.
330. R. S. K. Lam, J. M. Charnock, A. Lennie and F. C. Meldrum, *Crystengcomm*, 2007, **9**, 1226-1236.
331. D. Gebauer, P. N. Gunawidjaja, J. Y. P. Ko, Z. Bacsik, B. Aziz, L. J. Liu, Y. F. Hu, L. Bergstrom, C. W. Tai, T. K. Sham, M. Eden and N. Hedin, *Angewandte Chemie-International Edition*, 2010, **49**, 8889-8891.
332. B. Hasse, H. Ehrenberg, J. C. Marxen, W. Becker and M. Epple, *Chemistry-a European Journal*, 2000, **6**, 3679-3685.
333. J. C. Marxen, W. Becker, D. Finke, B. Hasse and M. Epple, *Journal of Molluscan Studies*, 2003, **69**, 113-121.
334. Q. Shen, H. Wei, Y. Zhou, Y. P. Huang, H. R. Yang, D. J. Wang and D. F. Xu, *Journal of Physical Chemistry B*, 2006, **110**, 2994-3000.
335. A. Katsifaras and N. Spanos, *Journal of Crystal Growth*, 1999, **204**, 183-190.

336. T. Y. J. Han and J. Aizenberg, *Chemistry of Materials*, 2008, **20**, 1064-1068.
337. X. G. Cheng, P. L. Varona, M. J. Olszta and L. B. Gower, *Journal of Crystal Growth*, 2007, **307**, 395-404.
338. Schroede.Jh, E. J. Dwornik and J. J. Papike, *Geological Society of America Bulletin*, 1969, **80**, 1613-1616.
339. K. E. Chave, *Journal of Geology*, 1954, **62**, 266-283.
340. W. D. Bischoff, F. T. Mackenzie and F. C. Bishop, *Geochimica Et Cosmochimica Acta*, 1987, **51**, 1413-1423.
341. S. H. Yu, H. Colfen, A. W. Xu and W. F. Dong, *Crystal Growth & Design*, 2004, **4**, 33-37.
342. C. L. Freeman, J. H. Harding, D. Quigley and P. M. Rodger, *Journal of Physical Chemistry C*, 2011, **115**, 8175-8183.
343. A. W. Xu, M. Antonietti, H. Colfen and Y. P. Fang, *Advanced Functional Materials*, 2006, **16**, 903-908.
344. S. X. Li, L. Yu, F. Geng, L. J. Shi, L. Q. Zheng and S. L. Yuan, *Journal of Crystal Growth*, 2010, **312**, 1766-1773.
345. Y. Yao, W. Y. Dong, S. M. Zhu, X. H. Yu and D. Y. Yan, *Langmuir*, 2009, **25**, 13238-13243.
346. N. Kroger, R. Deutzmann and M. Sumper, *Science*, 1999, **286**, 1129-1132.
347. N. Kroger, R. Deutzmann, C. Bergsdorf and M. Sumper, *Proceedings of the National Academy of Sciences of the United States of America*, 2000, **97**, 14133-14138.
348. M. B. Dickerson, K. H. Sandhage and R. R. Naik, *Chemical Reviews*, 2008, **108**, 4935-4978.
349. M. Sumper and N. Kroger, *Journal of Materials Chemistry*, 2004, **14**, 2059-2065.
350. M. M. Tlili, M. Ben Amor, C. Gabrielli, S. Joiret, G. Maurin and P. Rousseau, *Journal of Raman Spectroscopy*, 2002, **33**, 10-16.
351. J. Urmos, S. K. Sharma and F. T. Mackenzie, *American Mineralogist*, 1991, **76**, 641-646.
352. C. Gabrielli, R. Jaouhari, S. Joiret and G. Maurin, *Journal of Raman Spectroscopy*, 2000, **31**, 497-501.
353. N. Nassif, N. Pinna, N. Gehrke, M. Antonietti, C. Jager and H. Colfen, *Proceedings of the National Academy of Sciences of the United States of America*, 2005, **102**, 12653-12655.
354. E. Brunner, K. Lutz and M. Sumper, *Physical Chemistry Chemical Physics*, 2004, **6**, 854-857.
355. H. Daiguji, E. Matsuoka and S. Muto, *Soft Matter*, 2010, **6**, 1892-1897.
356. A. I. Petrov, A. A. Antipov and G. B. Sukhorukov, *Macromolecules*, 2003, **36**, 10079-10086.
357. A. Sepehrianazar, Hacettepe University, 2008.
358. J. J. Molino Cornejo, E. Matsuoka and H. Daiguji, *Soft Matter*, 2011, **7**, 1897-1902.
359. E. DiMasi, S. Y. Kwak, F. F. Amos, M. J. Olszta, D. Lush and L. B. Gower, *Phys. Rev. Letts.*, 2006, **97**, 4.
360. B. Njegic-Dzakula, L. Brecevic, G. Falini and D. Kralj, *Crystal Growth & Design*, 2009, **9**, 2425-2434.

361. D. L. Masica, S. B. Schrier, E. A. Specht and J. J. Gray, *Journal of the American Chemical Society*, 2010, **132**, 12252-12262.
362. Q. Yu, H. D. Ou, R. Q. Song and A. W. Xu, *Journal of Crystal Growth*, 2006, **286**, 178-183.
363. J. Donners, B. R. Heywood, E. W. Meijer, R. J. M. Nolte and N. Sommerdijk, *Chem. Eur. J.*, 2002, **8**, 2561-2567.
364. G. F. Xu, N. Yao, I. A. Aksay and J. T. Groves, *Journal of the American Chemical Society*, 1998, **120**, 11977-11985.
365. F. F. Amos, D. M. Sharbaugh, D. R. Talham, L. B. Gower, M. Fricke and D. Volkmer, *Langmuir*, 2007, **23**, 1988-1994.
366. E. DiMasi, V. M. Patel, M. Sivakumar, M. J. Olszta, Y. P. Yang and L. B. Gower, *Langmuir*, 2002, **18**, 8902-8909.
367. C. Zhong and C. C. Chu, *Langmuir*, 2009, **25**, 3045-3049.
368. T. Kato, A. Sugawara and N. Hosoda, *Advanced Materials*, 2002, **14**, 869-877.
369. T. Kato, T. Sakamoto and T. Nishimura, *MRS bulletin*, 210, **35**, 127-132.
370. A. Sugawara and T. Kato, *Chemical Communications*, 2000, 487-488.
371. N. Hosoda, A. Sugawara and T. Kato, *Macromolecules*, 2003, **36**, 6449-6452.
372. S. Babu Mukkamala and A. K. Powell, *Chemical Communications*, 2004, 918-919.
373. M. Balz, H. A. Therese, J. X. Li, J. S. Gutmann, M. Kappl, L. Nasdala, W. Hofmeister, H. J. Butt and W. Tremel, *Advanced Functional Materials*, 2005, **15**, 683-688.
374. Y. W. Fan and R. Z. Wang, *Advanced Materials*, 2005, **17**, 2384-2388.
375. S. Kumar, T. Ito, Y. Yanagihara, Y. Oaki, T. Nishimura and T. Kato, *Crystengcomm*, 2010, **12**, 2021-2024.
376. K. W. Kolasinski, *Current Opinion in Solid State & Materials Science*, 2006, **10**, 182-191.
377. T. X. Wang, A. Reinecke and H. Colfen, *Langmuir*, 2006, **22**, 8986-8994.
378. W. Zhu, J. Lin and C. Cai, *Journal of Materials Chemistry*, 2011, **22**, 3939-3947.
379. M. Balz, H. A. Therese, M. Kappl, L. Nasdala, W. Hofmeister, H. J. Butt and W. Tremel, *Langmuir*, 2005, **21**, 3981-3986.
380. R. Piazza, *Curr. Op. Coll. Int. Sci.*, 2004, **8**, 515-522.
381. F. J. Zhang, S. Weggler, M. J. Ziller, L. Ianeselli, B. S. Heck, A. Hildebrandt, O. Kohlbacher, M. W. A. Skoda, R. M. J. Jacobs and F. Schreiber, *Proteins-Struc. Func. Bioinform.*, 2010, **78**, 3450-3457.
382. S. C. Benson, N. C. Benson and F. Wilt, *Journal of Cell Biology*, 1986, **102**, 1878-1886.
383. S. Weiner, *American Zoologist*, 1984, **24**, 945-951.
384. S. Weiner, *Crc Critical Reviews in Biochemistry*, 1986, **20**, 365-408.
385. B. J. McKenna, H. Birkedal, M. H. Bartl, T. J. Deming and G. D. Stucky, *Angew. Chem. Int. Ed.*, 2004, **43**, 5652-5655.
386. C. R. MacKenzie, S. M. Wilbanks and K. M. McGrath, *Journal of Materials Chemistry*, 2004, **14**, 1238-1244.
387. E. Dujardin and S. Mann, *Advanced Materials*, 2002, **14**, 775.
388. A. R. Studart, *Advanced Materials*, 2012.

389. B. L. Smith, T. E. Schaffer, M. Viani, J. B. Thompson, N. A. Frederick, J. Kindt, A. Belcher, G. D. Stucky, D. E. Morse and P. K. Hansma, *Nature*, 1999, **399**, 761-763.

390. S. Kamat, X. Su, R. Ballarini and A. H. Heuer, *Nature*, 2000, **405**, 1036-1040.

391. X. D. Li, W. C. Chang, Y. J. Chao, R. Z. Wang and M. Chang, *Nano Letters*, 2004, **4**, 613-617.

392. A. P. Jackson, J. F. V. Vincent and R. M. Turner, *Proceedings of the Royal Society of London Series B-Biological Sciences*, 1988, **234**, 415-440.

393. H. J. Gao, B. H. Ji, I. L. Jager, E. Arzt and P. Fratzl, *Proceedings of the National Academy of Sciences of the United States of America*, 2003, **100**, 5597-5600.

394. L. N. Niu, K. Jiao, Y. P. Qi, C. K. Y. Yiu, H. Ryou, D. D. Arola, J. H. Chen, L. Breschi, D. H. Pashley and F. R. Tay, *Angewandte Chemie-International Edition*, 2011, **50**, 11688-11691.

395. P. Fratzl, H. S. Gupta, E. P. Paschalis and P. Roschger, *Journal of Materials Chemistry*, 2004, **14**, 2115-2123.

396. J. Orgel, T. C. Irving, A. Miller and T. J. Wess, *Proceedings of the National Academy of Sciences of the United States of America*, 2006, **103**, 9001-9005.

397. P. Fratzl, N. Fratzl-Zelman, K. Klaushofer, G. Vogl and K. Koller, *Calcified Tissue International*, 1991, **48**, 407-413.

398. S. Lees and H. A. Mook, *Calcified Tissue International*, 1986, **39**, 291-292.

399. P. Fratzl, N. Fratzlzelman and K. Klaushofer, *Biophysical Journal*, 1993, **64**, 260-266.

400. J. N. Cha, G. D. Stucky, D. E. Morse and T. J. Deming, *Nature*, 2000, **403**, 289-292.

401. H. Ehrlich, R. Deutzmann, E. Brunner, E. Cappellini, H. Koon, C. Solazzo, Y. Yang, D. Ashford, J. Thomas-Oates, M. Lubeck, C. Baessmann, T. Langrock, R. Hoffmann, G. Worheide, J. Reitner, P. Simon, M. Tsurkan, A. V. Ereskovsky, D. Kurek, V. V. Bazhenov, S. Hunoldt, M. Mertig, D. V. Vyalikh, S. L. Molodtsov, K. Kummer, H. Worch, V. Smetacek and M. J. Collins, *Nature Chemistry*, 2010, **2**, 1084-1088.

402. I. E. Chesnick, J. T. Mason, A. A. Giuseppetti, N. Eidelman and K. Potter, *Biophysical Journal*, 2008, **95**, 2017-2026.

403. S. Lees, *Biophysical Journal*, 2003, **85**, 204-207.

404. G. Falini, *International Journal of Inorganic Materials*, 2000, **2**, 455-461.

405. G. Falini, S. Fermani, M. Gazzano and A. Ripamonti, *Chemistry-a European Journal*, 1997, **3**, 1807-1814.

406. G. Falini, M. Gazzano and A. Ripamonti, *Advanced Materials*, 1994, **6**, 46-48.

407. G. Falini, S. Fermani, M. Gazzano and A. Ripamonti, *Journal of the Chemical Society-Dalton Transactions*, 2000, 3983-3987.

408. V. Drits, J. Srodon and D. Eberl, *Clays and Clay Minerals*, 1997, **45**, 461-475.

409. N. C. Blumenthal, V. Cosma and E. Gomes, *Calcified Tissue International*, 1991, **48**, 440-442.

410. D. C. Bassett, B. Marelli, S. N. Nazhat and J. E. Barralet, *Advanced Functional Materials*, 2012, **22**, 3460-3469.
411. E. Dalas, J. Kallitsis and P. G. Koutsoukos, *Journal of Crystal Growth*, 1988, **89**, 287-294.
412. F. Nudelman, E. Sonmezler, P. H. H. Bomans, G. de With and N. Sommerdijk, *Nanoscale*, 2010, **2**, 2436-2439.
413. N. H. de Leeuw and S. C. Parker, *Journal of Physical Chemistry B*, 1998, **102**, 2914-2922.
414. D. Chakraborty, V. K. Agarwal, S. K. Bhatia and J. Bellare, *Industrial & Engineering Chemistry Research*, 1994, **33**, 2187-2197.
415. Q. Hu, J. Zhang, H. Teng and U. Becker, *American Mineralogist*, 2012, **97**, 1437-1445.
416. C. Y. Tai and F. B. Chen, *AIChE Journal*, 1998, **44**, 1790-1798.
417. F. Caruso, R. A. Caruso and H. Mohwald, *Science*, 1998, **282**, 1111-1114.
418. M. Steinhart, R. B. Wehrspohn, U. Gosele and J. H. Wendorff, *Angewandte Chemie-International Edition*, 2004, **43**, 1334-1344.
419. Y. G. Sun, B. Mayers and Y. N. Xia, *Advanced Materials*, 2003, **15**, 641-646.
420. C. Gautier, P. J. Lopez, M. Hemadi, J. Livage and T. Coradin, *Langmuir*, 2006, **22**, 9092-9095.
421. C. R. Martin, L. S. Vandyke, Z. H. Cai and W. B. Liang, *Journal of the American Chemical Society*, 1990, **112**, 8976-8977.
422. Y.-L. Chen, X.-F. Pei, Y. Jiang, L. Zhou, J. Zhang, L.-F. Bi, H.-T. Li and Y.-G. Yang, *Chinese Journal of Chemistry*, 2008, **26**, 1323-1326.
423. S. Banerjee and A. Datta, *Langmuir*, 2010, **26**, 1172-1176.
424. Z. H. Cai and C. R. Martin, *Journal of the American Chemical Society*, 1989, **111**, 4138-4139.
425. R. V. Parthasarathy and C. R. Martin, *Chemistry of Materials*, 1994, **6**, 1627-1632.
426. G. Decher, J. D. Hong and J. Schmitt, *Thin Solid Films*, 1992, **210**, 831-835.
427. G. Decher, *Science*, 1997, **277**, 1232-1237.
428. G. Decher, M. Eckle, J. Schmitt and B. Struth, *Current Opinion in Colloid & Interface Science*, 1998, **3**, 32-39.
429. P. T. Hammond, *Advanced Materials*, 2004, **16**, 1271-1293.
430. M. Schonhoff, *Current Opinion in Colloid & Interface Science*, 2003, **8**, 86-95.
431. R. Kugler, J. Schmitt and W. Knoll, *Macromolecular Chemistry and Physics*, 2002, **203**, 413-419.
432. L. Y. Wang, M. Schonhoff and H. Mohwald, *Journal of Physical Chemistry B*, 2002, **106**, 9135-9142.
433. A. P. Ramos, F. G. Doro, E. Tfouni, R. R. Goncalves and M. E. D. Zaniquelli, *Thin Solid Films*, 2008, **516**, 3256-3262.
434. J. Tang, D.-M. Sun, W.-Y. Qian, R.-R. Zhu, X.-Y. Sun, W.-R. Wang, K. Li and S.-L. Wang, *Biological Trace Element Research*, 2012, **147**, 408-417.
435. M. Fukuhara, N. Fujii, J. Takada and Y. Kusano, *Journal of the American Ceramic Society*, 1998, **81**, 2746-2748.

436. W. Wei, G.-H. Ma, G. Hu, D. Yu, T. McLeish, Z.-G. Su and Z.-Y. Shen, *Journal of the American Chemical Society*, 2008, **130**, 15808-15810.

437. H. Sugihara, K. Inoue, M. Nakayama, T. Inoue, K. Nagaoka and Y. Takita, *Materials Letters*, 2009, **63**, 322-324.

438. N. Wada, S. Suda, K. Kanamura and T. Umegaki, *Journal of Colloid and Interface Science*, 2004, **279**, 167-174.

439. S. K. Zhang and K. E. Gonsalves, *Materials Science & Engineering C-Biomimetic Materials Sensors and Systems*, 1995, **3**, 117-124.

440. L. Vayssieres, *Advanced Materials*, 2003, **15**, 464-466.

441. F. Zhang, Y. Yiu, A. C. Aronson and S. S. Wong, *Journal of Physical Chemistry C*, 2008, **112**, 14816-14824.

442. F. Kratz, *Journal of Controlled Release*, 2008, **132**, 171-183.

Appendix: List of Abbreviations

AAO:	anodic aluminium oxide
ACC:	amorphous calcium carbonate
ACP:	amorphous calcium phosphate
ACS:	amorphous calcium sulphate
CaP:	calcium phosphate
ClAP :	chlorapatite
CCD:	charge-coupled device
CO_3AP:	carbonated apatite
CTAB:	cetyltrimethylammonium bromide
DCM:	dichloromethane
DCPA:	dicalcium phosphate anhydrous
DCPD:	dicalcium phosphate dihydrate
DI:	deionised
DOLLOP:	dynamically ordered liquid-like oxyanion polymer
DLS:	dynamic light scattering
DSC:	differential scanning calorimetry
DUBBLE:	Dutch-Belgian beamLine
EELS:	electron energy-loss spectrometry
ED:	electron diffraction
EDX:	energy dispersive X-ray spectroscopy
EDTA:	ethylenediaminetetraacetic acid
ESRF:	European synchrotron research facility
EXAFS:	extended X-ray absorption fine structure
FAP:	fluorapatite
FEGSEM:	field emission gun scanning electron microscopy
FTIR:	fourier transform infrared
HAP:	hydroxyapatite
HRTEM:	high resolution transmission electron microscopy
IR:	infrared
IDP :	intrinsically disordered proteins
LACC:	liquid amorphous calcium carbonate

LBL:	layer-by-layer
LCP:	liquid crystalline phase
LCPA:	long chained polyamines
LDSAED:	low-dose selected-area electron diffraction
MCPM:	monocalcium phosphate monohydrate
MRM:	magnetic resonance microscopy
OCP:	octacalcium phosphate
PAA:	poly(acrylic acid)
PAH:	Poly(allylamine hydrochloride)
PAM:	porous alumina membranes
PAsp:	polyaspartic acid
PhD	Doctor of Philosophy
PILP:	polymer-induced liquid-precursor
PNC:	prenucleation clusters
Poly-Glu:	poly-L-glutamate
PSS:	poly(styrenesulfonate)
PVA:	polyvinyl alcohol
SAED:	selected area electron diffraction
SAM:	self assembled monolayers
SAXS:	small-angle X-ray scattering
STEM:	scanning transmission electron microscopy
SLS:	solution-liquid-solid
SPS:	solution precursor solid
TCP:	tricalcium phosphate
TE	membranes: track-etched membranes
TEM:	transmission electron microscopy
TGA:	thermogravimetric analysis
TTCP:	tetracalcium phosphate
VLS:	vapour-liquid-solid
WAXS:	wide-angle X-ray scattering
XRD:	X-ray diffraction
XAS:	X-ray absorption spectroscopy